Facultad de Física
Departamento de Fisica Atómica, Molecular y Nuclear

TRITIUM: Design, Construction and Commissioning of an In-Water Tritium Detector

Marcos Martínez Roig

Doctorado en Física
7th October 2022

Under the supervison of:
José Díaz Medina
Nadia Yahlali Haddou

NADIA YAHLALI HADDOU, *Profesora Titular y* JOSÉ DÍAZ MEDINA, *Catedrático de Universidad, ambos miembros del Departamento de Física Atómica, Molecular y Nuclear de la Universitat de València*

CERTIFICAN:

Que la presente memoria "Design, Construction and Commissioning of an In-water Tritium Detector" ha sido realizada bajo nuestra dirección en el Departamento de Física Atómica, Molecular y Nuclear de la Universitat de València y el Instituto de Física Corpuscular (Centro mixto UV-CSIC) por D. Marcos Martínez Roig y constituye su Tesis Doctoral para optar al título de Doctor por la Universitat de València una vez cursados los estudios en el Doctorado en Física. Esta tesis contiene información sometida a la solicitud de patentes.

Y para que así conste, en cumplimiento de la legislación vigente, firmamos el presente certificado en Valencia a 11 de julio de dos mil veintidós.

Fdo.:José Díaz Medina   Fdo: Nadia Yahlali Haddou

Dedicated to
my family

Sometimes it is the people no one imagines anything of
who do the things that no one can imagine.

"Alan Turing"

Acknowledgements

Muchas personas han colaborado a lo largo de estos cuatro años para hacer posible este trabajo. En primer lugar, me gustaría agradecer enormemente a mis tutores, Jose Díaz Medina y Nadia Yahlali Haddou, por intentar transmitirme en todo momento tantos conocimientos como les ha sido posible. También agradecer su tiempo ya que, a pesar de sus muchas obligaciones, siempre han encontrado un hueco en sus agendas para ayudarme rápidamente con cualquier problema. Estoy muy agradecido por su cercanía y sus consejos, tanto en el mundo laboral como en la vida personal, los cuales me han ayudado a llegar a donde estoy ahora. Gracias de todo corazón por todo, nada de esto hubiera sido posible sin vosotros.

En segundo lugar, me gustaría agradecer a mis compañeros de laboratorio Andrea Esparcia Córcoles, Ana Bueno Fernández, Marcos Llanos Expósito y sobre todo a Mireia Simeó Vinaixa, con quienes los largos e interminables trabajos de laboratorio han sido mucho más fáciles, ayudándome en todo momento a comprender y mejorar los resultados experimentales obtenidos. También me gustaría agradecer a los técnicos e investigadores del LARAM, Clodoaldo Roldán García, Teresa Cámara García, Vanesa Delgado Belmar y Rosa María Rodríguez Galán, por su ayuda, su tiempo y sus esfuerzos en hacer que todo esto haya sido posible.

En tercer lugar, me gustaría agradecer a todos los investigadores del proyecto TRITIUM, gente que me ha acogido con los brazos abiertos,

que me ha ayudado en todo lo que les ha sido posible y con la que he tenido el placer de trabajar y aprender a su lado. Me gustaría agradecer en especial a Carlos Azevedo, junto al cual tuve el placer de trabajar. Gracias por todo el tiempo que invertiste en formarme en temas tan interesantes y dispares como programación con Arduino y Rasberry Pi (llegando a realizar proyectos en común) o simulaciones con el paquete de programación Geant4 (llegando a realizar mis propias simulaciones).

En cuarto lugar, me gustaría agradecer a David Calvo Díaz-Aldagalán, ingeniero del IFIC, por los diseños de las distintas PCBs utilizadas en el proyecto TRITIUM.

Finalmente, me gustaría dar las gracias a los investigadores de otros proyectos los cuales, pese a no ayudarme directamente en mi labor de investigación, han aportado a mi trabajo debido a las sinergias existentes entre los desarrollos experimentales de los proyectos:

- A los investigadores del proyecto DUNE, Anselmo Cervera, Miguel Angel García Peris y Justo Martín-Albo, los cuales me han ayudado con su tiempo, sus conocimientos y su instrumentación experimental a completar la caracterización de los SiPMs de TRITIUM.

- A los ingenieros del proyecto NEXT, Vicente Álvarez, Marc Querol, Javier Rodríguez y Sara Cárcel, con quienes he compartido laboratorio y, aun sin trabajar directamente con ellos, siempre han estado dispuestos a echarme una mano.

- A los investigadores del IFIMED, Gabriela Llosá, Ana Ros, Marina Borja, John Barrio, Rita Viegas y Jorge Roser e investigadores del proyecto ATLAS (Urmila Soldevila y Carlos Mariña) por prestarnos sus instalaciones y, en concreto, sus sistemas de control de temperatura los cual fueron necesario para la caracterización de los SiPMs.

- A los investigadores del laboratorio HYMNS, Ion Ladarescu y César

Domingo, quienes me ayudaron en mis primeros pasos con la electrónica PETsys además de asesorarme con las questiones que me han surgido a lo largo del camino.

- A los investigadores del ICMOL, Henk Bolink, Alejandra Soriano, Lidón Gil y Jorge Ferrando por ayudarnos con el protocolo de limpieza de las fibras centelleadoras además de permitirnos usar sus instalaciones.

- A toda la gente de los distintos departamentos del IFIC que me han ayudado con su tiempo y sus consejos. Me gustaría agradecer especialmente la ayuda de José Vicente Civera, Manolo Montserrate, José Luis Jordan y Daniel Tchogna del departamento de mecánica, Ximo Navajas, Ximo Nadal, Carlos Martínez y Francisco Javier Sánchez del departamento de informática y Manuel López, Jorge Nacher y José Mazorra del departamento de electrónica.

- A mis amigos del IFIC, Pepe, Kevin, José Antonio, Pablo, Stefan y Victor, los cuales, aun sin haber aportado directamente a mi trabajo, compartir mis días con ellos ha sido uno de los mayores apoyos de esta aventura. No solo me llevo amigos de esta etapa, me llevo una familia.

- A mi amigo, Galo, una amistad que empezó en el master, donde tuve el placer de compartir muchas de las duras horas de estudio, y continuó en el doctorado, donde hemos compartido muchos buenos momentos. Siento que esta amistad nos hemos ayudado a crecer mutuamente, tanto profesional como personalmente. Una amistad que, sinceramente, espero que dure para toda la vida.

- A todos los miembros de mi familia, quienes sin comprender exactamente en qué consiste mi trabajo, me han apoyado y animado ciegamente desde el principio. Fueron, son y serán una pieza imprescindible en todas las áreas de mi vida.

Finalmente me gustaría agradecer al programa INTERREG-SUDOE por financiar el proyecto TRITIUM, gracias al cual todo esto se ha podido materializar.

Abstract

In recent decades, many nuclear-based technologies have been developed and applied in various fields such as Energy, Medicine, Industry, etc. Due to nuclear applications, anthropogenic radioactive sources have emerged, which have led to the release of radioactive elements into the environment. Tritium is one of the most abundantly emitted radioisotopes by nuclear facilities and, specifically, by nuclear power plants. Large amounts of tritium are normally produced in the water of their cooling systems, which are subsequently discharged into the environment. As large releases of tritium are hazardous for human health and the environment, several regulations are issued around the world with the aim of controlling these radioactive emissions. The main ones are the European Directive 2013/51/Euratom which establishes the tritium limit for drinking water in Europe to 100 Bq/L and the Environmental Protection Agency (EPA) in the United States which limits tritium in drinking water to 20 nCi/L.

Due to the low energy of electrons emitted in the tritium decay, very sensitive detectors are needed for measuring tritium activity. The most widely used is liquid scintillation counting which is an offline method that requires a measurement time of 2 days or more, a time too long to detect a release issue in a nuclear power plant. Detectors based on solid scintillators are promising for building a tritium detector that works in quasi-real-time (less than 1 h). These detectors are being successfully developed for decades but without achieving the sensitivity required for the legal limits established

in Europe.

The results of the TRITIUM project are presented in this thesis. In the framework of this project, a quasi-real-time monitor for low tritium activities in water has been developed. This monitor is composed of several detection modules read out in parallel, a water purification system and a background rejection system. Each detection module is made up of hundreds of scintillating fibres read out by photosensors (PMTs or SiPM arrays).

The final objective of this monitor is radiological protection in the water-courses located in the vicinity of nuclear power plants. This monitor will provide an alarm in case of an unexpected tritium release that exceeds the legal limits established in Europe. The TRITIUM monitor is intended to be included in the early alarm system of Extremadura consisting of a network of detectors dedicated to control the impact of the Almaraz nuclear power plant on the environment.

Keywords: Very low-energy charged particle detectors, tritiated water, tritium detection, scintillating fibres, detector modelling and simulations, real-time radiation monitoring, environmental safety, radiological protection.

Acronyms and Symbols

Acronyms:

ALARA	—	As low as reasonably achievable
APD	—	Avalanche photodiode
BIXS	—	Beta-induced X-ray spectrometry
BWR	—	Boiling water reactor
CCD	—	Charge-coupled device
CNRS	—	Centre National de la Recherche Scientifique
CSN	—	Consejo de Seguridad Nuclear
DAQ	—	Data acquisition system
DOE	—	United States Department of Energy
EEC	—	European Economic Community
EIA	—	USA Energy Information Administration
EPA	—	USA Environmental Protection Agency
EU	—	European Union
EURATOM	—	European Atomic Energy Community
G − APD	—	Geiger avalanche photodiode
GCR	—	Gas-cooled reactor
HPGe	—	High purity germanium detector
HWR	—	Heavy water reactor
I3N	—	Institute for Nanostructures, Nanomodelling and Nanofabrication.
IAEA	—	International Atomic Energy Agency

IC	—	Ionization chamber
$ICRP$	—	International Commission on Radiological Protection
$ICRU$	—	International Commission of Radioactivity Units and Measurements
ISR	—	International Society of Radiology
$LARUEX$	—	Laboratorio de Radiactividad Ambiental de la Universidad de Extremadura
LED	—	Light-emitting diode
LSC	—	Liquid scintillation counting
LWR	—	Light water reactor
$MAPD$	—	Micro-pixel avalanche photodiode
MDA	—	Minimum detectable activity
$MPPC$	—	Multi-pixel photon counter
$MRS-APD$	—	Metal-resistor-semiconductor avalanche photodiode
NPP	—	Nuclear power plant
PCB	—	Printed circuit board
$PHWR$	—	Pressurized heavy water reactor
$PMMA$	—	Polymethyl methacrylate
PMT	—	Photomultiplier tube
POF	—	Plastic optical fibre
PVC	—	Polyvinyl chloride
PWR	—	Pressurized water reactor
RDL	—	Reference dose level
REA	—	Red de estaciones automáticas
REM	—	Red de estaciones de muestreo
ROI	—	Region of interest
SDD	—	Silicon drift detector
$SiPM$	—	Silicon photomultiplier
$SSPM$	—	Solid state photomultiplier
STP	—	Standard temperature and pressure conditions
UDL	—	Upper detection limit

$UNSCEAR$	—	United Nations Scientific Committee on the Effects of Atomic Radiation
WHO	—	World Health Organization

Symbols

A_m	—	Activity measured
CE	—	Collection efficiency
C_t	—	Terminal capacitance of SiPM
DCF	—	Dose conversion factor
δ	—	Multiplication factor of a PMT dynode
ΔTV_{op}	—	Temperature coefficient (mV/$^\circ C$) of SiPMs
E_b	—	Binding energy of the electron in a specific material
ε_{det}	—	Specific detector efficiency
E_e	—	Electron energy
E_γ	—	Photon Energy
FF	—	SiPM fill factor
F_{sci}	—	Plastic scintillator active surface
GL	—	Guideline level
G_{PMT}	—	PMT Gain
G_{SiPM}	—	SiPM Gain
η_{det}	—	Intrinsic detector efficiency
HV	—	High voltage
I_{DC}	—	PMT dark current
I_{PMT}	—	PMT current intensity
λ	—	Wavelength
λ_p	—	Most probable wavelength of a spectrum
MIP	—	Minimum ionizing particle
m_0	—	Electron rest mass
NaI(Tl)	—	Thallium doped sodium iodide
NA	—	Numerical aperture

OBT	—	Organically bound tritium molecule
P_{av}	—	SiPM avalanche probability
PDE	—	Photodetection efficiency of a SiPM
q	—	Annual volume of drinking water consumed per capita
QE	—	Quantum efficiency
q_e	—	Electron charge
Q_β	—	Energy released in a beta decay
R_q	—	SiPM Quenching resistance
S	—	Specific energy loss
S_{ij}	—	Singlet energy levels of electrons in a scintillator
S	—	Siemens unit
σ	—	Cross section of a radioactive process
σ^{rel}	—	Relative uncertainty
σ_{sys}	—	Systematic uncertainty
σ_{st}	—	Statistical uncertainty
σ_t	—	Total uncertainty
σ_{TM}	—	Uncertainty of a tritium measurement due to the scintillating fibres
$T_{1/2}$	—	Half-life time of a radioactive element
T_{ij}	—	Triplet energy levels of electrons in a scintillator
τ_r	—	Recovery time of a SiPM
V_{BD}	—	SiPM breakdown voltage
V_{bias}	—	SiPM bias voltage
V_{OV}	—	SiPM over voltage

Contents

Appendices

CONTENTS

List of Figures

List of Tables

Chapter 1

Introduction

1.1 Tritium and Nuclear Energy

Radioactivity is the process by which an unstable atomic nucleus decays through the emission of particles. This process is present in the Universe since the Big Bang. The formation of the Earth from the remains of supernova explosions explains why the different layers that make up the Earth contain radioactive elements.

Humanity has always been exposed to ionizing radiation, both from the Earth's crust radioactivity and cosmic rays (external natural irradiation). The human body also contains radioactive elements such as ^{3}H, ^{14}C and ^{40}K, introduced into it through food, water ingestion and air inhalation (internal natural irradiation). As it can be seen in Figure 1.1, most of the radioactive dose received by the population is due to both internal and external natural radioactivity, whose effective dose[1] is estimated to be 2.42 mSv/yr as shown in Table 1.1.

---

[1]The effective dose is the radioactive dose absorbed by the population, weighted by the radiosensitivity of each organ or tissue.
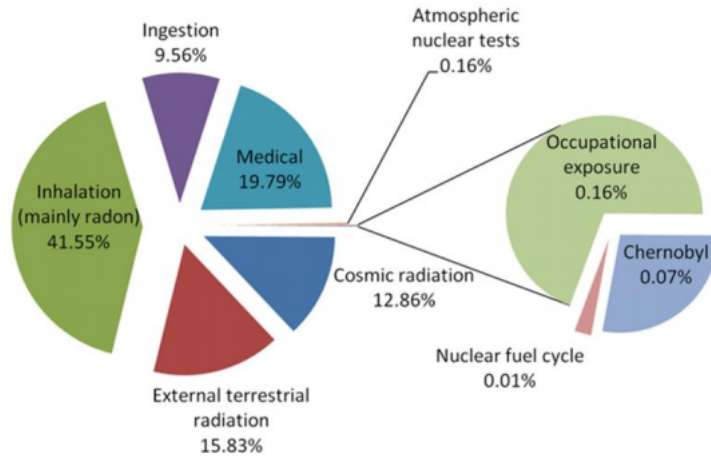
Figure 1.1 – Annual average distribution of the radioactive dose received by the population [Thea].

Since the discovery of radioactivity by Henri Becquerel in 1896, lots of nuclear-based technologies were developed and applied to various fields such as Energy, Chemistry, Biology, Technology, Medicine, Industry, etc. Due to nuclear applications, a number of anthropogenic radioactive sources have emerged in society, resulting in radioactive elements released into the environment. It can be noticed in Figure 1.1 that the most important part of the dose received by the population from artificial sources comes from medical practice. The growth of knowledge and the development of measurement techniques for radioactivity have provided evidence of the harmful effects of radioactivity on living organisms. This leads to the necessity of controlling the radiation to which the population is exposed, keeping it under safe limits. To accomplish this purpose, several organizations were created to propose recommendations for radiological protection to the different state organisms and governments at the international level. The main ones are:

1. The International Commission of Radiological Units and Measurements (ICRU) [Intb], created during the first International Confer-

Radiation source	Eff. dose (mSv/yr)	Typical range (mSv/yr)
Cosmic (external)	0.39	$0.3 - 1.0$
Terrestrial (external)	0.48	$0.3 - 0.6$
Inhalation (internal)	1.26	$0.2 - 10$
Ingestion(internal)	0.29	$0.2 - 0.8$
Total	2.42	$1 - 12.4$

Table 1.1: Annual average distribution of the effective dose received by the population due to natural radioactivity [Theb, Con].

ence of Radiology held in London in 1925 to define concepts and units necessary to quantify the negative effects of radioactivity.

2. The International Commission on Radiological Protection (ICRP) [Inta], created in 1928 by the International Society of Radiology (ISR) [Intc]. The ICRP aims to make recommendations and provide guidance on different aspects of protection against radioactivity. The ICRP does not have the legal capacity to enforce its recommendations, but these are widely included in the legislation of most countries.

3. The United Nations Scientific Committee on the Effects of Atomic Radiation (UNSCEAR) [Theb], created in 1955 with the goal of estimating and reporting the levels and effects of ionizing radiation on the population and the environment. These estimates are taken into account by governments worldwide to establish their safety standards.

4. The International Atomic Energy Agency (IAEA) [Thea], created in 1957 to promote the peaceful use of nuclear energy and to avoid its use for military purposes such as nuclear weapons. Although established independently from the United Nations through its international treaty, the IAEA reports regularly to both the United Nations and the Security Council.

5. The European Atomic Energy Community (EURATOM), created in

1957, which is an international organization ruled by the EURATOM treaty. Its objective is to coordinate research programs for the peaceful use of nuclear energy and the sharing of knowledge, infrastructures and funding of nuclear energy.

6. The Nuclear Safety Council (CSN) [Con] of Spain, created in 1980, is the authority in Spain for nuclear safety and radiation protection. It has the objective of protecting employees, the general population and the environment from the harmful effects of ionizing radiation from anthropogenic origin. For this goal, the CSN ensures that nuclear and radioactive facilities are operated safely and establishes the preventive and corrective measures to be applied in radiological emergencies. The CSN manages two detector networks to control the levels of radioactivity in the environment and to assess the impact of radioactive facilities:

   (a) The network of automatic stations REA (Red de Estaciones Automáticas) [CSNa]. The REA consists of several gamma detectors, distributed across the country as indicated in Figure 1.2a, which measure the radioactive dose in real time. The REA is employed for real-time detection of radiological issues to enable taking prompt safety measures.

   (b) The network of sampling stations REM (Red de Estaciones de Muestreo) [CSNb]. The REM consists of a collection of points, shown in Figure 1.2b, from which samples are taken and measured in a laboratory. About twenty Spanish laboratories integrate this network. The objective of the REM is to characterize the concentration and evolution of radioisotopes present in the radioactive background of Spain and to quantify the impact of radioactive facilities on the environment.

The goal of the TRITIUM project is to develop a monitor capable
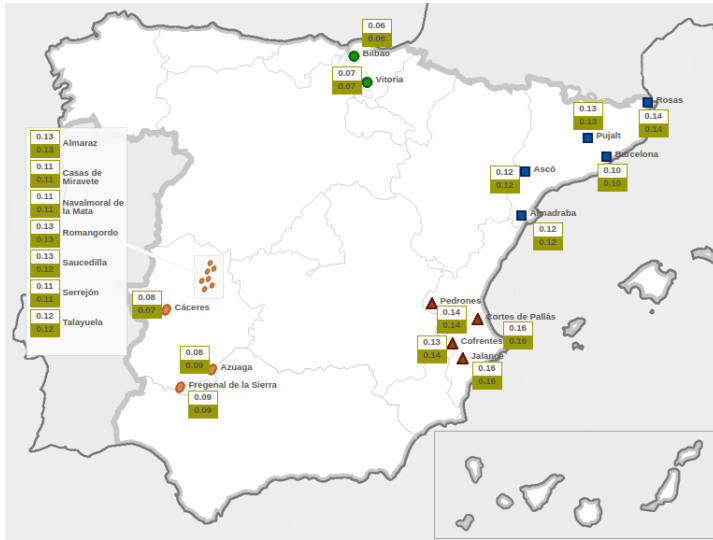
(a)
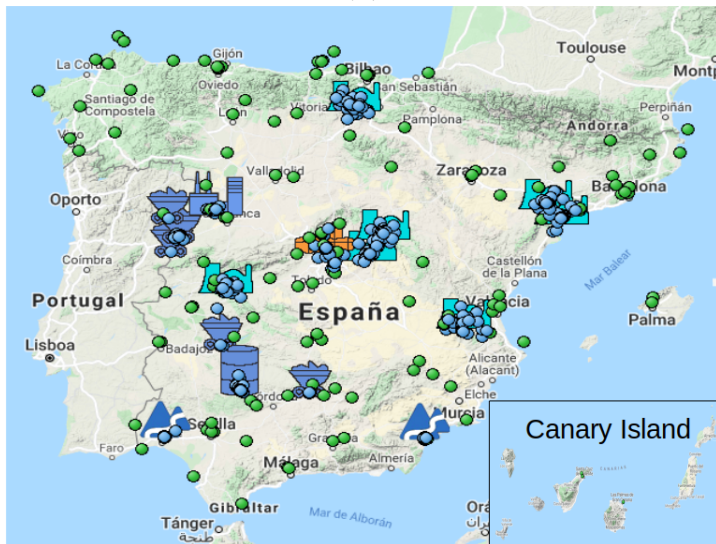
(b)

Figure 1.2 – Networks of automatic and sampling stations managed by the Spanish CSN. a) Measurement locations of the REA [CSNa]. The white and green insets are the daily and monthly average of the gamma dose, respectively. b) Measurement locations of the REM [CSNb]. Blue dots are locations near nuclear facilities, and green dots are locations uniformly distributed throughout the country.

of automatically measuring low levels of tritium in water in quasi-real-time[2]. This monitor is intended to be included in the REA.

Tritium is one of the radioactive isotopes routinely measured in REM tests. It is detected through the low-energy electrons produced in its beta decay, mainly using the Liquid Scintillation Counter technique (LSC). Due to the limitations of the current tritium detection techniques, described in section 2.1, the TRITIUM project was recently proposed with the objective of building a tritium detector based on scintillating fibres in contact with the water sample. The photons produced in these scintillating fibres are read out by photosensors, either photomultiplier tubes (PMTs) or silicon photomultipliers (SiPMs). The final emplacement of the TRITIUM monitor is a site close to the Arrocampo dam (Extremadura, Spain), whose water is used for the cooling system of the Almaraz nuclear power plant (NPP), located 4 km upstream from the Arrocampo dam. The monitor will be used to ensure that the tritium levels of the Arrocampo dam water are below the legal limit of 100 Bq/L specified in the EURATOM Directive 2013/59/Euratom [Eur14]. In addition, this will confirm the correct operation of the Almaraz NPP, since an increase of tritium activity released could indicate a malfunctioning of the reactor. This monitor could also be used in many different places with radioactive facilities like the future fusion power plants[3], nuclear research facilities[4] or tracking the pathway of tritium discharges to groundwater [Saw00].

Tritium is one of the most abundantly produced radioisotopes in an NPP, as it was verified in the United States Department of Energy (DOE) [Ber98b, Ber98a], in several research facilities in China [Hou18] and places close to them (ground, surface and wastewater). Tritium is produced in the nuclear reactor cooling water system of NPPs by neutron capture of

---

[2]Quasi-real-time is an approximation of real-time measurements. It means a relatively small time, like less than 1 h.

[3]The International Thermonuclear Experimental Reactor, ITER, will need up to several tens of kilograms of tritium to function, which corresponds to several TBq of activity.

[4]Tritium is one of the main emissions from nuclear research facilities [Fer19, Env].

deuterium existing in the heavy water (D_2O), semi-heavy water (HDO) or deuterium created by neutron capture in light water (H_2O). Tritium is finally released partially or totally into the environment in a quantity that depends on the reactor type, as shown in Table 1.2. The most common form in which tritium is released into the environment is HTO [Hou18].

Reactor type	Gaseous discharge (GBq/y)	Liquid discharge (GBq/y)
PWR	$3.70 \cdot 10^3$	$2.59 \cdot 10^4$
BWR	$1.85 \cdot 10^3$	$3.70 \cdot 10^3$
HWR	$7.40 \cdot 10^5$	$1.85 \cdot 10^5$
GCR	$7.40 \cdot 10^3$	$1.11 \cdot 10^4$

Table 1.2: Emission of tritium per year from different types of nuclear reactors: Pressurized Water Reactor (PWR), Boiling Water Reactor (BWR), Heavy Water Reactor (HWR) and Gas-Cooled Reactor (GCR) [Hou18].

NPPs are operational for more than 60 years and, nowadays, they are essential for providing a large part of the electric power used all over the world (more than 20% in Spain [Red19] and more than 10% in the world [Int14]). Although the Spanish government is planning to progressively shut all NPPs down, there are other countries like China [Eur16] or the United States [Noe19] that promote their use. NPPs are a profitable investment since they are one of the cheapest sources of energy production. Their energy production rate is stable since it does not depend on meteorological conditions. Moreover, NPPs do not emit greenhouse gases. Although there are alternative energy sources which are being developed quickly (photovoltaic, wind, tidal energy, etc.), as well as other concepts of energy production and saving (local production, energy efficiency, smart cities, etc.), they are currently not enough to cover the population needs. However, NPPs have some important drawbacks such as contamination of fresh water from uranium mining, nuclear waste, nuclear proliferation and the risk of radioactive contamination from accidents as happened in the past: Chernobyl, Fukushima and Three Mile Island [Wor20]. In any case,

world nuclear energy production is most likely not going to be stopped in the next decade. In fact, the United States Energy Information Administration (EIA) expects a future increase of nuclear energy production [EIA20]. Therefore, safety is not a negotiable aspect and there must be a development of safeguards, like alarm systems, that warn of any malfunction of NPPs.

1.2 Tritium Properties and Radiological Hazards

Tritium is the only radioactive isotope of hydrogen present in the environment. Tritium was produced artificially for the first time in 1934 in neutron capture on deuterium by Ernest Rutherford, Mark Oliphant and Paul Harteck [Oli34] and was isolated in 1939 by Luis Walter Alvarez and Robert Cornog [Alv39], who discovered that tritium is radioactive. Tritium has a half-life time of $T_{1/2} = 12.32$ years. It decays exclusively through β radiation to the ground state of the $^3_2$He isotope of helium, which is a stable nuclei, through the process,

$$^3_1\text{H} \longrightarrow \, ^3_2\text{He} + \text{e}^- + \overline{\nu}_\text{e} \tag{1.1}$$

In Figure 1.3, the scheme of tritium energy levels is shown. In this decay it is not possible to detect the neutrino because of its extremely weak interaction with matter ($\sigma \approx 10^{-44}$ cm^2) [Val07] and, since ^{3}He has a much larger mass than electrons and neutrinos, the energy carried by the daughter nucleus is very small. Therefore, the detection of tritium is done through its decay electron.

The energy released in the tritium decay is $Q_\beta = 18.6$ keV, shared between the decay products. Therefore, the energy spectrum of the decay
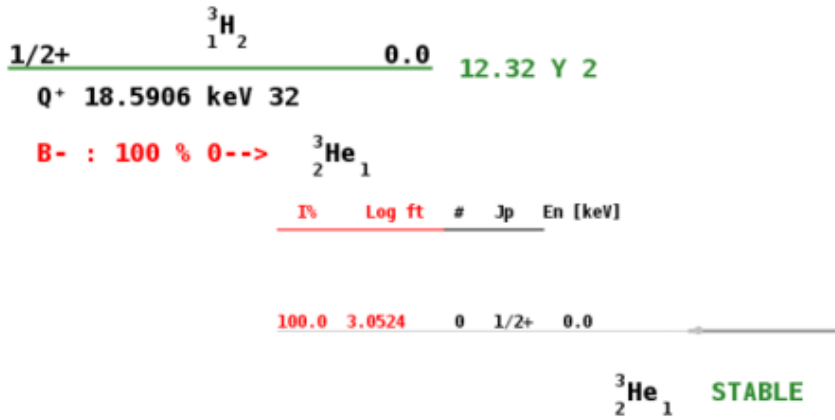
(a)
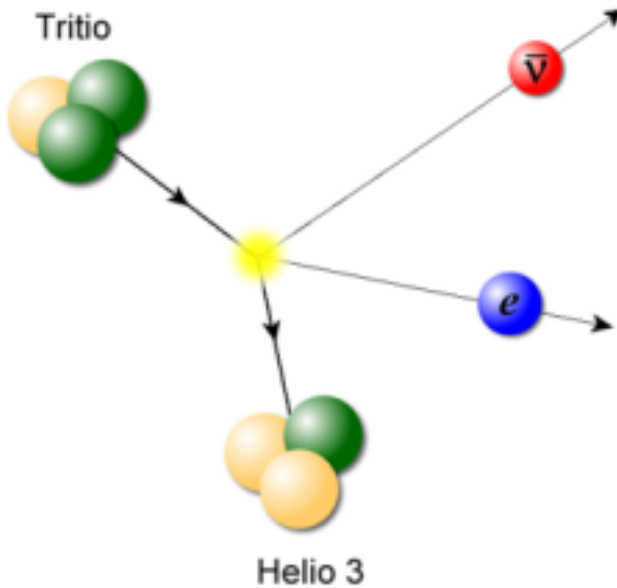
(b)

Figure 1.3 – a) Tritium energy levels [IAE]. b) Graphical representation of tritium decay.

9

electrons is a continuum with a maximum value of 18.6 keV, as shown in Figure 1.4. This energy spectrum has an average of 5.7 keV and the most likely energy is around 4.5 keV. Tritium is the radioactive isotope with the lowest energy released in β decay [Dep16]. Consequently, the β particle emitted has a very short mean free path, given in Table 1.3, which is a major issue in tritium detection, as electron detection requires a highly sensitive detector. Tritium electrons have low penetration in the human body and they are easily stopped by clothes or laboratory gloves, resulting in a low radiological hazard from external exposure. Nevertheless, the danger of tritium increases when it is ingested or inhaled since it binds to the molecules of the human body and undergoes the same chemical reactions as hydrogen.
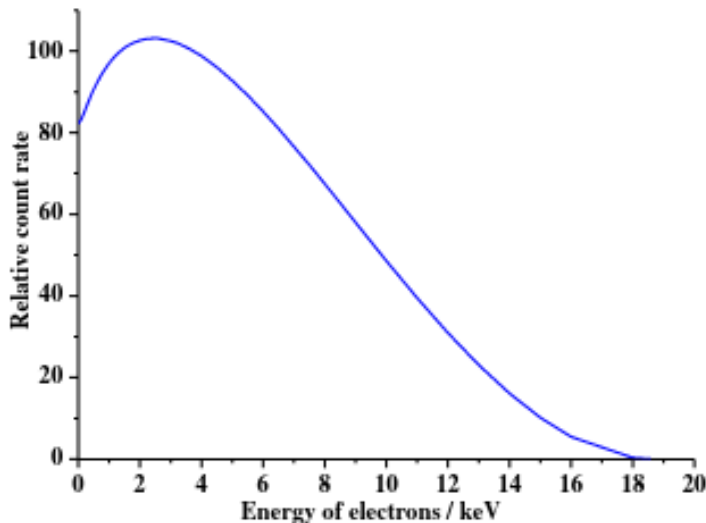
Figure 1.4 – Energy spectrum of tritium electrons [Lin20].

Tritium is naturally produced in the environment through the interaction of cosmic rays with elements of the upper atmosphere like nitrogen $^{14}N(n, {}^{3}H)^{12}C$ [Dep16] and oxygen $^{16}O(n, {}^{3}H)^{14}N$ [Hai14]. Around 99% of cosmogenic tritium forms water (HTO) and reaches the Earth's surface with an estimated production rate of $4 \cdot 10^6$ Ci/yr ($1.48 \cdot 10^8$ GBq/yr), producing a tritium concentration of $0.6 - 1.2$ Bq/L in precipitation [Hou18, Dep16].

Energy	5.7 keV	18.6 keV
Material	Penetration Depth	
$^3_1\mathrm{H}_2$	0.26 cm	3.2 cm
Air	0.036 cm	0.45 cm
Water, soft tissue (solid matter with a density of $1~\mathrm{g}\cdot\mathrm{cm}^{-3}$)	0.42 μm	5.2 μm

Table 1.3: Penetration depth of decay electrons with a mean (5.7 keV) and maximum (18.6 keV) energies in different media (tritium gas, air at STP and water) [Bla91].

Tritium can be produced artificially in the environment from different anthropogenic sources [Hou18, Dep16]. There is a large amount of tritium which was produced in military nuclear explosions between 1945 and 1975, with an estimated total production of $8\cdot10^9$ Ci ($2.96\cdot10^{11}$ GBq), a part of which remains to the date. In these nuclear explosions, tritium was produced mainly from the nuclear reactions $^{14}\mathrm{N}(\mathrm{n},{}^3\mathrm{H})^{12}\mathrm{C}$ and $^2\mathrm{H}(\mathrm{n},\gamma)^3\mathrm{H}$. Tritium is produced by commercial producers of radioluminescent and neutron generator devices ($1\cdot10^6$ Ci/yr), nuclear power and defence industries (around $2\cdot10^6$ Ci/yr) and several research facilities and nuclear reactors for energy production ($2\cdot10^6$ Ci/GWyr). The production cross sections of the relevant processes are shown in Table 1.4.

Source	Origin	Nuclear reaction	Cross section (b)
$^2_1\mathrm{H}$	Water coolant	$^2_1\mathrm{H}(\mathrm{n},\gamma)^3_1\mathrm{H}$	$5.2\cdot10^{-4}$
$^3_2\mathrm{He}$	Helium coolant	$^3_2\mathrm{He}(\mathrm{n},\mathrm{p})^3_1\mathrm{H}$	5330
$^6_3\mathrm{Li}$	Moderator	$^6_3\mathrm{Li}(\mathrm{n},\alpha)^3_1\mathrm{H}$	940
$^{10}_5\mathrm{B}$	Moderator, control rods	$^{10}_5\mathrm{B}(\mathrm{n},2\alpha)^3_1\mathrm{H}$	3835

Table 1.4: Most common nuclear reactions of artificial tritium production [Hou18].

Tritium levels in the water of the environment, excluding the current anthropogenic radioactive sources, are between 1 and 4 Bq/L, larger than expected from cosmogenic background levels ($0.6 - 1.2$ Bq/L) [Cal10]. This excess is attributed to nuclear weapon tests. Tritium levels in rivers around an NPP are between 1 and 10 Bq/L and even between 20 and 50 Bq/L at the water discharge site of NPPs [Cal10], where the produced tritium is partially or totally released into the environment, mainly in HTO form.

The effect of NPPs on tritium levels in the environment can be observed in the REM data, for example in the case of the Cofrentes NPP (Valencia, Spain). The tritium level is measured in three different places along the Júcar river, marked on the map shown in Figure 1.5. P1 is located on the river 6 km upstream from the NPP, and P2 and P3 are located 1 and 5 km downstream, respectively. The level of tritium measured in these three locations is shown as a function of time in Figures 1.6a, 1.6b and 1.6c respectively. In these figures, the detection limit and the measured activity are plotted with white and green dots, respectively. The measured activity is only displayed when it is larger than the corresponding detection limit. The tritium level in the river is larger near the discharge of the NPP and decreases 4 km downstream, as can be seen from these data. Two additional measurements of the tritium level in groundwater are included (points S1 and S2 on the map in Figure 1.5, located 1 km upstream and downstream from the NPP, respectively). Both tritium levels are shown in Figures 1.7a and 1.7b, respectively, where it can be observed that they are below the detection limit. It is important to note that, although the environmental tritium level is affected by the NPP in the case of Cofrentes, these levels are below the maximum allowed limit. The maximum level of tritium measured since January 2, 2006, is around 32 Bq/L, below the limit of 100 Bq/L recommended by the Euratom 2013 directive.

Tritium can be absorbed into our bodies by inhalation and ingestion. It is present in three different chemical forms, gaseous tritium (mainly
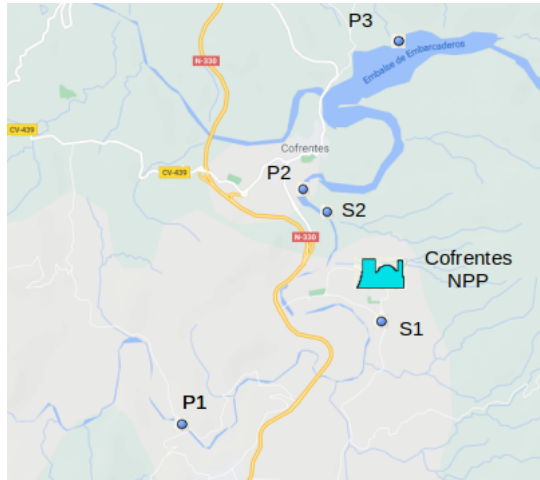
Figure 1.5 – Tritium sampling locations around Cofrentes NPP.

HT), tritiated water (mainly HTO) and organically bound tritium (OBT):

1. Gaseous tritium, usually found mixed in the air, is the least harmful form since less than $(3 - 5) \cdot 10^{-3}$ % is absorbed by the human body, which is negligible [Dep16]. However, gaseous tritium can be transformed into tritiated water, more harmful from the radiological point of view [Dep16], through oxidation and exchange reactions,

$Oxidation$: $Exchange$

$2 \cdot HT + O_2 \rightarrow 2 \cdot HTO$ $HT + H_2O \rightarrow H_2 + HTO$

$2 \cdot T_2 + O_2 \rightarrow 2 \cdot T_2O$ $T_2 + H_2O \rightarrow HT + HTO$
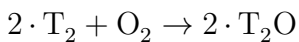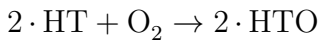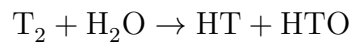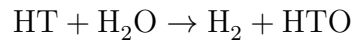
$$(1.2)$$

2. Tritiated water, called tissue-free water tritium, TFWT, is found in drinking water and food. This type of tritium molecule has a large impact since the 99% of it is absorbed [Dep16]. The biological lifetime of tritiated water corresponds to the water cycle in the body, around
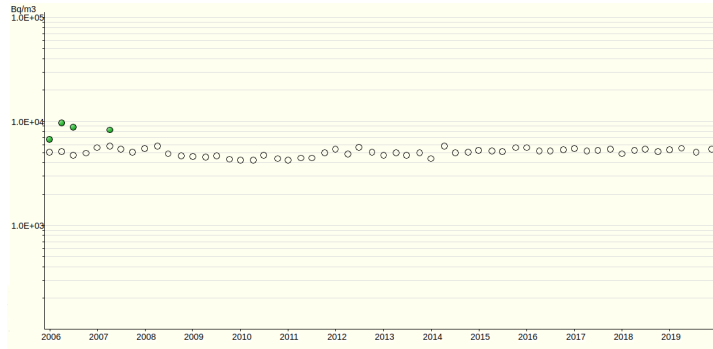
(a)
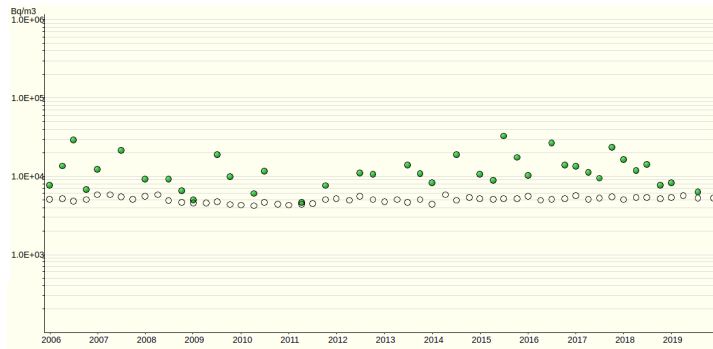
(b)
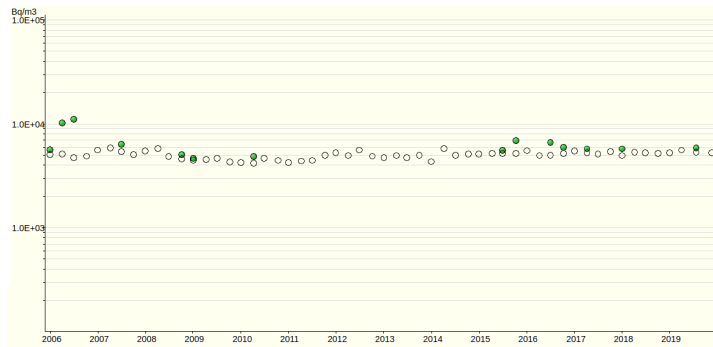
(c)

Figure 1.6 – Tritium activity levels in surface water around Cofrentes NPP from January 2006 to November 2019. a) 6 km upstream. b) 1 km downstream. c) 5 km downstream. The white points are the detection limits and the green points are the measured activity when this is above the detection limit [CSNb]. The maximum level of tritium measured since January 2, 2006, is around 32 Bq/L.
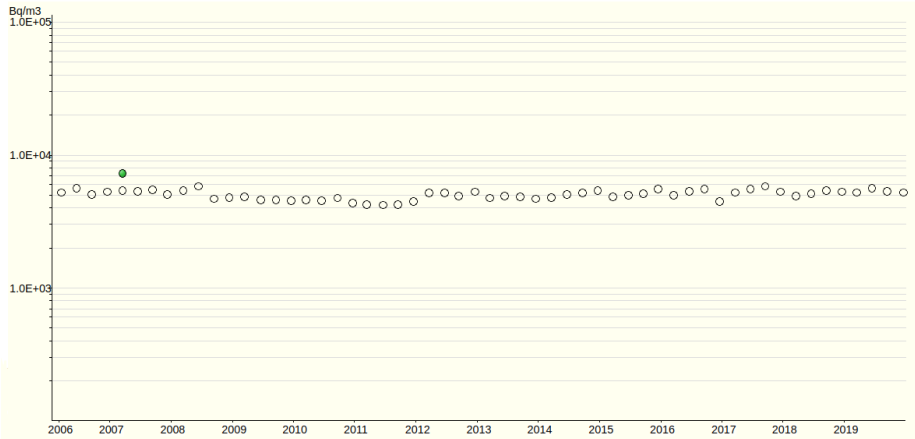
(a)
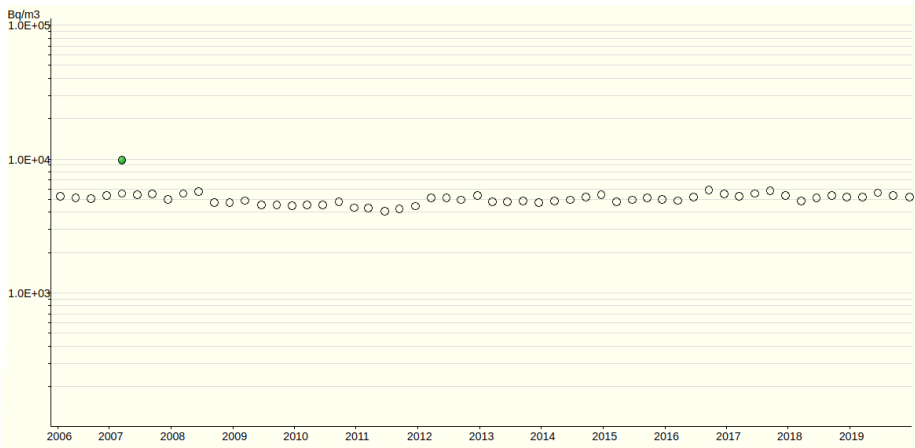
(b)

Figure 1.7 – Tritium activity levels in groundwater around Cofrentes NPP from January 2006 to November 2019 [CSNb]. a) 1 km upstream from the NPP. b) 1 km downstream from the NPP.

9.5 days ($\pm 50\%$), during which tritium remains in the body [Dep16, Cal10, Mas21, Lee18]. As in the case of water, the biological lifetime of tritiated water depends on various external parameters such as temperature, humidity, drinking habits, etc. and can be reduced by the use of diuretics [Dep16].

3. Organically bound tritium (OBT), normally found in food, forms a covalent bond with carbon molecules in organs. This form corresponds to $5 - 10$ % of tritium absorbed in the body. Although OBT is less absorbed in the body than tritiated water, it can be more harmful since it has a longer biological lifetime that varies from twenty to more than fifty days [Mar72, Lee18], depending on the type of bond that tritium forms, either OBT exchange (e-OBT), an unstable bond that can be eliminated by metabolic processes, or tightly OBT (t-OBT), a stable bond that cannot be eliminated by metabolic processes [Cal10, Mas21, PF81, Mar72].

Tritium can cause the same effects as X-rays or γ rays, such as DNA mutations or cell death. High exposure to tritium can produce the loss of functionality of organs or the development of tumours [Str93].

In summary, tritium is a naturally occurring radioactive element. It affects the health of living organisms if these are excessively or chronically exposed to tritium.

1.3 Current Legislation

Due to the radiological risk of tritium, the current legislation limits the release of tritium into the environment, ensuring that the levels are below a safe value for public health.

The guidelines to limit the radioactive elements in drinking water are based on the radiation protection methodology developed by the ICRP [ICR91] and the recommendations from WHO [WHO17]. The objective of the international radiation methodology is to protect people and the environment from the negative effects of ionizing radiation while allowing beneficial activities that involve reasonable radiation exposure. This is based on three main points, which are:

1. The justification: The benefit from radiological exposure must outweigh the detriment to health that it causes.

2. The ALARA principle ("As Low As Reasonably Achievable"): The radiological exposure must be kept as low as possible considering social and economic factors.

3. The dose limitation: Limit that must never be exceeded.

While the ICRP recommends a maximum dose of 1 mSv/yr, excluding the natural background and medical interventions, the WHO is more conservative, recommending a maximum dose of 0.1 mSv/yr, which corresponds to less than 5% of the annual dose due to background radiation, 2.42 mSv/year. The guideline reference level of each radionuclide in drinking water, GL, is usually calculated from these recommendations as,

$$GL(\text{Bq/L}) = \frac{RDL}{DCF \cdot q} \qquad (1.3)$$

where RDL is the reference dose level in Sv/yr, DCF is the dose conversion factor (the value provided by ICRP for tritium is $1.8 \cdot 10^{-11}$ Sv/Bq [ICR96]) and q is an estimation of the annual volume of drinking water consumed by a person (normally assumed two litres per day, 730 L/yr). The GL calculated for tritium in drinking water according to the ICRP and WHO recommendations is 76 103 Bq/L and 7 610 Bq/L respectively. This means that tritiated water with activities below these values is not considered harmful. Based on

these recommendations, the national organizations develop their legislation limits on exposure to radionuclides. In Spain, the responsible organization for this commitment is the CSN. Most of the countries in the world implement an RDL of 0.1 mSv/yr recommended by the WHO. The legal limit for tritium in drinking water, in this case, is 7 610 Bq/L but it is often approximated in different ways. Some countries like Switzerland [Dé17] or some organizations like the WHO [WHO17] take this value as 10 000 Bq/L. Others, like the territories of Canada of Ontario and Québec, truncate this value to 7 000 Bq/L [OME94, Hyd16]. Russia uses the more accurate value of 7 700 Bq/L [Int07]. Australia prefers to implement the RDL of 1 mSv/yr recommended by the ICRP, which corresponds to 76 103 Bq/L [NHM21]. Finland takes the ICRP recommendations but uses only half of this value, 0.5 mSv/yr, rounded to a legal limit of 30 000 Bq/L for tritium in drinking water [Fin93]. There are two different exceptions to these recommendations:

1. Most of the USA states, like California, establish an RDL of 4 mrem (0.04 mSv), which corresponds to a legal limit of 20 nCi/L (740 Bq/L) [Cal06]. This value was proposed by the United States Environmental Protection Agency (EPA) as a result of an analysis carried out on the available data [EPA01].

2. Most of the EU countries, such as France, Germany and Spain, consider a GL of 100 Bq/L, which is one of the most restrictive limit in the world [Ré18, Bun06, Gob16]. This value arises from the consideration that tritium is an indicator of the presence of other radionuclides more dangerous than tritium. These limits are fixed by the EURATOM Council Directive [Eur13].

All limits mentioned in this section are summarized in table 1.5.

Country/Agency	GL (Bq/L)
ICRP	76 103
WHO	10 000
Switzerland	10 000
Canada	7 000
Russia	7 700
Australia	76 103
Finland	30 000
United States	740
European Union	100

Table 1.5: Legal limits of tritium in drinking water (GL) established in several countries.

1.4   This Thesis

The objective of this thesis is to design, build and commission an automatic station for real-time monitoring of low tritium activities in the water. Its content is mainly focused on the development and optimization of the TRITIUM prototypes and the cosmic veto. This thesis is divided into eight chapters structured as follows:

1. **Chapter 1** provides a brief introduction to tritium detection, reports some important properties of tritium, and discusses the current legislation that limits tritium levels for human consumption in many countries around the world.

2. **Chapter 2** describes the state-of-the-art of tritium detection and introduces the TRITIUM project.

3. **Chapter 3** outlines the different parts of the TRITIUM monitor, which are the tritium detector, the water purification system and the background rejection system.

4. **Chapter 4** reports the calibrations of the different parts of the TRITIUM monitor and describes the developments aimed at improving the efficiency of tritium detection.

5. **Chapter 5** details the geometrical configuration of the different prototypes built in the TRITIUM project and the measurements taken with them.

6. **Chapter 6** details the Monte Carlo simulations performed in the TRITIUM project and presents the results obtained.

7. **Chapter 7** summarizes and discusses the most important results achieved by the TRITIUM collaboration.

8. **Chapter 8** Summarize the main results of this PhD work and discusses the future of the TRITIUM project.

Chapter 2

Methods of Detection of Tritium In Water

2.1 Tritium Detection State-of-the-Art

Measurement of tritium activity is one of the routine environmental controls that are carried out in the vicinity of nuclear research facilities and nuclear power plants during their energy production lifetime. This measurement is carried out with different available technologies according to the state of the art of tritium detection. The most employed techniques are summarized in Table 2.1. Nowadays, the most used technique for measuring tritium in water is liquid scintillator counting (LSC). This technique consists of mixing a liquid sample (some millilitres for environmental measurements or less for higher activities) with liquid scintillator. This mixture is usually made in a ratio of 50:50 but it depends on the detection system and the activity of the samples [AH99, Hof92a]. In this technique, the β particles emitted from the sample excite the molecular energy levels of the liquid scintillator which promptly decays emitting several photons with a well-

known energy (fluorescence), usually in the visible spectrum. Finally, these photons are detected with photosensors which convert the optical signal into a measurable electrical charge. The liquid scintillator technique has a very good detection sensitivity for low activity levels of tritiated water (< 1 Bq/L) [Pal07] but has the disadvantage of long measurement time (up to 2 days) and production of chemical waste, since liquid scintillators contain toluene which is toxic. In addition, the LSC technique requires special staff for sampling, a chain of custody and laboratory analysis which require economic and time resources. In order to overcome these difficulties, efforts were made to build a tritium monitor based on LSC which did not led a low enough minimum detectable activity (MDA) [Sig94].

	LSC	IC	Calorimetry	BIXS
Measured quantity	Scintillation photons	Ionization current	Heat	X-rays
MDA	$\sim$ Bq	$10 - 100$ kBq	$\sim$ GBq	$\sim$ MBq
Sample state	Liquid	Gas, vapor	All	All

Table 2.1: State-of-the-art tritium detection techniques. This table shows the measured quantity, the minimum detectable activity (MDA) and the sample form for four different techniques, liquid scintillator counting (LSC), ionization chamber (IC), calorimetry and beta induced X-ray spectrometry (BIXS).

The ionization chamber technique (IC) consists of an ionization chamber filled with gas (sample) which contains electrodes that collect the ionization current produced by the β radiation in the gas. This is a simple and fast system, but it has a high MDA (> 10 kBq) and requires samples in a state of gas or steam [Khe02, Che13]. The IC technique also requires sample conditioning, chain of custody and laboratory analysis.

The calorimetry method is based on the measurement of the heat

generated in the detection medium (normally platinum) [Ale11, BD13]. The disadvantages of this technique are its high MDA (of the order of a GBq) and the requirement of a long measurement time (2 days or more).

The Beta Induced X-ray Spectrometry (BIXS) is based on the measurement of the bremsstrahlung radiation produced by tritium decay electrons by a NaI(Tl) crystal coupled to a PMT [Mat07, Mat08] or silicon drift detector (SDD) [Nie15]. The limitation of this technique is its high MDA (of the order of MBq).

There are additional methods for tritium detection, although they are less employed or less developed, each one with its advantages and limitations. For example, the avalanche photodiode (APD) cannot be used in contact with water [Sha97], the mass spectrometry needs to store the sample for several months [JB10] and the cavity ring spectroscopy requires a special optical configuration that is not possible outside a laboratory [Bra15].

All the above techniques are offline methods that need a long time for sample collection, shipment to a laboratory and activity measurement. Therefore, they cannot be used for in-situ monitoring of tritium in water. The liquid scintillation technique is the only one with an MDA smaller than the requirement of 100 Bq/L of tritium in water established by the EURATOM directive.

The purpose of the TRITIUM project is to develop an alternative method, based on solid scintillators, that allows accomplishing the requirements of in-situ monitoring of levels as low as 100 Bq/L in quasi-real-time. There are several studies with solid scintillators so far:

1. The study by M. Muramatsu, A. Koyano and N. Tokunaga in 1967 used a scintillator plate read out by two PMTs in coincidence [Mur67].

2. The study by A. A. Moghissi, H. L. Kelley, C. R. Phillips and J. E. Regnier in 1969 used one hundred plastic fibres coated with anthracene

powder and read out by two PMTs in coincidence [Mog69].

3. The study by R. V. Osborne in 1969 used sixty stacked scintillator plates read out by two PMTs in coincidence [Osb70].

4. The study by A. N. Singh, M. Ratnakaran and K. G. Vohra in 1985 used a scintillator with several holes read out by PMTs in coincidence [Sin85, Rat00].

5. The study by K. J. Hofstetter and H. T. Wilson in 1991 tested different shapes of scintillator plastics like several sizes of beads, fibres, etc. The best result obtained for solid plastic scintillators was a tritium detection efficiency, ε_{det}, of the order of $10^{-3}(\mathrm{Ls}^{-1}\mathrm{kBq}^{-1})$ [Hof92a, Hof92b].

The results of those studies are summarized in Table 2.2. As the active surface of the plastic scintillator F_{sci} varies largely with the detector type, the specific detector efficiency η_{det}, which is the intrinsic efficiency normalized to its active surface, is used to compare the results. Finally, the MDAs in those studies are of the order of a few tens of kBq/L. The development of a detector with a much lower MDA is thus essential to comply with the EURATOM directive of 100 Bq/L of tritium in water for human consumption.

2.2 The TRITIUM Project

As a conclusion of section 2.1, the current techniques cannot be used for tritium monitoring in quasi-real-time since either they have a high MDA or they work in off-line mode. To overcome these limitations, the TRITIUM project [Int16], with the title of "Design, construction and commissioning of automatic stations for quasi-real-time monitoring of low radioactive levels

Reference	$\eta_{det} \times 10^{-3}$ L kBq^{-1}s^{-1}	F_{sci} cm^2	$S_{det} \times 10^{-6}$ L kBq^{-1}s cm^{-2}	MDA kBq L^{-1}
[Mur67]	0.39	123	3.13	370
[Mog69]	4.50	> 424	< 10.6	37
[Osb70]	12	3000	4	37
[Sin85]	41	3000	13.7	< 37
[Hof92a]	2.22	$\sim$ 100	< 22.2	25

Table 2.2: Results of scintillator detectors developed for experiments of tritiated water detection. This table shows for the quoted studies the efficiency of the detector (η_{det}), its active surface (F_{sci}), its specific efficiency, defined as the efficiency normalized to the active surface ($S_{det} = \eta_{det}/F_{sci}$), and MDA.

of tritium in water", was proposed. This project was funded by the Interreg Sudoe program of the European Economic Community in the 2016 call, with reference number SOE1/P4/EO214. The TRITIUM collaboration is an international consortium of six institutions from three European countries: The I3N[1] in Portugal, the University of Bordeaux and the Centre National de la Recherche Scientifique (CNRS, Section Aquitaine-Limousin) in France and the University of Extremadura, the Junta de Extremadura and the University of Valencia in Spain. The tritium detector consists of a bundle of scintillating fibres in contact with the water sample which detects the tritium decay electrons. These fibres are read out with photosensors (PMTs or SiPMs). Additional elements are used to improve the tritium detection sensitivity such as a water purification system, which prepares the water sample before introducing it into the detector for tritium measurement, and a cosmic veto and a passive shielding which reduce the natural radioactive background of the tritium detector. Several electronic modules which control the different parts of the monitor analyze the tritium measurement and send an alarm if the configured limit (100 Bq/L) is exceeded.

---

[1]Institute for Nanostructures, Nanomodelling and Nanofabrication, University of Aveiro.

(a)
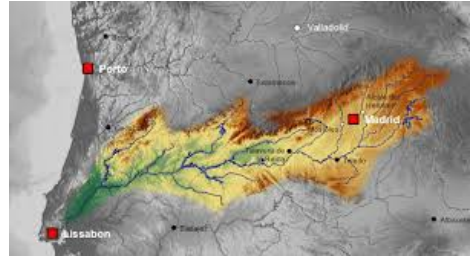
(b)

Figure 2.1 – a) Arrocampo dam and Almaraz Nuclear Power Plant. b) Tagus river through Spain and Portugal.

A crucial problem is to distinguish tritium signals from the background because tritium events have low energy ($\sim$ keV) and fall in an energy range of the spectrum where background events are significant. To reduce the background of the TRITIUM monitor, coincidence techniques are employed.

The TRITIUM monitor will be installed in the Arrocampo dam, Almaraz (Spain), displayed in Figure 2.1, where the Almaraz NPP releases the water from its secondary cooling circuit. This NPP has two nuclear reactors of PWR type. Arrocampo dam is located near the Tagus river, shown in Figure 2.1b, which is the longest river in Spain, with a length of 1007 km. This river rises in Aragon (Spain) and flows into the Atlantic Ocean through Lisbon (Portugal). The water of this river is used for agriculture and drinking water by both Spanish and Portuguese people. For this reason, international cooperation is necessary to control and maintain the quality of the Tagus river water.

Each institution of the TRITIUM collaboration is dedicated to the development of a different part of this project:

1. The University of Extremadura group has developed and installed the water purification system to produce water with very low conductivity, $\sigma \approx 10$ μS/cm (two orders of magnitude less than raw water,

1000 μS/cm). This purification process is very important for two reasons. On the one hand, for maintaining the TRITIUM detector pristine, which is critical for its long-term functionality. On the other hand, to reduce the natural background since several natural radiactive isotopes are present in the water sample. This system is described in section 3.3.

2. The French group has developed the passive shielding for the detector. This shielding is made of lead with low intrinsic activity in order to reduce the external natural background of the system. This shielding is presented in section 3.4.

3. The Aveiro and Valencia groups have collaborated for designing, developing and building four different prototypes of the TRITIUM detector and active vetos for reducing cosmic events. These prototypes and vetos are described in chapter 5 and section 3.4.2, respectively. These groups have also carried out simulations of the TRITIUM monitor, which are reported in chapter 6.

The important characteristics required for the TRITIUM detector are:

1. *Compactness.* This is an important requirement because in the place where the detector is planned to be installed there is little space. Compactness also allows portability and cost reduction.

2. *Modularity.* The modularity of the TRITIUM detector is important for flexible geometrical configuration and for improving its tritium detection sensitivity. Modularity also facilitates construction and maintenance.

3. *Thin active volume and large active area.* The mean free path of β particles from tritium decay is very short. Thus, a thin detector active

volume is needed. In practice, an active thickness beyond the mean free path of the tritium electrons only contributes to the background. In addition, as reported in section 2.1, the efficiency of this type of detector scales with the active area, so it is crucial to design a detector with the largest possible active area.

4. *High detection efficiency for tritium.* As the tritium activities to be measured are very low, the loss of tritium events strongly affects the accuracy of measurements.

5. *High specificity to tritium.* The monitor must be able to distinguish tritium signals from other radioactive decays in the sample.

6. *Quasi-real-time response.* It is crucial that the system operates in quasi-real-time (1 h or less) in order to detect any anomalous tritium release as fast as possible.

7. *Ruggedness.* The final goal of the project is to install an automatic system working for several years requiring occasional interventions of specialized operators. Therefore, a rugged monitor is required.

In order to measure in quasi-real-time, it is needed to work *in situ*, that is, in the same place where the water sample is taken. Working *in situ* has some advantages such as: 1) Cheap running cost, since sampling process, chain of custody, etc. are eliminated. 2) Quasi-real-time measurements. 3) Safe monitoring since personal dose is reduced. 4) Changes in activity can be detected quickly.

Chapter 3

Design Principles and Components of TRITIUM

3.1 Detector System Overview

To achieve the aim of the TRITIUM project, the TRITIUM collaboration has developed a monitor consisting of several parts:

1. The tritium detector, described in chapter 5, compose of several modules read out in parallel. Each module consists of hundreds of plastic scintillating fibres in contact with the water sample measured and read out by two coincident photosensors. The photosensors considered are photomultiplier tubes (PMT) and silicon photomultipliers (SiPM) (section 3.2).

2. The water purification system (section 3.3) that prepares the water sample for the measurement. This system removes all the minerals dissolved and all the particles with a diameter greater than 1 μm without affecting the tritium content of the sample. This system is important

for two reasons: First, because the mean free path of tritium in water is very short, 5 to 6 μm, hence it is essential to avoid organic and mineral depositions onto the fibres surface since this would prevent the tritium decay electrons from reaching the fibres. Second, minerals dissolved in water may contain radioactive isotopes like ^{40}K, which would increase the background. As the activity limit to be measured is low (down to 100 Bq/L), background reduction is crucial.

3. The background rejection system (section 3.4) which is composed of two different parts. The first one is a passive shield, consisting of a lead castle inside which the TRITIUM detector is located. This castle is employed to suppress the background from natural radioactivity and cosmic rays with energies up to 200 MeV. The second part is an active veto, consisting of two plastic scintillating plates located inside the passive shield, above and below the tritium detector, which are read out by photosensors. The goal of this active veto is to suppress the remaining high energy events (> 200 MeV) from cosmic rays that cross the passive shield and contribute to the background. The technique employed consists of reading the tritium detector in anti-coincidence with the active veto.

4. A readout electronic system which allows the acquisition and processing of data to provide an alarm signal in case the tritium level exceeds the required limit of 100 Bq/L.

The TRITIUM system is planned to be part of the network of automatic stations, REA.

3.2 TRITIUM Detector

As discussed in section 2.1, the TRITIUM monitor consists of a chain of three main elements, plastic scintillating fibres that produce scintillation

photons in response to a tritium electron decay, the photosensor that detects the photons produced in the scintillator and produces an electric pulse that gives information on the detected photons, and the electronic system which processes and analyzes the electric pulses provided by the photosensor. A scheme of a scintillation detector setup is shown in Figure 3.1.
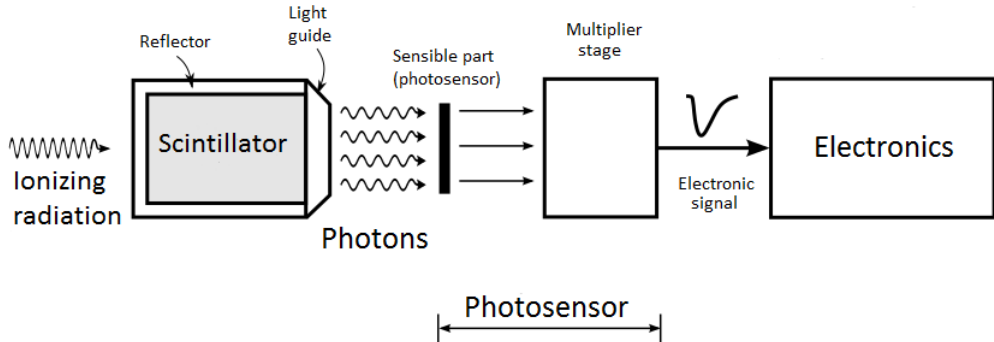
Figure 3.1 – Scheme of a scintillator detector.

3.2.1 Interaction of Fast Electrons and Photons with Matter

The interaction of particles with matter is described in this section, focusing on the particles and energy range relevant for this thesis, electrons $(0 - 18$ keV$)$, photons in the visible range (approx. $380 - 750$ nm) and γ rays from the background and high energy cosmic rays.

Electrons have a charge, so their interaction with matter is mainly through the orbital atomic electrons by the Coulomb force. The electron trajectories are much more tortuous than those of heavier particles because of their small mass. Furthermore, electrons lose a significant amount of energy in each collision. The specific energy loss, defined as $S = -\dfrac{dE}{dx}$, gives the energy loss of a particle per unit of path length. In the case of

electrons, the total energy loss has two main contributions, the collisions (elastic and inelastic) and the radiative processes (bremsstrahlung) which are roughly proportional [Kno10, Leo94],

$$\frac{dE}{dx} \approx \left(\frac{dE}{dx}\right)_c + \left(\frac{dE}{dx}\right)_{br} \; ; \qquad \frac{\left(\frac{dE}{dx}\right)_{br}}{\left(\frac{dE}{dx}\right)_c} \approx \frac{EZ}{700} \qquad (3.1)$$

where E is the energy of the electron in MeV and Z is the atomic number of the absorbing material. Due to this energy loss, electrons penetrate a material to a depth where they have lost their kinetic energy. This distance, known as the range, is quoted for tritium electrons in Table 1.3.

The material chosen for the detection of tritium decay electrons is organic plastic since, due to its low density, there is a reduced backscattering. It has been chosen in the form of fibres in order to increase the active area and, therefore, the efficiency of the detector.

As photons do not have any charge, their possible interactions with matter are the photoelectric effect, Compton effect, coherent scattering and pair production. The probability of each process, displayed in Figure 3.2, depends on the energy of the photon, $E_\gamma = h\nu$, and on the atomic number of the material, Z. The optical photons have a wavelength between 400 and 700 nm, that corresponds to energies of the order of the eV. Therefore, pair production does not play any role for optical photons since this requires photon energy of at least 1.022 MeV.

The photoelectric effect occurs when a photon interacts with an orbital electron in the material, losing all its energy. This energy is absorbed by an electron that is ejected from the atom (ionization). The energy of the resulting electron, E_e, is [Kno10, Leo94],

$$E_e = E_\gamma - E_b \qquad (3.2)$$
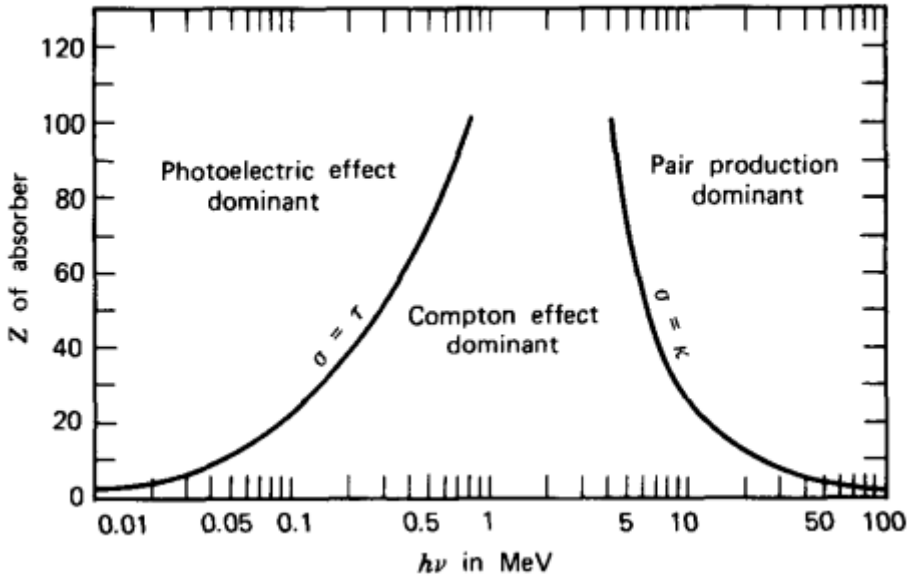
Figure 3.2 – Domain regions of the three most probable types of interactions of gamma rays with matter. The lines show the atomic number Z and gamma energy $h\nu$ where two interaction processes are equally likely [Kno10].

where E_b is the binding energy of the electron in the material. The probability of this effect depends on the number of available electrons in matter through the atomic number Z, and the energy of the electron according to the expression [Kno10],

$$\tau \approx \frac{Z^n}{E_\gamma^{3.5}} \tag{3.3}$$

Thus, the photoelectric effect is most probable for elements with a high atomic number. This is the reason why these types of elements are the best shields against gamma radiation and why the passive shield of the TRITIUM monitor consists of lead bricks (section 3.4.1).

The Compton effect occurs when a photon interacts with an orbital electron of the material, transferring part of its energy to the electron which is scattered at an angle θ with respect to the direction of the incident photon.

If the electron binding energy is neglected, the energy transferred to it, E_e, is given by [Kno10, Leo94],

$$E_e = \frac{\dfrac{E_\gamma^2}{m_0 c^2}\left(1 - cos\theta\right)}{1 + \dfrac{E_\gamma^2}{m_0 c^2}\left(1 - cos\theta\right)} \tag{3.4}$$

where m_0 is the rest mass of the electron and c is the speed of light in the vacuum. The probability of the Compton effect is proportional to the atomic number Z and decreases with the energy of the photon. As it can be seen in Figure 3.2, for photon energies in the visible spectrum (of the order of eV), the Compton effect is only likely for very light materials ($Z < 4$). For heavier materials the photoelectric effect is dominant.

In the coherent scattering, the atom is neither excited nor ionized and the photon conserves its energy in the collision. Coherent scattering is probable for photons with low energies and materials with high atomic numbers.

Finally, in the pair production process, the photon is converted into an electron and a positron,

$$\gamma \longrightarrow e^- + e^+ \tag{3.5}$$

As can be seen in Figure 3.2, this is the dominant interaction process for high-energy photons, which are the photons produced by cosmic rays.

3.2.2 Plastic Scintillators

Scintillators are materials widely employed for radiation detection in nuclear physics. Scintillators convert the kinetic energy of the incoming particles into light which can be detected and quantified. Light emission is produced

due to the photon deexcitation of atoms of fluorescent molecules in the material.

Light production is linear with deposited energy for a wide energy range of incoming particles. Scintillators should have good optical properties, such as being transparent to the wavelength of their emission and having a refractive index close to that of photosensor windows in order to optimize optical coupling and light transmission. Photon emission in scintillators is a statistical process that follows a Poisson distribution.

Scintillators can be organic or inorganic. Inorganic scintillators normally have a high atomic number and density, so their light output is high. For these reasons, they are suitable for gamma-ray spectroscopy. Organic scintillators are generally fast and are used for charged particles and neutron detection. This section is focused on organic scintillators since they are the ones used in the TRITIUM detector. Organic scintillators are based on fluorescent molecules dissolved in a base solvent, usually aromatic hydrocarbons such as $C_{18}H_{14}$, $C_{24}H_{22}N_2O$ or $C_{15}H_{11}NO$ with an average atomic number between 3.5 and 5. The fluorescent molecules of organic scintillators have a π-electron structure. The energy levels of their electrons are commonly illustrated with a Jablonsky diagram, shown in Figure 3.3. This diagram shows the ground singlet states, S_{0i}, the excited singlet states, S_{jk}, and the excited triplet states, T_{lm}. The energy difference between S_1 and S_0 states is around 3 to 4 eV, which corresponds to the visible photon emission. As shown in the figure, each energy state is split into close sublevels separated by around 0.15 eV. This fine energy structure is due to excitations of molecular vibrational modes tagged by the second index of the energy states. As the energy levels and sublevels have energy larger than the thermal energy, 0.025 eV, electrons are in the ground state S_{00} at STP. When a particle deposits its kinetic energy in a scintillator, the valence electrons are excited very fast ($\tau \approx 1$ ps) to higher singlet energy states and are quickly deexcited to the first singlet excited state, S_{10}, through non-radiative processes known as internal conversion. These

electrons can deexcite to the fundamental singlet state, S_{00}, through three different physical mechanisms:
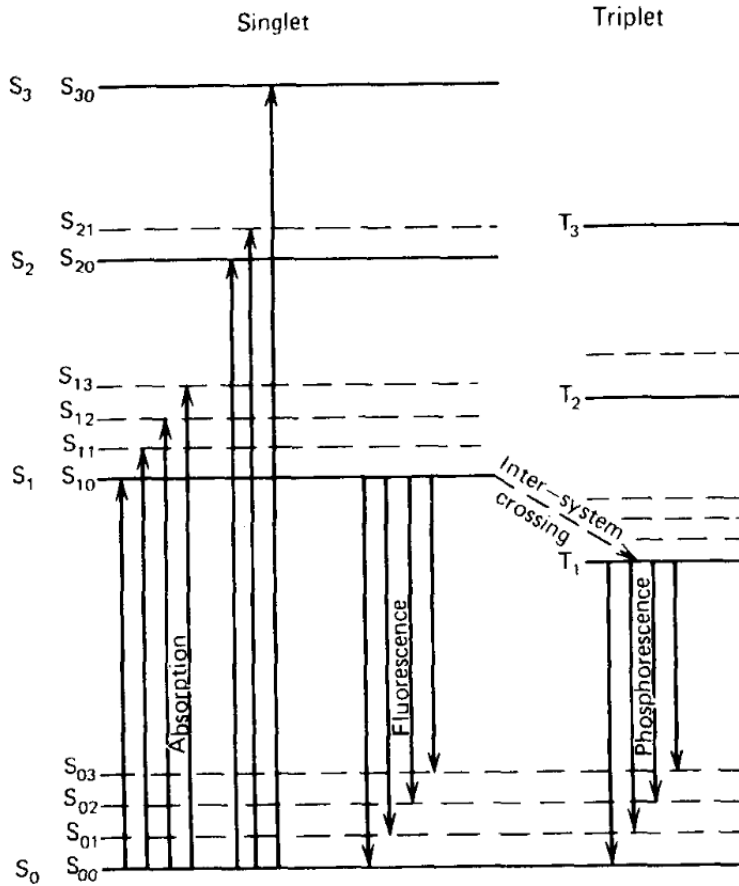
Figure 3.3 – Jablonsky diagram [Kno10].

1. Prompt fluorescence. The electron in the S_{10} level is de-excited to a sublevel of the ground state S_{0i}, emitting a photon. This process happens immediately after the excitation of the scintillator molecules (of the order of nanoseconds after excitation). Each scintillator has a characteristic emission spectrum. Organic scintillators are practically transparent to their own fluorescence emission because scintillation

photons have less energy than the excitation energy. This effect is called the Stokes shift and it is represented in Figure 3.4. The intensity of the fluorescence emission versus time in an organic scintillator is the combination of two exponential functions, one associated with the lifetime of the level τ (of the order of nanoseconds), and the other associated with the energy level population τ_1 (of the order of picoseconds) [Kno10],

$$I = I_0 \left(e^{-t/\tau} - e^{-t/\tau_1} \right) \qquad (3.6)$$
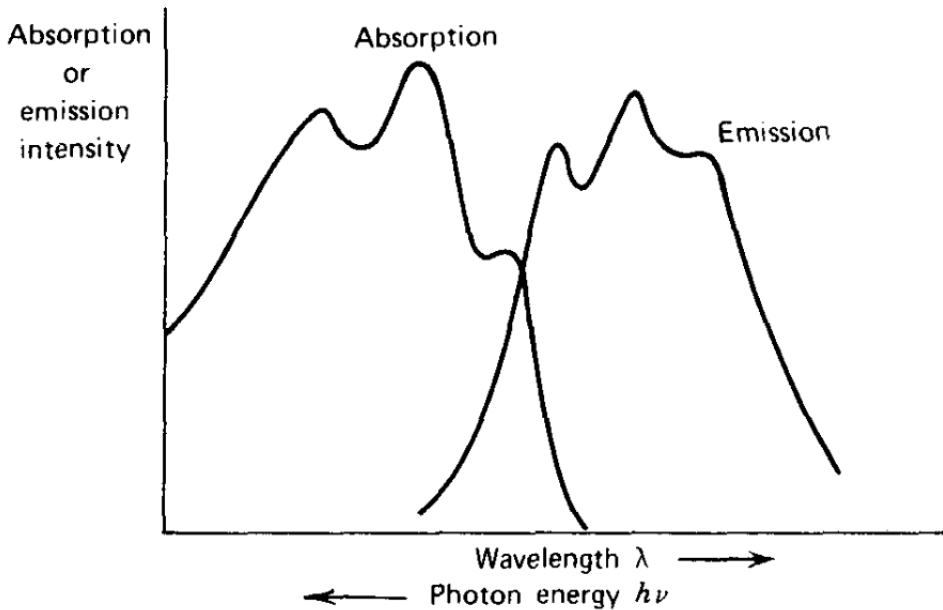
Figure 3.4 – The Stokes shift [Kno10].

2. Phosphorescence. The electron that is in the first singlet excited state crosses to a triplet excited state. Such a transition process is called "intersystem crossing". The triplet state is a metastable state with a longer lifetime than fluorescence, of the order of milliseconds after scintillator excitation.

3. Delayed fluorescence. It occurs when an electron is in a triplet excited state but its transition to the ground state is forbidden. In this case, the electron interacts with another electron in a similar state, falling to the first singlet state and quickly de-exciting to the ground state,

$$T_1 \; + \; T_1 \; \longrightarrow \; S_1 \; + \; S_0 \; + \; phonons \tag{3.7}$$

This emission has the same emission spectrum as the prompt fluorescence, but with a longer lifetime (≈ 1 ms).

As the prompt fluorescence light produces the scintillator signal, the detector design should optimize its collection and detection and reduce other possible physical mechanisms like phosphorescence or delayed fluorescence. One of the most important parameters that characterize the scintillator is the scintillation yield, defined as the number of photons emitted per unit of absorbed energy. This yield depends on the type of particle and on other mechanisms that do not produce prompt fluorescence light, like phosphorescence, delayed fluorescence, and non-radiative processes like internal conversion. The scintillator yield is normally quoted by the manufacturer for MIPs[1].

Plastic scintillators are easy to machine to any desired shape. The chosen shape for the TRITIUM detector is the fibre, specifically, commercial fibres BCF-12 from Saint-Gobain Crystals Inc [Sai21b]. This type of fibre was chosen as the result of a comparative study [Sol17] among some of the best-known commercial manufacturers. The BCF-12 fibres consist of a scintillating polystyrene core with the possibility of being covered by polymethyl methacrylate (PMMA) claddings.

When a particle deposits all or part of its kinetic energy in a scintillating fibre, photons are produced in the fibre core as a result of the

---

[1]A MIP or minimum ionizing particle is a particle that has a speed at which the ionization produced is minimal.

fluorescence process. The number of photons produced depends on the scintillating efficiency and its value is around 2.4% for the BCF-12 fibres, which means that a scintillation yield of about 8000 photons per MeV is produced for a MIP. For instance, for tritium electrons of 18.6 keV, these fibres emit at least 149 photons since electrons of these energies are not MIPs. The emission spectrum of the fibres employed in this work is shown in Figure 3.5.
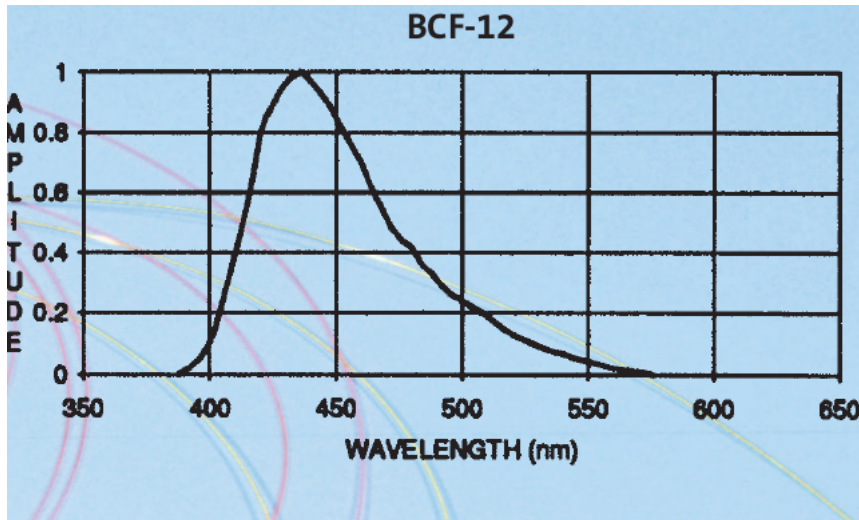
Figure 3.5 – Emission spectrum of BCF-12 scintillating fibres of Saint-Gobain [Sai21b].

The scintillation light is guided to the sensitive part of the photo-sensor according to Snell's law [Bor19]. The guiding mechanism is determined by the interface between the core and the surrounding material. When a photon hits this interface, it is refracted (and therefore lost) following the Snell equation [Bor19],

$$n_0 \ sen\theta_0 = n_1 \ sen\theta_1 \tag{3.8}$$

where θ_0 is the incident angle formed by the photon and the normal to the surface of the first medium with refractive index n_0, and θ_1 is the refraction

angle formed by the photon and the normal to the second medium with refractive index n_1. If the surrounding material has a lower refractive index than the core of the fibre, as it is the case with scintillating fibres, there exists a critical angle, θ_c, beyond which photons will be totally reflected ($\theta_1 = 90°$) and therefore kept within the fibre as illustrated in Figure 3.6,

$$\theta_c = \arcsin\left(\frac{n_1}{n_0}\right) \tag{3.9}$$

The trapping efficiency or photon collection efficiency is defined as the efficiency of the scintillator to guide photons. For BCF-12 fibres with optical clad this efficiency is between 3.4% and 7% per meter of fibre (depending on the emission point, it is minimum on the fibre axis and maximum near the core-clad interface). In Figure 3.6, the light collection in a fibre is illustrated.
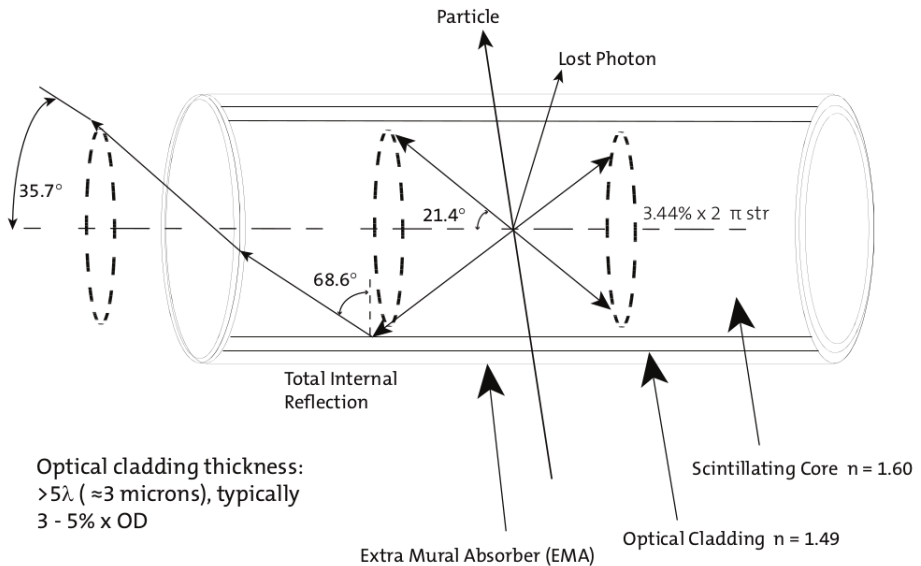
Figure 3.6 – Photon collection in a single clad fibre [Sai21b].

The cladding material has a higher refractive index than air and

Material	Refractive index	Critical angle (°)
Air	1	38.68
Water	1.33	56.23
Cladding of PMMA	1.49	68.63

Table 3.1: Critical angles associated to different interfaces between polystyrene ($n_0 = 1.6$) and other materials.

water. Therefore, it increases the critical angle and reduces the light collection. However, it is useful for protecting the core surface from dirt and aggressive external agents that would reduce the light collection. Three different cases are shown in Table 3.1, where the cladding effect is illustrated. As can be seen, the critical angle for uncladded fibres surrounded by water or air is smaller than for cladded fibres, which implies a larger trapping efficiency. However, in practice, it is difficult to achieve a perfect air-core or water-core interface, and this affects light collection. As commercial claddings are thicker (30 µm) than the mean free path of tritium decay electrons in water (around 5 µm), cladded fibres are not an option for the TRITIUM detector. Hence, special attention is needed for achieving a good enough water-core interface. To achieve this goal a special method was developed in the ICMOL laboratory[2] for preparing fibres for tritium detection, described in section 4.1. The relevant parameters of the scintillating fibres used for the TRITIUM detector are given in Table 3.2.

3.2.3 Light Detection in Photosensors

The scintillation photons created in the core of the fibre and directed to its ends are detected by photosensors. Photosensors have a sensitive part that is optimized to detect photons in a range of energy (usually in the visible

---

[2]ICMOL, *Instituto de Ciencia Molecular*, is a research institute located in the *Parc Científic* of the University of Valencia.

Characteristics	Value
Core material	Polystyrene
Core refractive index	1.60
Density (g/cm^3)	1.05
Cladding material	Acrylic (PMMA)
Cladding refractive index	1.49
Cladding thickness	3% ⌀
Numerical aperture	0.58
Trapping efficiency	3.4% to 7%
# of H atoms per cc (core)	$4.82 \cdot 10^{22}$
# of C atoms per cc (core)	$4.85 \cdot 10^{22}$
# of electrons per cc (core)	$3.4 \cdot 10^{23}$
Radiation length (cm)	42
Emission peak (nm)	435 (blue)
Decay time (ns)	3.2
1/e Attenuation length (m)	2.7
Scintillator yield ($\#\gamma$/MeV)	~ 8000
Operating Temperature	$-20°$C to $50°$C

Table 3.2: Characteristics of BCF-12 scintillating fibres from Saint-Gobain Inc. [Sai21b].

range) with a certain probability, called quantum efficiency. Photosensors produce an electronic signal that carries information about the detected photons such as their number, detection time, etc. Many available photosensors rely on various physical processes, such as photomultiplier tubes (PMTs), silicon photomultipliers (SiPM) or charge-coupled devices (CCD).

The optimization of the efficiency of a scintillation detector is essential. To do so, the emission spectrum of the scintillator (Figure 3.5 for the fibres used) must match as much as possible the detection efficiency spectrum of the photosensor. The efficiency of a detector is proportional to the product of the emission and the detection efficiency spectra and is largest when both spectra match.

The requirements imposed on the photosensor of the TRITIUM detector are fast response, high gain and high photodetection efficiency. Two different proposals for the TRITIUM detector are investigated, SiPMs and PMTs. Both meet these requirements since they are very fast (of the order of ns), have high gain (of the order of 10^6) and have a high photodetection efficiency (around 50% for SiPMs and 30% for PMTs). Each proposal has its own advantages. SiPMs are more robust and need a lower supply voltage (of the order of 50 V) than PMTs (of the order of 1000 V). Furthermore, due to this difference in supply voltage, SiPMs have a smaller cost per channel than PMTs. However, PMTs, which are the conventional choice, have a lower dark count rate than SiPMs and a much lower dependence of gain with temperature.

3.2.3.1   Photomultiplier Tubes (PMTs)

Photomultiplier tubes are employed as photosensors in nuclear physics for decades. They detect the scintillation photons that reach its sensitive part, the photocathode, and produce an electronic signal, large enough to be easily measured. In Figure 3.7 a schematic drawing of a PMT is given. PMTs consist of a vacuum tube that has a glass window through which photons can penetrate. The electrons created in the photocathode travel in the vacuum. The signal production has two phases:

1. In the photocathode, photons are converted into photoelectrons through the photoelectric effect. The photocathode consists of a thin layer of material, of the order of nanometers, deposited on the inner surface of the PMT window. The material of the photocathode is chosen to optimize the probability of photoelectric effect with the scintillation photons. The PMTs used in different R&D setups of the TRITIUM experiment at the University of Valencia are R8520-406 from Hama-

43
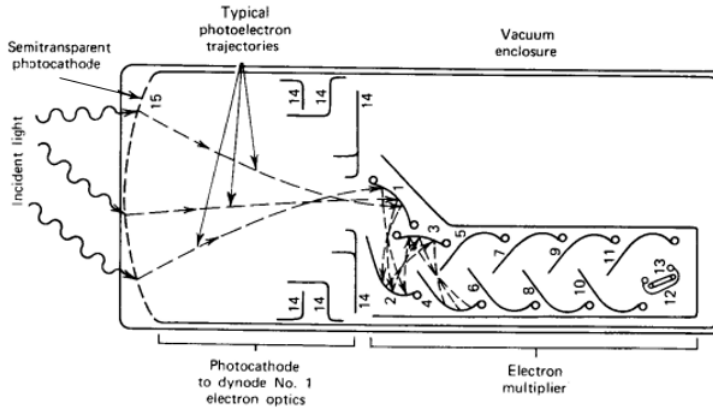
Figure 3.7 – Scheme of a PMT [Kno10].

matsu [Ham19] and the material of their photocathode is Bialkali[3].

The response of the PMT has a strong dependence on the energy of the photon. The quantum efficiency (QE) spectrum, shown in Figure 3.8 for the PMTs mentioned above, is defined as the ratio of the number of photoelectrons produced at the photocathode of the PMT and the number of photons reaching it.

The maximum value of the PMT quantum efficiency is usually between 20% and 30% [Kno10] (slightly less than 30% for the PMTs used in this thesis). The emission spectrum of the scintillating fibres used, Figure 3.5, matches the quantum efficiency spectrum of the PMTs used, Figure 3.8, and the positions of both peaks are very close, 435 nm and 420 nm for fibres and PMT respectively. Thus, the intrinsic efficiency of the TRITIUM detector is maximized.

2. As the number of photoelectrons produced in the photocathode is very small, an electron multiplication stage is employed to obtain an electronic signal of sufficient size to be processed by the electronic system. The amplification stage is based on three elements, focusing electrodes, dynodes and the anode, which are metallic plates with a

---

[3]The bialkali material is based on the elements $^{121}_{51}$Sb, $^{85}_{37}$Rb and $^{132}_{55}$Cs
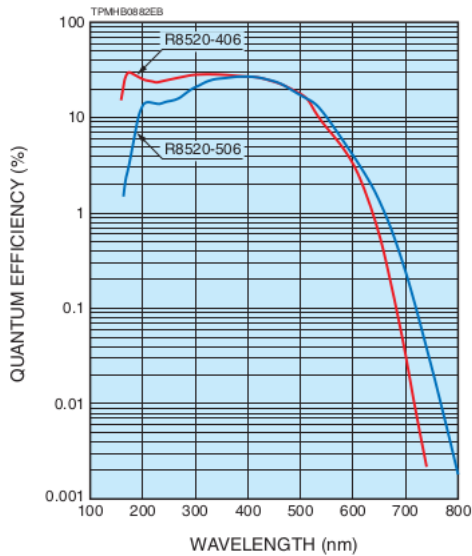
Figure 3.8 – Quantum efficiency spectrum for the PMT used in TRITIUM R&D studies (R8520-406) [Ham19].

shape and position designed to optimize the collection and multiplication of electrons. A high voltage (HV) is applied to the PMT which is distributed between all these elements, including the photocathode, with the help of a voltage divider circuit. A positive HV, grounded in the photocathode, is convenient for measuring PMT currents, and a negative HV, grounded in the anode, gives a faster response. The electronic scheme of the voltage divider circuit of Hamamatsu is shown in Figure 3.9.

Focusing electrodes guide the photoelectrons to the first dynode. They have a collection efficiency (CE) defined as the ratio of the number of photoelectrons reaching the first dynode to the number of those leaving the photocathode. The value of CE depends on the voltage between photocathode and the first dynode and reaches 100% at voltages typically above 100 V. The dynodes produce the electron multiplication. A voltage difference between adjacent dynodes accel-
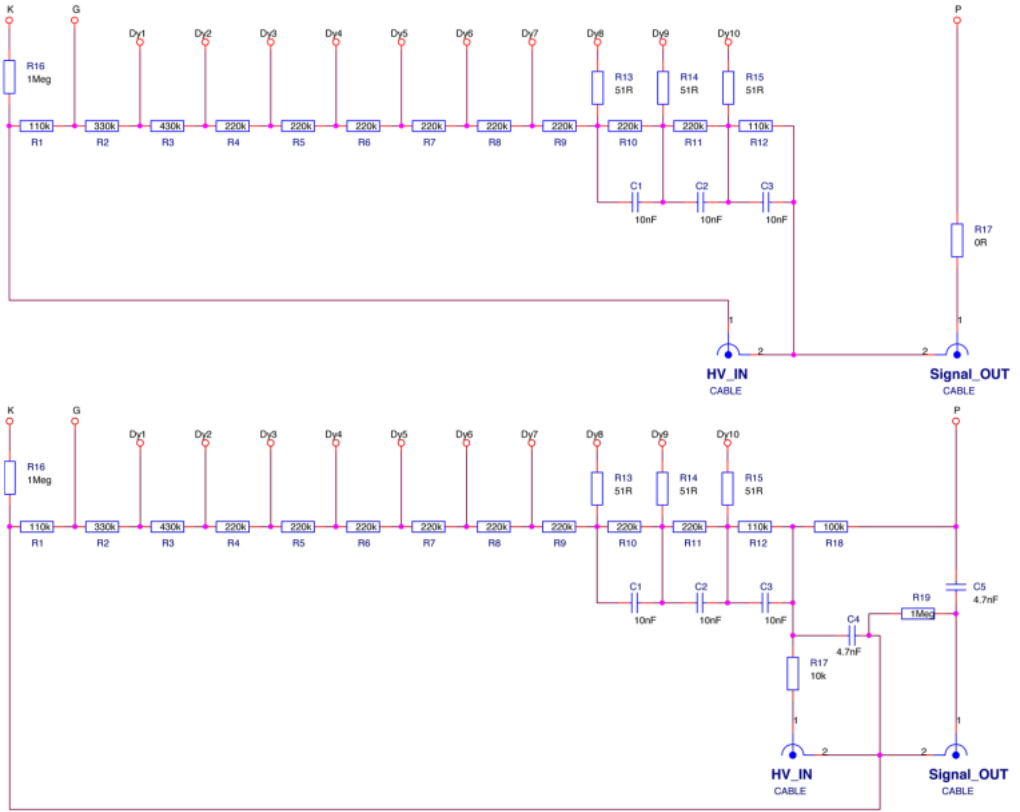
Figure 3.9 – Hamamatsu commercial voltage divider electronic circuit with negative (up) and positive (below) supply high voltage [Ham19].

erates the electrons and produces their multiplication. The multiplication factor δ of each dynode is usually around 5 and depends on the HV. If all dynodes have the same gain, the overall gain of a PMT with N dynodes is given by [Kno10],

$$G_{PMT} = CE \cdot \delta^N \qquad (3.10)$$

and is of the order of 10^6, strongly dependent on the applied HV.

The multiplication process follows a Poisson statistical. For each electron reaching the first dynode, G_{PMT} new electrons are created with
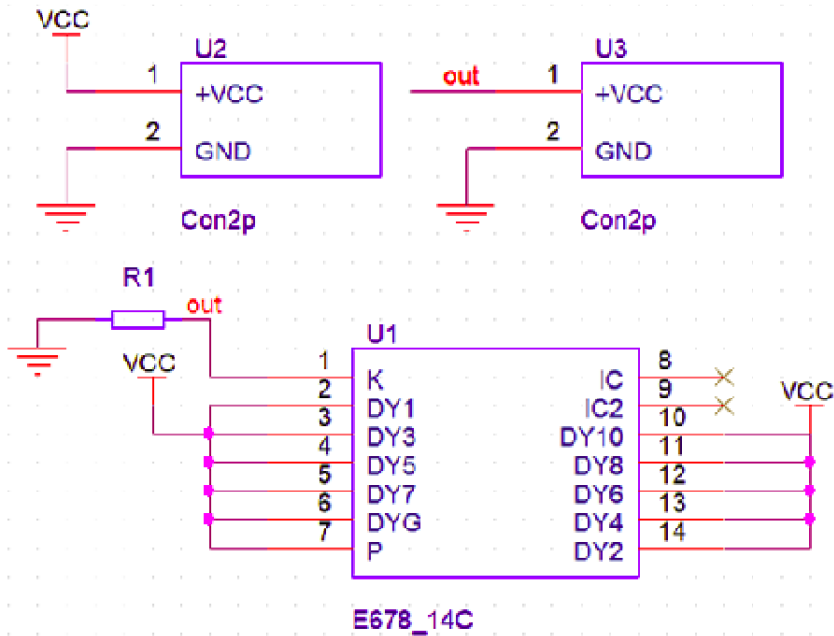
Figure 3.10 – Electronic scheme of the voltage divider circuit used for working with PMTs without internal gain.

a standard deviation of $\sqrt{G_{PMT}}$. To count the number of photons that reach the PMT, the gain is eliminated and, therefore, its contribution to the counting standard deviation. This can be done by short-circuiting all the dynodes and the anode and collecting the signal directly from the first dynode. This is implemented in the voltage divider circuit used for fibre characterization, shown in Figure 3.10.

The output pulse of a PMT has a width of the order of tens of nanoseconds and its amplitude is linear with the number of photons that reach its sensitive part up to a saturation limit, after which the linearity is lost. This limit depends on the PMT characteristics. The photocathode may emit electrons in the absence of light. Their intensity I_{DC}, called dark current, is due to thermionic emission. For the PMTs employed in this work, the dark current at room temperature is around 2 nA according to their data sheet.

3.2.3.2 Silicon Photomultiplier Array

The Silicon Photomultiplier (SiPM), also called Multi-Pixel Photon Counter (MPPC), is a type of photosensor based on silicon developed in the last two decades. SiPMs are replacing progressively conventional PMTs in many experiments and applications. They have outstanding photon counting capabilities at the single photon level with similar gain and higher photodetection efficiency than PMTs. In addition, SiPMs have several advantages as insensitivity to magnetic fields, low operating voltage, compactness and ruggedness. Their main drawback with respect to PMTs is their high dark count rate (between 100 kHz and 1 MHz).

SiPMs are formed by a matrix of Avalanche Photodiodes (APDs) connected in parallel and operating in Geiger mode. APDs, shown in Figure 3.11, are based on p-n junctions. The voltage V_{BD} at which a SiPM starts
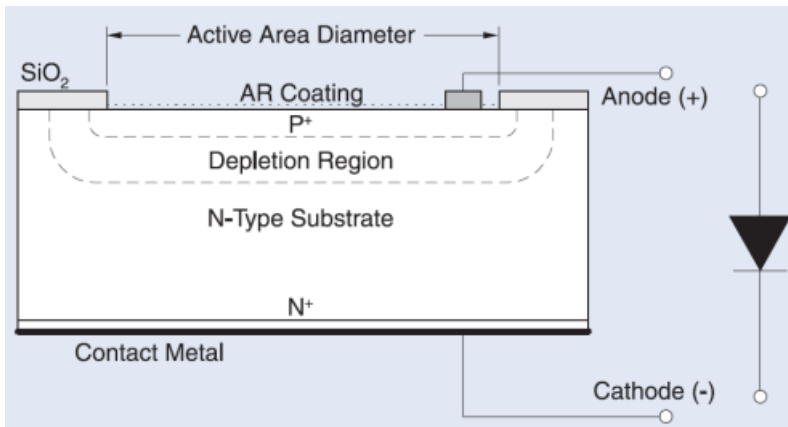
Figure 3.11 – Scheme of an APD and electrical symbol used [OSI].

operating in Geiger mode is called the breakdown voltage. At voltages lower than V_{BD}, SiPMs work in the proportional mode in which the signal of each APD is proportional to the energy deposited. The measurement of V_{BD}, described in section 4.2, is important to characterize a SiPM since its characteristics depend on the overvoltage V_{OV} defined as the SiPM bias

voltage above V_{BD},

$$V_{OV} = V_{bias} - V_{BD} \qquad (3.11)$$

The SiPM APDs, called pixels, are connected in parallel to give the SiPM output signal. If the photon flux is low enough, each SiPM pixel detects at most one photon. All pixels produce a similar output signal, regardless of the energy deposited. Therefore, the charge of the output signal when n pixels are simultaneously fired is n times the charge of a single pixel. This behaviour is illustrated in Figure 3.12 where the output signals corresponding to a different number of fired pixels are shown. Hence, the number of detected photons is proportional to the integrated output signal. Once the SiPM is calibrated, the energy of tritium events can be determined. If the photon flux is high (typically several thousands of photons per event) more than one photon impinges simultaneously on the same pixel, producing an output signal corresponding to a single photon. This effect, known as saturation, produces a loss of linearity of the output signal. In the TRITIUM detector, this effect is negligible since tritium electrons produce few photons.

Different sizes of SiPM pixels are available[4]. For a given SiPM active area, a small pixel size allows a high dynamic range at the cost of reducing the photon detection efficiency (PDE). As tritium electrons produce few photons, the SiPMs chosen have a large pixel size (75 μm) since we are well within the dynamic range.

A SiPM can be modelled as an electrical circuit, shown in Figure 3.13a. The depletion zone is represented by a capacitance, C_d. When a photon impinges on the pixel, the capacitor is discharged, creating an electronic pulse. Each pixel of a SiPM has a quenching resistance[5] R_q that limits the avalanche current produced when this pixel is fired. When the discharge is produced, a current flows through the resistance, reducing the reverse voltage seen by the diode. The current through the diode eventu-

---

[4]Pixel sizes for commercial SiPMs are 25, 50 and 75μm [Ham16a, Ham16c, Ham16d]

[5]The typical value of this quenching resistance for commercial SiPMs is around 500 kΩ
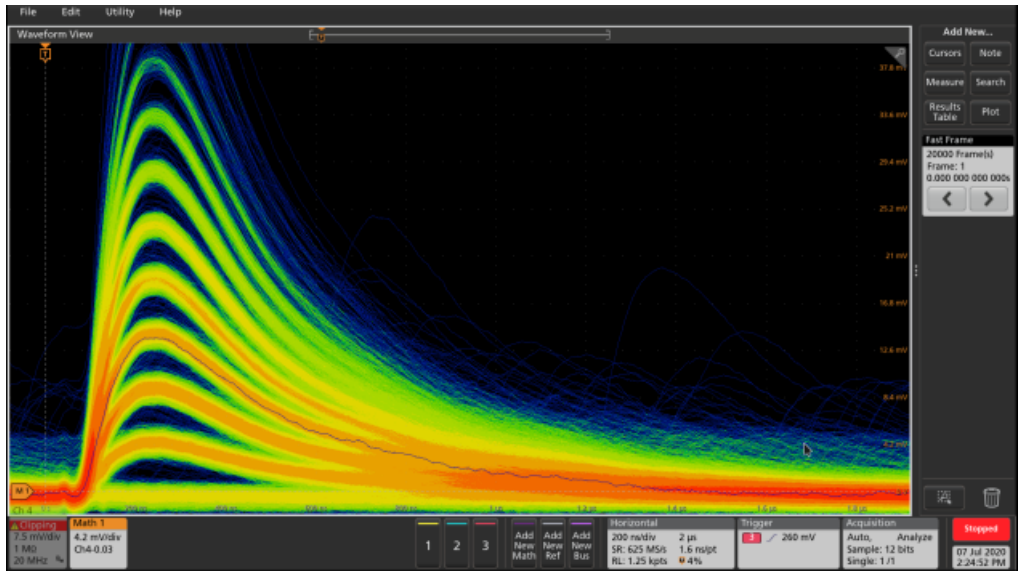
Figure 3.12 – SiPM output pulses displayed on the oscilloscope, model MSO44X from Tektronix [Tek21]. Several height pulses are observed, associated to a different number of SiPM pixels fired at the same time. The persistence function of the oscilloscope is used.

ally vanishes and the bias voltage is reset. This pixel is ready to detect a new photon. This behaviour is schematically shown in Figure 3.13b. The voltage after photon detection is characteristic of an RC circuit, described by the equation:,

$$V(t) = V_{bias} \left(1 - e^{-t/\tau_r}\right) \tag{3.12}$$

where τ_r is the recovery time constant of the system given by $\tau_r = C_d R_q$.

The SiPM gain (typically of the order of 10^6) is defined as the number of e-h pairs produced when a pixel is fired. The gain can be measured from the SiPM single photon spectrum (SPS) which is the spectrum obtained when the SiPM output signal is integrated. The SiPM gain is highly dependent on temperature. As the temperature cannot be controlled with an accuracy better than $1°C$ in the final location of the TRITIUM monitor, a gain stabilization method is necessary to compensate for gain variations

(a)

(b)
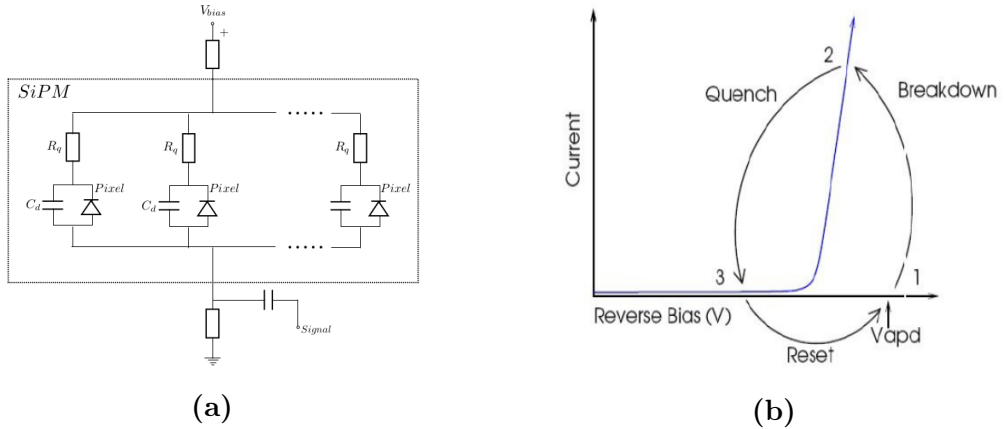
Figure 3.13 – (a) Electronic scheme of a SiPM and (b) output current of a SiPM as a function of the reverse voltage. As shown, quenching is an essential working mechanism of SiPMs [Sen17].

due to temperature changes.

An important parameter for SiPMs is the PDE, defined as the percentage of the incident photons that are detected. The PDE of a SiPM depends on three different parameters: the fill factor (FF), which is the ratio between the active area of the SiPM and its total area, the quantum efficiency (QE), which is the probability of producing a photoelectron when a photon hits the SiPM, and the probability P_{av} that an avalanche is produced. Thus,

$$PDE = FF \times QE \times P_{av} \tag{3.13}$$

SiPMs produce a dark current that depends on temperature. The dark current and photon events are identical, so they cannot be discriminated. Therefore, it is essential to determine the magnitude of the dark current in the TRITIUM detector.

Avalanche electrons in a pixel can emit secondary optical photons[6].

---

[6]Around 20 secondary optical photons are emitted in each pixel for gains of the order of 10^6 [Spi97]

These optical photons can reach other pixels, producing new avalanches. This effect, called optical cross-talk, produces photoelectrons that add to those truly induced by incident photons, and hence leads to an overestimation of the number of photons detected. The probability of producing an optical crosstalk event depends on the number of electrons produced in the avalanche and, therefore, on temperature and overvoltage. This probability is typically less than 10% at the overvoltage recommended at 25°C by the manufacturer.

Due to imperfections existing in the crystal lattice of a SiPM, called traps, an electron of an avalanche can be captured and released after a characteristic time τ_a. If this characteristic time is longer than the pixel recovery time, typically 3τ, this electron can trigger a new avalanche which will be seen as a new event. These events, called afterpulses, are often emitted around 1 μs after the incident photon pulses. The afterpulse probability was not measured since it is not relevant for the TRITIUM detector because SiPMs are read out in coincidence within 10 ns time.

The initial SiPM candidate for the TRITIUM detector and the one which was characterized in this thesis is the model S13360-1375 from Hamamatsu Photonics [Ham16b] whose characteristics are given in Table 3.3. This model was mainly chosen due to its large pixel size, 75 μm, which implies high PDE and gain. This SiPM model was later replaced by the model S13360-6075 from Hamamatsu Photonics [Ham16d], whose characteristics are also listed in Table 3.3. The only difference between this model and the first is its larger active area (6×6 mm^2) that allows reading more scintillating fibres but at the price of a higher dark count rate (typically 2 Mcps). The parameters quoted in Table 3.3, are typical values provided by the manufacturer. They can vary from one SiPM to another of the same model. Thus, it is necessary to measure them. Some of these measurements are reported in section 4.2. This SiPM was also chosen because its maximum PDE is reached at $\lambda_{p,SiPM} = 450$ nm, as can be observed in Figure 3.14. This wavelength is very close to the peak of the

Characteristics	S13360-1375	S13360-6075
Series	$S13360$	$S13360$
Model	1375	6075
Pixel Pitch (μm)	75	75
Effective photosensitive area (mm^2)	1.3×1.3	6.0×6.0
Number of pixels	285	6400
Fill factor	82%	82%
Refractive index of windows material	1.55	1.55
Operating temperature range (°C)	$[-20, 60]$	$[-20, 60]$
Spectral response range, λ (nm)	$[320, 900]$	$[320, 900]$
Peak sensitivity wavelength, λ_p (nm)	450	450
PDE (%)	50	50
Dark counts, Typical/Maximum (kcps)	90/270	2000/6000
Terminal capacitance, C_t (pF)	60	1280
Gain	$4 \cdot 10^6$	$4 \cdot 10^6$
V_{BD} (V)	50.97	53
Cross talk probability(%)	7	7
Temperature coefficient (mV/°C)	54	54

Table 3.3: Characteristics of SiPM S13360-1375 and S13360-6075 from Hamamatsu Photonics [Ham16b].

emission spectrum of the scintillating fibres used, $\lambda_{p,fibre} = 435$ nm. The
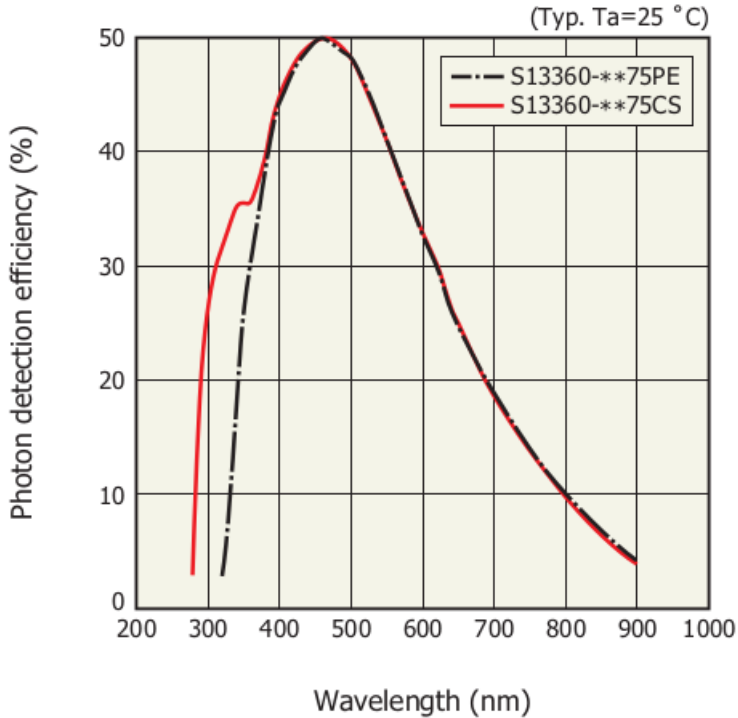
Figure 3.14 – PDE spectrum for SiPM S13360-**75 models [Ham16b].

characteristics was carried out at the level of a single SiPM to measure its characteristics and to test the gain control method.

3.2.3.3   Photosensors of TRITIUM

Two different types of photosensors are proposed for the TRITIUM monitor, PMTs and SiPM arrays. Each type of photosensor has advantages and disadvantages and must be tested to determine the most suitable option. PMTs are used in the TRITIUM prototypes developed by the Aveiro experimental group while SiPM arrays are used in the TRITIUM prototypes developed at IFIC. The IFIC group has chosen SiPM arrays as photosensors

for their advantages over PMTs, which are compactness and robustness, necessary to work for several years without supervision, larger efficiency for detection of photons in the visible range and more economical price of both photosensors and electronics.

3.2.4 Electronics

In this section, the PETsys electronics for SiPM arrays and the electronics for single SiPM and PMT characterization are described. For the final TRITIUM prototype there are two different proposals for the DAQ system: the PETsys system and a specific electronic system developed by the Aveiro group to read the TRITIUM monitor with PMTs. This electronics is described in Appendix D.

3.2.4.1 Electronics for PMTs

PMTs are used in the TRITIUM experiment for two main objectives. On the one hand, to determine the number of incident photons that reach the PMT photocathode and, on the other hand, to measure the energy spectrum of tritium events in the laboratory prototypes.

To determine the number of photons reaching the photocathode, the PMT should work without gain which is a source of uncertainty. For this, the bias circuit shown in Figure 3.10 was employed. As electrons are not multiplied, the output current of the photosensor is very small (currents in the nA range). This output current was read out by a Keithley 6487 Picoammeter/Voltage Source [Keia].

The energy of the events was measured using PMTs powered with the voltage divider shown in Figure 3.9. A scheme of the electronics is shown in Figure 3.15. The PMTs were powered by a TC 952 High Voltage

(a)

(b)

(c)
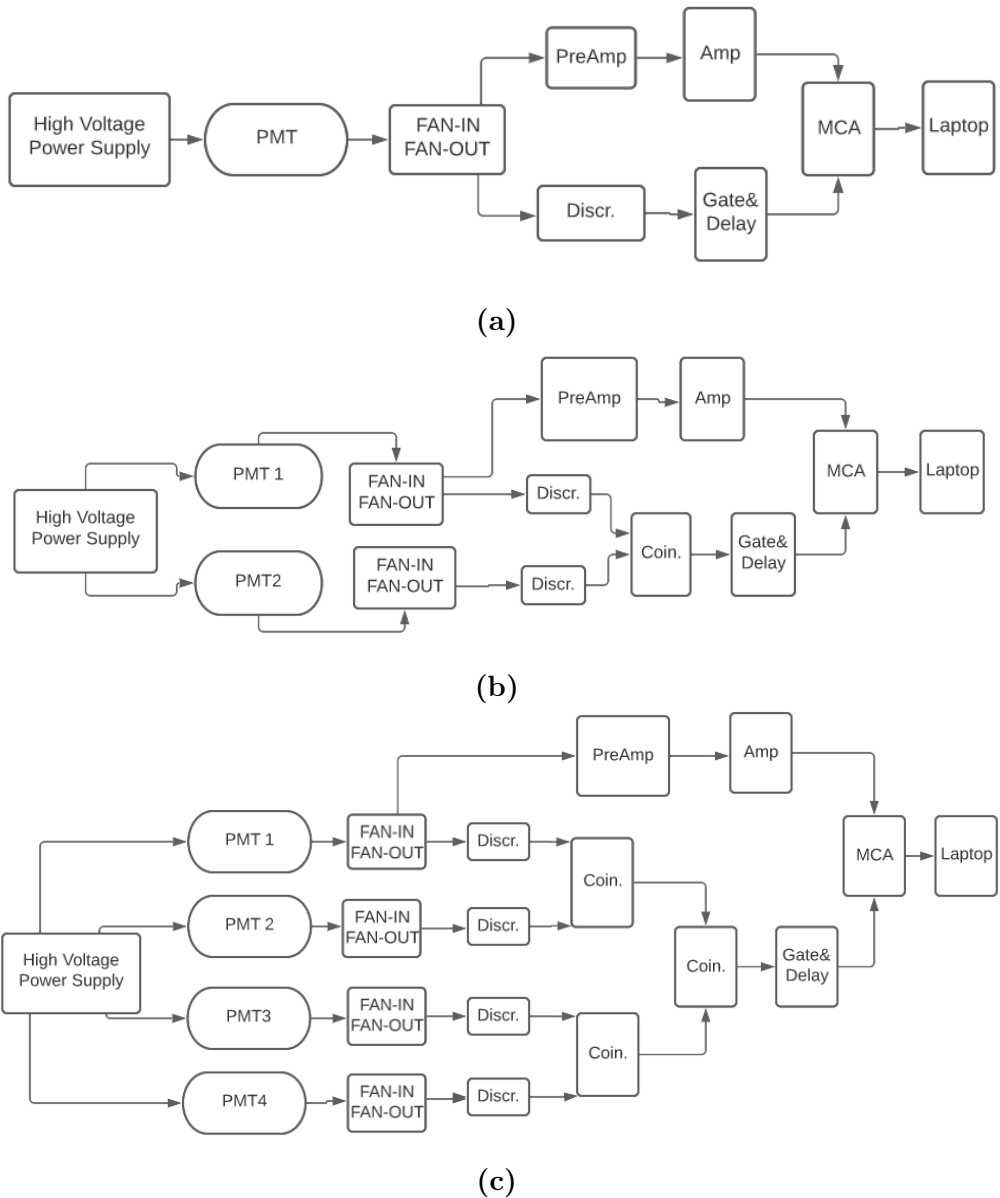
Figure 3.15 – Electronic schemes employed for measuring with a) one PMT, b) two PMTs in coincidence and c) four PMTs in coincidence.

Supply from Tennelec [Mir] and a HV Power Supply N 1130-4 from Wenzel Elektronik [Wen]. The PMT output signals were split by an analogue FAN IN-OUT model 740 from Phillips Scientific [Phi] to feed the amplification and time coincidence lines. The amplification line consists of a preamplifier, model 9326 FAST PREAMP from ORTEC [ORTd], which gives an output signal with a height proportional to the charge of the input pulse and of an amplifier, model 575A or 671 from ORTEC [ORTb, ORTc], which produces a Gaussian shaped output signal. An example of the 575A amplifier output signal is shown in Figure 3.17, in green color.

The time coincidence line consists of the following branches:

1. A constant fraction discriminator, either module CF8000 from OR-TEC [ORTe] or model 84 from CAEN [CAE91].

2. In the case of two or four PMTs, a coincidence module, either 465 from LeCroy [LeC] or Coincidence Type N6234 from CERN-NP [CER], to generate an output signal of 20 ns width when both inputs are in coincidence.

3. In the case of four PMTs, an additional coincidence stage is employed. In Figure 3.16, coincidences of 4 PMTs signals are shown. Case d) shows a coincident event.

4. A Gate and Delay Generator, model 416A from ORTEC [ORTa], to produce a positive logic signal of 8 V height and 2 μs width. This module delays the time windows until they overlap with the energy signal as shown in Figure 3.17.

The energy signal and the coincidence signal, shown in Figure 3.17, are recorded by an MCA model 8000D from AMPTEK [Amp].

(a)

(b)

(c)

(d)
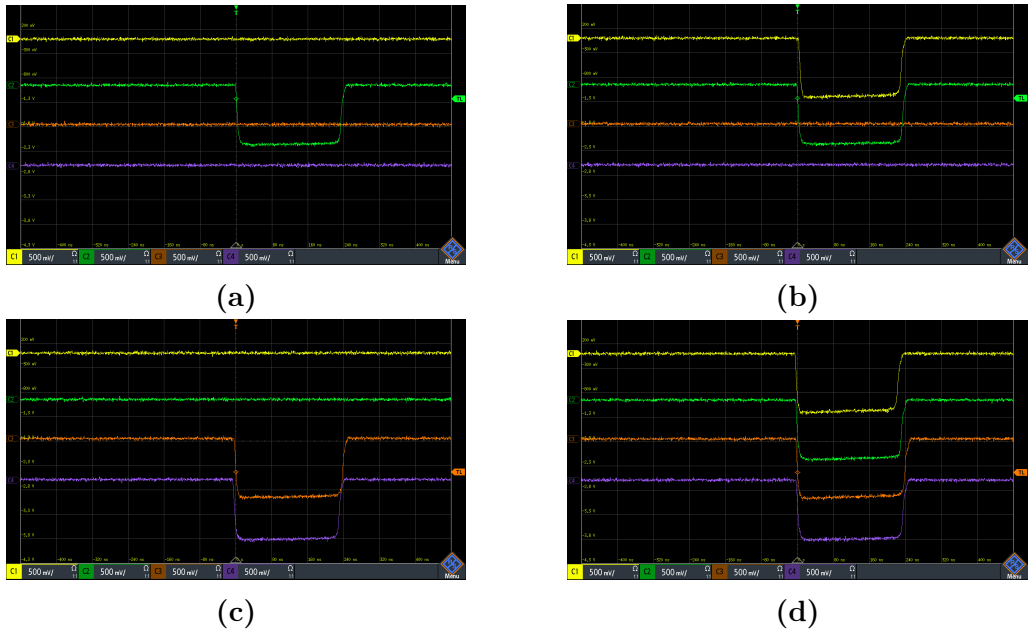
Figure 3.16 – Different possibilities for coincidence of four PMTs. Case d) shows coincident events.

Figure 3.17 – Amplified signal and logic gate (input signals of the MCA).

3.2.4.2 Electronics for SiPMs

The TRITIUM SiPMs are arrays of 4×4, model S13361-6050 from Hamamatsu [Ham16e]. The electronics chosen to acquire and analyze the output signals of these SiPM arrays is PETsys [PET], displayed in Figure 3.18. PETsys is a commercial readout system designed for Hamamatsu SiPM arrays which includes QDCs[7] and TDCs[8], providing time and energy digitalization of up to 1024 SiPM channels.
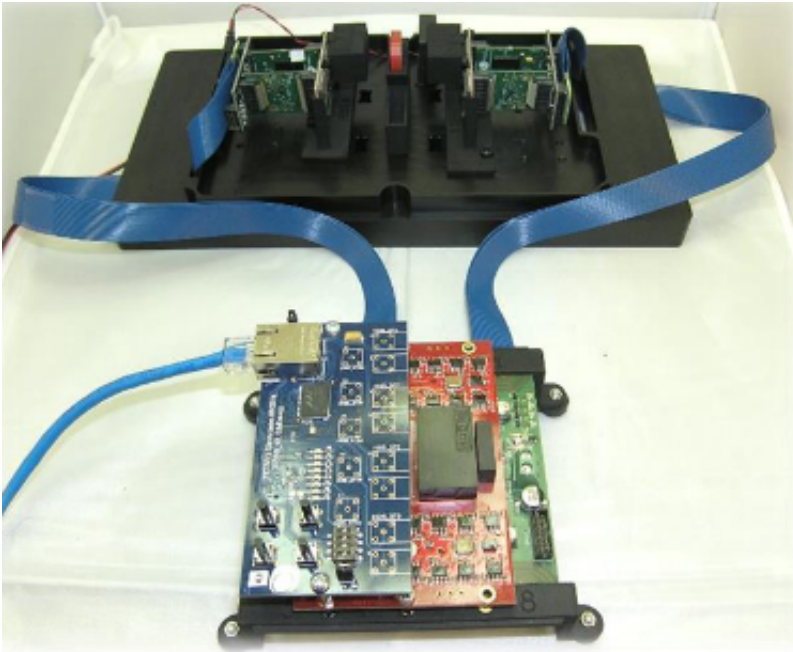
Figure 3.18 – A general view of the PETsys system [PET].

TRITIUM is a modular detector whose sensitivity could be improved by adding more modules and, therefore, its readout electronics should be scalable. This requirement is fulfilled by PETsys since it has an additional module, called Clock & Trigger, with which up to 16 different PETsys

---

[7]charge-to-digital converter
[8]time-to-digital converter

basic boards can be read out in parallel. This module gives to PETsys a capacity of reading up to 256 SiPM arrays.

The PETsys software is based on C++ and Python scripts that drive the main tasks required, such as time coincidence options between SiPM arrays or energy discrimination. This software is open source, giving the possibility of modifying the current scripts or developing others with additional functions. PETsys has a time resolution better than 30 ps which is one of the best time resolutions of available commercial systems available. Its price is around 10 €/channel, which is cheaper than similar electronic systems. The PETsys system can monitor the temperature of the SiPM arrays and ASICS. In PETsys, the stabilization method of the SiPM gain, reported in section 4.2, can be implemented.

Some characterization measurements were carried out using the PETsys system to verify that the system works properly but the SiPM characterization was carried out at the level of a single channel (individual SiPM). The reason is that the output information of PETsys is delivered integrated and digitized which cannot be used for the calibration of SiPMs. Therefore, to characterize a SiPM, the PCB shown in Figure 3.19 was designed to bias the SiPM and to amplify its output signal.

This PCB was powered at ± 6 V using an ISOTECH IPS-4303 voltage source [ISO] and the SiPM was biased by a KEITHLEY 6517B electrometer [Keib]. The output signal was connected to a LeCroy WaveRunner 625Zi oscilloscope [Tel17] that recorded the data which were subsequently analyzed using ROOT.
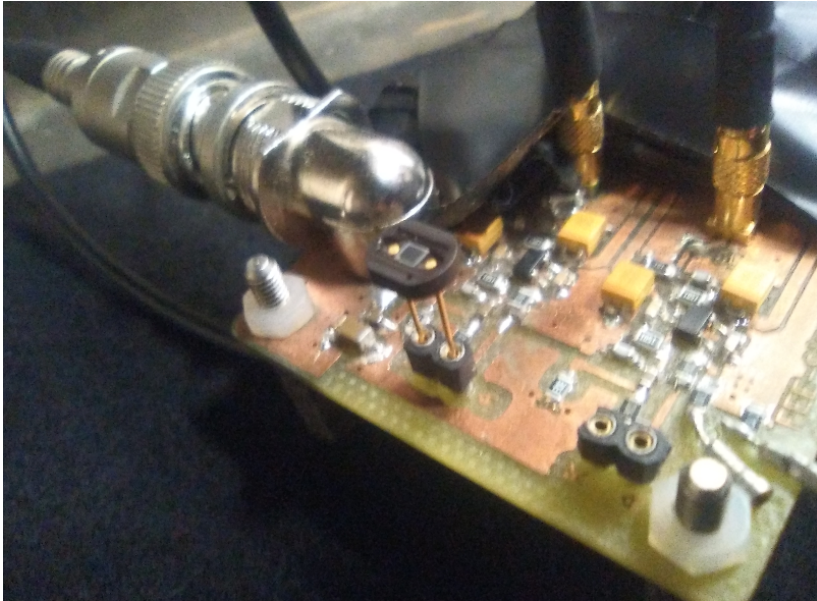
(a)
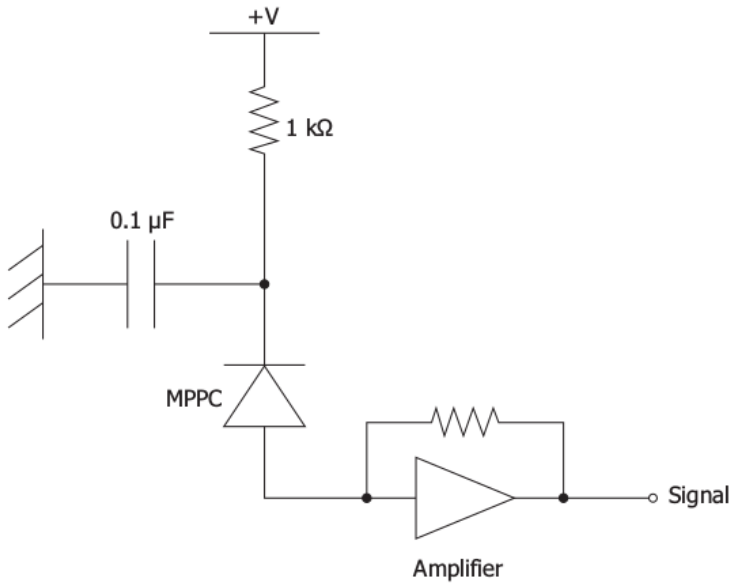
(b)

Figure 3.19 – a) Electronic board used in the SiPM characterization. b) Electronic scheme on which this PCB is based.

3.3 The Water Purification System

3.3.1 Objectives

The water samples to be measured by the TRITIUM detector are taken directly from the Tagus river, at a site 4 km downstream from the water discharge of Almaraz NPP. These samples contain minerals, organic deposits, and living matter, which should be removed for the following reasons:

1. The mean free path of tritium electrons in water is around 5 μm and even less in solid materials. If the analyzed water contains particles that may deposit on the fibres, a deposit could be formed, which would prevent tritium decay electrons from reaching the fibres, reducing drastically the tritium detection efficiency. Therefore, the detector must be kept pristine.

2. The tritium monitor does not have any spectrometric capability that could be used to distinguish tritium from other radioactive elements present in the water.

3.3.2 Design of the Water Purification System

The water purification system was designed to remove organic matter and mineral particles with a size over 1 μm without modifying the tritium level in the water. The requirements of this system are:

1. A high degree of purification of the water sample extracted from the dam, reducing its conductivity by approximately two orders of magnitude (from 1000 μS/cm to 10 μS/cm).

2. Low maintenance cost and manpower.

3. Remote management of the system.

The LARUEX laboratory designed and built the water purification system, whose scheme is shown in Figure 3.20. This system is installed in
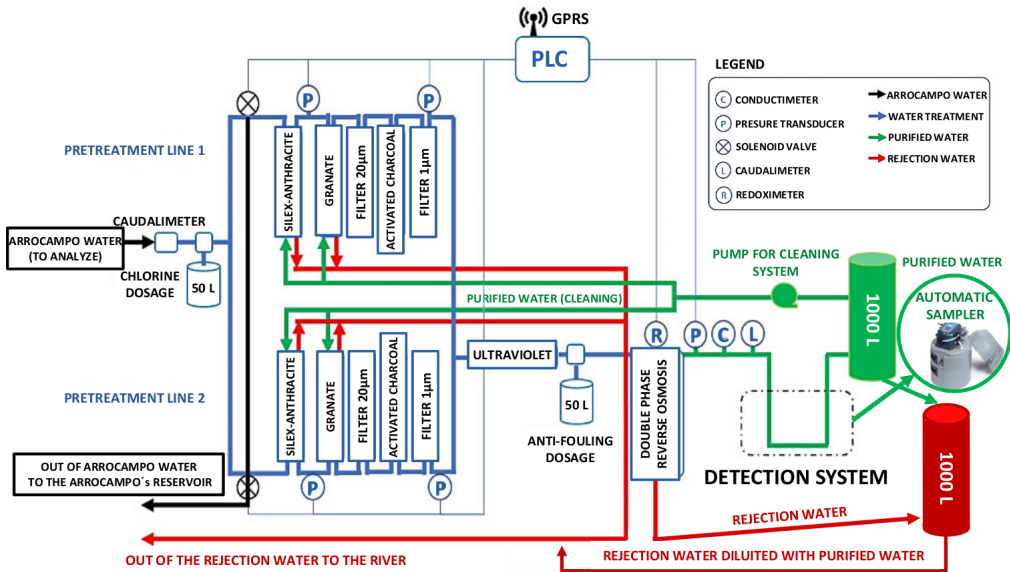
Figure 3.20 – Scheme of the water purification system of TRITIUM.

the Arrocampo site and consists of four different stages:

1. The raw water from the Tagus river passes through two different filters, the first made of silex-anthracite and the second of garnet, with which rough filtering is made (the largest particles are eliminated). This system has two identical parallel lines and implements a self-cleaning function by injecting purified water in the opposite direction.

2. The outlet water from the first stage, called the fine filtration stage, passes through a 20 μm filter (formed by a synthetic mesh) and activated charcoal filters (one per line) that remove chlorine and iron particles present in the water.

3. The outlet water from the second stage goes into a super-fine filtering stage consisting of a 1 μm filter, made of a dense polypropylene mesh and of UV lamps. The filter removes all the particles with a diameter larger than 1 μm and the UV lamps sterilize the water, eliminating bacteria and microscopic life.

4. Finally, the water is introduced into the last stage which consists of double-phase reverse osmosis for reducing the conductivity of the water to about 10 μS/cm.

As a result of the purification process, besides the pure water that is introduced into the TRITIUM detector, rejection water is produced, which contains the particles removed from the sample. The water purification system can process up to 0.850 m^3/h with a single operating line or 1.480 m^3/h with both lines.

The software used for remote controlling the water purification system is the Siemens Programmable Logic Controller (Siemens PLC), which gives information of the state of the valves, the pressure probes and the amount of ultrapure water production in real-time. The appendix B contains several pictures of different parts of this system.

3.4 The Background Rejection System

The aim of the background rejection system is to reduce the radioactive and cosmic background of the TRITIUM monitor. The TRITIUM project follows the ALARA principle for the tritium activity measurement, that is, to measure a tritium activity *as low as reasonably achievable*. The detection limit of tritium activity is set by the uncertainty of the background measured by the TRITIUM detector since tritium activities below this uncertainty cannot be resolved. Therefore, the background must be reduced as much

as possible. The total uncertainty is given by the rms of the statistical σ_{st} and systematic σ_{sys} uncertainties. Because of the Poissonian nature of the process, the statistical uncertainty is given by the square root of the total activity A_m which can be reduced by minimizing the background,

$$\sigma_T^2 = \sigma_{st}^2 + \sigma_{sys}^2; \qquad \sigma_{st} = \sqrt{A_m} \qquad (3.14)$$

The background rejection system of the TRITIUM monitor suppresses the background of the TRITIUM detector, reducing the total uncertainty.

The background of TRITIUM has two different sources. On the one hand, the radioactive elements present in the Earth's crust, mainly ^{40}K and elements from the four natural radioactive series, listed in Table 3.4. On the other hand, cosmic ray radiation. The primary cosmic radiation, of extra-terrestrial origin, is composed of high-energy particles, mainly protons and α particles, which interact with the Earth's atmosphere and generate a shower mainly composed of muons, electrons, photons and neutrons. Cosmic radiation depends on several parameters like the longitude, latitude, and the solar activity cycle. The spatial distribution of cosmic rays, mainly muons, follows a $\cos^2\theta$ distribution with the zenith angle θ.

Mass Num.	Series	Primary	Half life (y)	Final
4n	Thorium	^{232}Th	$1.41 \cdot 10^{10}$	^{208}Pb
4n+1	Neptunium	^{237}Np	$2.14 \cdot 10^{6}$	^{209}Pb
4n+2	Uranium-Radium	^{238}U	$4.51 \cdot 10^{9}$	^{206}Pb
4n+3	Uranium-Actinium	^{235}U	$7.18 \cdot 10^{8}$	^{204}Pb

Table 3.4: Classification of natural radioactive series [The96, Eva95]. The information displayed for each radioactive series is the name of the series, the primary and final element and the half-life of the primary element.

Two different techniques are employed for background suppression:

1. The soft background component, with energy below 200 MeV, is

      stopped by a lead castle.

2. The hard background component, with energy greater than 200 MeV, is harder to stop and the technique employed is the use of a cosmic veto in anti-coincidence with the TRITIUM detector.

3.4.1 Passive Shield

The soft background component is suppressed by a lead shield inside which the TRITIUM detector is placed. This lead shield is efficient for suppressing radiation that originates from the Earth's natural radioactivity and the soft component of cosmic radiation with energies below 200 MeV. This lead shield consists of 158 low intrinsic radioactivity lead bricks of 25 mm thickness. The bricks are chevron shaped, as shown in Figure 3.21, specially designed for a perfect fit and easy assembly. As can be seen in Figures 3.22a and 3.22, these lead bricks are arranged in two layers with a total thickness of 50 mm. An aluminium structure capable of supporting the

Figure 3.21 – Lead bricks.

total weight of 2.4 tons of lead bricks, shown in Figure 3.23, was designed by the Mechanical Engineering Department of the CENBG. The internal room of the lead shield is divided into two parts, as indicated in Figure 3.23. The larger one has internal dimensions of $90.5 \times 41 \times 51$ cm^3 and is used to place the TRITIUM detector. The smaller one, with dimensions of
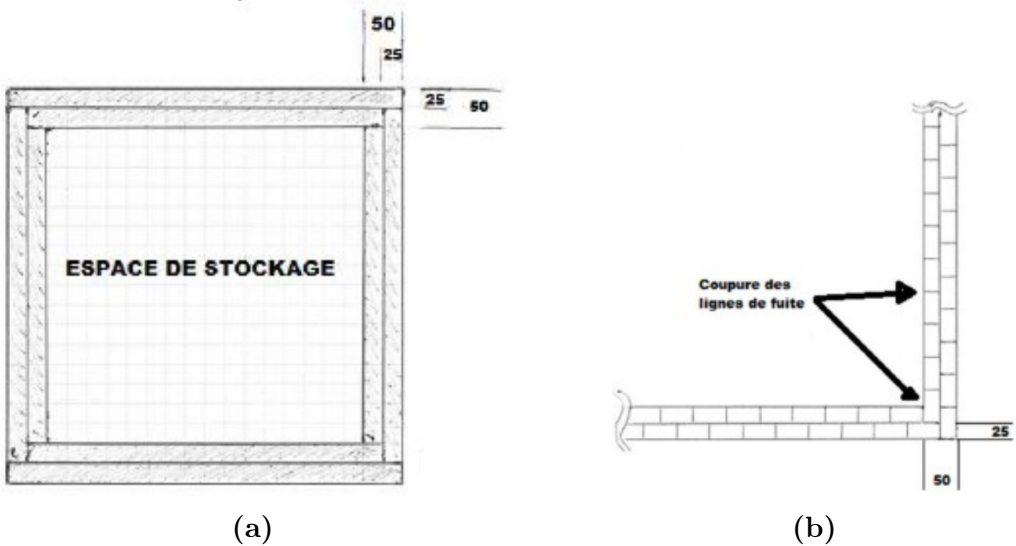
Figure 3.22 – Two layers for the lead bricks of the shield. a) General view of the lead castle. b) Detail of the lead brick arrangement.

$33 \times 41 \times 51$ cm^3, contains the DAQ system of the detector. The external dimensions of the lead shield are $148 \times 60 \times 70$ cm^3 and its total weight is 2.5 tons.

3.4.2 Active Shield

As hard radiation cannot be stopped by a moderate lead thickness, cosmic vetos are employed which consist of two complementary detectors in co-incidence that provide a signal for events simultaneously detected in both of them. As shown in Figure 3.24, the two complementary detectors are placed one above and the other below the TRITIUM detector. The distance between both detectors is 34.2 cm, just enough to enclose the TRITIUM IFIC prototype.

A hard cosmic event crossing simultaneously both cosmic detectors is sketched in figure 3.25a. Each cosmic detector has two photosensors,

(a) (b)
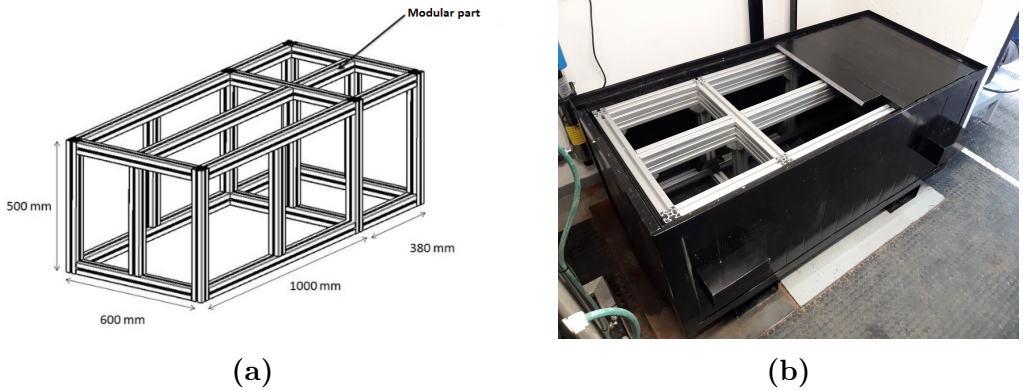
Figure 3.23 – a) Scheme of the aluminium structure of the shield. b) The lead shield partially mounted.

so the electronic configuration given in Figure 3.15c is used to make coincidence. The TRITIUM detector is read out in anti-coincidence with the cosmic veto to reject the hard cosmic events from the tritium measurements. The expected hard cosmic rate at sea level for muons is 7×10^{-3} cm^{-2}s^{-1}sr^{-1} [Zyl20, Sag12], as shown in Figure 3.26. As time coincidences are triggered by logic gates of about 10 ns, the probability of recording two different hard cosmic events in coincidence is negligible.

The vetos are made of plastic scintillator from Epic-Crystal [Epi20] whose characteristics are given in Table 3.5 and its energy emission spectrum is displayed in Figure 3.27. The energy spectrum has a peak very close to that of the scintillating fibres used, so the same photosensors are used for their readout. The dimensions of the scintillator plates are $45 \times 17 \times 1$ cm^3. They are wrapped in three different layers, PTFE sheet, aluminium leaf and black tape, as shown in Figure 3.28. These layers prevent external photons from reaching the plastic scintillator and photons generated by the scintillator from escaping before reaching the photosensor. Two 2.5×2.5 cm^2 windows are made on the wrapping for coupling the photosensors.

The solid angle subtended by each veto plate on the other is $\omega =$
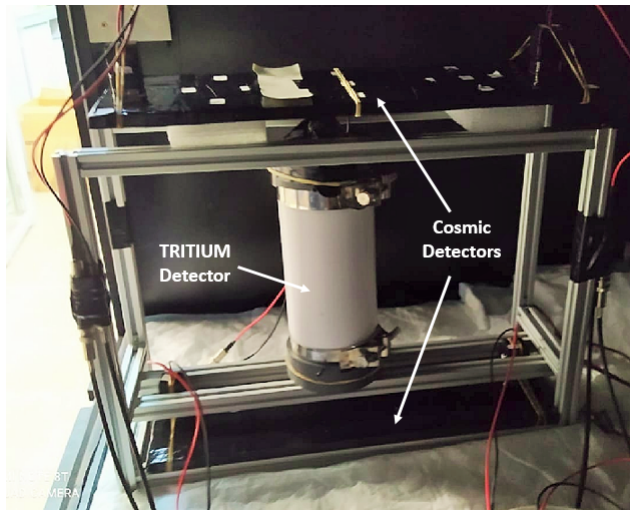
Figure 3.24 – Cosmic veto and Tritium-IFIC-2 prototype inside the aluminium mechanical structure developed at IFIC.

0.5434 sr and the area is 765 cm^2. Considering the expected hard cosmic rate of 7×10^{-3} cm^{-2}s^{-1}sr^{-1} at sea level the expected hard cosmic ray rate is 2.909 Hz, which is used in section 4.4 to determine the efficiency of the veto.

(a)   **(b)**
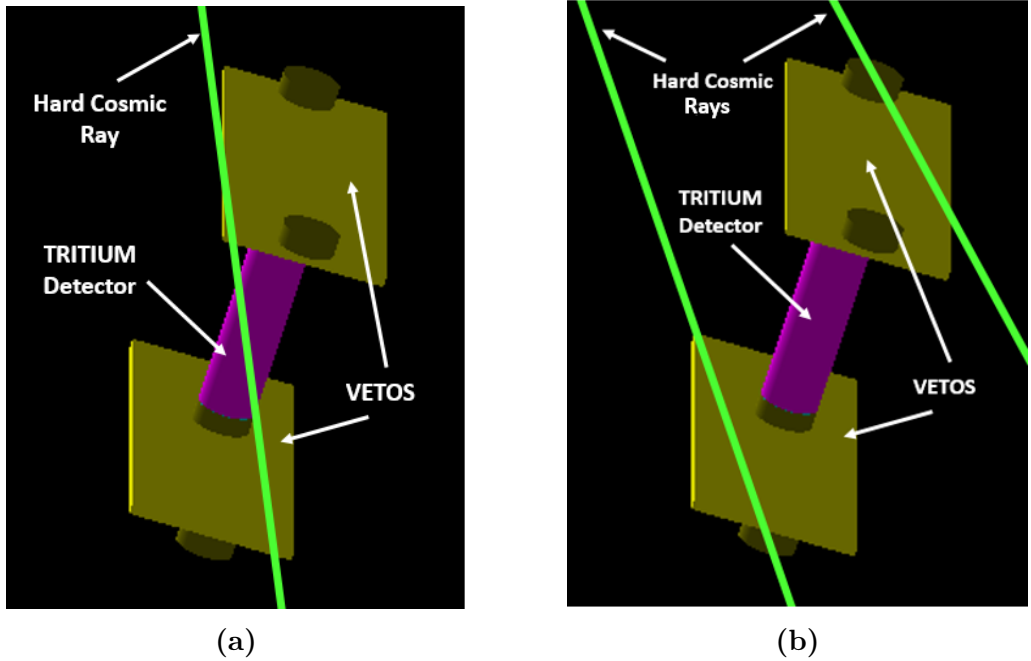
Figure 3.25 – Hard cosmic events detected with the cosmic veto of TRI-TIUM: a) Real coincidence event. b) Random coincidence event.

Characteristic	Value
Base material	Polystyrene
Growth method	Polymeric
Density (g/cm^3)	1.05
Refractive index	1.58
Soften temperature (°C)	75-80
Light output (anthracene)	50-60%
H/C ratio	1.1
Emission peak (nm)	415 (blue)
Decay Time (ns)	2.4
Hygroscopic	No

Table 3.5: Characteristics of the plastic scintillator from Epic-Crystals [Epi20].
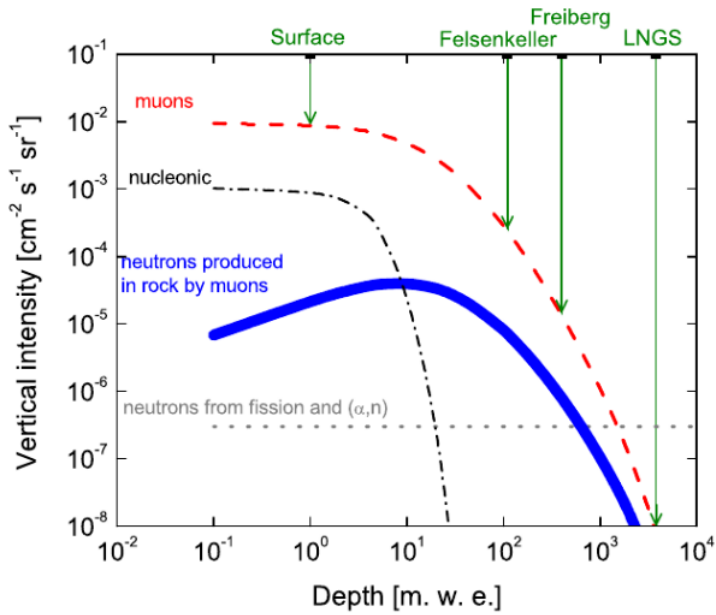
Figure 3.26 – Hard cosmic muon rate at different depths [Szu15].
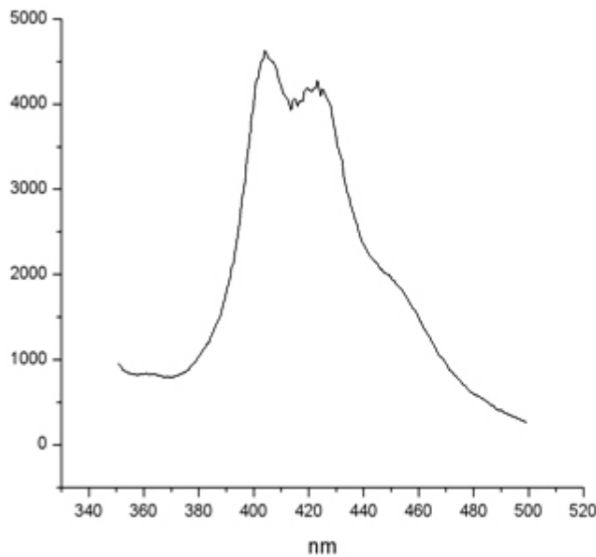
Figure 3.27 – Emission spectrum of the plastic scintillator from
Epic-Crystals [Epi20].

(a)   **(b)**   **(c)**   **(d)**
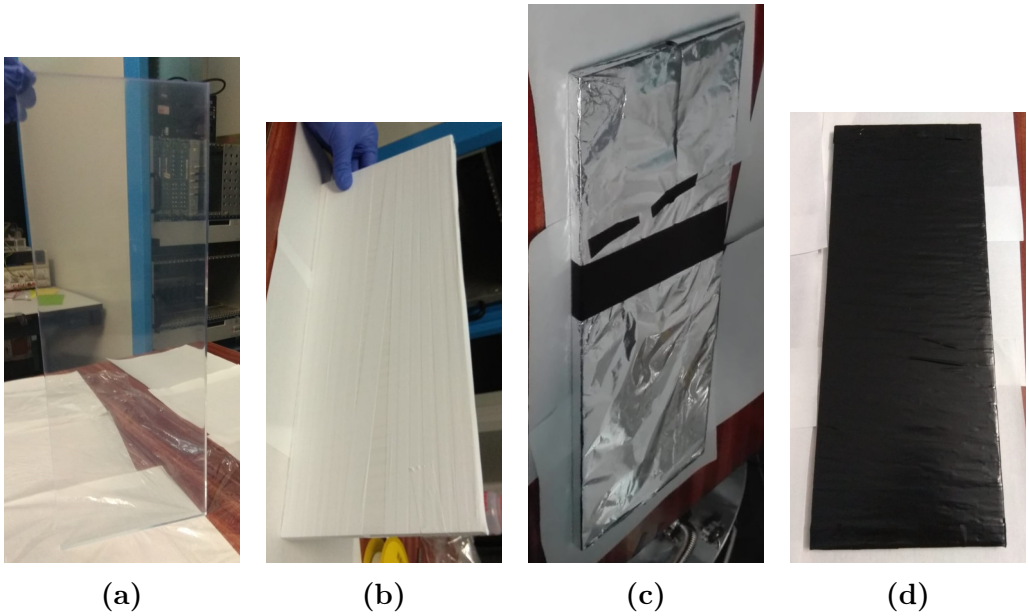
Figure 3.28 – Different layers used to wrap the cosmic veto detectors. a) Scintillator without wrapping. b) PTFE wrapping. c) Aluminium wrapping. c) d) Black tape wrapping.

Chapter 4

TRITIUM Monitor R&D

The characterization of the different parts of the TRITIUM monitor, including scintillating fibres, SiPMs, the water purification system and the background rejection system, are described in this chapter. This characterization is crucial to understanding the behaviour of the different parts and the measurement results. Furthermore, several developments were made to improve the parameters of the TRITIUM monitor components to enhance its sensitivity to low levels of tritium in water.

4.1   R&D for the Scintillating Fibres

Measurements of the plastic scintillating fibre parameters relevant for tritium detection, such as the collection efficiency and the systematic uncertainty of the measured tritium activity are reported in this section. The TRITIUM detector is composed of thousands of scintillating fibres which have to be prepared. Various mechanical and electronic devices were developed to prepare a large number of fibres simultaneously.

4.1.1 Preparation of Scintillating Fibres

A surface-conditioning of the scintillating fibres, which consists in cleaving, polishing and cleaning, was implemented to improve their photon collection efficiency. These methods are described in the following subsections.

4.1.1.1 Cleaving of Scintillating Fibres

The first step in the TRITIUM design was to choose the fibre length and the fibre diameter (1 or 2 mm) for which the signal of tritium events is optimized. For a given active area, the longer the fibres, the smaller the number of photosensors needed. However, in long fibres photons are reflected on their boundaries many times before reaching the photosensors which may produce a deterioration of the tritium signal. To determine the optimal fibre length, several simulations, described in section 6.2.3, were carried out using Geant4 [GEA]. It was concluded that the optimal fibre length for measuring tritium in water is around 20 cm, which is the fibre length used in the TRITIUM prototypes developed at IFIC and for most of the characterization studies carried out in this thesis. As the manufacturer [Saia] delivers 1 m long fibres, an effective cleaving technique had to be developed with stringent requirements on the cleaving quality, since this greatly affects the transmission of photons and, consequently, the detection efficiency of the TRITIUM detector. The cleaving must be done perpendicular to the fibre axis and with small uncertainty in the cleaving position to enable optimal coupling of the fibre to the photosensor. It is also important that the fibre integrity be preserved, without cracks or deformations that may contribute to photon loss.

Cleaving plastic fibres is a current challenge. There are many different techniques such as milling, laser cleaving, focused-ion-beam, blade cleaving, etc. The blade cleaving technique was chosen because of its mechanical simplicity and because, unlike other techniques, it preserves the in-
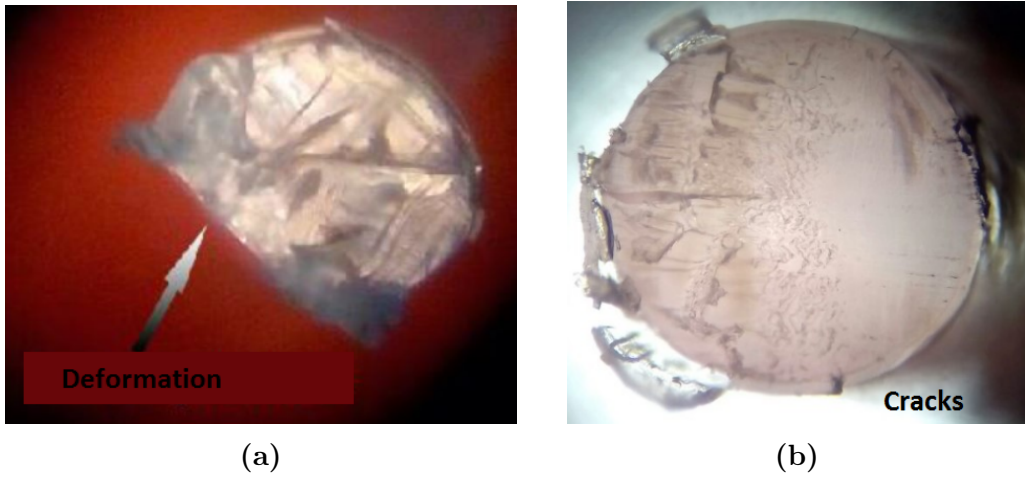
Figure 4.1 – Results of using commercial techniques for cleaving the scintillating fibres a) Fibre end deformation b) Fibre end cracks. Pictures taken with a microscope PB 4161 from EUROMEX.
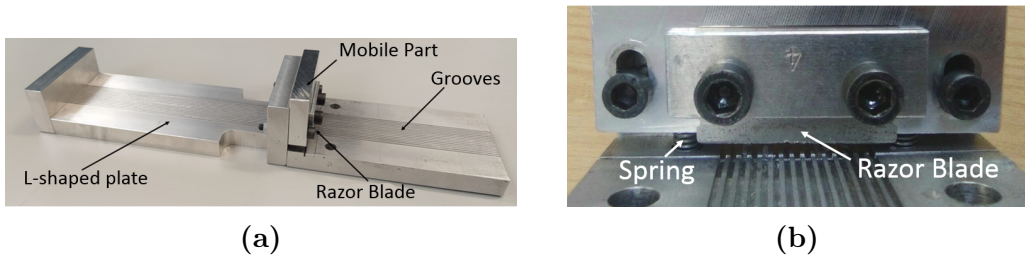
Figure 4.2 – Plastic fibre cleaver developed in the TRITIUM project.

tegrity of plastic fibres. Many commercial devices based on blade cleaving, such as the one provided by Thorlabs with a diamond-tipped blade [Tho06], or guillotines designed for industrial fibre optics [Ind], were tested in a comprehensive study with unsuccessful results [Sol17]. As can be seen in Figure 4.1, commercial techniques produce deformations, cracks and imperfections so they do not yield results with the quality standard required for the detector. As commercial devices are not suitable for polymer fibres, a cleaving device, shown in Figure 4.2, was designed and built at the IFIC laboratory. This device consists of an aluminium plate endowed with fourteen grooves

to accommodate the fibres. A thin razor blade attached to a mobile piece is used to cleave the fibres. The perpendicular cleave, which is one of the requirements, is ensured since the moving piece to which the blade is attached is placed perpendicular to the fibre axis. The blade used is a typical 0.1 mm thick commercial razor blade, which is the thickness that gave the best results. The blade was positioned with a 5° inclination with respect to the horizontal axis since it was found in several studies that this helps to obtain a less aggressive and cleaner cleave [SR15, Law06]. As it can be seen in Figure 4.3, the integrity of the fibre is preserved and no deformation is observed. However, it can be noticed some tears on the clad, but it is reported in section 4.1.2.2 that these tears affect negligibly the photon collection.

An additional parameter that could affect the cleaving quality of the fibre ends is the temperature of both fibre and blade. A study was carried out in which both were subject to different temperatures, from room temperature to 110°C. No significant conclusions were obtained [Sol17]. Thus, the cleaving process was carried out at room temperature to make the cleaving process easier.

A second L-shaped aluminium plate with grooves was attached to the first one (see Figure 4.2) to set accurately the length of the fibres to 200 mm, with an uncertainty of ±1 mm.

4.1.1.2 Polishing Scintillating Fibres

As can be seen in Figure 4.3, a slightly darkened zone at the bottom of the fibre is observed. This is an unavoidable effect of the cleaving process of plastic fibres which produces unpolished end surfaces. To polish the end surfaces, a method implemented by Thorlabs was applied [Tho06].
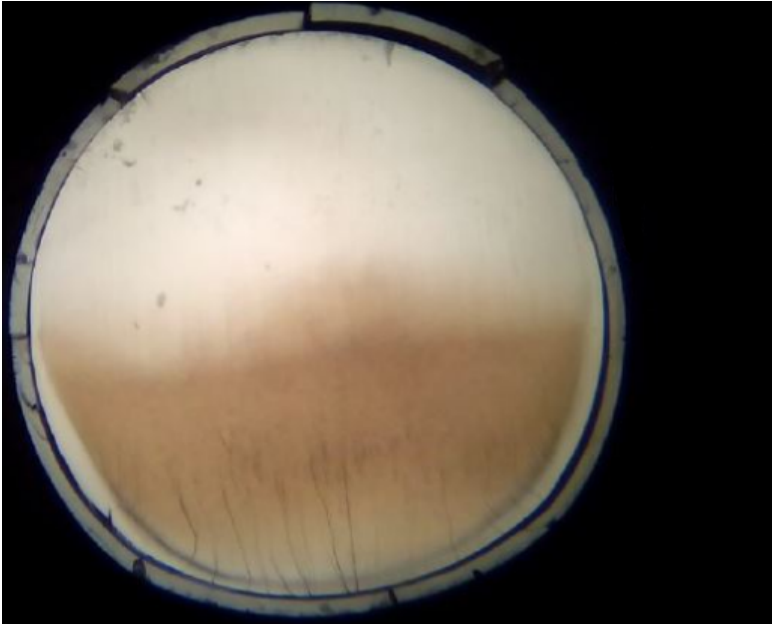
Figure 4.3 – Fibre end after cleaving using the homemade cleaver. Pictures taken with the microscope PB 4161 from EUROMEX.

Manual Polishing Method

The Thorlabs polishing method consists in rubbing the fibre ends with five different polishing papers made of aluminium oxide grains with a decreasing grain size (30 μm, 20 μm, 12 μm, 5 μm and 0.3 μm). To polish the fibre, this is placed into a polishing connector, shown in Figure 4.4, and a shape of an 8 must be outlined on each polishing paper for 2 minutes (approximately 120 movements).

The result obtained after polishing is shown in Figure 4.5b where it can be noticed that the darkened zone has completely disappeared. The fibre end is uniform which favours optimal coupling and transmission of photons of the scintillating fibres to the photodetectors.
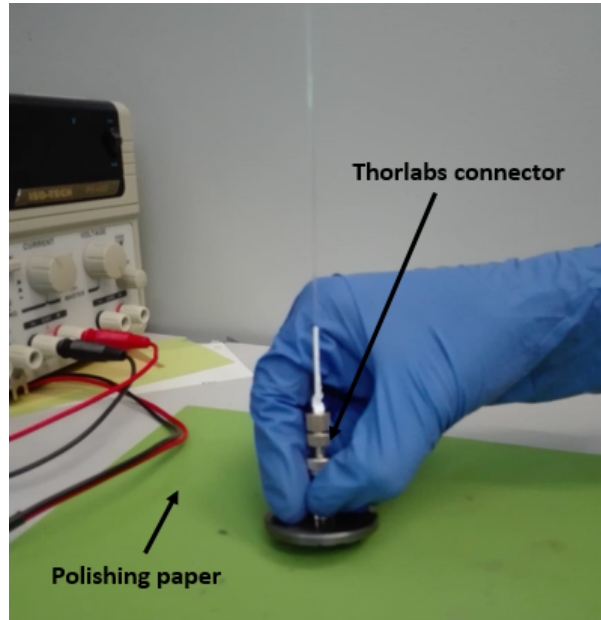
Figure 4.4 – Manual polishing method implemented by Thorlabs.

Automatic Polishing Machine

The main drawback of the manual polishing method is that it takes more than 10 minutes to polish a fibre. This implies an unaffordable time to polish the thousands of fibres needed for the TRITIUM detector (see section 5.4). For this reason, an automated polishing machine was developed within this thesis work. This machine was designed and built in the laboratory for automatically polishing up to one hundred plastic scintillating fibres at the same time. This machine is easily scalable to a larger number of fibres. This automatic polishing machine, displayed in Figure 4.6, consists of two main parts:

1. A polishing table, shown in Figure 4.7a, where the fibres are polished. This is composed of two parts, a static part, to which the fibres are attached, and a movable part on the bottom of the static part, where the polishing papers are attached. It was decided to move the polishing

(a)   (b)
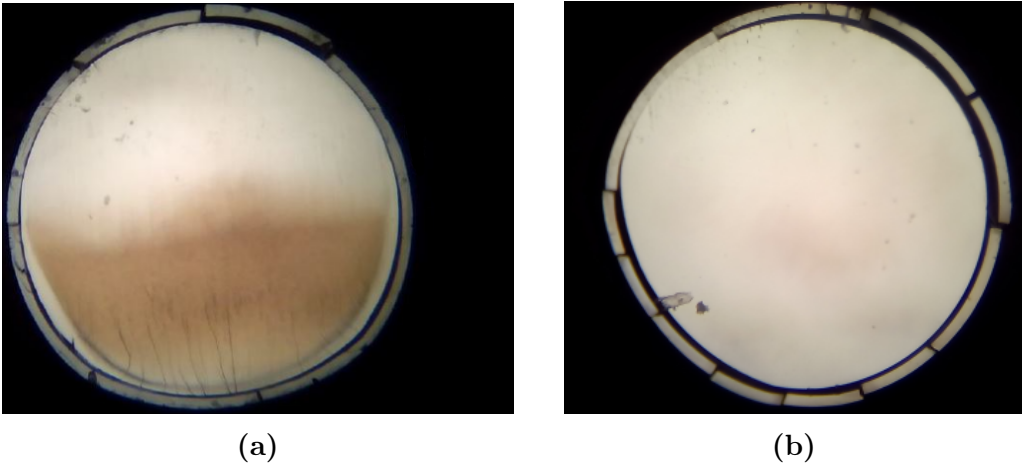
Figure 4.5 – Result of the polishing process. a) Fibre end after cleaving b) Fibre end after cleaving and manual polishing with Thorlabs technique. Pictures taken with the microscope PB 4161 from EUROMEX.

paper instead of the fibres to avoid damaging them.

The static part that holds the fibres, shown in Figure 4.7a, consists of a plastic piece locked to the system by four vertical screws. There are two nuts on each screw used to set the height and the inclination of fibres relative to the polishing paper. This piece contains one hundred holes in which a hundred fibres can be lodged.

As the fibres are too light (0.16 g) to make the necessary pressure on the polishing paper by gravity, a plastic belt and a piece of metal of about 1.5 g weight were attached to the individual fibres, as shown in Figure 4.7b, to increase their contact pressure in a similar way as with manual polishing connectors.

The movable part of the polishing table consists of a flat PMMA plate of 18×18 cm^2 to which the polishing paper is attached. This part is locked to a structure [IGU] that contains two horizontal screws, perpendicular to each other, which allow a movement in the horizontal plane, as shown in Figure 4.7c.
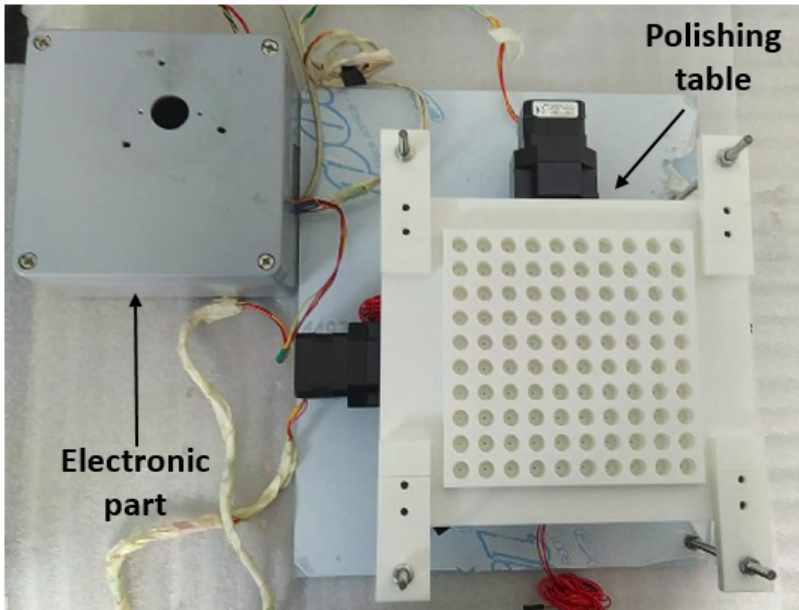
Figure 4.6 – Polishing machine developed for TRITIUM.

The polishing system contains several high accuracy switches, model DB1 6A250, shown in Figures 4.7a, 4.7c and 4.7d, which are used to find the origin of coordinates when the system is reinitiated and to stop the movable part when the end of the path is reached.

2. An Arduino-based electronics that controls the movement of the polishing paper, shown in Figure 4.8. It consists of two stepper motors controlled by an Arduino UNO [ARD] that uses a CNC shield [OSO17]. The stepper motor is a type of DC motor in which a full rotation is divided into a number of steps that define the stepping angle. The stepper motors used for the polishing machine are model NEMA ST4209S1404-A [Nan06], with a bipolar voltage of 2.77 V_{DC}, 1.33 A maximum current and a stepping angle of 0.9° (400 steps/rev). They can be operated with a position sensor for feedback control. These stepper motors are used to move the horizontal screws to which the PMMA plate that holds the polishing paper is attached. Two drivers
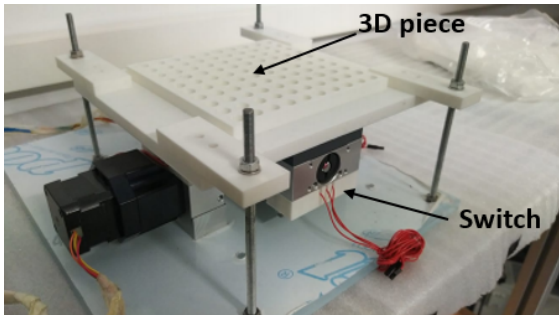
(a)
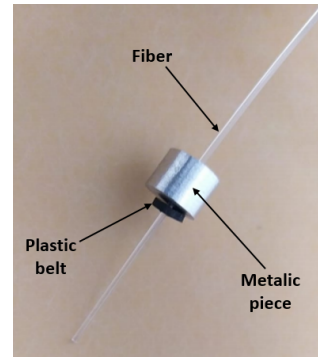
(b)
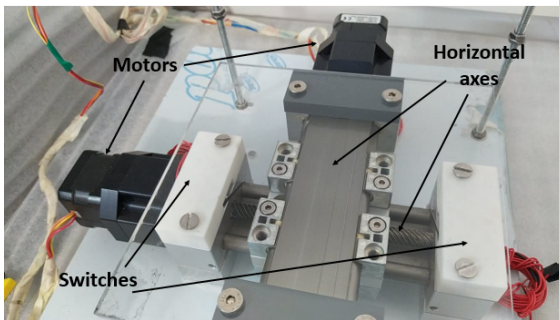
(c)
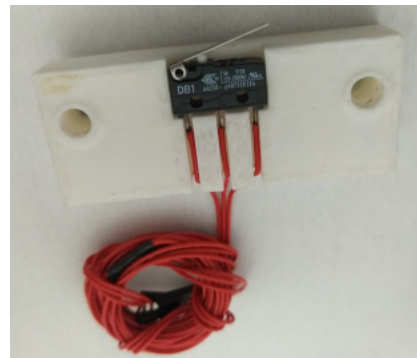
(d)

Figure 4.7 – Components of the fibre polishing machine. a) Polishing table. b) Fibre with ballast metal piece. c) Horizontal screws and PMMA plate. d) A movement switch with its cables inserted inside its holding piece.

connected to the CNC shield limit the current supplied to the motors. Choosing the right drivers is crucial because overpowering the motors could damage them while underpowering them would induce an inadequate stepping. Several drivers were successively tested: the driver Pololu A4988 (35 V, 2 A and 16 steps) [All11], the driver DRV8825 (45 V, 2.5 A and 32 steps) [Tex14] and the TMC2208 (35 V, 2.5 A and 256 steps with more microstepping modes which result in a more accurate and smooth movement) [Int19]. The last driver includes a StealthChop function that allows operating in silence mode for low motor velocities. The TMC2208 driver is the one used for the control of the stepper motors since it produces the most accurate and smooth movement. A cooling system, shown in Figure 4.8, was needed to ensure the correct operation of the polishing system. This consists of a copper heat sink in contact with both controllers and a fan which prevents heat accumulation inside the electronics box. The cooling power can be improved by a PELTIER cell.

The polishing machine is controlled by a Raspberry Pi computer board [Ras] through the Universal G-code Sender software, a graphical interface based on the GRBL package [GRB]. In this software, there are several pre-programmed functions such as "HOME" which finds the system origin of coordinates when it is turned on. The GRBL software loads a file containing the G-code that defines the 120 movements required for polishing.

Experimental Test

The improvement of the light transmission of scintillating fibres due to polishing was tested with twenty uncladded scintillating fibres of 15 cm long. These fibres were arranged in a bundle that was coupled to two PMTs and read out in coincidence, as shown in Figure 4.9.

This experiment was carried out inside a light-tight box, to avoid
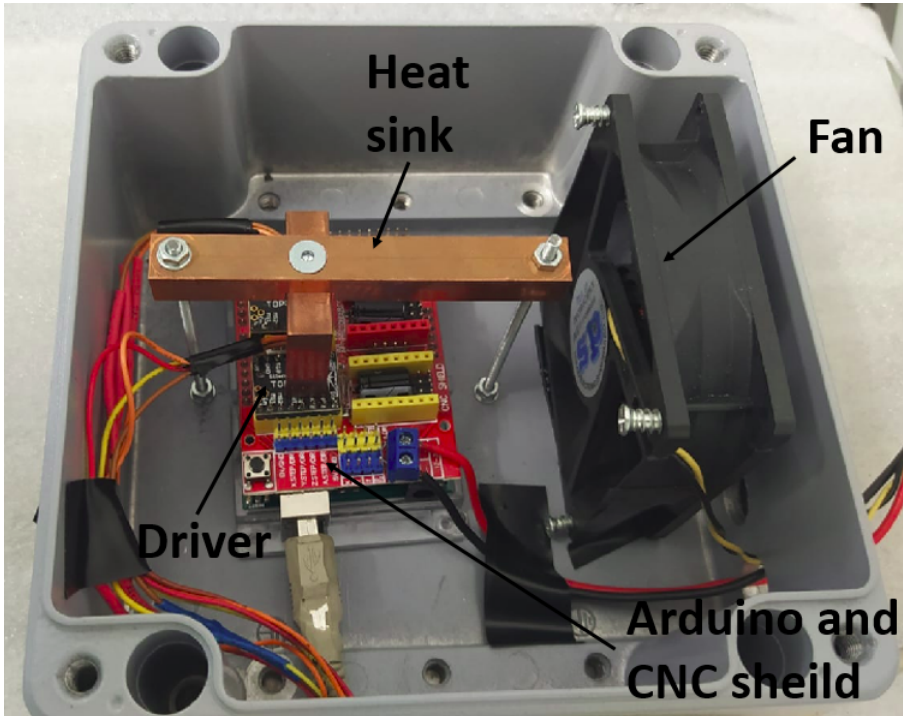
Figure 4.8 – Electronic system of the polishing machine.

external light. The spectra produced by background radiation before and after the polishing process are displayed in Figure 4.10. As it can be seen in this figure, the energy spectrum after polishing is shifted to the right which means that the detected events have more energy than before polishing, i. e., more photons per event reach the PMTs. The improvement of the photon collection efficiency of the scintillating fibres is quantified by a parameter F defined as,

$$F = \frac{A_P}{A_{NP}} \tag{4.1}$$

where A_P and A_{NP} are the integrals of the energy spectra measured after and before the polishing process, respectively. The polishing results in a factor 2.2 improvement in the light collection. The test was repeated with two radioactive sources, an encapsulated ^{60}Co source of 715 kBq activity and a ^{90}Sr source of 17.8 kBq activity. The radioactive sources were placed
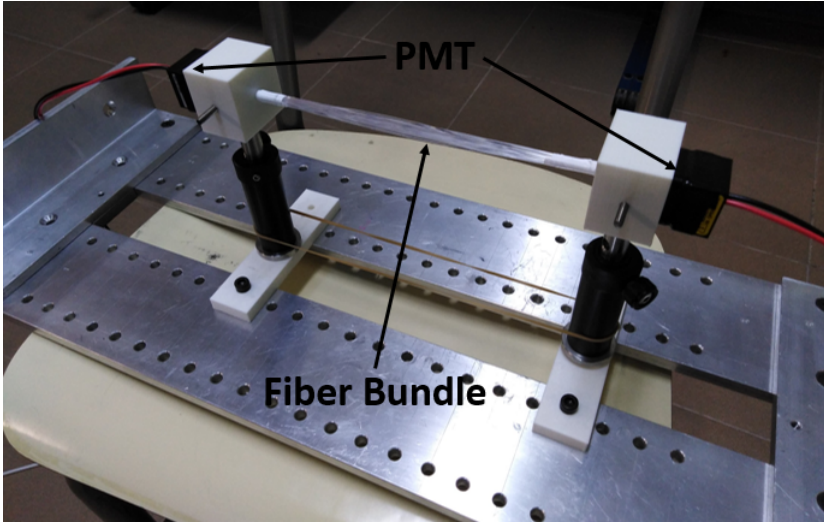
Figure 4.9 – Setup used to quantify the improvement of the light collection of the fibres and their transmission to the PMTs due to the polishing process. This setup was placed inside a light-tight box for the measurements.
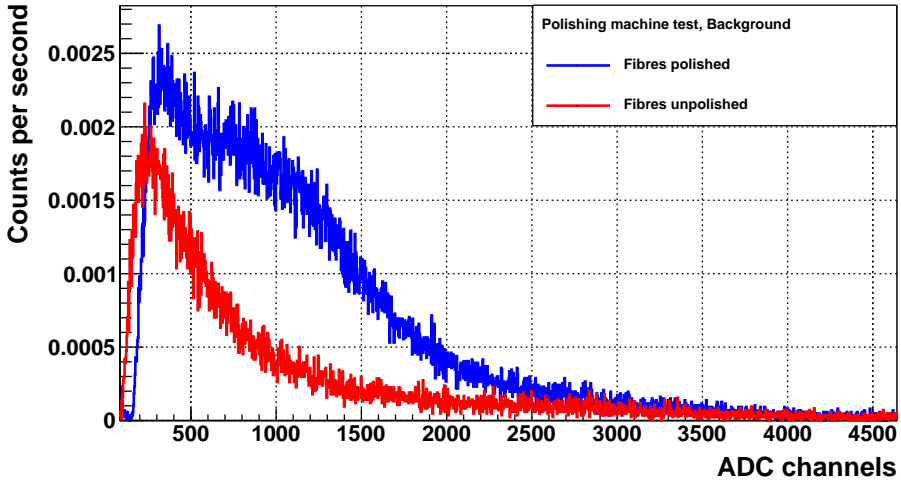
Figure 4.10 – Background energy spectra recorded with polished and unpolished fibres.

next to the centre of the fibre bundle (at 7.5 cm from each PMT). The energy spectra recorded for both radioactive sources are shown in Figure 4.11. It can be noticed that both energy spectra are shifted to the right after polishing, obtaining an improvement of factors 1.7 and 2 with respect to the spectra before polishing for the ^{60}Co and ^{90}Sr sources, respectively.

In summary, the photon collection efficiency of the fibres was significantly improved by polishing (mainly due to the improvement of the interface between fibres and PMTs). As the expected number of photons per tritium event is quite low (less than 20, as demonstrated by both simulations and measurements), it is crucial to achieving a high light collection.

4.1.1.3   Cleaning of Scintillating Fibres

As it is demonstrated in subsection 4.1.2, the quality of the interface between the core of uncladded fibres and the environment (tritiated water in the case of the TRITIUM detector) affects conspicuously the photon collection efficiency. To improve the quality of the interface, a fibre cleaning process was implemented, aiming to remove particles deposited on the fibres, such as dust and grease. Through this cleaning process, the wetting property of the fibres is improved, as illustrated in Figure 4.12. The contact angle between fibres and water is decreased, preventing air molecules from attaching to the fibres and producing a uniform contact between fibres and water. This cleaning process was developed and carried out in the clean room of ICMOL. Three different beakers were used, the first filled with alkaline soap, the second with pure water (conductivity of the order of 10 μS/cm) and the third with isopropanol. The fibres were manually rubbed with alkaline soap for 5 minutes and afterwards introduced into the first beaker which was placed in an ultrasonic bath at 17 kHz frequency for 3 minutes. Subsequently, the fibres were cleaned with a constant flow of water for 5 minutes, they were placed in the second beaker for an ultrasonic bath for 3 minutes and afterwards placed in the third beaker for an ultrasonic bath
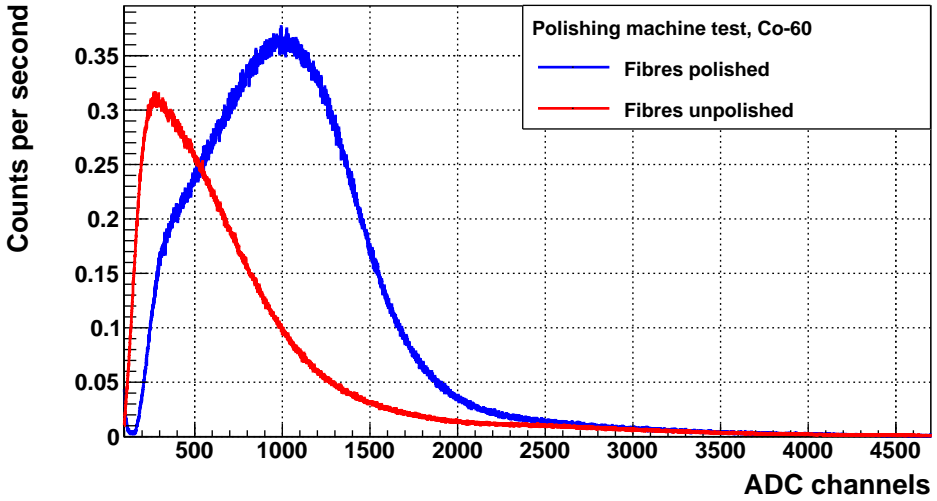
(a)
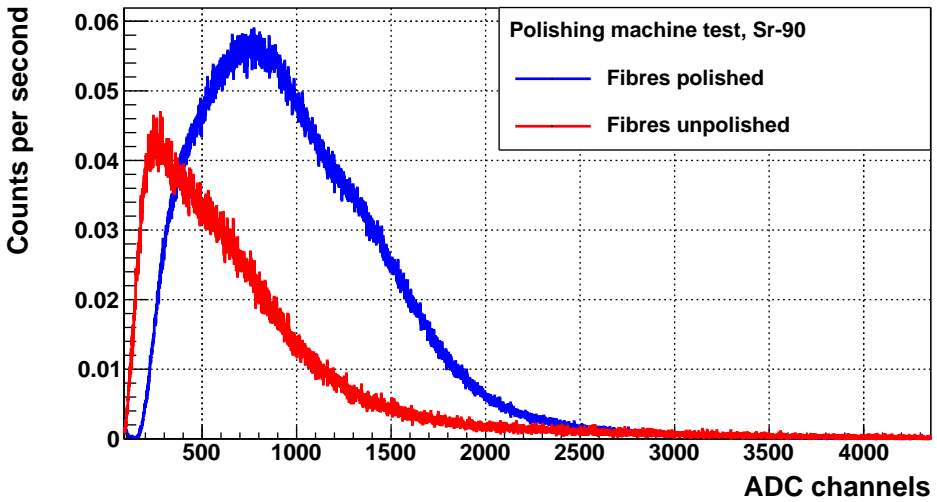
(b)

Figure 4.11 – Energy spectra recorded with polished and unpolished fibres. a) ^{60}Co source. b) ^{90}Sr source.
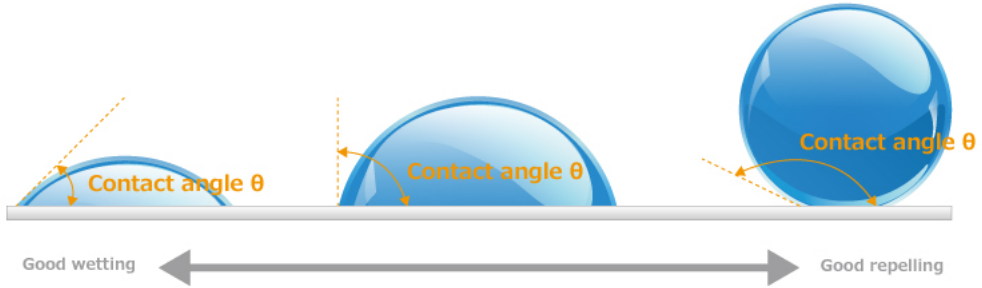
Figure 4.12 – Schematic representation of the wetting properties of a flat surface (grey) in contact with a drop of liquid (blue). The wetting property is characterized by the angle formed between the surface of both objects. The smaller angle, the better the wetting property of the material. [San]

for 3 minutes. Finally, the fibres were dried with a flow of gaseous N_2 and kept in clean conditions until their introduction into the detector vessel. The improvement of the light collection of the scintillating fibres after this cleaning process was determined by measuring the energy spectra of a bundle of twenty uncladded fibres of 15 cm in length before and after undergoing this cleaning process. The setup used for these measurements is shown in Figure 4.9. The energy spectra were measured for the background and for ^{90}Sr and ^{137}Cs radioactive sources, shown in Figures 4.13 and 4.14, respectively. A shift of the spectra to higher energies was observed for the clean fibres with respect to the spectra of fibres without cleaning. Equation 4.1 was used to quantify the improvement achieved by the cleaning process. Although no improvement in the number of detected events was observed for the background measurement, an improvement in the photon collection efficiency of a factor of 1.26 and 1.35 was obtained for the ^{90}Sr and ^{137}Cs sources, respectively.
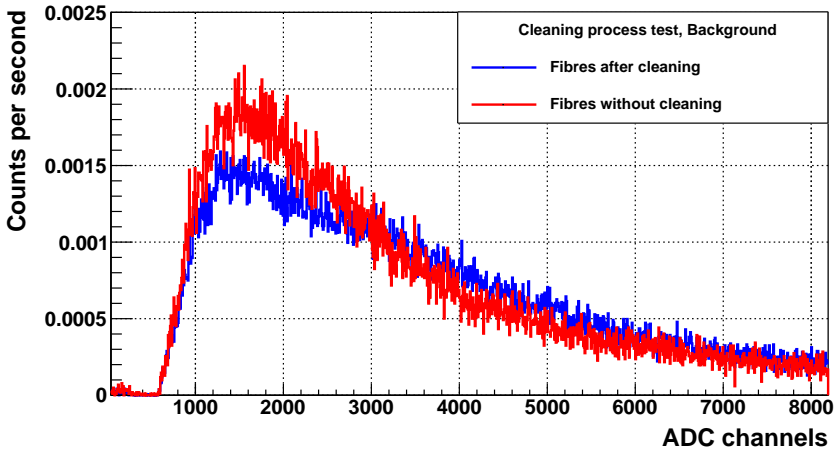
Figure 4.13 – Measured background energy spectra before and after cleaning.

4.1.2 Characterization of Scintillating Fibres

In this section, the characterization of uncladded BCF-12 fibres from Saint-Gobain, selected for the TRITIUM monitor, is described. These fibres are compared to single clad and multiclad BCF-12 fibres with the same external diameter to quantify the influence of the clad on their photon collection efficiency. The difference between these three types of fibres is that uncladded fibres consist of a polystyrene core with a refractive index of 1.60, whereas single clad and multiclad fibres have a PMMA clad of 30 μm thickness and a refractive index of 1.49. Multiclad fibres have additionally a second fluor-acrylic clad of 10 μm thickness and a refractive index of 1.42. Commercial clads are too thick for tritium measurements but a sufficiently thin clad could be obtained by vapour deposition if needed. The characterization was carried out for individual scintillating fibres and consisted of a comparative study of the fibre photon collection. The setup employed, shown in Figure 4.15, consists of an optical board on which a LED and a PMT were placed in front of each other. It was used a LED (LED435-03 from Roithner LaserTechnik Gmbh [Roi10]) with an emission spectrum similar to that of
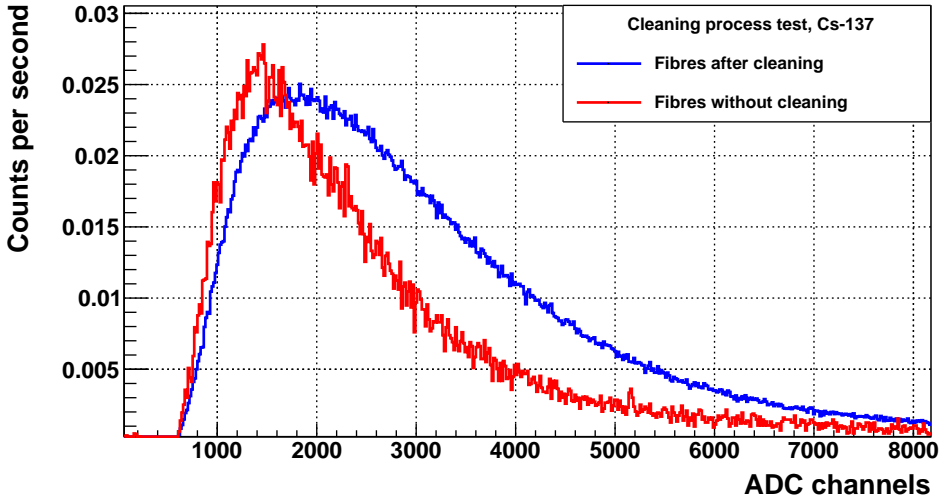
(a)
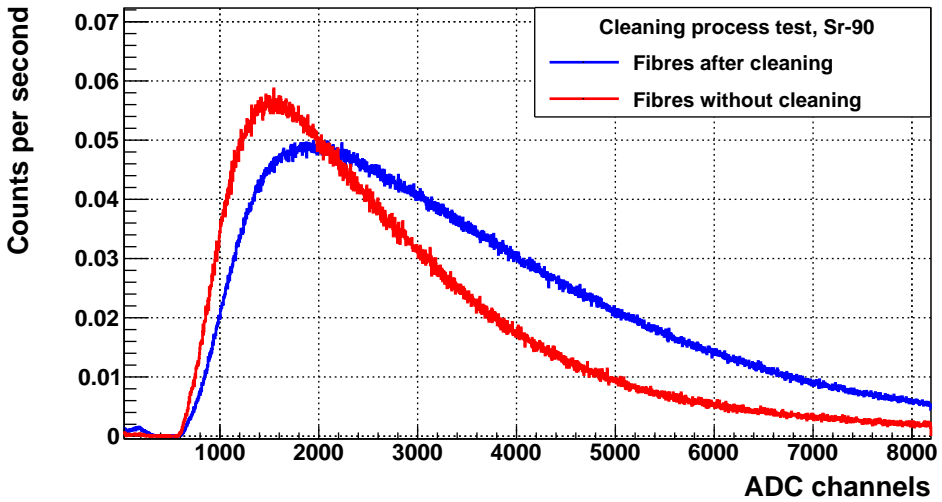
(b)

Figure 4.14 – Energy spectra obtained for a radioactive source before and after cleaning. a) ^{137}Cs. b) ^{90}Sr.

the scintillating fibres. The emission spectrum of the LED, given in Figure 4.16, was measured using a spectrometer and fitted to a Gaussian function. The LED emission peak is at 434 nm with a σ of 8 nm. The LED was fed in current mode with a sourcemeter. A calibrated Hamamatsu R8520-06SEL PMT with quantum efficiency $QE = 29.76\%$ at $\lambda = 430$ nm was employed. A 20 cm long fibre was placed between the LED and the PMT, optically
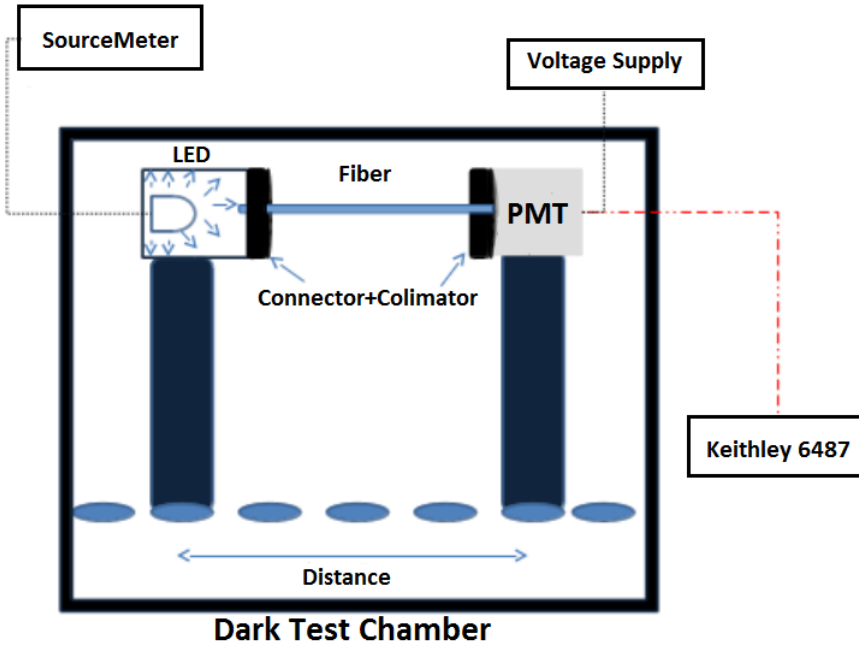
Figure 4.15 – Setup used for fibre characterization.

coupled to their end surfaces by optical grease [Saib]. Two collimators were used to ensure that only photons emitted from the LED were detected by the PMT. Two FH-ST connectors from RoHS [Thoc] were used to fasten the fibre to the system. To determine the photon collection efficiency, the rate of photons reaching the active area of the PMT was measured for the different types of fibres. The photon rate R_γ reaching the photocathode was calculated from,

$$R_\gamma = \frac{(I_{PMT} - I_{DC})}{q_e \cdot QE \cdot CE} \tag{4.2}$$
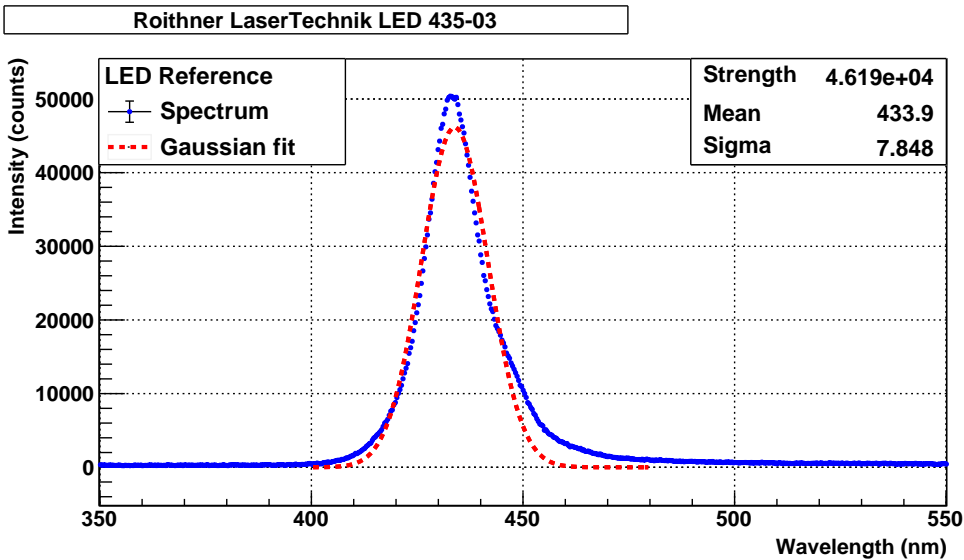
Figure 4.16 – Emission spectrum measured for the 435-03 LED from Roithner LaserTechnik Gmbh.

where I_{PMT} is the output current of the PMT, I_{DC} is the dark current, CE is the photoelectron collection efficiency and q_e is the electron charge.

4.1.2.1   Measurement Conditions

The experimental setup was placed inside a light-tight box whose light-tightness was carefully checked. To select the optimal PMT HV, the photocurrent was measured as a function of the first dynode voltage between 0 and 800 V without fibres, first with the LED off (PMT dark current) and then with the LED current at 1 mA. The number of photons detected by the PMT (difference between both spectra) is plotted in Figure 4.17. The PMT HV was taken as the voltage at the beginning of the plateau (250 V). At this HV the CE is equal to 1 and no secondary electrons are produced.

The linear response of the PMT (in absence of fibres) was verified in two different ranges, $[0 - 30]$ photons/ns which is the expected number
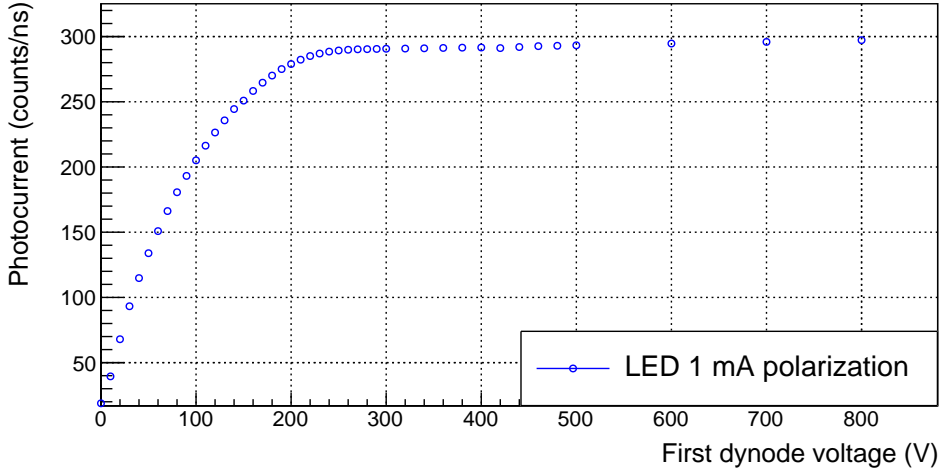
Figure 4.17 – PMT photocurrent as a function of the first dynode voltage with the dark current subtracted. Error bars are smaller than dot size.

of photons for tritium events, and $[0 - 2500]$ photons/ns, employed for fibre characterization. The results for the low and high illumination cases are plotted in Figure 4.18. No saturation of the PMT response is observed.

4.1.2.2 Results of the Characterization of Scintillating Fibres

Cleaving and polishing add a systematic dispersion σ_{sys-SF} to the intrinsic fibre response. In addition, the positioning of the connectors that lock the fibre to the experimental setup produces an additional systematic uncertainty $\sigma_{sys-pos}$. Since both uncertainties are independent, the total systematic uncertainty is given by,

$$\sigma_{sys} = \sqrt{\sigma_{sys-SF}^2 + \sigma_{sys-pos}^2} \tag{4.3}$$
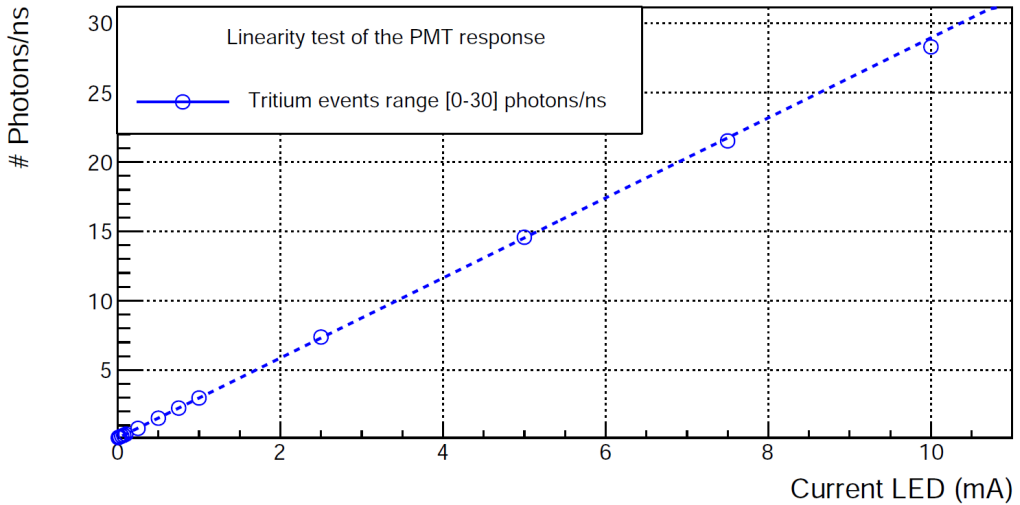
(a)
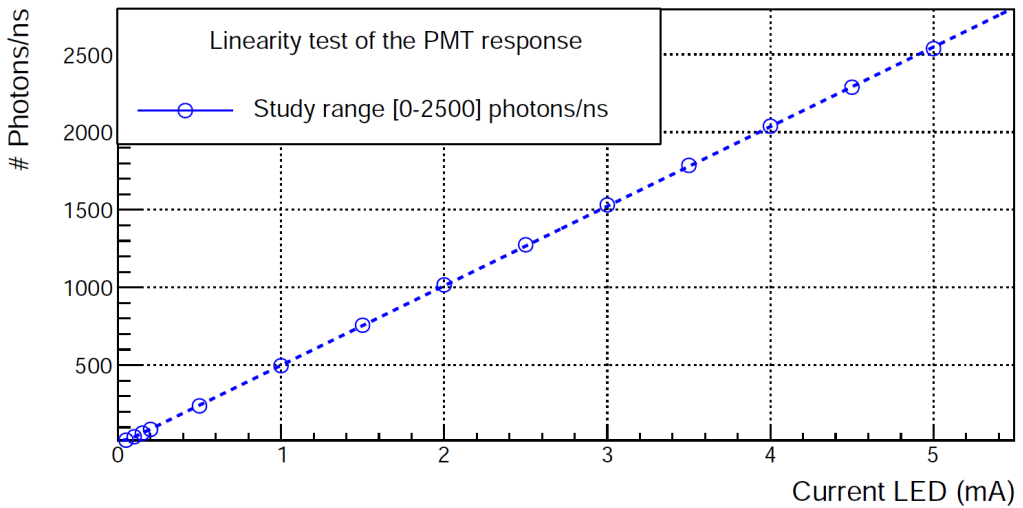
(b)

Figure 4.18 – Rate of photons measured by the PMT as a function of the LED current. a) Response of the PMT in the intensity range of tritium events. b) Response of the PMT in the range $0 - 2500$ photons/ns. Error bars are smaller than the dot size.

Two different experiments were designed, the first giving only the systematic uncertainty $\sigma_{sys-pos}$, and the second the total uncertainty. The uncertainty due to fibre positioning $\sigma_{sys-pos}$ was measured to extract σ_{sys-SF} from the total systematic uncertainty. Thus, σ_{sys-SF} is given by,

$$\sigma_{sys-SF} = \sqrt{\sigma_{sys}^2 - \sigma_{sys-pos}^2} \qquad (4.4)$$

The test designed to measure $\sigma_{sys-pos}$ consisted in preparing one conditioned fibre of each type (uncladded, single clad and multiclad), all of 1 mm diameter and 20 cm length. Each fibre was locked to the setup, and the PMT photocurrent was measured for the LED fed at 1 mA. These measurements were repeated ten times for each fibre, removing and inserting the fibre each time. The mean $\bar{x}$, the standard deviation and the relative standard deviation $\sigma_{sys-pos}^{rel}$ of the PMT photocurrent for each fibre type are shown in Table 4.1. The relative standard deviation is defined as

$$\sigma_{sys-pos}^{rel} = \frac{\sigma_{sys-pos}}{\bar{x}} \qquad (4.5)$$

As it can be noticed, larger photon rates are obtained for single clad and multiclad fibres than for uncladded fibres. The reason could be that the interface between the core and the clad of the fibre is more uniform for single clad and multiclad fibres than for uncladded fibres for which the interface is air. External conditions such as dirt may produce significant interface fluctuations. The statistical error of the intensity is three orders of magnitude smaller than the systematic uncertainties $\sigma_{sys-pos}$ and is neglected.

To determine the total systematic uncertainty σ_{sys}, ten different samples of each fibre type were prepared and the response of each fibre was measured as described above. These measurements were done for 0.05, 0.1, 0.15 and 0.2 mA LED bias current. The results for uncladded fibres are plotted in Figure 4.19, where it can be seen that, although each fibre shows a linear trend with increasing LED bias current, a dispersion of the fibre response is clearly observed. Similar results, displayed in figure 4.20, were

Fibre type	Photon rate (ns^{-1})	$\sigma_{sys-pos}$ (ns^{-1})	$\sigma_{sys-pos}^{rel}$ (%)
Uncladded	524.09 ± 0.01	17.7	3.4
Single Clad	1071.70 ± 0.01	9.1	0.9
Multiclad	949.93 ± 0.03	9.9	1

Table 4.1: Mean, standard deviation and relative standard deviation due to fibre positioning in the setup of the photon rate that reaches the PMT for 0.1 mA LED bias current.

obtained for single clad and multiclad fibres.
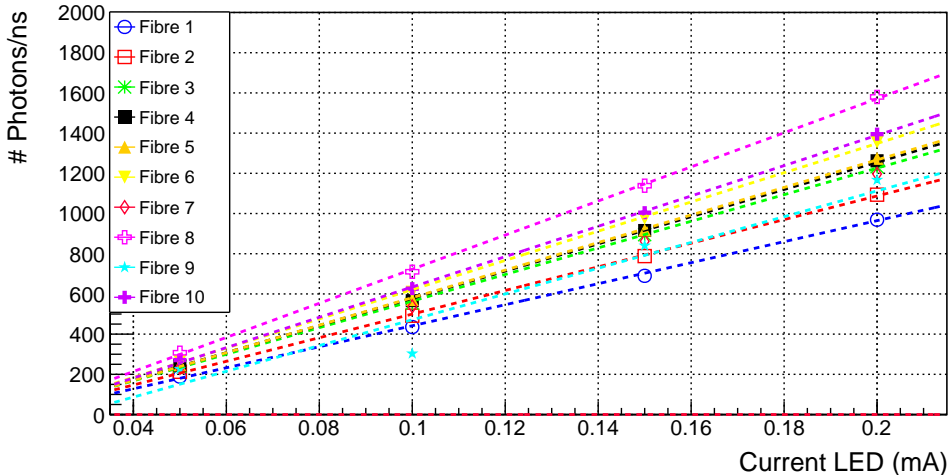
Figure 4.19 – Rate of photons reaching the PMT for 10 uncladded fibres. Error bars are smaller than the dot size.

The average photon rate and the relative standard deviation versus the LED bias current for each type of fibre are given in Tables 4.2 and 4.3 respectively, and are plotted in Figure 4.21 where it can be noticed that the average fibre response is linear with the current. Single clad and multiclad fibres give larger signals than uncladded fibres (a factor of two in the case of single clad) which indicates that the clad has a significant effect on the fibre
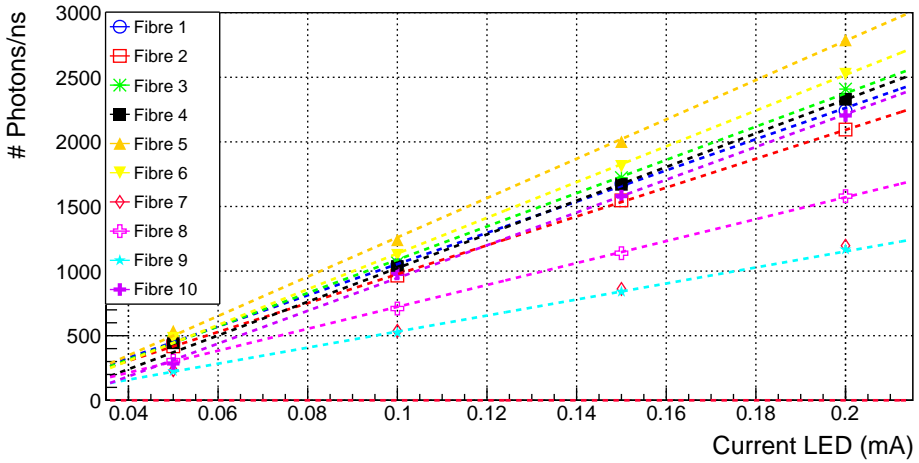
(a)
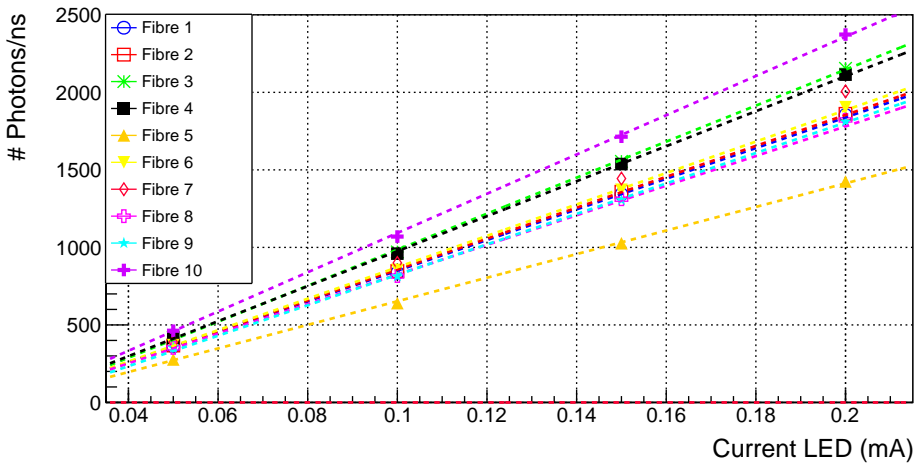
(b)

Figure 4.20 – Photon rate reaching the PMT for ten different fibres. a) Single clad fibres. b) Multiclad fibres. Error bars are smaller than the dot size.

collection efficiency. It can also be observed in Table 4.3 that the relative standard deviation σ_{sys}^{rel} does not vary with the LED bias current. The largest uncertainty was found for single clad fibres, despite of their higher light collection. This is most probably due to the cleaving process that produces cracks in the clad as observed in Figure 4.3. This damage seems to be reduced for multi-clad fibres, probably due to their larger mechanical resistance.

	Photon rate (10 ns^{-1})		
Intensity (mA)	Uncladded	Single clad	MultiClad
0.05	24.5 ± 1.1	38 ± 3	37.7 ± 1.5
0.1	57 ± 3	92 ± 7	87 ± 4
0.15	92 ± 4	149 ± 12	140 ± 6
0.2	127 ± 6	205 ± 17	193 ± 8

Table 4.2: Photons rate versus LED bias current for the different types of fibres.

	$\sigma_{sys}^{rel}(\%)$		
Intensity (mA)	Uncladded	Single clad	MultiClad
0.05	4.4	8.7	4
0.1	4.6	8	4
0.15	4.3	8.1	4
0.2	4.4	8.1	3.9
Mean	4.4	8.2	4

Table 4.3: Relative standard deviation of the photon rate $\sigma_{sys}^{rel}(\%)$ versus LED bias current for the different fibre types.

The average of σ_{sys}^{rel}, $\sigma_{sys-pos}^{rel}$ and σ_{sys-SF}^{rel} are given in Table 4.4. The smallest relative standard deviation was found for uncladded fibres, which means that the damage occurs mainly in the fibre clad, as illustrated in Figure 4.5 where cracks in the clad due to the cleaving process can be
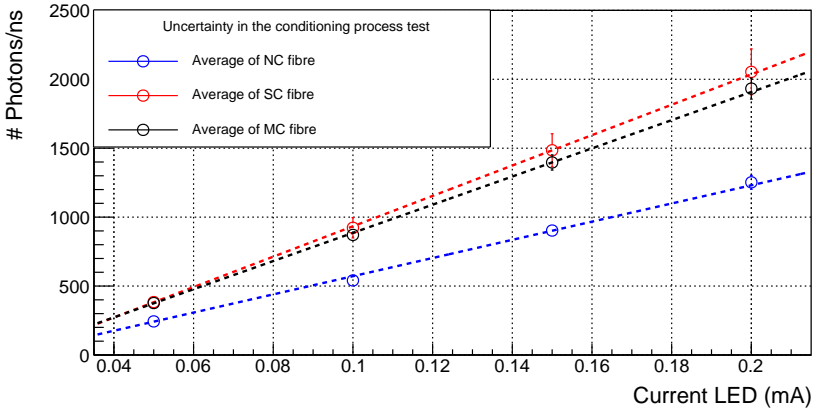
Figure 4.21 – Average photon rate versus LED bias current for 10 samples of different fibre types (uncladded, single clad and multiclad fibres). Error bars are smaller than the dot size.

seen. It was checked under a microscope that this damage only occurs at the end of the fibre. Also, the largest relative standard deviation is obtained for single clad fibres, which indicates that a second clad increases the tolerance of the fibre to conditioning.

Fibre type	σ_{sys}^{rel} (%)	$\sigma_{sys-pos}^{rel}$ (%)	σ_{sys-SF}^{rel} (%)
Uncladded	4.4	3.4	2.9
Single clad	8.2	0.9	8.1
Multiclad	4	1	3.8

Table 4.4: Measured relative standard deviations σ_{sys}^{rel}, $\sigma_{sys-pos}^{rel}$ and σ_{sys-SF}^{rel}.

In summary, the relative statistical deviation due to fibre conditioning was quantified for the different fibre types. It was found that a fibre clad improves the photon collection efficiency but at the cost of worsening its standard deviation. Larger uncertainties (a factor two) in the light collection were observed in single clad fibres compared to multiclad and uncladded ones. This may be due to the damage in the clad produced by the

cleaving of fibres.

The absolute photon collection efficiency of 10 cm scintillating fibres CE_{10} was measured for each type of fibre. Ten different fibres of 10 cm length for each fibre type were prepared and the photon rates were measured. The results are summarized in Table 4.5. CE_{10} was calculated as the ratio of the collected photon rate to that of a fibre of 20 cm length,

$$CE_{10} = \frac{R_{ph}(20 \text{ cm})}{R_{ph}(10 \text{ cm})} = e^{-10/L} = 96\% \tag{4.6}$$

where $L = 270$ cm is the attenuation length provided by the manufacturer and an exponential attenuation of the photon rate R_{ph} with length is assumed [Leo94],

$$R_{ph}(x) = R_{ph}(x_0) \times e^{-(x-x_0)/L} \tag{4.7}$$

The measured CE_{10}, shown in Table 4.6, were somewhat smaller than the calculated from the attenuation length for all the scintillating fibre types.

	Photon rate (10^2 ns^{-1})		
Intensity (mA)	Uncladded	Single clad	MultiClad
0.05	3.2 ± 0.6	5.5 ± 0.7	4.8 ± 0.8
0.1	7.4 ± 1.4	12.7 ± 1.6	11.1 ± 1.9
0.15	11.8 ± 2.3	19.8 ± 2.3	18 ± 3
0.2	16 ± 3	25.1 ± 2.1	23 ± 4

Table 4.5: Average photon rate versus LED bias current for 10 different samples of 10 cm length for uncladded, single clad and multiclad fibres.

4.2 Characterization of SiPM

The characterization of the most relevant parameters of the SiPM S13360-1375 from Hamamatsu, which was the first choice for the TRITIUM monitor

Fibre type	CE_{10} (%)
Uncladded	76 ± 8
Single clad	78 ± 6
Multiclad	83 ± 7

Table 4.6: Measured average collection efficiency CE_{10} for different types of scintillating fibres.

photosensor, is described in this section. The most relevant SiPM parameters are breakdown voltage V_{BD}, gain, gain dependence on operating voltage and temperature $G_{SiPM}(V_{bias}, T)$ and temperature coefficient ΔTV_{op}. Additional parameters were measured to verify the accuracy of the characterization such as the quenching resistance R_q, the pixel capacitance C_d, and the terminal capacitance C_t. The afterpulse probability was not measured since, as reported in section 3.1, it is negligible when time coincidence windows of 10 ns are employed. The SiPM characterization was carried out inside a climatic chamber, model CCM 81 from DYCOMETAL [DYC]. This climatic chamber allows controlling both temperature and humidity with a precision of 0.1°C and 0.1%, respectively. In addition, this chamber works as a Faraday cage. A special black blanket [Thob] screened the SiPM from external light.

The quenching resistance and the breakdown voltage were measured from the output current of the SiPM as a function of its forward and reverse bias voltage, respectively. The output current of the SiPM was measured by a Keithley 6487 Picoammeter/Voltage Source [Keia]. The LabView software was used to take the data. The current-voltage curves are shown in Figure 4.22. As can be seen, when the SiPM is forward biased (Figure 4.22a) there is no output current until a potential drop of $V_0 = 0.5$ V is reached. When the current starts to flow, the intensity is linear with the
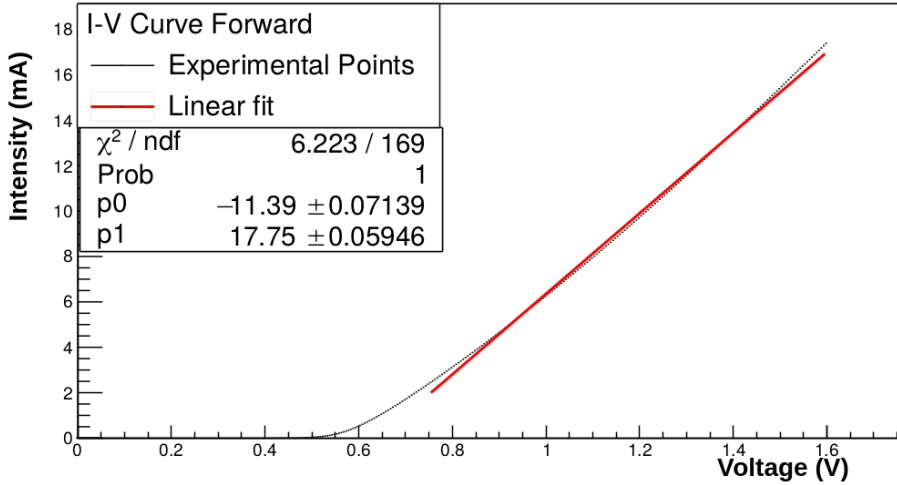
(a)
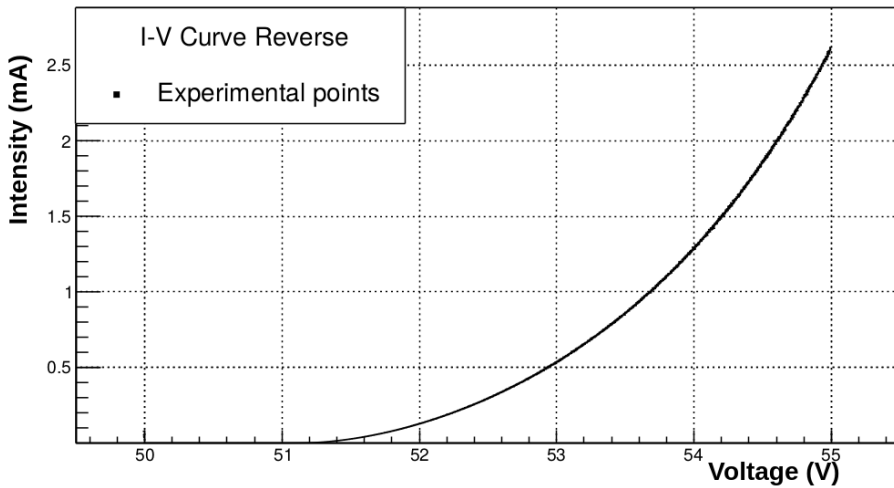
(b)

Figure 4.22 – I-V curves measured for the S13360-1375 SiPM model from Hamamatsu. a) Forward bias. b) Reverse bias. The measurements were taken at $T = 25°C$ and $H = 45\%$.

applied voltage. The equivalent resistance R_{eq} was determined from,

$$I = \frac{1}{R_{eq}}V; \qquad \frac{1}{R_{eq}} = \sum_{i=1}^{N} \frac{1}{R_q} = \frac{N}{R_q} \qquad (4.8)$$

where R_q is the pixel quenching resistance. A value of $R_q = 360.56 \pm 0.07$ kΩ was obtained from a linear fit to the data, which is in agreement with the typical values given by Hamamatsu. The breakdown voltage V_{BD} was obtained from the reverse bias voltage plot (Figure 4.22b). V_{BD} is the point at which the SiPM begins to operate in avalanche mode for reverse bias. V_{BD} is calculated from the maximum of the function

$$f = \frac{1}{I}\frac{dI}{dV} \qquad (4.9)$$

The value obtained $V_{BD} = 51.02$ V is in agreement with the value provided by Hamamatsu, given in Table 3.3.

To measure the SiPM gain G_{SiPM}, the electronic board described in section 3.1 with an amplification factor of $F_{amp} = 170$ was employed. An incoherent light source, LED435-03 [Roi10], described in section 4.1, was used to illuminate the SiPM with low enough intensity. The SiPM output signal shows various well-defined pulse heights, shown in Figure 4.23, corresponding to the number of pixels simultaneously fired. The single photon spectrum SPS is displayed in Figure 4.23. This spectrum was obtained by integrating and histogramming the SiPM output pulses within a time window wide enough to contain the whole charge of the pulse. The time window used for these measurements was $t_w = 500$ ns. The light source provides a trigger signal for the measurement, represented in the green line in Figure 4.23. The well-separated peaks in the SPS spectrum correspond to the charge produced by a different number of pixels fired. The first peak in the spectrum is the pedestal, which is the charge measured when no pixel is fired. This peak is caused by the electronic noise of the system. The second peak corresponds to one fired pixel and so on. The SiPM gain G_{SiPM} can
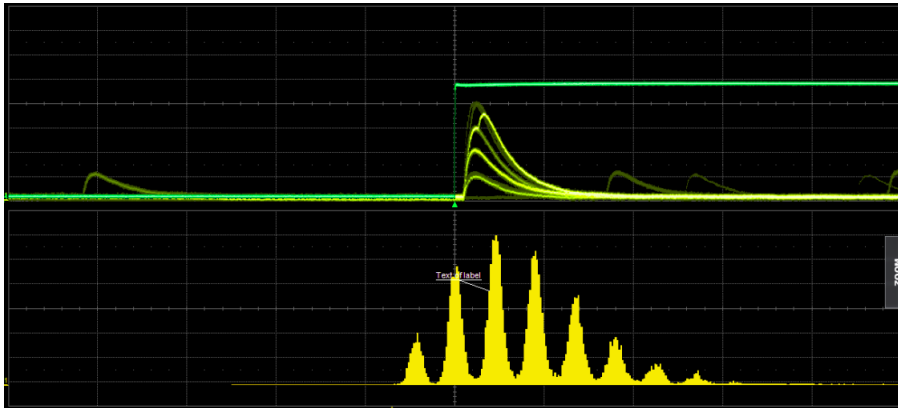
Figure 4.23 – Above) Trigger signal (green) and SiPM output pulses (yellow). Below) SPS spectrum obtained by integrating and histograming the SiPM output pulses. This measurement was done at $T = 25°C$, $V_{bias} = 53.98$ and $H = 60\%$.

be obtained from the SPS spectrum from the equation,

$$G = \frac{\overline{\Delta Q}}{q_e \, F_{amp}} \tag{4.10}$$

where q_e is the electron charge and $\overline{\Delta Q}$ is the average peak distance in the SPS spectrum, corresponding to the charge released by a fired pixel. To obtain the value of $\overline{\Delta Q}$, a macro was written in ROOT [Bru19a, Bru19b]. This macro extracts the background (the pedestal subtracted output signals when the SiPM is not illuminated), which is crucial in some cases like high temperatures or high bias voltages since the background can hide peaks. After subtracting the background, this macro finds all peaks in the SPS spectrum and fits each one to a Gaussian function, as shown in Figure 4.24a. The charge produced by multiple fired pixels is obtained from the centroid of the peaks. The charge fitted versus the number of fired pixels is shown in Figure 4.24b. Up to 10 simultaneously fired pixels were obtained with a relative uncertainty of the charge measurement of less than 2%. The slope of the straight line in Figure 4.24b corresponds to $\overline{\Delta Q}$. For the case
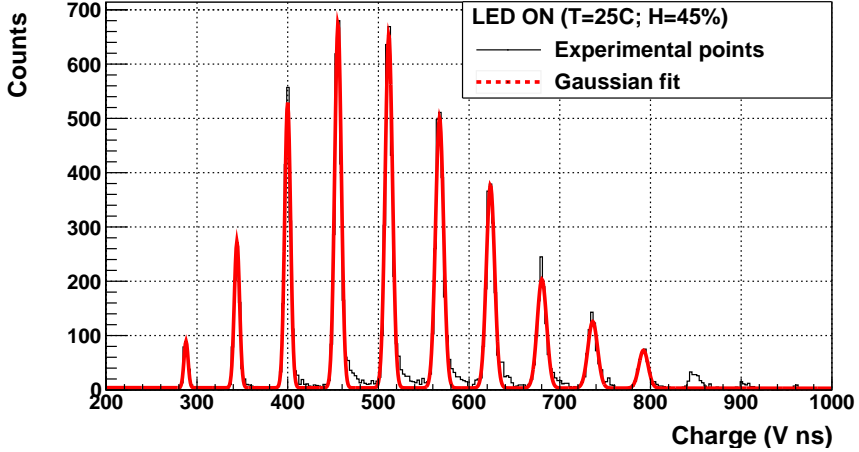
(a)
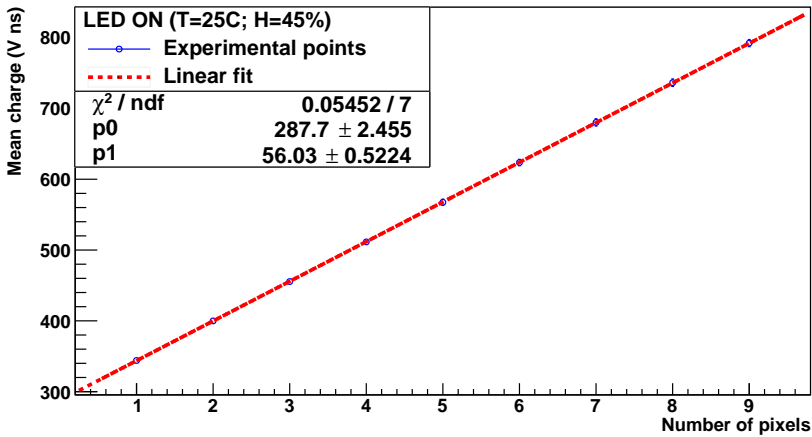
(b)

Figure 4.24 – a) Fit of the SPS spectrum to Gaussian functions. b) Charge as a function of the number of pixels fired. Error bars are within point size. Data taken at $T = 25°C$, $V_{bias} = 53.98$ V and of $H = 45\%$.

studied, which corresponds to a temperature of 25°C and a bias voltage of 53.96 V (overvoltage of 2.94 V), the value obtained for the SiPM gain is $G_{SiPM} = (4.11 \pm 0.04) \cdot 10^6$, very close to the data sheet value, given in Table 3.3.

A method for SiPM gain stabilization against temperature changes was implemented. This is necessary for the TRITIUM project since the temperature in the final location of the tritium detector cannot be controlled with sufficient accuracy to avoid significant variations of the SiPM gain. This method consists in compensating variations of the SiPM gain caused by temperature changes by a controlled modification of the bias voltage. For this task, the dependence of the SiPM gain on the temperature and bias voltage was measured. The SiPM gain was measured from 15°C to 41°C in steps of 2°C which comprises the temperature range in the final detector location. The bias voltage was $V_{bias} = V_{BD} + 2.94$. The SiPM gain was measured at several overvoltages from 1 V to 5 V in steps of 0.2 V. The temperature was $T = 25°C$. Data are shown in Figure 4.25. Excellent linear behaviour is obtained for both cases. It is obtained from a linear fit,

$$G_{SiPM} = a \cdot T + b; \quad G_{SiPM} = c \cdot V_{bias} + d$$
$$a = (-82.5 \pm 1.6) \cdot 10^3; \quad c = (137.7 \pm 1.5) \cdot 10^4$$
$$b = (618 \pm 5) \cdot 10^4; \quad d = (-762 \pm 8) \cdot 10^5$$

The breakdown voltage V_{BD} and the terminal capacitance C_t can be obtained from the linear fit of the SiPM gain versus the bias voltage V_{bias},

$$G_{SiPM} = \frac{Q_{pixel}}{q_e} = C_d \frac{V_{bias} - V_{BD}}{q_e} = c \cdot V_{bias} + d \qquad (4.11)$$

where C_d is the pixel capacitance. From the linear fit of Figure 4.25b, $V_{BD} = 51 \pm 0.6$ V and $C_d = 220.6 \pm 2.4$ fF are obtained. The terminal capacitance of the SiPM is calculated as $C_t = N_p \cdot C_d = 62.9 \pm 0.7$ pF, where N_p is the SiPM number of pixels. Both breakdown voltage and terminal
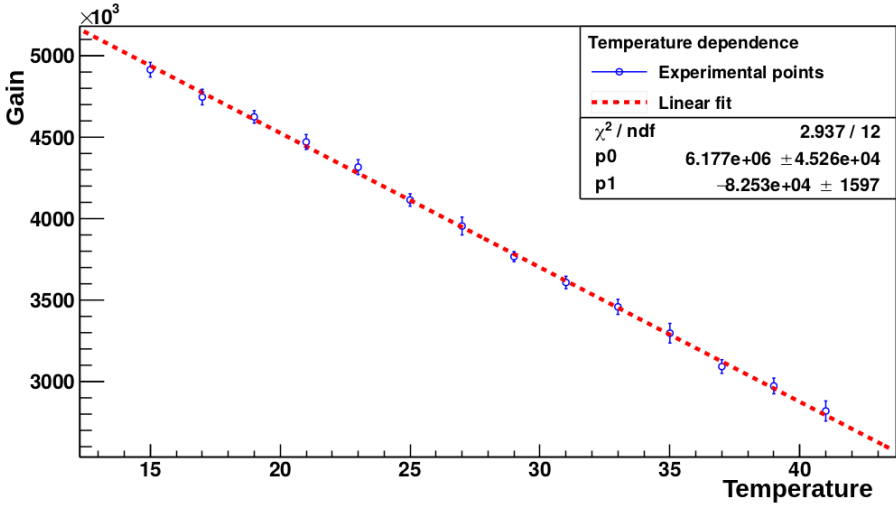
(a)
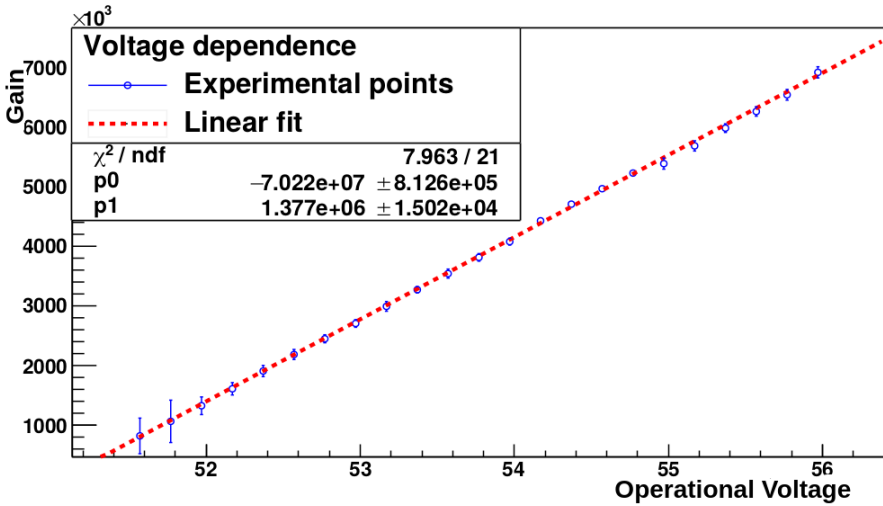
(b)

Figure 4.25 – SiPM gain versus a) Temperature. b) Bias voltage.

capacitance are in agreement with the values given in Table 3.3. Finally, the bias voltage needed to compensate for the variation of the SiPM gain due to temperature changes is obtained from the derivatives of the linear relations,

$$G_{SiPM} = a \cdot T + b \longrightarrow \frac{\partial G_{SiPM}}{\partial T} = a$$

$$G_{SiPM} = c \cdot V_{bias} + d \longrightarrow \frac{\partial G_{SiPM}}{\partial V_{bias}} = c$$

The total variation of the SiPM gain produced by the variation of both V_{bias} and T must cancel,

$$dG_{SiPM,tot} = \frac{\partial G_{SiPM}}{\partial T}dT + \frac{\partial G_{SiPM}}{\partial V_{bias}}dV_{bias} = a \cdot dT + c \cdot dV_{bias} = 0$$

$$dV_{bias} = -\frac{a}{c}dT = -edT$$

where the parameter

$$e = \Delta T V_{op} = 59.9 \pm 1.3 \text{ mV/}^\circ\text{C}$$

agrees with the temperature coefficient provided in the data sheet, given in Table 3.3. Taking finite increments,

$$\int_{V_i}^{V_f} dV_{bias} = -e \int_{T_i}^{T_f} dT \longrightarrow \Delta V_{bias} = -e\Delta T \qquad (4.12)$$

the variation of the voltage ΔV_{bias} that keeps constant the SiPM gain for a variation in temperature ΔT is obtained. To determine the bias voltage V_{bias} as a function of the temperature T, a reference value is needed. The reference considered is $V_{ref} = V_{BD} + 2.94 \text{ V} = 53.98 \text{ V}$ and $T_i = T_{ref} = 25^\circ\text{C}$, at which the measured gain is $4.2 \cdot 10^6$. Thus, we get,

$$(V_{bias} - V_{ref}) = -e\,(T - T_{ref})$$

$$V_{bias}(\mathrm{V}) = 55.48 - 59.93 \cdot 10^{-3} \cdot T(^{\circ}\mathrm{C}) \qquad (4.13)$$

To test the gain stabilization, the temperature was varied from 21°C to 29°C (expected working range) and the bias voltage was modified according to Equation 4.13. The value of the SiPM gain obtained as a function of the temperature is shown in Figure 4.26. The red dotted line indicates the
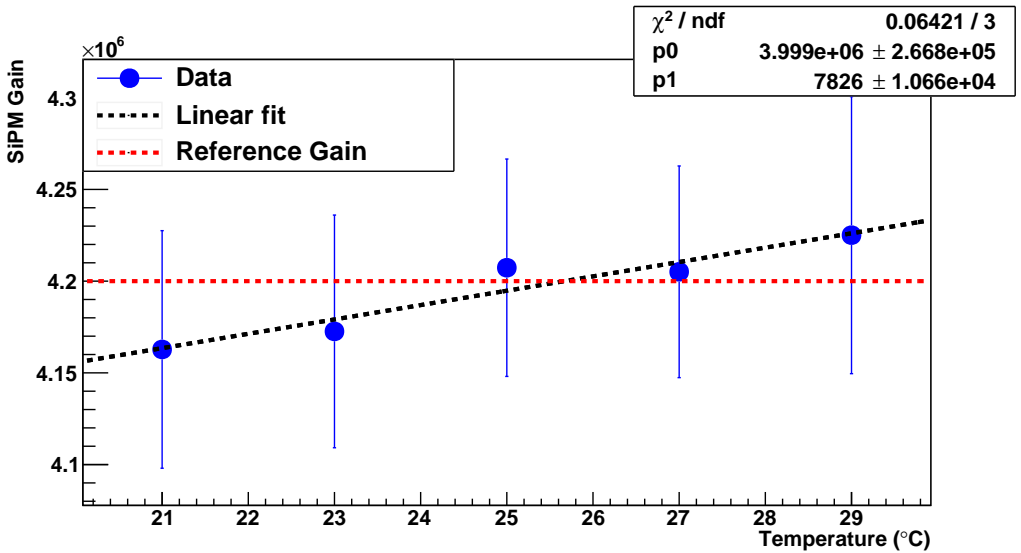
Figure 4.26 – SiPM gain as a function of the temperature after implementation of the gain stabilization method.

reference SiPM gain. As it can be seen, the relative gain variation with temperature is $1.9 \cdot 10^{-3\circ}\mathrm{C}^{-1}$ which is negligible. Therefore, this method stabilizes the gain of the SiPM against temperature variations.

4.3 Characterization of the Water Purification System

The characterization of the water purification system carried out by the TRITIUM LARUEX group is described in this section. This system guarantees that the quality of the water sample fulfils the requirements of the TRITIUM detector. These requirements are:

1. A low water conductivity, around 10 μS/cm, to avoid particles in the water to be deposited on the fibres, which would drastically reduce the detector efficiency.

2. The radioactive elements (other than tritium) in the water sample should be removed to avoid background.

3. The tritium activity of the sample should not be affected by the water purification process.

To verify that these requirements are fulfilled, a characterization of the water sample for both raw and purified water was done. This characterization consisted in measuring the water sample conductivity, the activity of the different radioactive elements present in the sample, the turbidity and the chemical components of the water sample. The sample of raw water is taken at a depth of two meters in the river and 40 meters distance from the TRITIUM monitor site towards the NPP. The chemical composition of the water, shown in Table 4.7, was measured by physico-chemical analysis before the purification process. The water sample contains components that must be removed to prevent their deposition on the scintillating fibres of the detector.

The water turbidity[1] was measured using the Hanna Hi 9829 port-

---

[1]The turbidity of water is the loss of transparency due to dissolved particles, normally

Chemical components	Concentration (mg/L)
CO_3H^-	154
Mg^{++}	46
Ca^{++}	105
NO_3^-	16
Cl^-	196
NO_2^-	0.03
K^+	11
Na^+	173
SO_4^-	217
Dry Residue	1029

Table 4.7: Chemical components measured in the raw water sample.

able multiparameter system from Hanna Instruments [Han], obtaining a value of 29 NTU, much higher than the limit of 5 NTU for drinking water recommended by the WHO. The water conductivity was also measured for raw, pure and reject water using the same instrument. The results are shown in Table 4.8. As it can be seen in the first column, raw water has a high conductivity due to its content of ions. It can be noticed in the second column of the table that the conductivity of pure water was reduced by almost two orders of magnitude, to values close to 10 μS/cm. In the third column, it can be remarked that the reject water conductivity is higher than that of raw water because this water contains the ions removed from the purified water.

The gamma radioactive elements present in both raw and purified water were identified and their activities measured by an HPGe detector. A gamma analysis was carried out to determine the emitters with a long enough lifetime to be measured. The radioactive isotopes found in the raw water with measurable activities were ^{40}K and ^{226}Ra which were not

measured in Nephelometric Units of Turbidity, NTU, as the intensity of scattered light at 90 degrees.

	Conductivity (μS/cm)		
Date	Raw	Pure	Reject
1/8/18	970	11.85	1442
7/8/18	958	11.8	1632
14/8/18	966	12.04	1725
22/8/18	980	12.54	1702
28/8/18	987	9.9	1692
5/9/18	1009	12.02	1645

Table 4.8: Conductivity of different samples of water.

detected in the purified water.

The tritium activity was measured by liquid scintillation counting (LSC) to check if it was modified by the purification process. Raw water was filtered at 0.45 microns to remove any particles that could cause the extinction of the scintillation signal. Table 4.9 shows the tritium activity measured for different water samples before and after purification. As seen in the table, tritium activity is not affected by the purification process.

	Activity (Bq/L)	
Date	Raw	Pure
7/8/18	24 ± 3	26 ± 4
11/12/19	13.2 ± 2.1	13.9 ± 2.2
15/01/20	31 ± 4	30 ± 4

Table 4.9: Tritium activity measured for different samples of both raw and purified water.

4.4 Characterization of the Cosmic Veto

The characterization of the cosmic active shield (cosmic veto), which was carried out using PMTs as photosensors, is reported in this section. The quality of the veto wrapping was checked. The configuration of the electronics used was the one given in Figure 3.15b. The surface of the veto was divided in 9 parts, depicted in Figure 4.27, on which a gamma source was placed for this test. Two different tests were carried out:
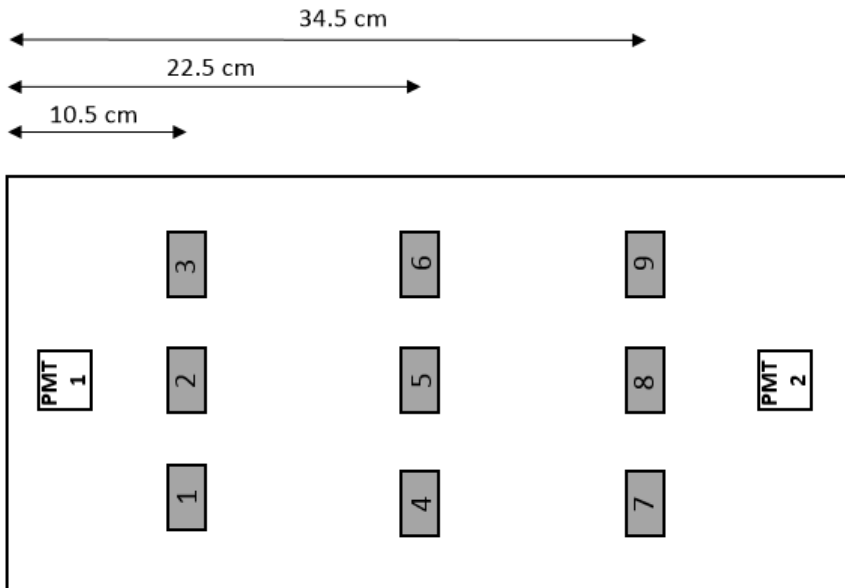
Figure 4.27 – Test points used for the cosmic veto mapping.

1. To quantify the improvement of the veto signal due to wrapping, a ^{137}Cs source was placed at point 2 before wrapping and the energy spectrum was measured. The measurement was repeated after wrapping. The spectra obtained are displayed in Figure 4.28.

   The spectrum of the wrapped veto is shifted about a factor of two to higher energies, which means that more photons per event are collec-
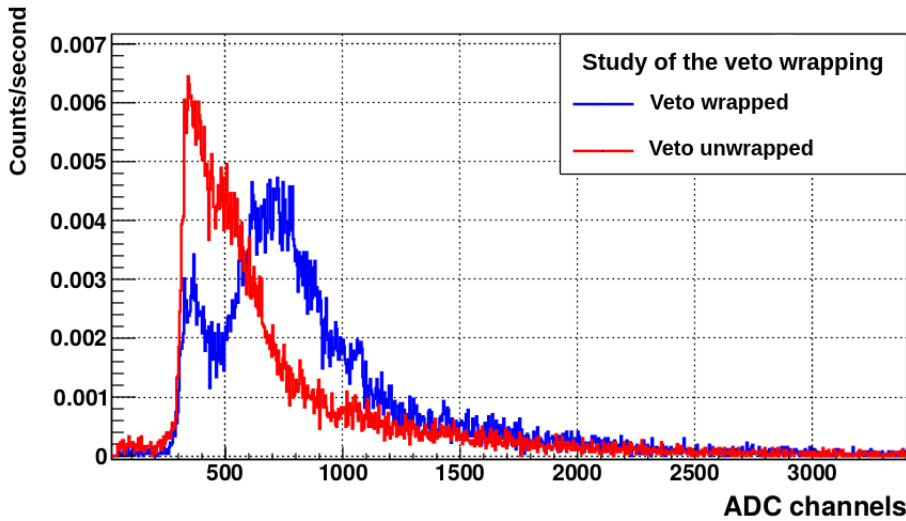
Figure 4.28 – Energy spectra measured with the ^{137}Cs radioactive source with and without wrapping the veto.

ted. No improvement was obtained in the number of events detected, only on the photon collection efficiency.

2. The spatial uniformity of the signal of the wrapped veto was evaluated. A mapping of the veto response to a ^{60}Co source placed successively on each test point was done for two different veto modules and the energy spectra obtained were integrated. The counting rates obtained are plotted in Figure 4.29. It can be observed that the veto signal has a uniform response on its whole surface, giving a fairly similar counting rate at all points.

In a second test, two cosmic vetos were studied in coincidence. The electronic configuration of Figure 3.15c was employed. The output signal of the coincidence module was connected to an 1145 CAEN Quad Scaler And Preset Counter-Timer module [CAE]. The goal of this test was to find the PMT high voltage and the threshold discrimination for which the detection of cosmic rays is optimized. The test consisted in finding the PMT high
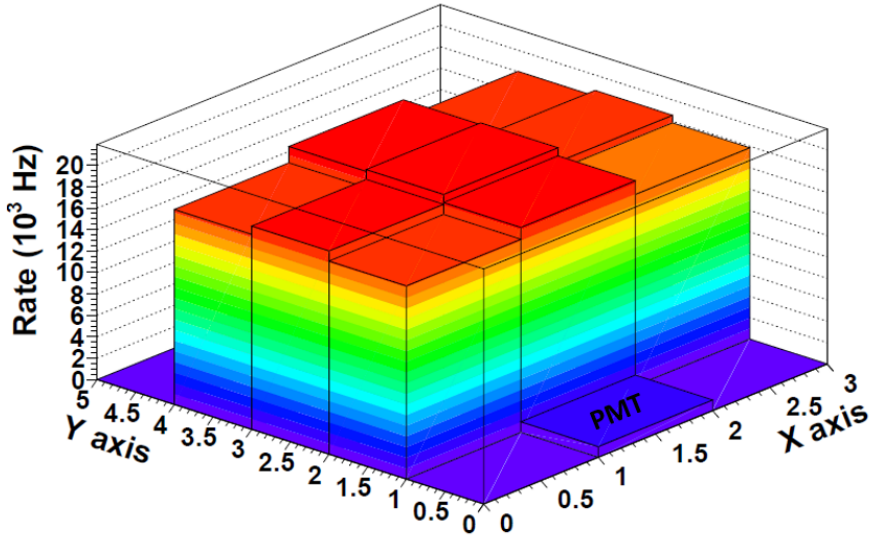
(a)
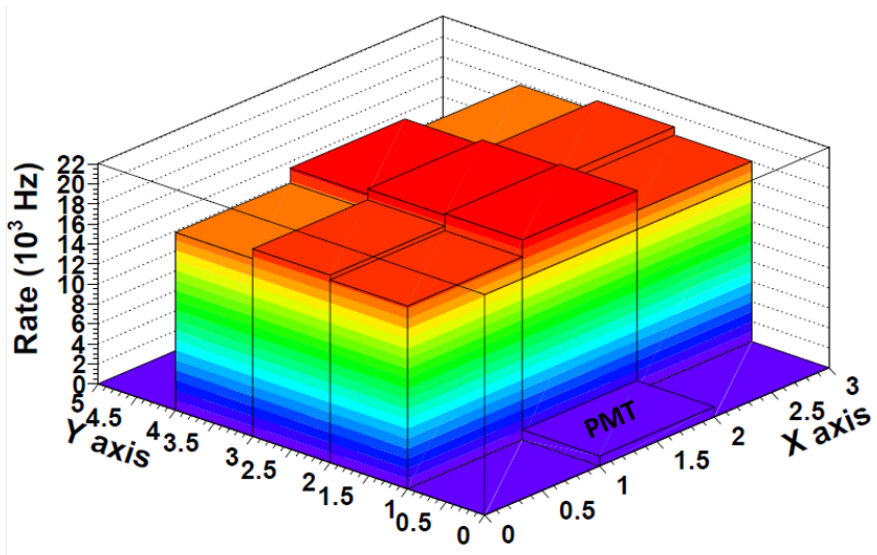
(b)

Figure 4.29 – Bidimensional graph of the counting rate (mapping) measured for two different cosmic vetoes using a ^{60}Co source.

voltage plateau on which the veto efficiency is constant and the discriminator threshold plateau on which no loss of cosmic events is produced. The counting rate was measured versus the PMT high voltage at three different thresholds (60 mV, 100 mV and 200 mV) and versus the threshold at three different PMT high voltages (700 V, 730 V and 780 V). The counting rate was measured during intervals of 300 s. The results are plotted in Figure 4.30. The PMT high voltage chosen was 800 V since it is on the plateau for the three threshold settings and the threshold chosen was 200 mV which is on the plateau for the selected high voltage.

The energy spectrum of cosmic rays was measured using the electronics of Figure 3.15c. A plot of this spectrum is shown in Figure 4.31. As expected, this energy spectrum fits well to a Landau function. The cosmic ray rate determined from the area of this spectrum is 2.5 event/s. The expected cosmic rate calculated in section 3.4.2 is 2.9 event/s. Thus, the efficiency of the active veto is 85%, which is a typical value of the efficiency of plastic detectors for MIPs. Finally, the detected cosmic ray rate versus the separation distance between the two cosmic vetoes was measured. The spectra are shown in Figure 4.32a. The counting rate decreases with the distance but the spectrum shape and peak position remain unchanged. The integrated spectrum as a function of distance was fitted to a second-degree polynomial. The fit is shown in Figure 4.32b and allows us to estimate the cosmic ray rate for a given veto separation.
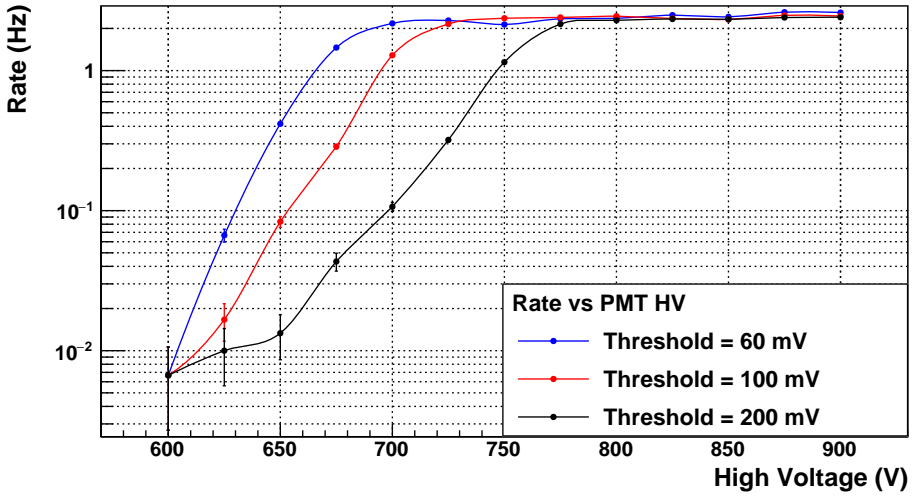
(a)
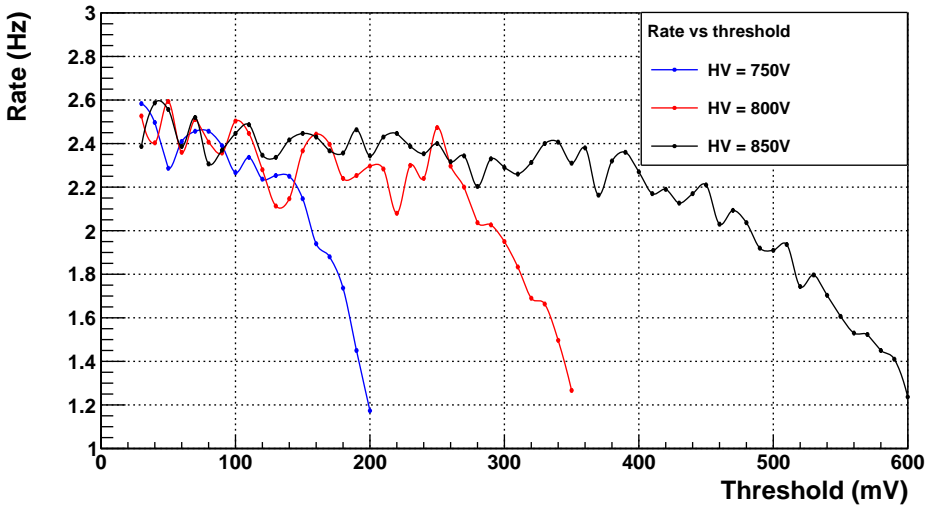
(b)

Figure 4.30 – Counting rate of two cosmic vetoes in coincidence a) as a function of PMT HV for three different thresholds and b) as a function of the threshold for three different high voltages.
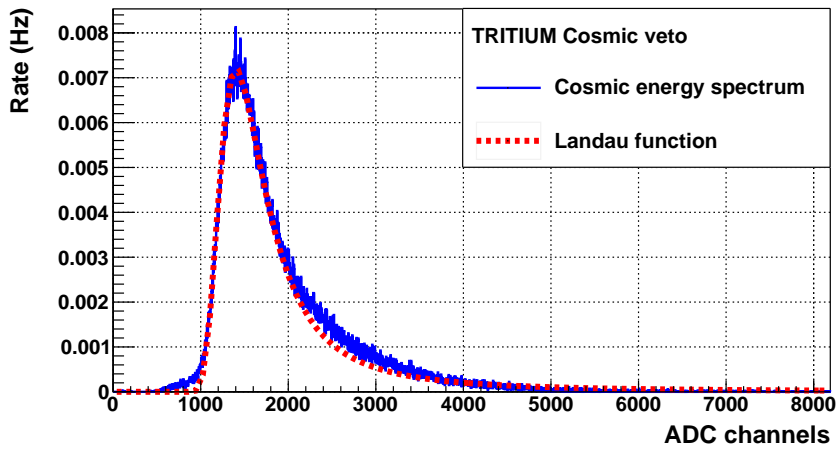
Figure 4.31 – Energy spectrum measured with the cosmic veto.
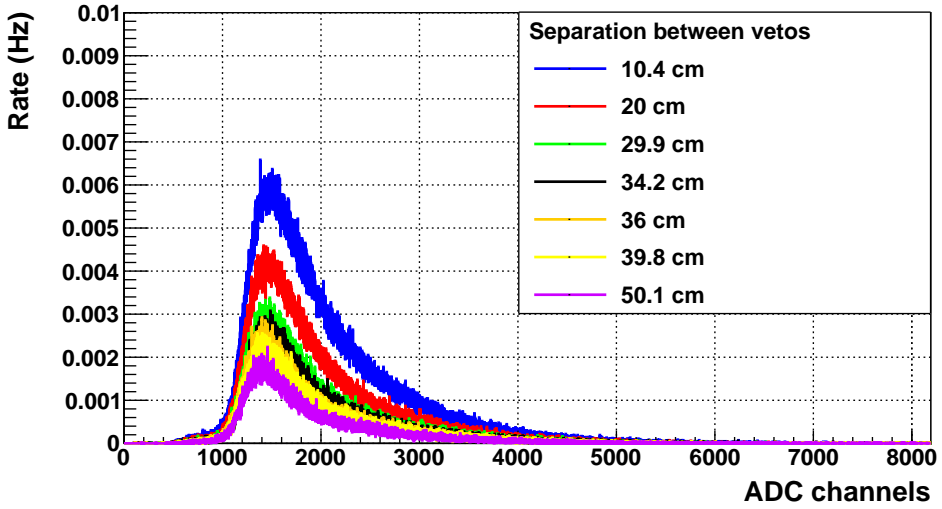
(a)
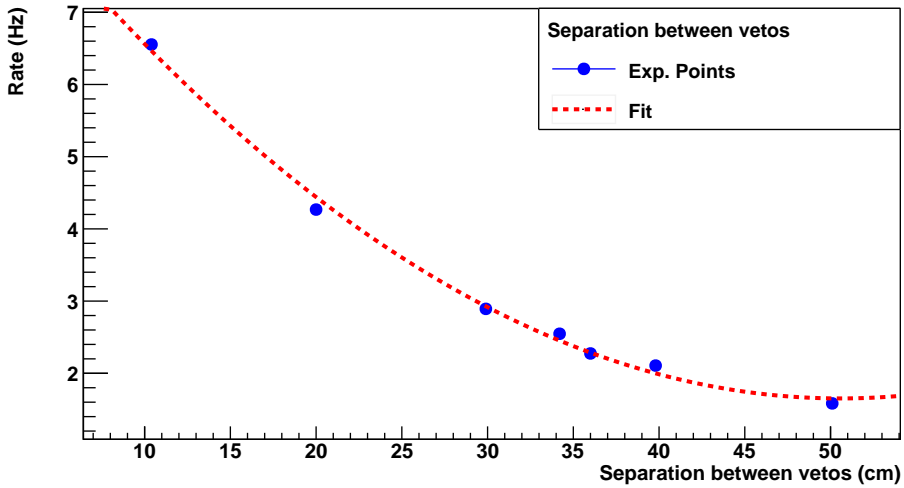
(b)

Figure 4.32 – a) Energy spectra of the cosmic veto for several separations of the scintillators. b) Fit to a second-degree polynomial of the cosmic ray rate versus the separation of the veto scintillators.

Chapter 5

TRITIUM Detector Prototypes

The different prototypes developed in the framework of the TRITIUM project, their characterization and their measurements in the labortories and Arrocampo dam are described in this chapter. They are named TRITIUM-IFIC-0, TRITIUM-IFIC-1, TRITIUM-Aveiro and TRI-TIUM-IFIC-2, listed in chronological order of their construction. The first two prototypes, TRITIUM-IFIC-0 and TRITIUM-IFIC-1, were used to learn about in-water tritium detection and to define the monitor design. TRITIUM-Aveiro and TRITIUM-IFIC-2 have an optimized design based on the lessons learned from the former prototypes. These detectors were filled with tritiated water following a specific method and several water tightness and filling tests were carried out. At the end of the chapter, the final monitor design of the TRITIUM detector is described.

5.1   First IFIC prototypes

The preliminary prototypes, TRITIUM-IFIC-0 and TRITIUM-IFIC-1, were designed and built at the IFIC workshop. They are a small-scale proof of

concept of the final TRITIUM detector module. They allowed us to learn about in-water tritium detection, to identify design issues and to implement improvements for the final monitor.

5.1.1 TRITIUM-IFIC-0

TRITIUM-IFIC-0 was the first prototype developed in the TRITIUM project aiming to prove the feasibility of the technology proposed by TRITIUM, that is, to employ plastic scintillating fibres to detect tritium in water with sufficient sensitivity. As liquid radioactive sources were involved, special attention was paid to radiation safety in the design.

TRITIUM-IFIC-0 consists of a bundle of 35 fibres 20 cm long, which were cleaved and polished with the techniques reported in section 4.1. This bundle is attached to the vessel through metallic pieces located at its ends, as shown in Figure 5.1. The PVC[1] vessel, shown in Figure 5.2, was designed in a U-shape to improve radiological safety. However, this shape was not appropriate as we learned afterwards. A frame of methacrylate and steel, shown in Figure 5.2, was designed and built to hold the prototype. Two calibrated Hamamatsu R8520-06SEL PMTs [Ham19] were coupled to the fibre bundle with optical grease [Saib]. The voltage divider circuit employed is shown in Figure 3.9. The high voltage was set to -800 V, at which the gains are $1.26 \cdot 10^6$ and $1.01 \cdot 10^6$, and the quantum efficiencies are 29.76% and 28.66% at $\lambda = 430$ nm, respectively. The two PMTs were read out in coincidence by the electronics shown in Figure 3.15b.

Two identical prototypes were built. The first one, called "TRITIUM-IFIC-0 Background", was filled with pure water (39 mL, uncertainty of 0.05%) and was used to measure the background, whereas the second one, called "TRITIUM-IFIC-0 Signal", was filled with a radioactive liquid source

---

[1]Polyvinyl Chloride, PVC

(a) **(b)**
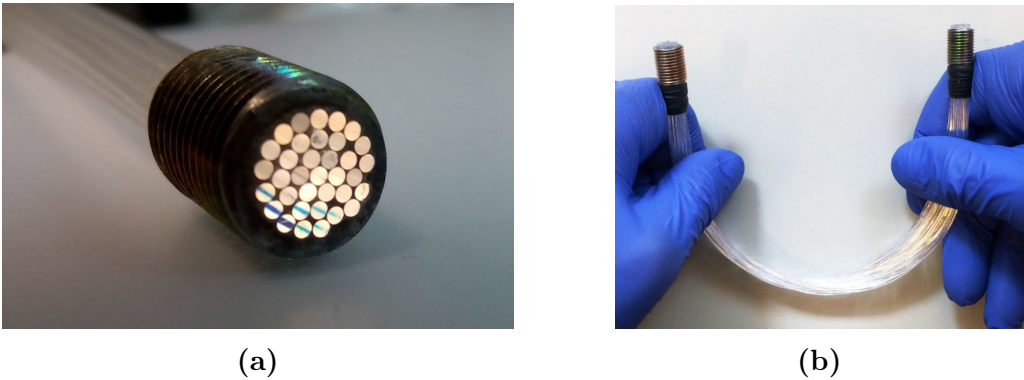
Figure 5.1 – a) Metallic piece of the fibre bundle. b) Bundle of 35 fibres of 20 cm length used in TRITIUM-IFIC-0.

of tritiated water of specific activity of 99.696 kBq/L (2.24% uncertainty) as reported in Appendix C. This second prototype was employed to measure the total signal (tritium + background). The tritium signal was determined by subtracting the background from the total signal. The number of coincident events was too low due to photon escape from the fibers caused by several reasons such as the excessive curvature of the fibre bundle and the poor quality of the interface between tritiated water and fibres. The implementation of the cleaning process described in section 4.1 was motivated by this result.

A transparent glass vessel similar to the TRITIUM-IFIC-0 prototype vessel, shown in Figure 5.3a, was built to study the effect of the fibre bundle curvature. The LED described in section 4.1 was used to asses the reduction in photon collection of the fibre bundle. As can be seen in Figure 5.3b, most of the photons introduced from one side of the bundle do not reach the other side. This test showed essential to keep a straight fibre arrangement in the design of the next prototypes. A second point is that the fibre bundle was too compact which possibly prevented water from flowing adequately between the fibres. In the TRITIUM-IFIC-1, the fibres were sufficiently spaced by using a PTFE matrix.
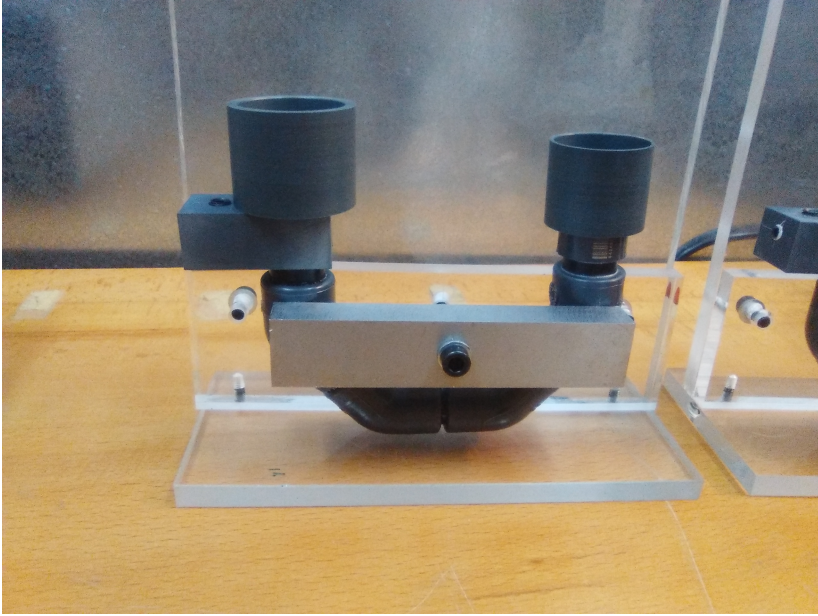
Figure 5.2 – TRITIUM-IFIC-0 prototype.

Data with TRITIUM-IFIC-0 were taken with a single PMT. The energy spectra measured for both the signal and background prototypes are shown in Figure 5.4a. The difference between signal and background, shown in Figure 5.4b, corresponds to the energy spectrum of tritium. The counting rates obtained for the three spectra are given in Table 5.1. The tritium

Spectrum	Rate (Hz)
Signal	2.27 ± 0.06
Background	2.06 ± 0.06
Tritium	0.21 ± 0.09

Table 5.1: Rates obtained by TRITIUM-IFIC-0.

detection efficiency obtained by TRITIUM-IFIC-0, calculated as the ratio of the tritium counting rate to the specific activity of the tritium liquid source, is

$$\eta = (2.1 \pm 0.9) \cdot 10^{-3} \text{ L kBq}^{-1}\text{s}^{-1}$$

(a)

(b)
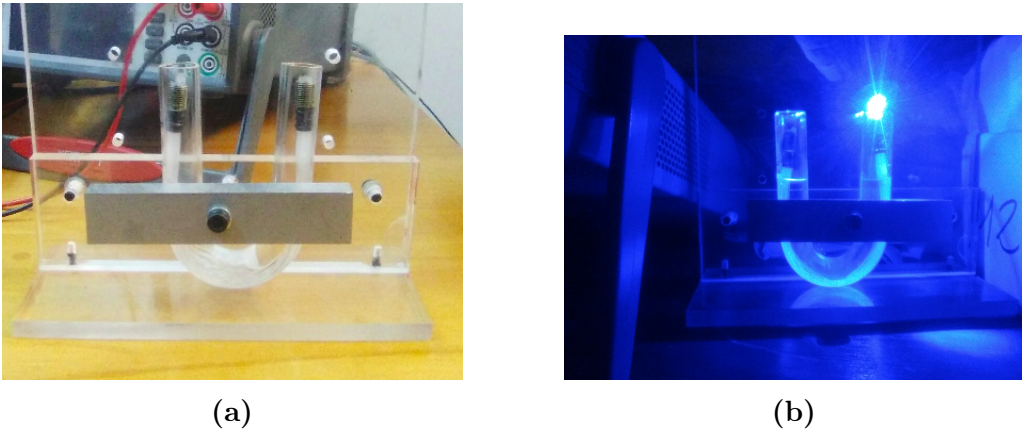
Figure 5.3 – a) Fibre bundle in a PMMA vessel. b) Illumination test of the bundle to visualize the light loss due to fibre curvature.

As reported in section 2.1, the tritium detection efficiency scales with the active area of the scintillator used. Therefore, to compare the efficiency with other detectors in the literature and with other prototypes developed in the TRITIUM project, the specific efficiency S, calculated by normalizing the detection efficiency to the scintillator area, is

$$S = (9.6 \pm 3.9) \cdot 10^{-6} \text{ L kBq}^{-1}\text{s}^{-1}\text{cm}^{-2}$$

As can be seen in Table 2.2, the specific efficiency is somewhat larger than that obtained by Muramatsu [Mur67], $S = 3.13 \cdot 10^{-6} \text{ LkBq}^{-1}\text{s}^{-1}\text{cm}^{-2}$, and similar to that obtained by Moghissi [Mog69], $S = 10.6 \cdot 10^{-6} \text{ LkBq}^{-1}\text{s}^{-1}\text{cm}^{-2}$. These efficiencies are too low to achieve the objective of measuring activities of the order of 100 Bq/L.

5.1.2   TRITIUM-IFIC-1

TRITIUM-IFIC-1 was designed to correct the issues found in TRITIUM-IFIC-0. The main improvements were:
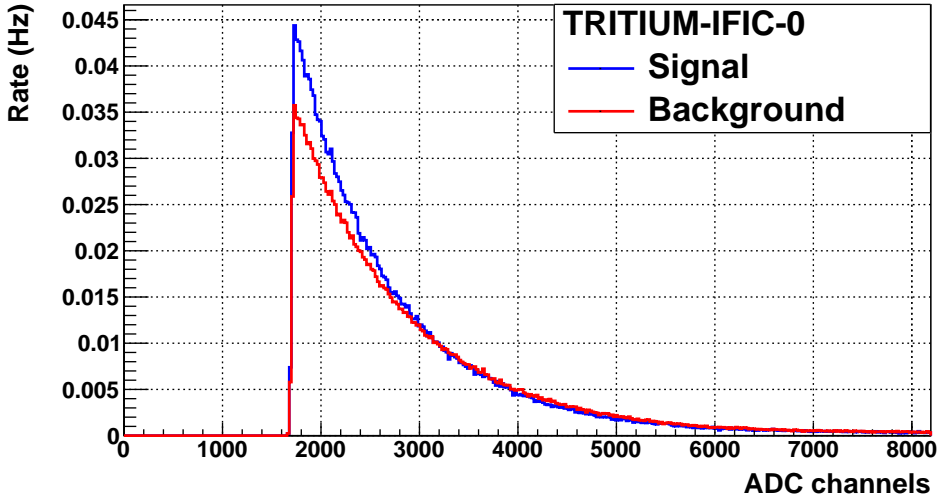
(a) .
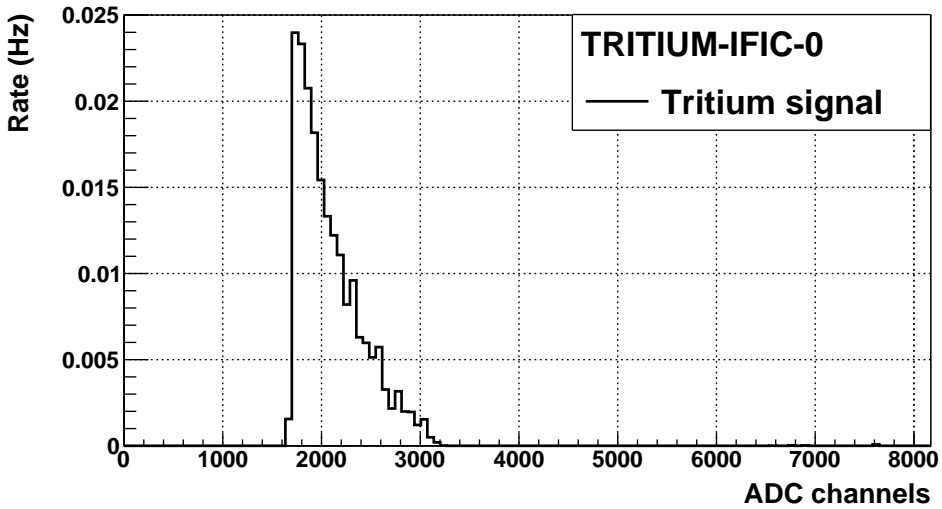
(b)

Figure 5.4 – Energy spectra measured by TRITIUM-IFIC-0. a) Signal and background energy spectra. b) Tritium energy spectrum.

1. The fibre bundle was arranged straight to optimize the photon collection efficiency of the fibres. In addition, a PTFE matrix was used to maintain a distance of 1 mm between fibres.

2. A special fibre cleaning method, described in section 4.1, was applied to the fibres to improve the quality of the interface between fibres and tritiated water. This method produces a better wetting property of the fibres, which improves their photon collection efficiency.

3. A PTFE vessel was used to improve the collection of photons inside the prototype. Indeed, PTFE has a reflectivity of around 93% [Gui11] at the fibre scintillating wavelengths. Thus, the photons that escape from fibres and hit the vessel walls are reflected into the scintillating fibres.

TRITIUM-IFIC-1 consists of 64 straight scintillating fibres of 20 cm in length, arranged in an 8×8 PTFE squared matrix, as shown in Figure 5.5. This structure is placed within a cylindrical PTFE vessel of 48 mm
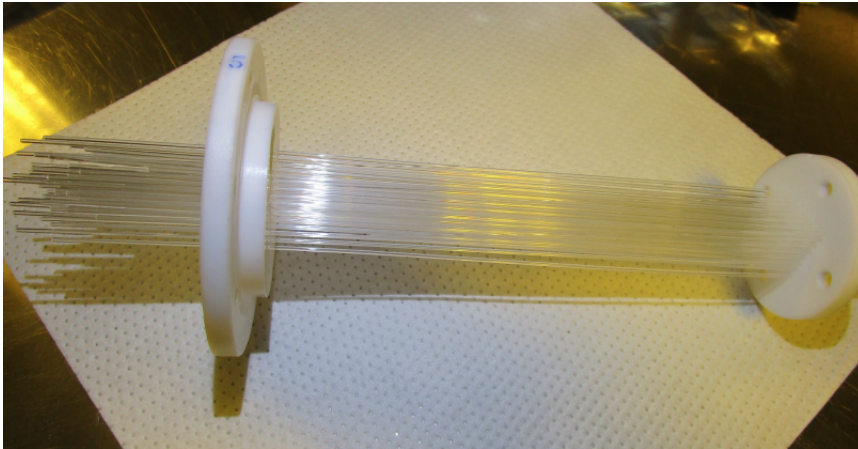
Figure 5.5 – PTFE structure used to arrange the fibres of TRITIUM-IFIC-1 prototype in a matrix of 8×8.

diameter and 200 mm in length, shown in Figure 5.6. The cleaning process
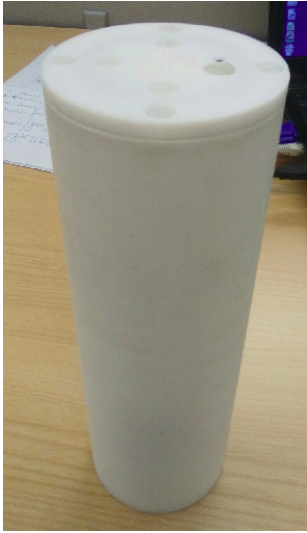
(a)   **(b)**

Figure 5.6 – Pictures of the TRITIUM-IFIC-1 PTFE vessel.

described in section 4.1 was applied to the fibres to achieve a better inter-
face between tritiated water and fibres. A PVC piece was used to couple
a photosensor to the prototype and to prevent external light, as shown in
Figure 5.7. The prototype was instrumented with a PMT, model R8520-
06SEL from Hamamatsu Photonics [Ham19], coupled directly to the fibre
bundle by optical grease [Saib]. The quantum efficiency of this PMT is
28.66% at $\lambda = 430$ nm. The PMT high voltage was -800 V. The DAQ was
the same as for TRITIUM-IFIC-0. In the first measurement, this proto-
type was filled with pure water (118 mL, uncertainty of 0.05%) and several
background measurements were taken during a week. Subsequently, it was
emptied and refilled with 118 mL (uncertainty of 0.05%) tritiated water of
99.696 kBq/L activity. The measured signal and background energy spectra
are shown in Figure 5.8a. The tritium spectrum is shown in Figure 5.8b
[Aze18, Aze20b]. The rates obtained from the integration of the spectra are
given in Table 5.2.

Figure 5.7 – Picture of TRITIUM-IFIC-1. The photosensor lodging is shown.

The tritium detection efficiency for TRITIUM-IFIC-1 is

$$\eta = (3.84 \pm 0.16) \cdot 10^{-2} \text{ L kBq}^{-1}\text{s}^{-1}$$

The specific efficiency is

$$S = (9.6 \pm 0.4) \cdot 10^{-5} \text{ L kBq}^{-1}\text{s}^{-1}\text{cm}^{-2}$$

Spectrum	Rate (Hz)
Signal	7.82 ± 0.11
Background	3.99 ± 0.08
Tritium	3.83 ± 0.13

Table 5.2: Counting rates obtained by TRITIUM-IFIC-1.
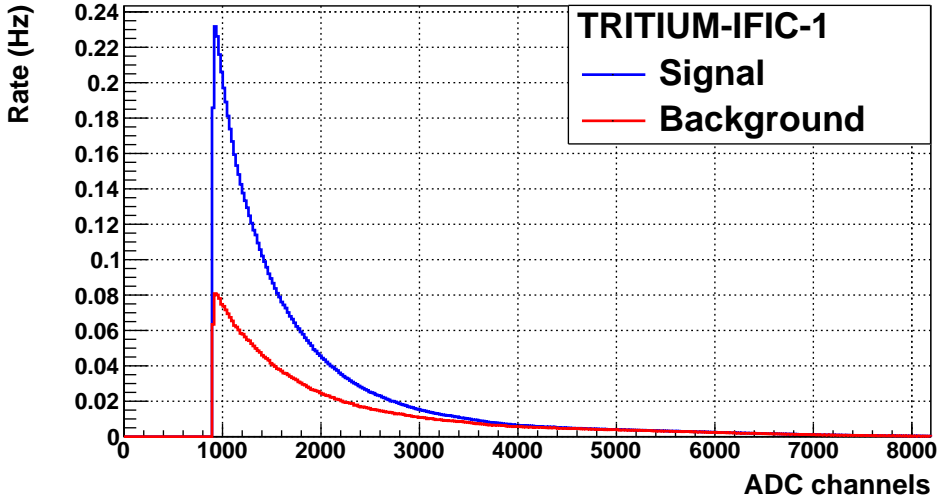
(a)
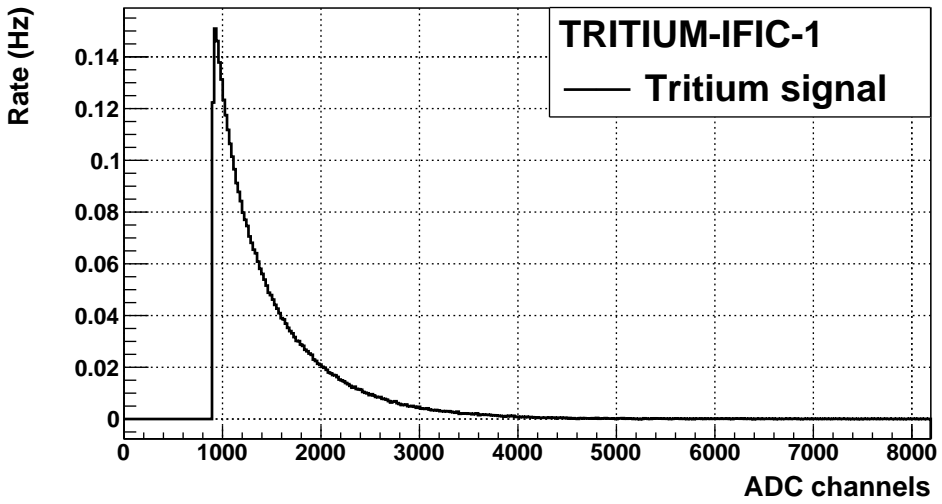
(b)

Figure 5.8 – Energy spectra measured by TRITIUM-IFIC-1. a) Signal and background energy spectra. b) Tritium energy spectrum.

which is a factor ten better than that of TRITIUM-IFIC-0. Furthermore, compared to the scintillating detectors of tritium in water given in table 2.2, the efficiency of this prototype is very close to the best result obtained by Singh [Sin85, Rat00], $\eta = 4,1 \cdot 10^{-2}$ L kBq^{-1}s^{-1}, and the specific efficiency, which is the most relevant parameter for comparison, is almost 5 times larger than that obtained by Hofstetter [Hof92a, Hof92b], $S < 22.2 \cdot 10^{-6}$ L kBq^{-1}s^{-1}cm^{-2}.

5.2   Latest TRITIUM Prototypes

TRITIUM-Aveiro and TRITIUM-IFIC-2 have a different design than the previous prototypes that allows the reading of a large number of straight fibres with two photosensors operating in coincidence. Furthermore, the activity of the radioactive liquid source employed was much lower than for the first prototypes to investigate the MDA. The main differences between TRITIUM-Aveiro and TRITIUM-IFIC-2 are:

1. The diameter of the scintillating fibres, which is 2 mm for TRITIUM-Aveiro and 1 mm for TRITIUM-IFIC-2. A larger diameter may facilitate the flow of water between the fibres, reducing issues related to surface tension and ensuring that the entire active volume of the fibres participates in tritium detection. In addition, a large radius increases the rigidity of the fibres, improving their robustness. However, the detector active volume for 2 mm fibres is smaller than for 1 mm fibres for the same filling volume. In addition, the volume of the fibres unreachable by tritium decay electrons, which contributes to the background, is larger for 2 mm fibres. Consequently, the larger the radius the smaller the signal-to-background ratio.

2. The whole surface-conditioning method, consisting of cleaving, polishing and cleaning, was applied to the scintillating fibres of TRITIUM-

IFIC-2. However, only the cleaving method was applied to the scintillating fibres of TRITIUM-Aveiro.

3. TRITIUM-Aveiro uses PMTs as photosensors. Although most of the development of TRITIUM-IFIC-2 was made with PMTs, it is intended to employ SiPM arrays that provide a larger photodetection efficiency than PMTs for a similar price. In addition, no high voltage is needed for SiPMs, which reduces the price of both electronics.

4. TRITIUM-Aveiro uses a homemade PCB-based electronics which is cheaper than PETsys. However, the PETsys system is quite stable and meets the TRITIUM monitor scalability requirement without any additional development.

The development and operation of these two prototypes aim at defining the best design for the final TRITIUM monitor.

5.2.1 TRITIUM-Aveiro

TRITIUM-Aveiro is a proposal for the final TRITIUM detector module. This prototype, shown in Figure 5.9, was designed and built in the University of Aveiro. It consists of a PTFE vessel, shown in Figure 5.10, with an internal cylindrical hole of 43 mm in diameter and 18 cm in length. This vessel contains 360 BCF-10 uncladded scintillating fibres of 180 mm in length from Saint-Gobain [Sai21b], which are similar to the BCF-12 fibres except for the diameter and the attenuation length (2.2 m for BCF-10 and 2.7 m for BCF-12). The scintillating fibres are stacked within the PTFE vessel in the maximum number that allows water to flow around them. These fibres were cleaved with the device described in section 4.1, but they were neither polished nor cleaned because the automatic polishing machine was not yet developed and it was not feasible to polish 360 fibres by hand. The PTFE vessel is totally closed and a water inlet and a water outlet were
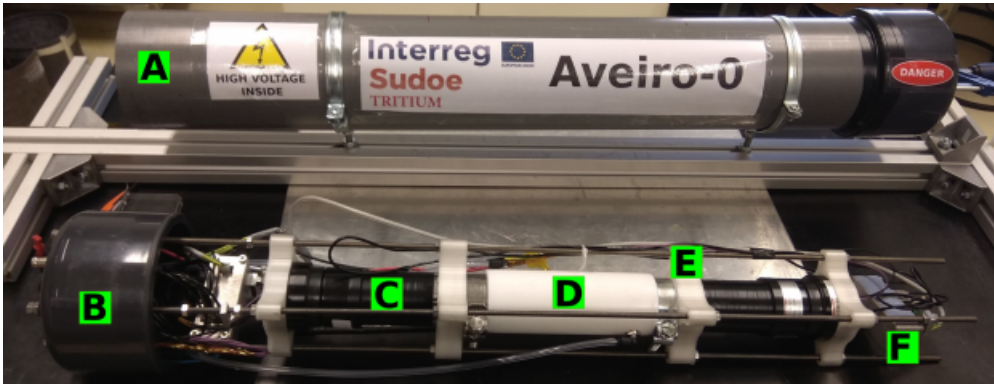
Figure 5.9 – TRITIUM-Aveiro prototype. A and B are the PVC structure, C is the PMT, D is the PTFE vessel, E is the 3D printer piece and F is the electronics.

installed to allow a constant water flow through it. Two PMMA 10 mm thick windows located at both ends of the fibre bundle are used to read out the fibres. Two clamps are used to make a tight junction of the PTFE walls and the PMMA windows. PMMA was chosen for its optical properties, especially its transmission coefficient which is larger than 95% at the scintillating fibre wavelength. Two R2154-02 2" PMTs from Hamamatsu [Ham10], shown in Figure 5.9, are used to read out this prototype in coincidence. The PMT quantum efficiency is 26% at $\lambda = 430$ nm and the HV was set at -1500 V. The PMTs are optically coupled to the PMMA windows through optical grease [Saib]. The Aveiro prototype and its electronics were arranged in a structure composed of several clamps and four stainless-steel screws locked to an external PVC structure. This structure protects the prototype from physical damage and provides a light-tight operation environment. Only one prototype was built, which was designed to be installed in the Arrocampo dam. Two graphical interfaces were developed to control the PMT power supply and the data acquisition, respectively.

Measurements to characterize the detector were carried out in the I3N and LARUEX laboratories. The prototype was in the first place filled

Figure 5.10 – PTFE vessel and fibre bundle used in TRITIUM-Aveiro prototype.

with pure water to measure the background and next with a radioactive liquid tritium solution of 30 kBq/L activity, which was used to measure the prototype efficiency and MDA. The volume of pure water and tritium solution used in TRITIUM-Aveiro was 58 mL.

To quantify the background attenuation by a lead shield, measurements without shielding and with 2.5 mm and 5 mm lead shields were carried out at I3N. A background reduction by factors of about 2 and 4 was obtained by the 2.5 mm and 5 mm lead shields, respectively, as shown in Figure 5.11.

The prototype was installed in the LARUEX laboratory in order to be tested with tritiated water. The background was measured for 4 days with the prototype filled with pure water and shielded by 5 cm lead. The events were grouped in 1 min time bins and the data were fitted to a Gaussian function as shown in Figure 5.12. An average rate of $N_b =$
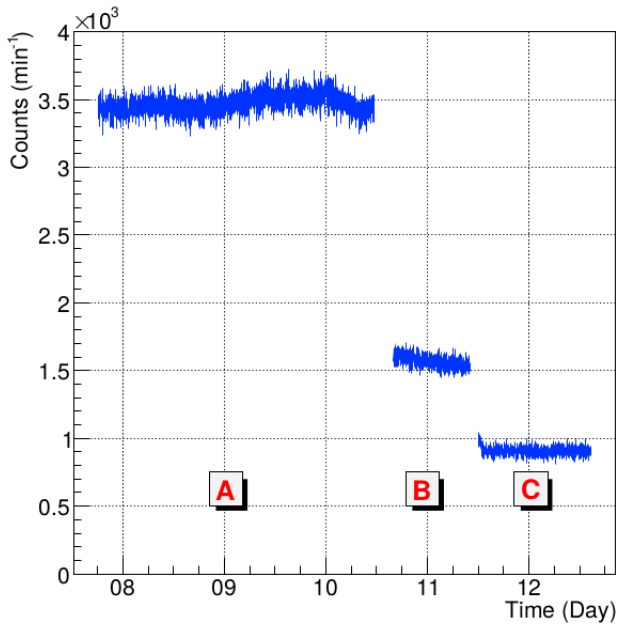
Figure 5.11 – Background rate of TRITIUM-Aveiro. A) Without shielding. B) With a lead shield of 2.5 mm thickness. C) With two lead shields of 2.5 mm thickness each [Aze22].

540 min^{-1} with a standard deviation of $\sigma_{N_b} = 23$ min^{-1} was obtained. To calculate the MDA, the detection limit criterium developed by Lloyd A. Currie [Kno10] was applied. This criterium defines a critical level L_C above which the probability of a false-positive is less than 5% and a level N_D for which the probability of a false-negative is less than 5%. They are given by,

$$L_C = 2.33 \cdot \sigma_{N_b} = 53 \text{ min}^{-1}$$
$$N_D = 4.65 \cdot \sigma_{N_b} + 2.71 = 111 \text{ min}^{-1}$$
(5.1)

L_C and N_D are calculated from the total signal after background subtraction. Therefore, the critical level L'_C and the minimum count rate distinct from the background N'_D are

$$L'_C = N_b + L_C = 540 + 53 = 593 \text{ min}^{-1}$$

133

and

$$N'_D = N_b + N_D = 540 + 111 = 651 \ \text{min}^{-1}$$

To find the MDA, tritiated water was slowly added to the prototype so that the tritium water activity increased continuously till measuring a counting rate as close as possible to N'_D. A rate of (656 ± 26) min^{-1} was obtained. Its corresponding activity, measured with a Quantulus LSC, was MDA=(29.8 ± 3.6) kBq/L.

The tritium detection efficiency was calculated from the ratio of the net tritium rate measured, (1.9 ± 0.6) sec^{-1}, and the activity of the tritium source used, 29.8 kBq/L. The tritium detection efficiency obtained is

$$\eta = (6.5 \pm 1.9) \cdot 10^{-2} \ \text{L kBq}^{-1}\text{s}^{-1}$$

and the specific efficiency is

$$S = (1.6 \pm 0.5) \cdot 10^{-5} \ \text{L kBq}^{-1}\text{s}^{-1}\text{cm}^{-2}$$

Compare to the specific efficiency obtained with scintillating detectors in the literature (Table 2.2), the specific efficiency of TRITIUM-Aveiro is close to the largest value $S < 2.22$ LkBq^{-1}s^{-1}cm^{-2} [Hof92a, Hof92b]. TRITIUM-Aveiro has a lower specific efficiency than TRITIUM-IFIC-1, which could be attributed to the absence of polishing and cleaning of the fibres of this prototype. The efficiency uncertainty obtained is larger than for the first TRITIUM prototypes because of the shorter measurement time (1 minute instead of several hours). As the MDA depends directly on the background uncertainty, longer measurements are needed. The data for an integration time of 60 min are shown in Figure 5.13. The mean and the uncertainty of the measured background data are $N_b = 3.186 \cdot 10^4$ h^{-1} and $\sigma_{N_b} = 225$ h^{-1} respectively. From Equation 5.1, $L_C = 524$ h^{-1} and $N_D = 1048.96$ h^{-1} are obtained. Assuming linearity between the activity and the counting rate, $N'_D = 3.291 \cdot 10^4$ h^{-1} corresponds to MDA=(3.6 ± 0.1) kBq/L. A daily oscillation is clearly observed in Figure 5.13, indicating that the measurements
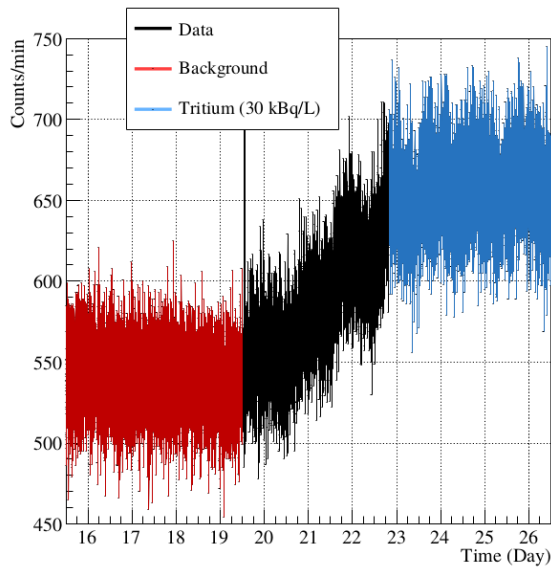
(a)
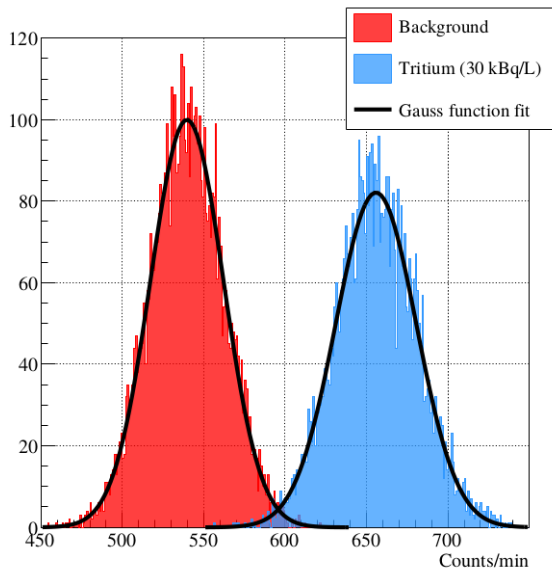
(b)

Figure 5.12 – Background and tritium liquid source (29.8 kBq/L) of TRITIUM-Aveiro [Aze22]. a) Counts per minute measured as a function of time. b) Distribution of the acquired data.

are affected by external light. This oscillation begins on the 19th day when the water closed-circuit pump was installed, so it is likely due to a light leak in the system. This prototype was finally installed in the Arrocampo
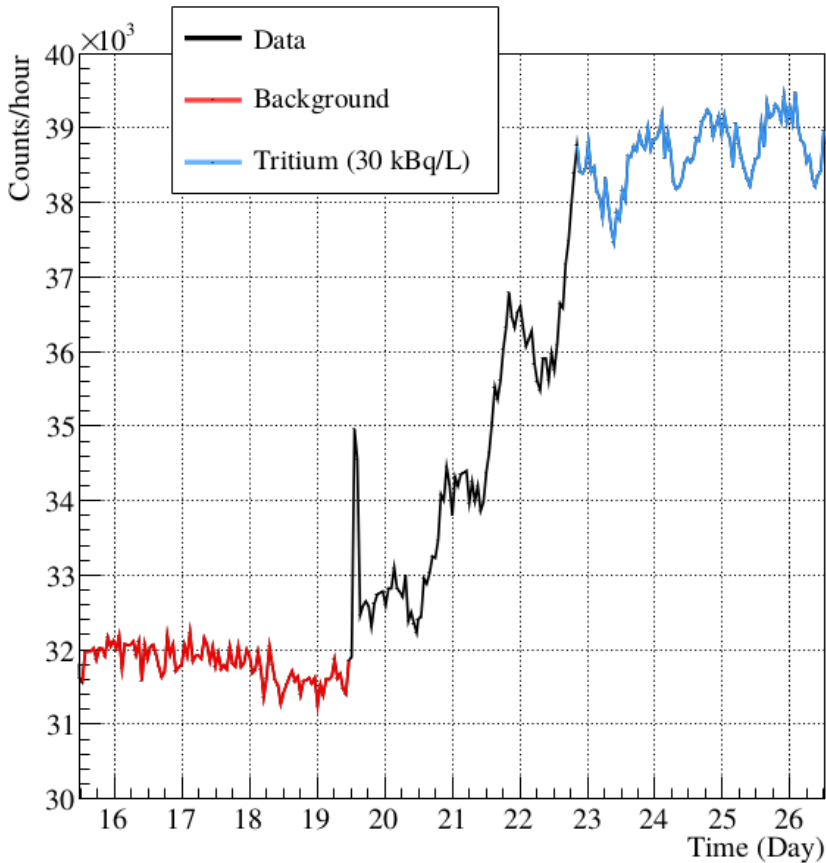
Figure 5.13 – Background and tritium liquid source counting rates measured with TRITIUM-Aveiro [Aze22].

dam to test its functionality and to begin with the tritium level monitoring reported in section 5.3.

5.2.2   TRITIUM-IFIC-2

The last prototype developed was TRITIUM-IFIC-2, shown in Figure 5.14. This prototype, built in the IFIC workshop, consists of 800 uncladded BCF-12 scintillating fibres of 200 mm length and 1 mm diameter placed inside a cylindrical PTFE vessel shown in Figure 5.15. The internal length and diameter of the PTFE vessel are 210 mm and 36 mm, respectively. The number of fibres used is larger than for the Aveiro prototype but they are contained in a smaller volume. The scintillating fibres are tightly stacked but allow water to flow between them. The fibres were cleaved, polished and cleaned with the conditioning processes described in section 4.1. Two 5 mm thick PMMA windows allow reading the scintillation light out as in Tritium-Aveiro. The windows thickness is enough to seal the vessel since
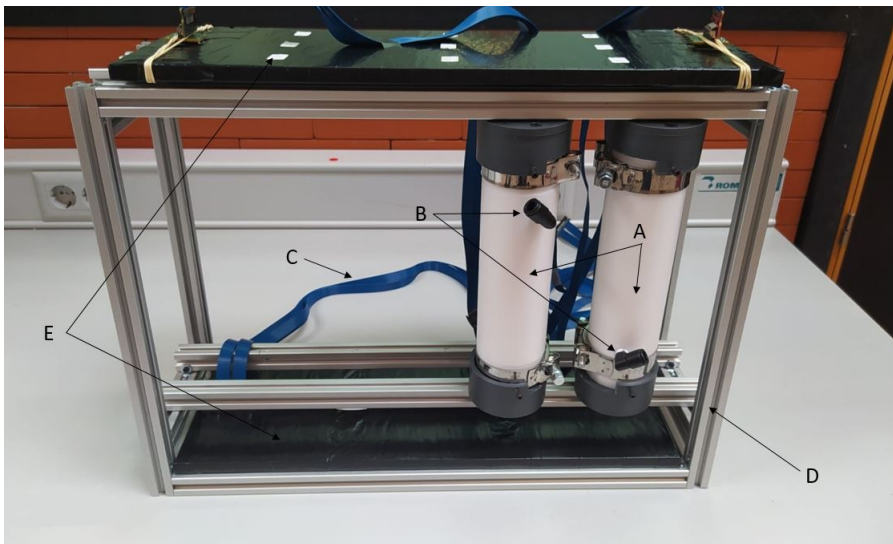
Figure 5.14 – A) TRITIUM-IFIC-2 prototype, B) water inlet/outlet, C) PETsys flat wires, D) the metallic structure and E) active veto.

the detector works at very low water pressure. PMMA was chosen for its optical properties, especially its transmission coefficient which was measured at ICMOL and is plotted in Figure 5.16. This transmission coefficient

(a)   (b)

Figure 5.15 – a) TRITIUM-IFIC-2 PTFE vessel. b) TRITIUM-IFIC-2 PTFE vessel with two PVC caps that provide a light-tight environment for the SiPM arrays.

is approximately 95% at the working wavelength (435 nm). Two clamps keep the prototype sealed as in TRITIUM-Aveiro. A water inlet/outlet was
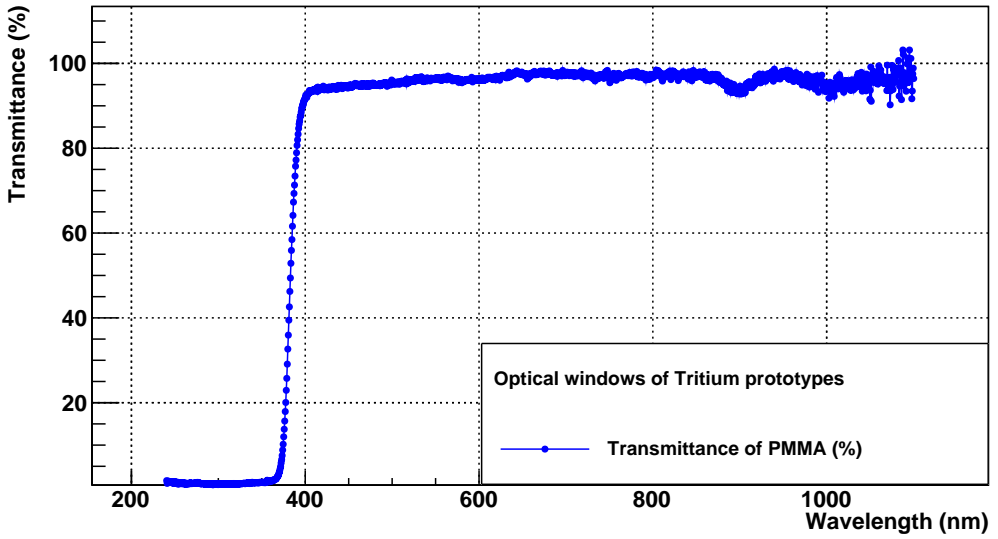
Figure 5.16 – Light transmission spectrum of a 5 mm thick PMMA plate, measured at ICMOL.

implemented in the PTFE vessel to allow a constant water flow.

Two R8520-460 Hamamatsu PMTs [Ham19] were used. Measurements with SiPM arrays controlled by PETsys were also performed. PETsys has a graphical user interface that allows remote control of the different input and output options such as SiPM arrays bias voltage, thresholds, etc., via a computer terminal. A picture of the GUI is shown in Figure 5.17.

An aluminium structure was built to accommodate up to 10 TRITIUM-IFIC-2 modules and two cosmic vetoes, shown in Figure 5.14. The available space inside the lead shield in the Arrocampo site could lodge up to 5 structures. This means that the final TRITIUM monitor could be composed of up to 50 TRITIUM-IFIC-2 modules and 5 different cosmic vetoes.
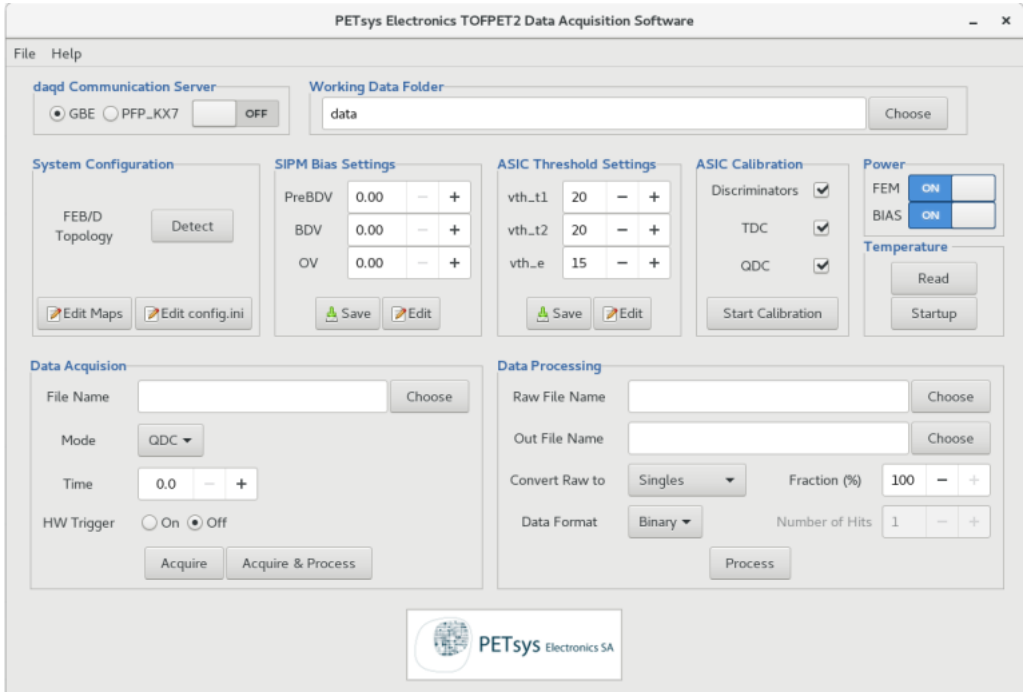
Figure 5.17 – Graphical user interface of PETsys.

Two identical TRITIUM-IFIC-2 prototypes were built. One was filled with pure water and the second with a tritium liquid source to measure the background and the signal, respectively. The water volume in both cases was 82 mL (uncertainty of 0.05%). The activity of the tritium source employed was 10 kBq/L (uncertainty of 2.24%). The signal and background energy spectra are shown in Figure 5.18. The energy spectrum of tritium was obtained by subtracting the background from the signal spectrum. The rates obtained from these three spectra are given in Table 5.3.

The tritium detection efficiency obtained for this prototype is

$$\eta = (7.11 \pm 0.28) \cdot 10^{-1} \text{ L kBq}^{-1}\text{s}^{-1}$$

This efficiency is larger than those reported in the literature (Table 2.2). This is an expected result since the active area of this prototype is the
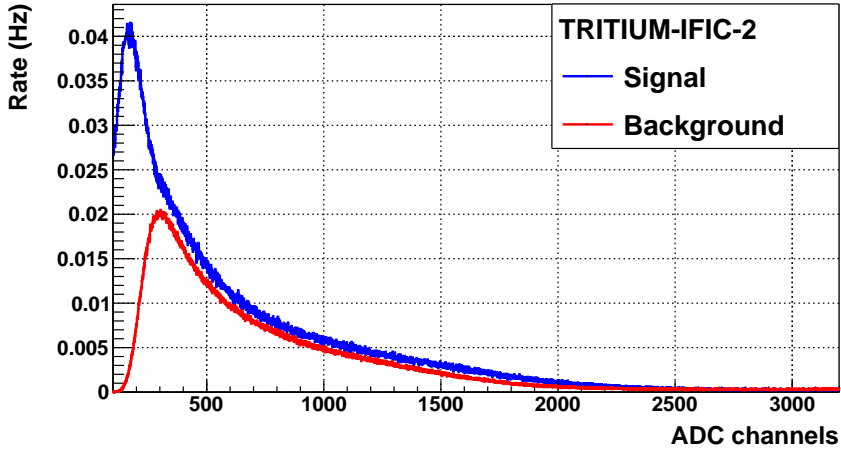
(a)
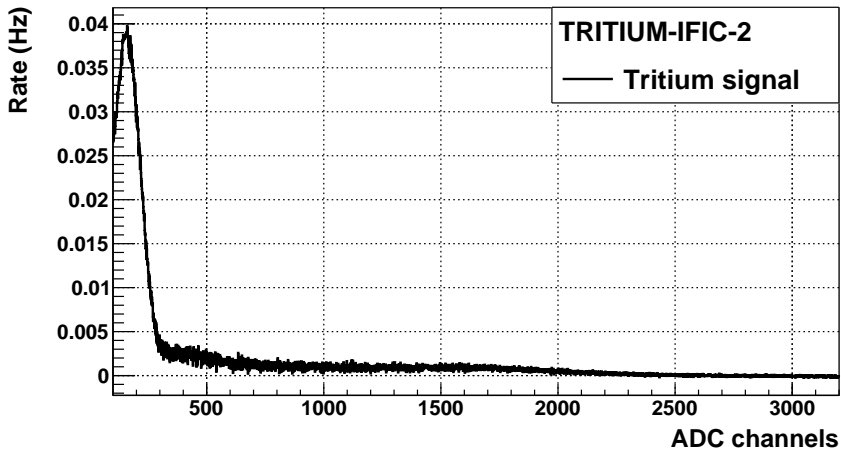
(b)

Figure 5.18 – Energy spectra measured with TRITIUM-IFIC-2. a) Signal and background energy spectra. b) Tritium energy spectrum.

Spectrum	Rate (Hz)
Signal	19.05 ± 0.18
Background	11.54 ± 0.14
Tritium	7.11 ± 0.23

Table 5.3: Counting rates measured by TRITIUM-IFIC-2.

largest. The specific efficiency is

$$S = (14.1 \pm 0.6) \cdot 10^{-5} \text{ L kBq}^{-1}\text{s}^{-1}\text{cm}^{-2}$$

which is the largest reported for tritium detection.

A detector calibration in units of photons detected per event can be obtained from the single-photon distribution of the PMTs, shown in Figure 5.19. Fitting the single-photon distribution to a Gaussian function, the mean and uncertainty obtained are around 172 and 66 ADC channels, respectively, for one PMT and 173 and 57 ADC channels, respectively, for the other. The tritium rate given in the number of photons detected per event is obtained as the ratio of the tritium energy spectrum and the single-photon distribution mean. A maximum of 15 photons per tritium event is measured, which is in agreement with the results of the simulations described in Chapter 6.

Monitoring of the signal and background prototypes was carried out for several months. The rates measured are shown in Figure 5.20. No quenching of the signal with time was observed, which indicates the detector efficiency remained stable for about 6 months. A relative standard deviation of 2.5% of the measured tritium rate was obtained.

To calculate the MDA, the background was binned in 10 min and 60 min intervals. The mean values and standard deviation of these measurements are shown in Table 5.4. The N_D and the L_C obtained from the
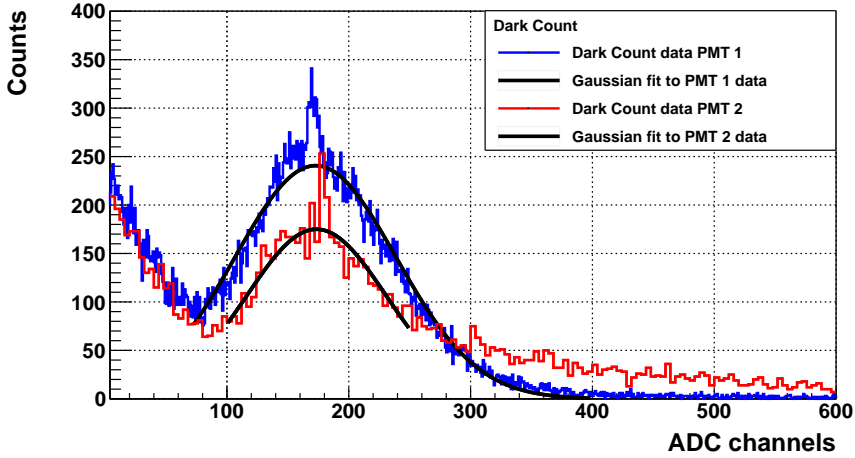
(a)
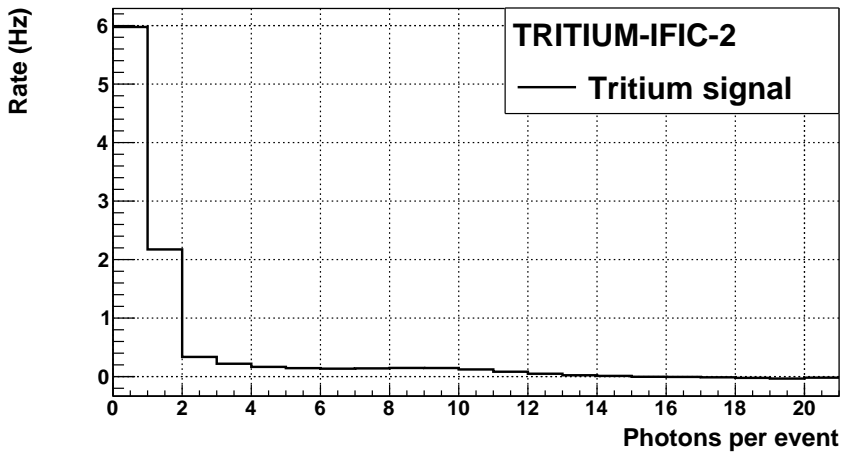
(b)

Figure 5.19 – a) Single photon distribution of TRITIUM-IFIC-2 PMTs. b) Tritium energy spectrum measured with TRITIUM-IFIC-2 versus the number of photons detected per event.
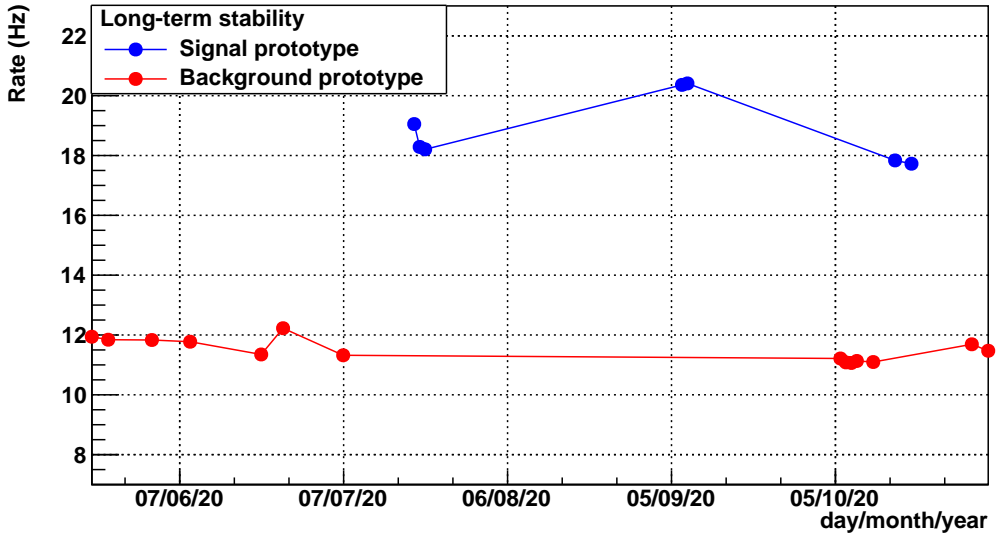
Figure 5.20 – Signal and background rates of TRITIUM-IFIC-2 along several months.

Currie criterium (Equation 5.1) are given in Table 5.4. The N'_D referred to

Time (min.)	N_b	σ_{N_b}	L_C	N_D
10	5635	82	191	384
60	33969	158	368	737

Table 5.4: Mean value N_b and standard deviation σ_{N_b} of fourteen background measurements. N_D and L_C obtained from the Currie criterium.

the detector signal before background subtraction are 6019 and 34706 for an integration time of 10 min and 60 min, respectively. The MDA of tritium is obtained from N'_D by associating the mean value of the background to a null tritium activity and the mean value of the signal to a tritium activity of 10 kBq/L, assuming that the counting rate scales linearly with activity. This results in an MDA of 677 Bq/L and 218 Bq/L for an integration time of 10 min and 60 min, respectively. In addition, it has to be taken into ac-

count that one of the most important properties of the TRITIUM detector is scalability, which means that results can be improved by increasing the number of modules. The MDA of the TRITIUM monitor is expected to be reduced by the square root of the number of modules, according to equation 5.1. The plot of the MDA versus the number of modules is shown in Figure 5.21, where it can be seen that the goal of the TRITIUM project of measuring 100 Bq/L in quasi-real-time is achieved with 45 TRITIUM-IFIC-2 modules read out in parallel with an integration time of 10 min or 5 TRITIUM-IFIC-2 modules with an integration time of 1 h, which is the cheaper and more realistic option.
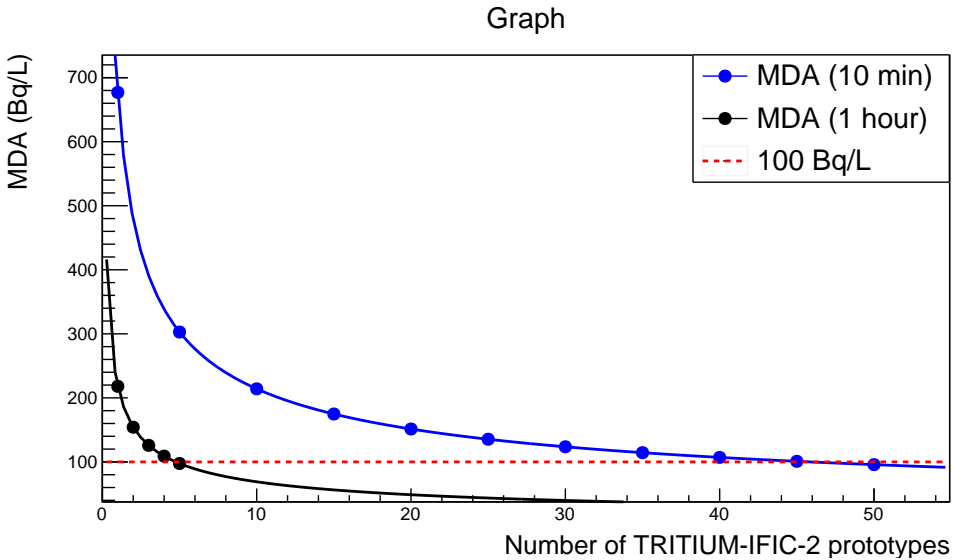
Figure 5.21 – MDA as a function of the number of TRITIUM-IFIC-2 modules read out in parallel for an integration time of 10 min (blue line) and 1 h (black line). The dotted red line corresponds to 100 Bq/L.

5.3 Results from Measurements at Arrocampo Dam

The measurements obtained with the TRITIUM-Aveiro prototype in the Arrocampo dam are reported in this section. This prototype recorded data for more than four months (27/03/2019 to 18/08/2019). The data acquired during this time are plotted in Figure 5.22, for bins of 60 minutes. The data look stable during the measuring period. An average rate of 9.3 s^{-1} was obtained. A narrow peak is observed on May 2 caused by the removal of part of the lead shield top for an intervention in the prototype. The data are magnified in the inset of the figure. The MDA measured in the Arrocampo dam for a 60 min integration time is 6 times larger than in the laboratory measurements (section 5.2.1). This may be due to the electric noise introduced by the pumps of the water purification system and the instability observed in the electronic boards.

5.4 Modular TRITIUM Detector

The proposal for the final TRITIUM monitor, which consists of several TRITIUM modules read out in parallel, is presented in this section. A schematic design is shown in Figure 5.23. The design of the modules will be made according to the results obtained from the prototypes. This monitor is shielded from the environmental radioactivity by three different techniques:

1. An external lead shield that stops the environmental radioactivity and soft cosmic rays (particles with energies below 200 MeV).

2. Active vetoes are placed below and above the TRITIUM detector and are read out in anticoincidence to mitigate high energy background, mainly cosmic ray particles of energies above 200 MeV.

3. A water purification system which eliminates radioactive elements present in the water samples measured by the TRITIUM monitor.

The water purification system, the lead shield and a TRITIUM-Aveiro prototype are currently in operation at the Arrocampo site. Furthermore, two additional TRITIUM-Aveiro prototypes and four active vetoes currently under construction will be installed in parallel with this prototype. The electronics of the TRITIUM-Aveiro prototype are based on a RaspberryPi and cannot read more than one module due to hardware limitation. An FPGA-based counter board will replace these electronics.

Three TRITIUM-IFIC-2 prototypes and two active vetoes are already built and will be installed at Arrocampo as soon as possible. At present, lateral cosmic vetoes for the TRITIUM-IFIC-2 modules are not foreseen since the influence of side cosmic rays is expected to be small ($\propto \cos^2(\theta)$), but they can be included in the future if necessary.

One of the most important aspects of the TRITIUM monitor is its modular design, which allows scalability to reach the required sensitivity of 100 Bq/L. The only scalability restriction is the available space which is set by the lead shield and the cabin in which the setup is installed. In the currently available space, five different structures as the one shown in Figure 5.24 can be placed, each containing 10 modules and two active vetoes. If 50 TRITIUM modules are installed, the sensitivity of the TRITIUM monitor could be improved by a factor of around $\sqrt{50}$ with respect to the sensitivity of a single module.
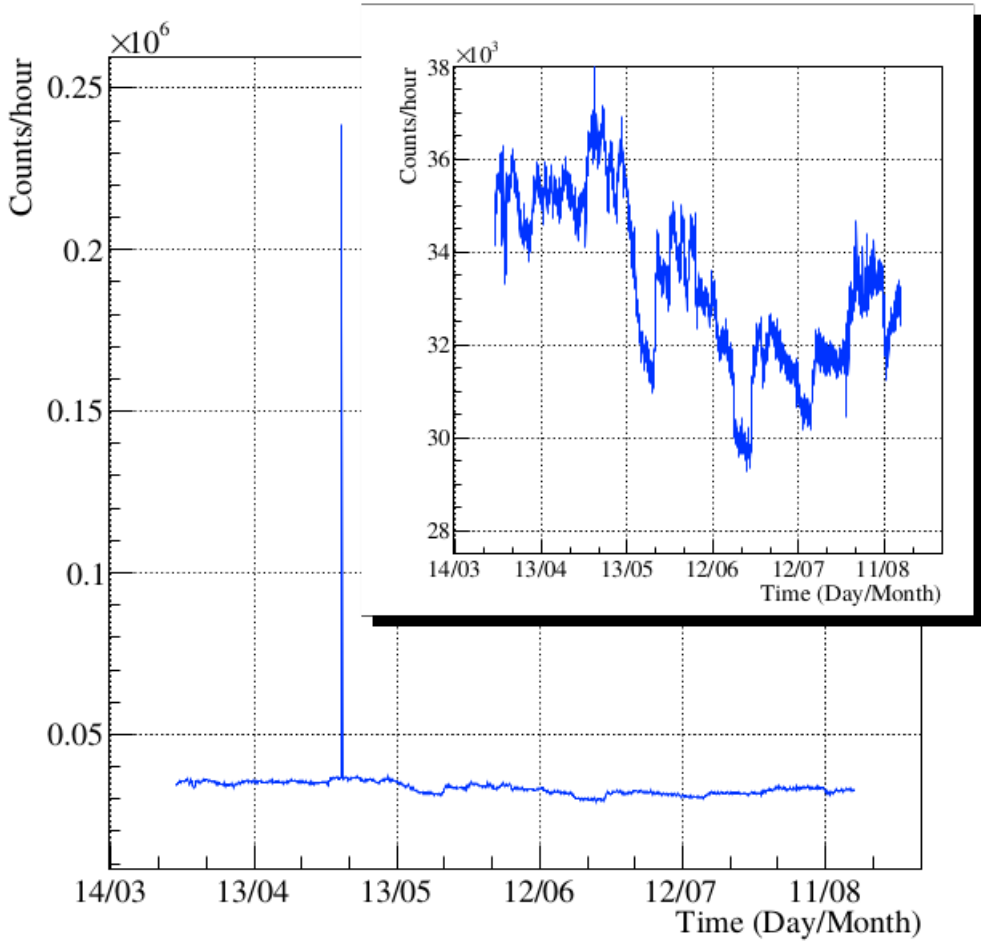
Figure 5.22 – Background measured with TRITIUM-Aveiro in the Arrocampo site [Aze22].
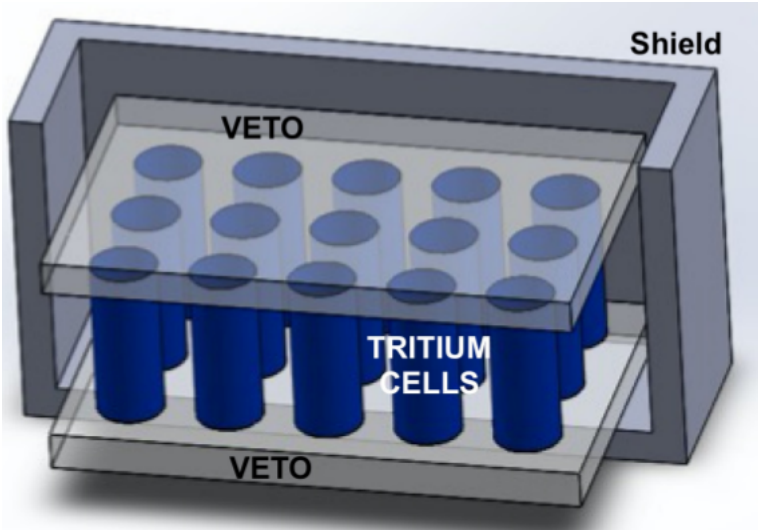
Figure 5.23 – A schematic design of the TRITIUM detector.
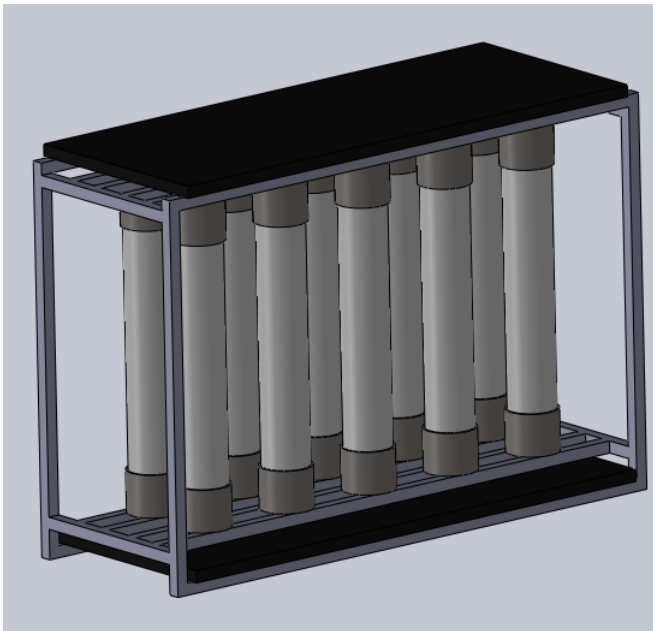
Figure 5.24 – A TRITIUM monitor design based on TRITIUM-IFIC-2.

Chapter 6

Simulations

The Monte Carlo simulations performed in the TRITIUM project are described in this chapter. They were carried out to optimize the design of the TRITIUM detector, understand its behaviour and investigate its limitations. This chapter is divided into two different sections. The first section contains the results of simulations done to improve the design of the TRITIUM detector, while the second section describes the simulation results of a full TRITIUM monitor composed of several TRITIUM-IFIC-2 modules read out in anticoincidence mode with an active cosmic veto. Furthermore, several tests were carried out to check the different steps such as the simulated tritium source, the energy deposition and the production of photons in the fibres. The simulation environment employed is Geant4 [GEA, Ago03].

6.1   Geant4 Environment

Geant4 is a software toolkit for the simulation of the passage of particles through matter developed at CERN, based on object-oriented technology implemented in the C ++ programming language. Geant4 allows the defin-

ition of the different aspects of the simulation process such as detector geometry, materials, particles, physical processes of particle and matter interactions, the response of sensitive detectors, generation, storage and analysis of event data and visualization.

Geant4 simulates particle-by-particle physics. This means that the tritium events are generated one by one, generating energy, momentum, position, etc. The propagation of each tritium decay electron and its interaction with the scintillator is simulated, and optical photons are created. The propagation of these optical photons is also simulated one by one and the simulation ends when all the created optical photons have been absorbed by either the sensitive detector or other materials present in the simulation. The physics list used for these simulations is G4EmLivermorePhysics, which is specially designed to work with low-energy particles. This list includes the most important electromagnetic processes at low energies such as bremsstrahlung, Coulomb scattering, atomic radiation and other related effects. The materials included in these simulations were water (the tritiated water source), PMMA (the optical windows of the prototype), polystyrene (the scintillating fibres), PTFE (the prototype vessel), silicone (the optical grease), silicate glass (windows of the PMTs) and bialkali (the photocathode material of the PMT). The properties of water, PTFE and polystyrene were taken from the Geant4 NIST database and the other materials were built by specifying their atomic composition. The following optical properties not included in the database were added:

1. The refraction index, the light attenuation coefficient obtained from ref. [Bui94] and the tritium decay electron spectrum uniformly distributed in the volume obtained from ref. [Mer15] for water.

2. The spectra of refractive index, light attenuation, photon emission, scintillation yield and decay time coefficient obtained from the data sheet [Sai21b] for polystyrene.

152

3. The quantum efficiency spectrum for the photocathode material of the PMTs [Ham19]. A refraction index of 1.46 for optical grease [Saib].

4. The optical data for PMMA windows, PTFE and silicate glass from ref. [Arg11].

6.2 Simulations for the design of the TRITIUM Detector

Several simulations were performed during the design of the TRITIUM detector to optimize the diameter and the length of the scintillating fibres to optimize tritium detection. As the tritium electrons have a very short mean free path, the shape of the simulated tritium source was optimized to reduce computing time.

6.2.1 The Tritiated Water Source

The mean free path of tritium electrons in water is only around 5 μm, so most electrons emitted in tritiated water do not reach the scintillating fibres. These electrons do not provide useful information and only consume computing resources. To optimize the simulation, the dimensions of the simulated tritium source were set to maximize the number of tritium events reaching the scintillating fibres. The distribution of the initial energy of tritium electrons capable of penetrating a fibre and depositing energy, shown in Figure 6.1b, is shifted to high energies and has a peak centred at 10 keV.

A 20 cm long and 2 mm diameter scintillating fibre surrounded by a tritiated water source of the same length and 0.5 mm thickness (100 times greater than the mean free path of tritium electrons) was simulated. Only the energy deposition of tritium electrons in the fibre was registered,
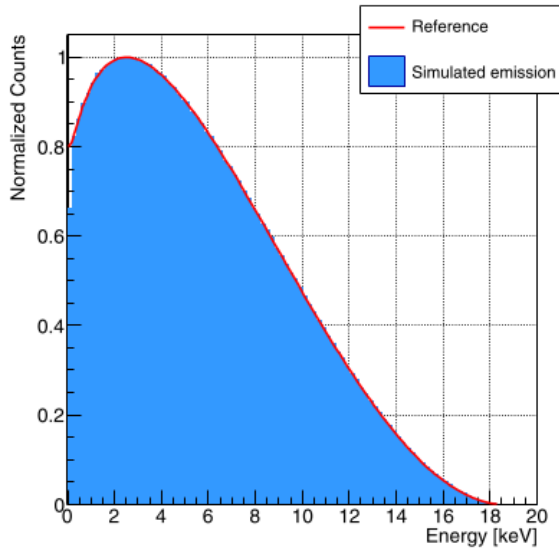
(a)
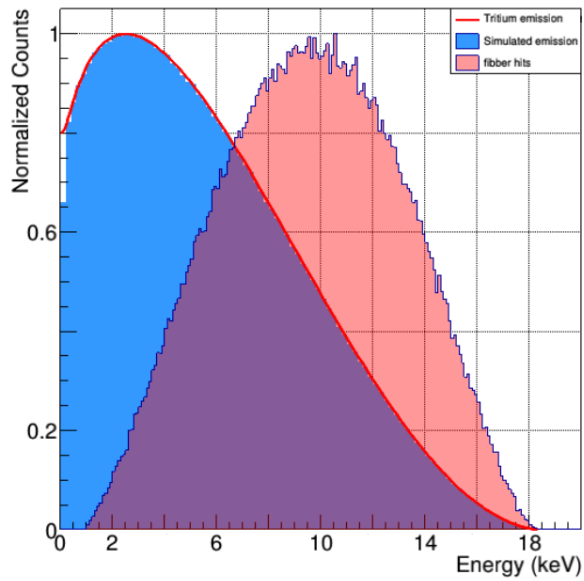
(b)

Figure 6.1 – Energy distribution of a) simulated tritium decays b) Initial energy of tritium decays that reach the scintillating fibres (red histogram) compared to all simulated tritium events (blue histogram) [Aze20a].

excluding optical processes. The goal of these simulations was to find the radial thickness of the simulated tritium source beyond which no significant number of tritium decay electrons are detected. In Figure 6.2a, a transversal cut of the 2 mm scintillating fibre, the 0.5 mm thick tritium source surrounding the fibre and the positions where happen the tritium decays that deposit energy in the scintillating fibre are shown. Furthermore, the distribution of the radial distance between the position where tritium decays take place and the surface of the scintillating fibre is shown in figure 6.2b. The thickness of the simulated tritium source was 5 μm since 99.4% of the events that deposit energy in the fibres are produced at a shorter distance. These results are independent of the fibre diameter.

6.2.2   Energy Deposition and Light Output in Scintillating Fibres

The scintillation yield provided by the manufacturer, 8000 photons/MeV, is only valid for MIPs. As tritium electron energies are not MIP particles, the output light generated by the scintillating fibres was studied. The emission of scintillation photons was also simulated.

When particles that are not MIP are detected in plastic scintillators, an output light quenching effect happens, which can be parametrized by the Birk's coefficient[Bir51],

$$\frac{dL}{dx} = S\frac{\dfrac{dE}{dx}}{1 + k_B\dfrac{dE}{dx}} \tag{6.1}$$

Where $\dfrac{dL}{dx}$ is the output light per unit of path length, $\dfrac{dE}{dx}$ is the energy deposited per unit of path length and S is the scintillation yield for MIPs, provided by the manufacturer. A Birk's coefficient $k_B = 0.126$ mm/MeV is
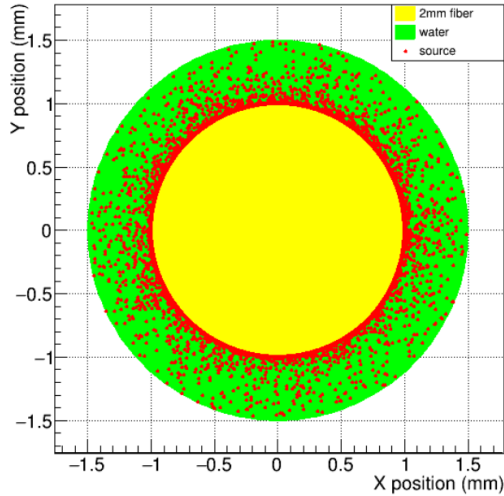
(a)
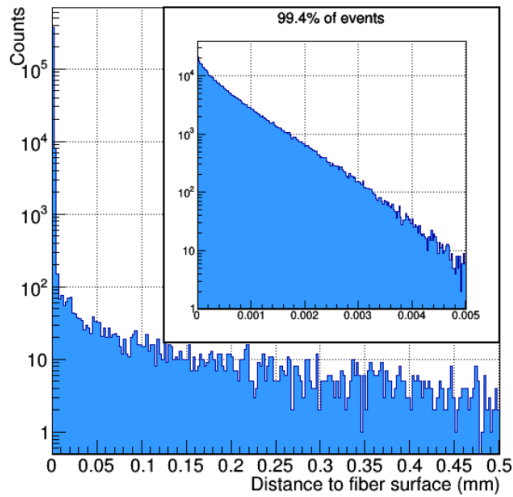
(b)

Figure 6.2 – a) Cross-section of a simulated scintillating fibre (yellow) and the tritium source (green) with various tritium decays (red dots) b) Distribution of the radial distance between the position where the tritium decays take place and the surface of the scintillating fibre [Aze20a]. A zoom of low-energy events is shown in the inset.

156

typically used for scintillators based on polystyrene [Lev11]. In this section, the importance of quenching for tritium detection is discussed.

A study of the energy deposition of tritium electrons on scintillating fibres was carried out. In Figure 6.3, the initial energy of simulated tritium electrons that reach the scintillating fibres is compared to the energy deposited in them. A shift to lower energies caused by the energy loss of tritium electrons in water is observed. The cut at about 1 keV is produced by the default energy threshold of 990 eV in the G4EmLivermorePhysics list. Figure 6.4 shows two distributions of the number of photons produced
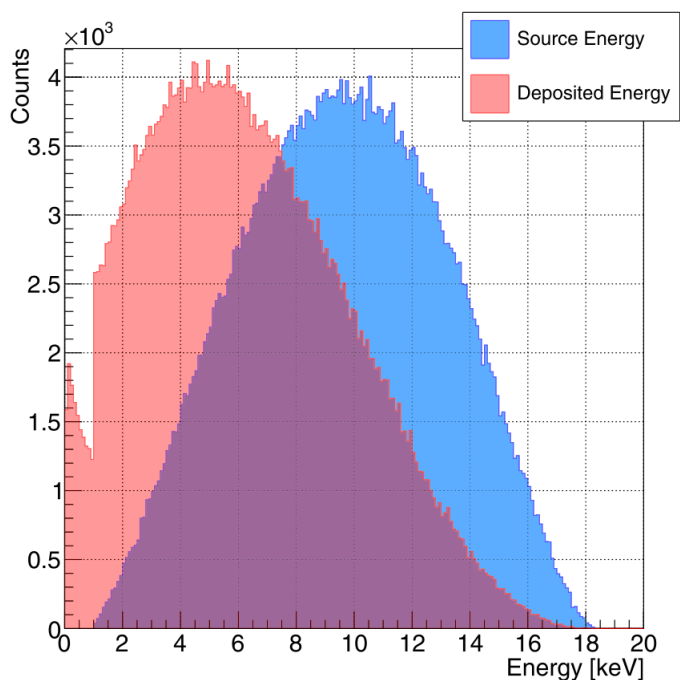
Figure 6.3 – Distribution of the initial energy of tritium events that reach the scintillating fibres (blue histogram) and the energy deposited in them (red histogram) [Aze20a].

in scintillating fibres by tritium events, one in which the quenching effect is not considered ($k_B = 0$) and the other with the Birk's coefficient set to

$k_B = 0.126$ mm/MeV. A distribution with a peak close to 40 photons per
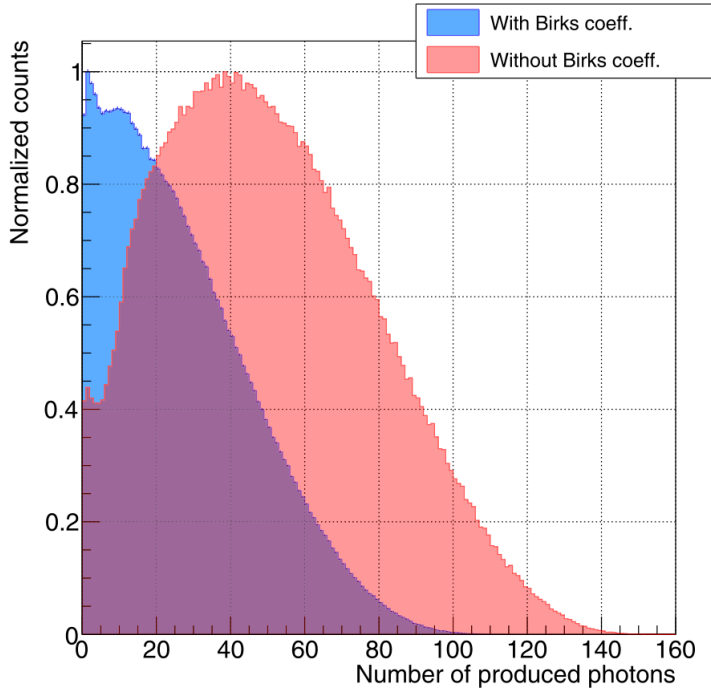
Figure 6.4 – Energy distributions of photons produced in a scintillating fibre without Birk's coefficient (red histogram) and with Birk's coefficient $k_B = 0.126$ mm/MeV (blue histogram)[Aze20a].

tritium event and a maximum of about 150 photons were obtained when the quenching effect is not considered. A significant reduction of the output light is observed when Birk's coefficient is included, obtaining a distribution peaked at around 10 photons and a maximum of 110 photons. The quenching effect is also observed in Figure 6.5, in which the number of photons produced as a function of the energy deposited in the fibres is displayed in a two-dimensional plot. In this figure, in addition to a reduction in the number of photons produced per unit of energy deposited, a broader distribution is obtained when Birk's coefficient is considered, indicating an increase in the fluctuations of the energy deposited.
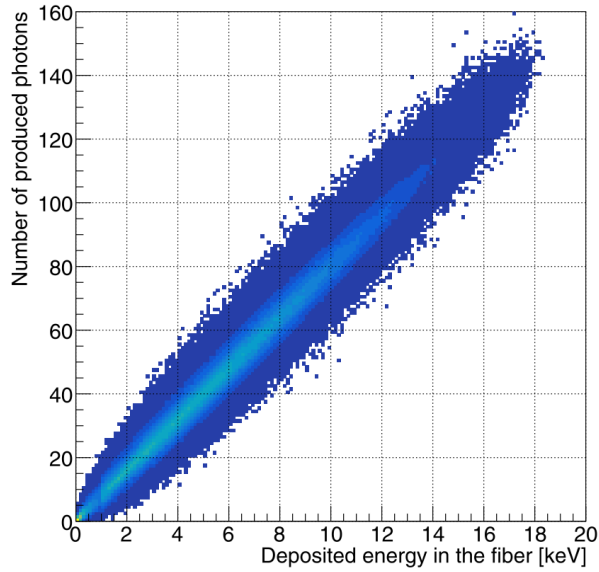
(a)
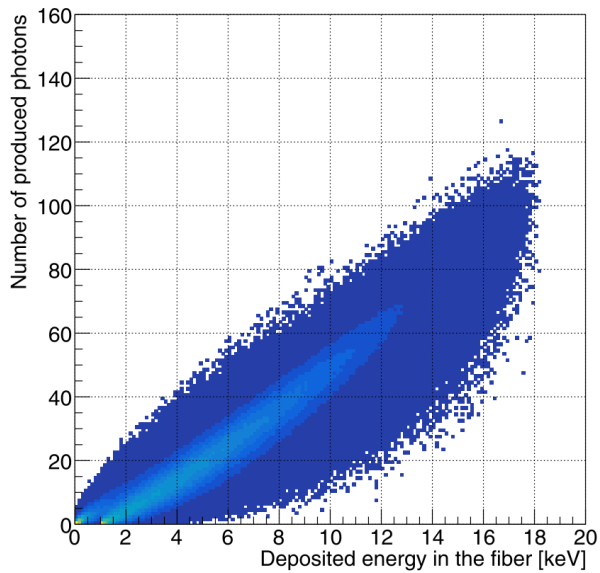
(b)

Figure 6.5 – Number of photons produced versus the energy deposited in the scintillating fibres when a) $k_B = 0$ b) $k_B = 0.126$ mm/MeV [Aze20a].

6.2.3 Optimization of the Fibre Length

A study to find the optimal fibre length was carried out. Two different lengths of scintillating fibres, 1 m and 20 cm, and two different tritium source activities, 0.5 kBq/L and 2.5 kBq/L, were considered. Five detectors were simulated for the case of 20 cm long fibres to have the same active area as one detector of 1 m long fibres. The advantage of using long fibres is their large active area for the same number of photosensors which would reduce the price of the TRITIUM monitor. However, short scintillating fibres reduce photon absorption, which increases the tritium detection efficiency per unit of active area. The Tritium-Aveiro prototype, consisting of 360 scintillating fibres of 2 mm diameter, was simulated. The number of photons produced in a scintillating fibre per tritium electron for all the electrons that reach the scintillating fibres and for only those that generate photons detected in coincidence by the photosensors is plotted in Figure 6.6. Tritium events that produce a large number of photons are almost always detected but events that produce few photons are seldom detected, resulting in a peak centred at around 25 photons. The number of counts per hour during a week as a function of time for the tritium activities and fibre lengths studied is shown in Figure 6.7. A signal 20% larger is seen for the shorter fibre length and the two activities considered, due mainly to the lower absorption and the refraction loss of photons in shorter fibres. In addition, not simulated effects like dirt and mechanical imperfections of fibre surface increase photon loss.

6.2.4 Fibre Diameter Influence on Cosmic Background

A study of the cosmic ray background as a function of the fibre diameter was carried out. Simulations of a single 20 cm length scintillating fibre of 1 mm and 2 mm were compared. The energy deposited in the scintillating fibres by cosmic rays is proportional to the active volume so, the expected cosmic ray signal is larger for 2 mm diameter fibres. The objective of this
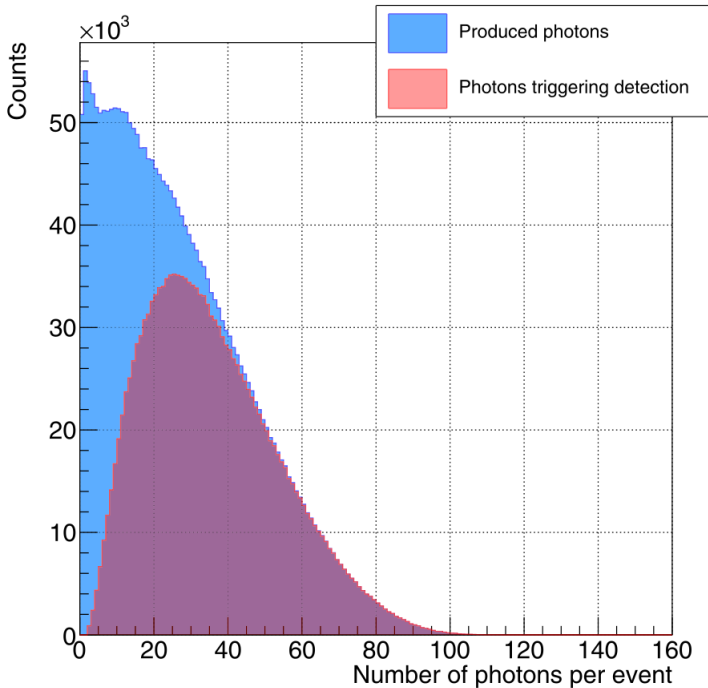
Figure 6.6 – Number of photons per tritium event produced in a fibre for all tritium electrons that reach the fibre (blue histogram) and for only tritium electrons producing photons detected in coincidence by photosensors (red histogram) [Aze20a].

study is to simulate the cosmic ray background in the tritium energy range. The tritiated water source was replaced by a cosmic ray source generated by the CRY library[1] [Com, Hag07], a package implemented in C++. This library generates cosmic-ray showers for different particles (muons, neutrons, protons, electrons, photons and pions). The cosmic source employed is a horizontal square of 1×1 m^2 located 35 cm over the detector with the typical distribution of cosmic particles at sea level. The distributions of energy deposited in the scintillating fibres of 1 mm and 2 mm diameters by cosmic rays are shown in Figure 6.8. As can be seen in the figure, a background about 50% smaller is obtained for 1 mm fibre diameter in the

---

[1]CRY library, Cosmic-Ray Shower library
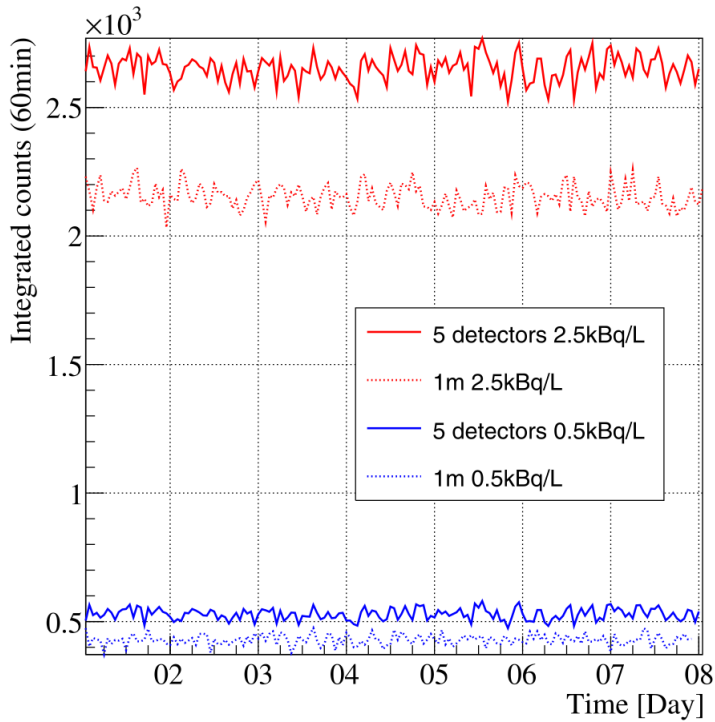
Figure 6.7 – Simulated counting statistics normalized to the active area in 1 h bins during a week for 1 m (dashed lines) and 20 cm (solid lines) and 0.5 kBq/L (blue lines) and 2.5 kBq/L (red lines) activities [Aze20a].

tritium energy range which implies a smaller detector MDA.

6.2.5 Influence of the PMMA Windows on the Tritium Signal

In the prototypes TRITIUM-IFIC-0 and TRITIUM-IFIC-1, the fibres were directly coupled to the photosensor, so only photons guided along the fibres were detected. However, in TRITIUM-Aveiro and TRITIUM-IFIC-2, two PMMA windows are used which allows the transmission to the photosensors of photons propagated through the water. To quantify the importance of
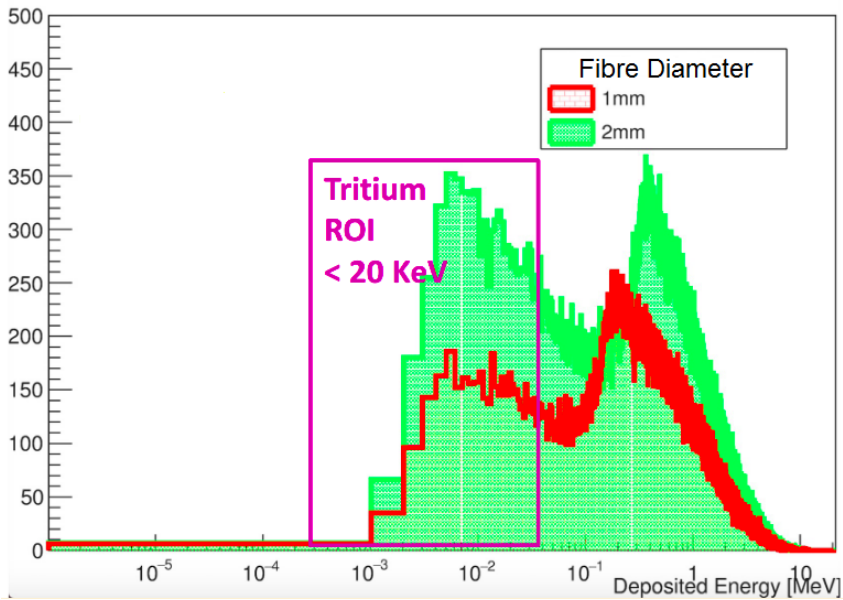
Figure 6.8 – Comparison of the energy deposition by cosmic rays in scintillating fibres of 1 mm and 2 mm diameter [Aze20a].

this contribution, the TRITIUM-Aveiro prototype was simulated. The distribution of the number of photons that reach the PMMA window per tritium event is shown in Figure 6.9. Fibre-guided photons are shown in red while those travelling in water are plotted in blue. It can be seen that the tritium signal obtained from the water-guided photons is as important as that obtained from the fibres. Therefore, PMMA windows improve tritium detection efficiency by around a factor of 2.

6.3   Simulations of the TRITIUM Monitor

The simulations of a TRITIUM monitor consisting of several TRITIUM-IFIC-2 modules in parallel and a background rejection system are described in this section.
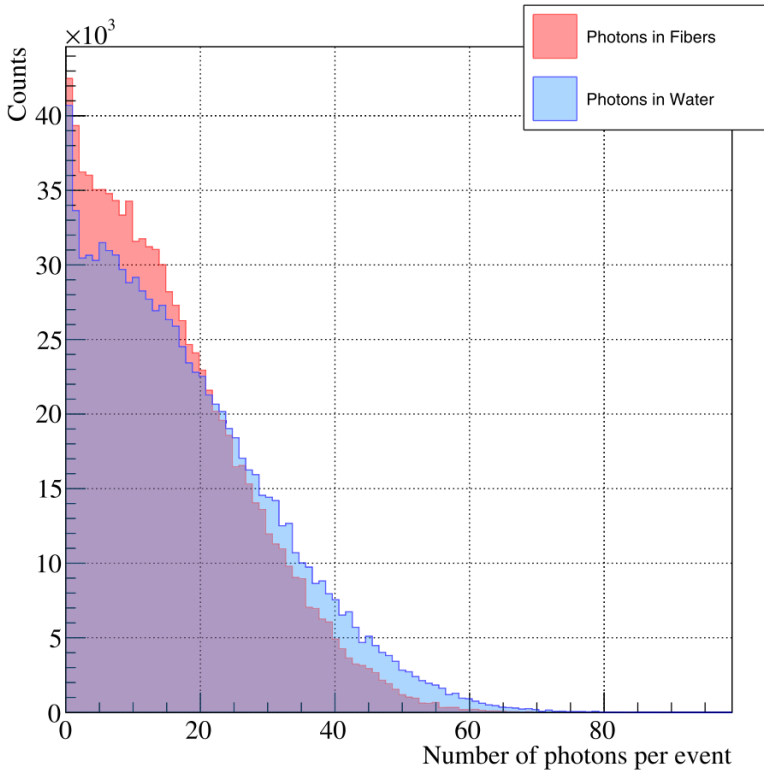
Figure 6.9 – Distribution of photons reaching the PMMA windows. The red histogram corresponds to the photons guided by fibres and the blue histogram to photons guided through water [Aze20a].

6.3.1 Simulation of the TRITIUM-IFIC-2 Prototype

A Tritium-IFIC-2 prototype of 800 fibres of 1 mm diameter uniformly distributed in sixteen different layers of increasing radius, as illustrated in Figure 6.10, was simulated. The source consisted of a 5 μm thick cylindrical ring of tritiated water around each fibre. Scintillating fibres were arranged within a cylindrical PTFE vessel. Two PMMA windows of 5 mm thickness closed the vessel. A 0.5 mm layer of optical grease on each PMMA window was included. Two R8520-460 PMTs from Hamamatsu [Ham19] were simulated. The inner part of the simulated TRITIUM-IFIC-2 geometry is shown
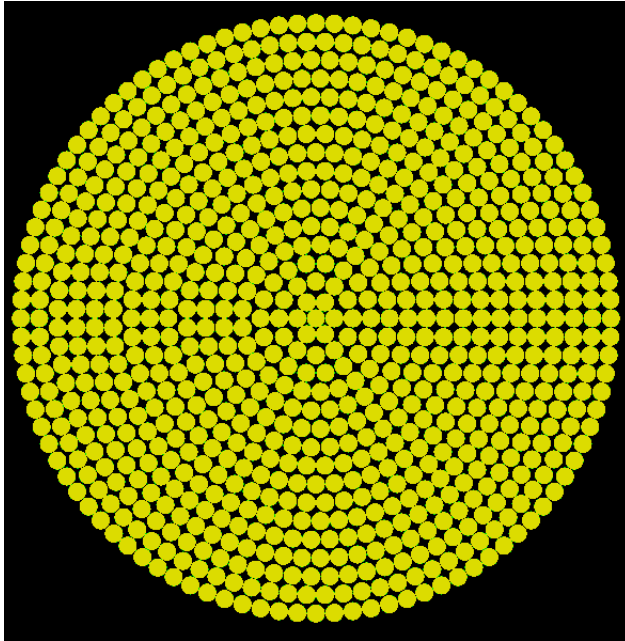
Figure 6.10 – Distribution of the scintillating fibres in the simulations of the TRITIUM-IFIC-2 prototype.

in Figure 6.11 in which the PMTs, the optical grease, the PMMA windows, the tritiated water and the scintillating fibres are shown. The PMT active area is smaller than the scintillating fibre bundle cross section. The aim of these simulations was to calculate the activity resolution of the prototype and the improvement obtained by increasing the integration time and the number of modules read out in parallel. The detection of a tritium electron in TRITIUM-IFIC-2 is shown in Figure 6.12. The paths of the photons created in scintillating fibres are represented by green lines ending in red dots when they are absorbed in the fibre or the water and blue dots when they are absorbed in the PMTs (detected). The fibre in which the tritium electron is detected is clearly seen. Some photons go out of the fibre and are not collected. Blue dots in both PMTs indicate that photons are detected in coincidence. The distribution of the number of photons detected by photosensors per tritium event is shown in Figure 6.13. A maximum of 17
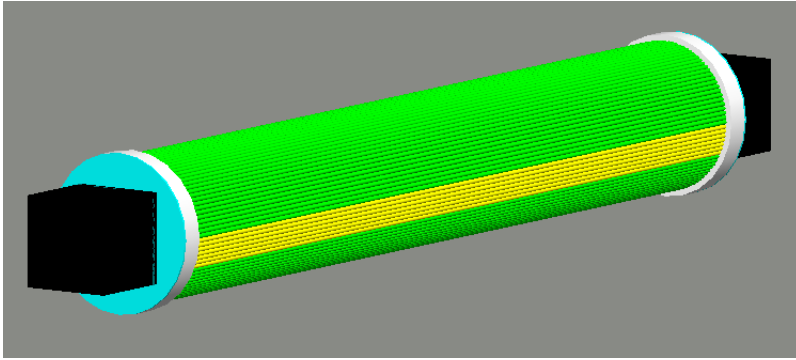
Figure 6.11 – Simulation of the inner part of the TRITIUM-IFIC-2 prototype. PMTs (black), optical grease (blue), PMMA windows (white), tritiated water (green) and scintillating fibres (yellow).

photons is obtained, which is in agreement with the distribution of photons per tritium event measured experimentally, shown in Figure 5.19. The experimental distributions are lower than the simulations mainly in the range from 3 to 8 photons per event, probably due to detector imperfections not included in the simulations.

Activities from 100 Bq/L to 5 kBq/L, for three months of data taking and an integration time of 10 min, were simulated. The simulation results are presented in Figure 6.14. A difference in activity smaller than 250 Bq/L cannot be distinguished because of the overlapping of the distributions. To reduce the width, the statistics should be increased, either by increasing the integration time or the number of prototypes read out in parallel. To check the role of the integration time, distributions for integration times of 10 min, 30 min and 60 min were generated. The effect of increasing the integration time is to reduce the distribution width and improve the activity resolution of the TRITIUM monitor, as seen in Figure 6.15. Differences as low as 250 Bq/L are clearly discriminated with only one TRITIUM-IFIC-2 module and an integration time of 60 min which could still be considered a quasi-real-time measurement. Similarly, these distributions are shown in Figure 6.16 for 10 min integration time and 1, 5 and 10
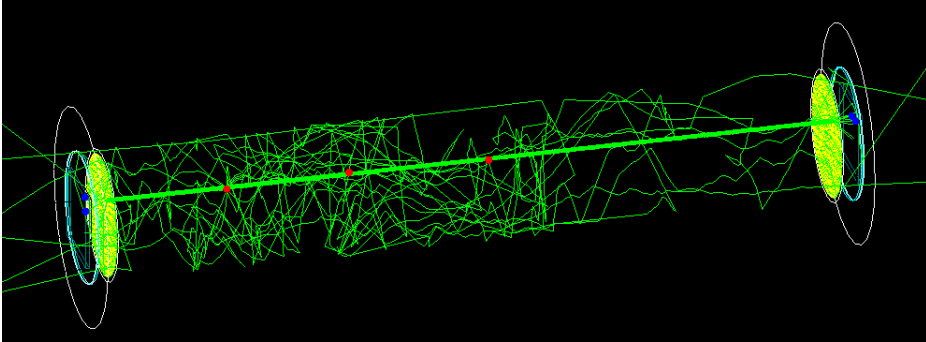
Figure 6.12 – Tritium electron detected in the simulated TRITIUM-IFIC-2 prototype. The path of the optical photons is represented by green lines and the position in which they are absorbed is represented by red and blue dots for absorption in water or PMT, respectively.
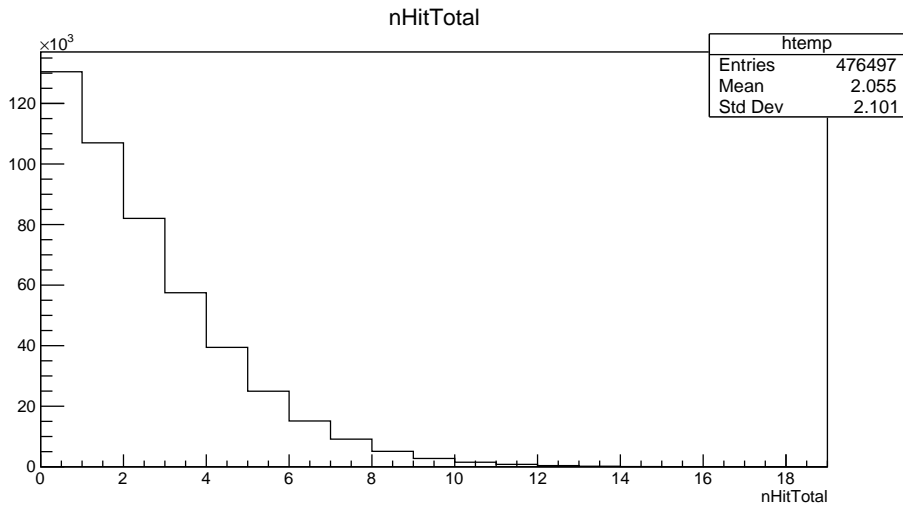
Figure 6.13 – Photons detected by both PMTs per tritium event in the simulated TRITIUM-IFIC-2 prototype.

modules read out in parallel. A reduction of the distribution width with the increasing number of modules which improves the activity resolution of the detector is visible in this figure. Differences of 250 Bq/L are clearly resolved with an integration time of 10 min and 5 TRITIUM-IFIC-2 modules. The resolution, defined as

$$\text{Resolution}(\%) = \frac{\text{FWHM}}{\text{centroid}} \cdot 100 \tag{6.2}$$

is plotted as a function of the source activity for several integration times and numbers of modules in Figure 6.17. It can be observed that the resolution improves with integration time and the number of modules. The studied cases are summarized in Table 6.1. The decision adopted by the TRITIUM collaboration is to install 5 TRITIUM-IFIC-2 modules with an integration time of 1 h that provide an MDA of 100 Bq/L, as seen in Figure 5.21. With this configuration, differences of 100 Bq/L are expected to be resolved according to Table 6.1.

# of modules	10 min	30 min	60 min
1	< 1000 Bq/L	500 Bq/L	200 Bq/L
5	200 Bq/L	150 Bq/L	100 Bq/L
10	150 Bq/L	100 Bq/L	$\approx$ 50 Bq/L

Table 6.1: Tritium activity difference that can be visually resolved for different integration times and different numbers of TRITIUM-IFIC-2 modules.

6.3.2 Simulation of the Lead Shield and Cosmic Veto

The lead shield and the active vetoes were included in the simulation of TRITIUM-IFIC-2 to quantify the reduction of cosmic background detected. A flat cosmic ray source of 1×1 m^2 placed at a height of 70 cm was simulated with the cosmic ray generator of the CRY library. Two R8520-460 PMTs from Hamamatsu were simulated to read each plastic scintillator
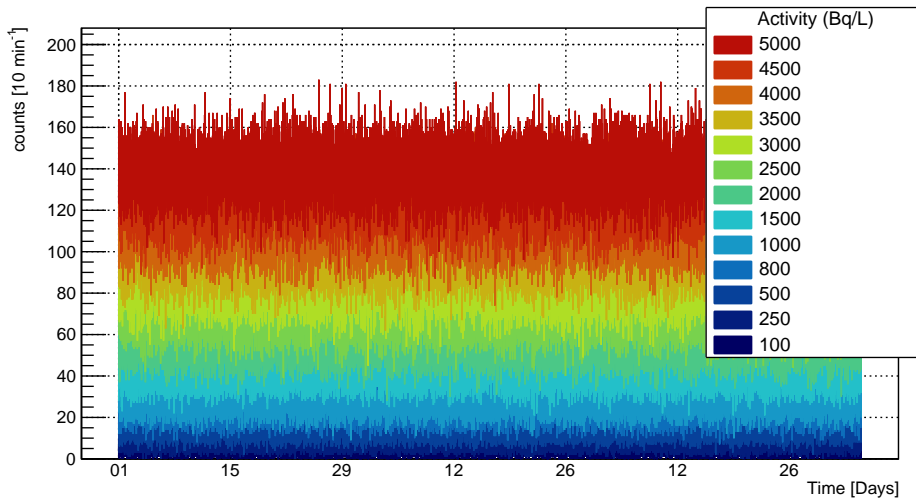
(a)
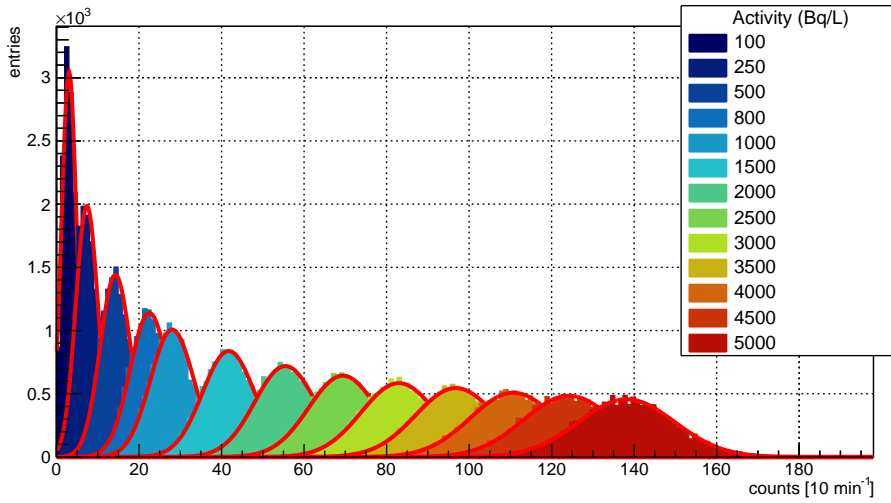
(b)

Figure 6.14 – a) TRITIUM-IFIC-2 simulated statistics with an integration time of 10 min during three months (13248 bins for each activity). b) Distribution of counting statistics versus activity.
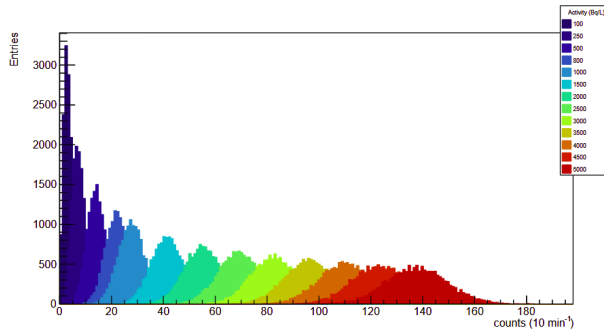
(a)
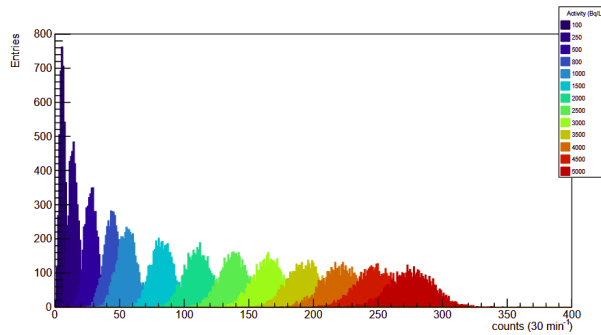
(b)
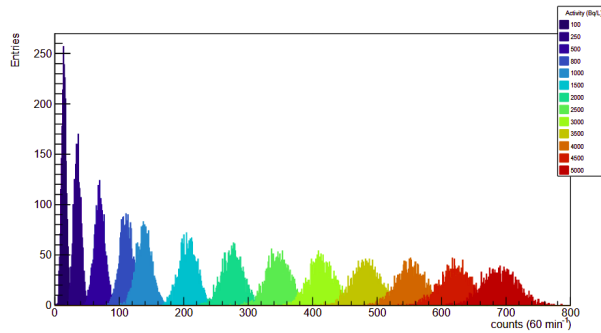
(c)

Figure 6.15 – Simulated counting distributions obtained with a TRITIUM-IFIC-2 prototype for three months and for each of the tritium activities in the insets and three different integration times: a)10 min, b) 30 min and c) 60 min.
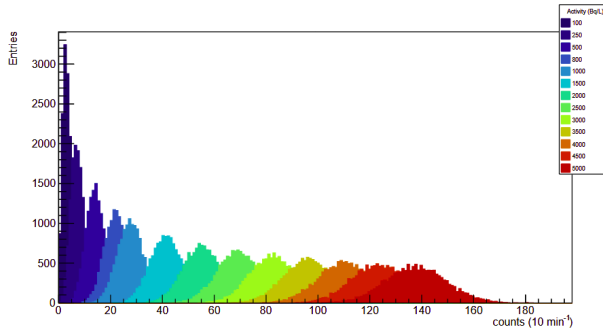
(a)
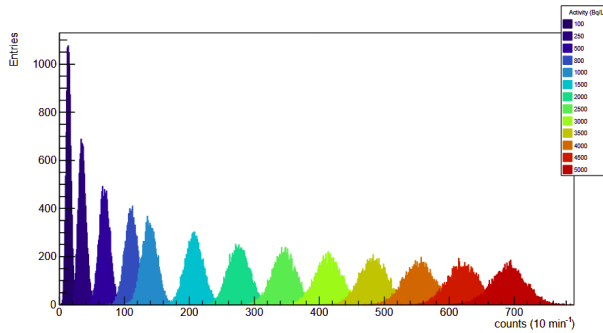
(b)
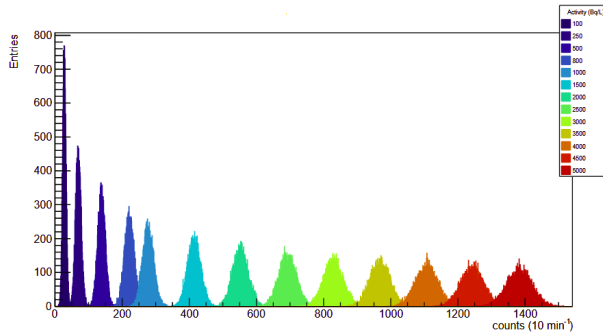
(c)

Figure 6.16 – Simulated counting distributions for three months and an integration time of 10 min for each of the tritium activities in the insets and different numbers of TRITIUM-IFIC-2 modules: a) 1 module, b) 5 modules and c) 10 modules.

171
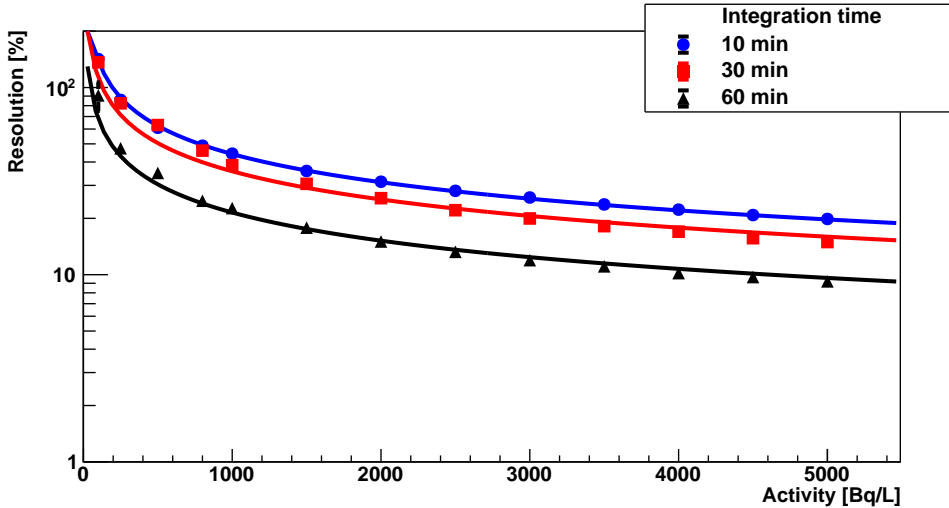
(a)
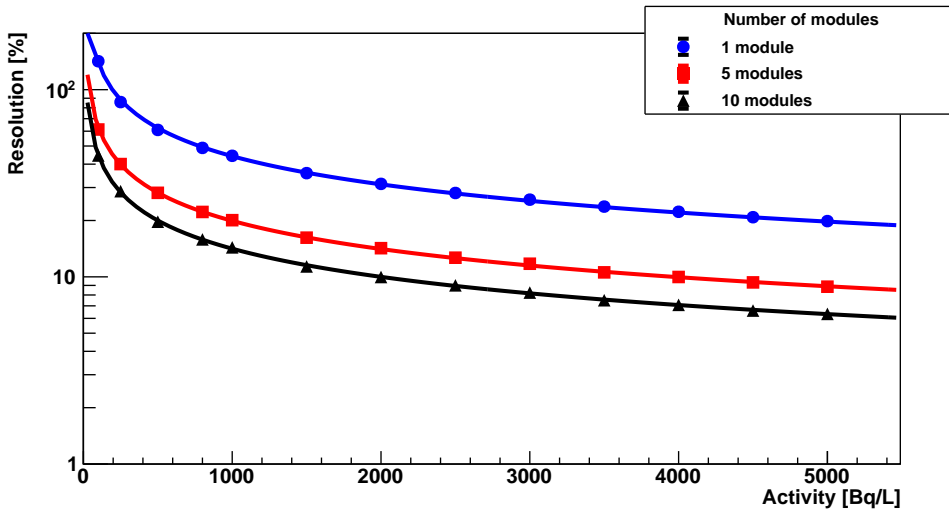
(b)

Figure 6.17 – a) Resolution of TRITIUM-IFIC-2 versus tritium activity for different integration times using one TRITIUM-IFIC-2 module. b) Resolution of TRITIUM-IFIC-2 versus tritium activity for different numbers of modules and 10 min integration time.

out, as described in section 3.4. The lead shield was simulated with the lead properties taken from the Geant4 NIST database. The dimensions of the simulated lead shield were $60 \times 60 \times 70$ cm^3, suitable for one TRITIUM-IFIC-2 prototype and an active cosmic veto. These dimensions were set smaller than the real dimension of the lead shield at Arrocampo to save computing time and resources. Energy, position and momentum distribution were produced. Simulations with three different shielding configurations were carried out with the aim of quantifying the background rejection due to the passive shield and the active veto. The first configuration consisted of one TRITIUM-IFIC-2 prototype and the cosmic ray source. In the second configuration, a lead shield was added and in the third one, the cosmic veto was also included. The cosmic events detected by TRITIUM-IFIC-2 are shown in Figure 6.18, for the three configurations. Cosmic rays detected by TRITIUM-IFIC-2 are reduced by a factor around 5.5 when a lead shield 5 cm thick is included (this is the width of the shield currently installed at Arrocampo). This reduction is caused by the suppression of the soft cosmic radiation (energy lower than 200 MeV). The natural background of the installation site, which would be also mitigated by the lead shield, was not included in this simulation. Therefore, the expected background reduction due to the passive veto would be even better. Around 60% of the cosmic rays that penetrate the lead shield and reach TRITIUM-IFIC-2 are mostly hard cosmic rays which are detected by the cosmic veto and suppressed from the background. In summary, cosmic rays that would be detected and misidentified as tritium electrons by TRITIUM-IFIC-2 are reduced by 92.6% by the background rejection system. Since the natural background of the site was not included in the simulations, the actual background reduction is expected to be even larger. The simulated veto efficiency was found smaller than the experimentally measured (85%), probably because the wrapping of the scintillating plastics was not included in the simulation. Therefore, the total background rejection is expected to be larger than the simulated.
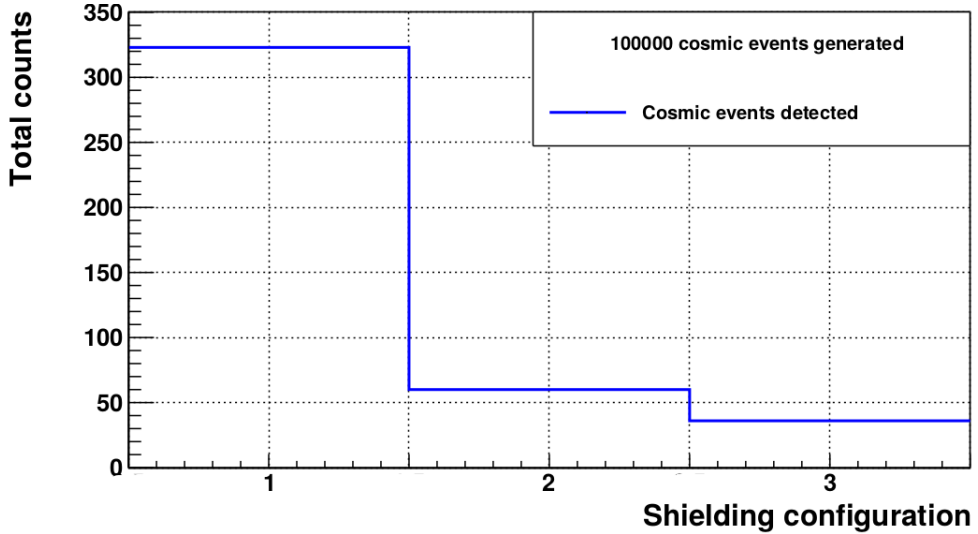
Figure 6.18 – Cosmic ray events detected and misidentified as tritium events by TRITIUM-IFIC-2 from 10^5 generated cosmic rays for the three different shielding configurations. Bin 1 corresponds to the absence of the background rejection system. Bin 2 corresponds to the passive shield and bin 3 corresponds to both the lead shield and cosmic veto.

Chapter 7

Present Status and Summary of the Results of the TRITIUM Project

In this chapter, the most important results and prospects of the TRITIUM project are summarized and discussed.

Tritium, a radioactive isotope of hydrogen, is one of the most abundantly produced radioisotopes in nuclear facilities such as nuclear power plants and research facilities. Due to its radiotoxicity, an excessive amount of tritium released into the environment could directly (drinking tritiated water) or indirectly (irrigation with tritiated water) affect human health and the environment. The legal limit of tritium activity in drinking water in Europe is 100 Bq/L, established by the EURATOM Council Directive [Eur13]. This is the most restrictive limit in the world.

The TRITIUM project was funded to investigate the feasibility of a monitor for measuring low tritium activities in water in quasi-real-time. The goal of this project is to design, build, install and commission a tritium

in water monitor that measures tritium activities as low as 100 Bq/L in 1 hour or less. The TRITIUM monitor consists of three different parts:

1. The TRITIUM detector, which is composed of modules of hundreds of uncladded scintillating fibres read out in parallel. Various configurations of the TRITIUM module were tested such as different diameters of the scintillating fibres (1 mm or 2 mm) and types of photosensors (PMTs or SiPM arrays).

2. The background rejection system, which suppresses the radioactive background that affects the tritium activity measurements. This is based on a lead passive shield that reduces the soft component of cosmic rays (energies below 200 MeV) and the environmental radioactive background, and an active veto that reduces the hard component of cosmic rays (energies above 200 MeV).

3. The water purification system, which removes particles and minerals present in the water samples measured by the TRITIUM detector.

The results obtained by the TRITIUM collaboration are the following:

1. For the detector development, the following R&D tasks were carried out:

   (a) Simulations were performed by the TRITIUM Aveiro team using the Geant4 package to optimize tritium detection efficiency. It was found that in 25 cm long fibres the light signal is a factor 23% larger than in 1 m long fibres.

   (b) A surface-conditioning method for scintillating fibres, which consists of cleaving, polishing and cleaning the fibres, was developed in the frame of this PhD thesis. A polishing machine based on

Arduino technology was developed. The objective of this machine was to automate the polishing of hundreds of fibres simultaneously, a task that if done manually requires an unaffordable time for the number of fibres needed for the TRITIUM monitor. The surface-conditioning method increases by a factor of 2 the light collected by the fibres due to polishing and an additional 30% due to cleaning.

(c) Characterization of the scintillating fibres was performed in this PhD thesis. A photon collection efficiency of $76 \pm 8\%$ was obtained, which is smaller than stated by the manufacturer (96%). The typical deviation of the photon collection efficiency after applying the surface-conditioning method was also measured, obtaining about 3% which is acceptable for tritium measurements.

(d) Characterization of the S13360-1375 Hamamatsu SiPM was carried out in this PhD thesis. The most relevant parameters of the SiPM such as gain, breakdown voltage, temperature coefficient and others such as quenching resistance and terminal capacitance, were measured and compared to the values provided by the manufacturer. The charge of the single photoelectron spectrum was measured with a resolution of 1% for each photoelectron peak and up to 10 photoelectron peaks were resolved.

(e) Due to the strong dependence of the SiPM gain on temperature, a gain stabilization method was implemented in the temperature range of interest. This method consists in compensating for the variation of the gain due to changes in the temperature by a variation of the bias voltage. Indeed, the gain depends linearly on both temperature and voltage, increasing with voltage and decreasing with temperature. This enables to stabilize the gain to its nominal value at 25°C by a variation of 59.9 ± 1.3 mV/°C of the bias voltage. This stabilization method was tested, obtaining variations in the SiPM gain smaller than 0.1% in the $[20-30]$°C temperature range, which is the expected temperature range of

operation. These results indicate that a stable operation of the SiPM readout can be obtained by an automatic implementation of a temperature-dependent SiPM bias.

2. The background rejection system consists of an active veto and a passive shield. The latter consists of a lead castle of 5 cm thick walls, designed by the TRITIUM CENBG team and presently installed in the Arrocampo site. A reduction factor of 5.5 for cosmic ray events due to the lead shield was obtained by simulations performed in this PhD thesis. Most of the background of the environmental radioactivity in the Arrocampo site (which was not included in these simulations) would also be suppressed by this shield.

   The active veto, built and characterized in this PhD thesis, consists of two parallel plastic scintillator plates of 1 cm thickness, separated 34.2 cm distance and enclosing the TRITIUM modules. The plastic scintillator plates were threefold wrapped in PTFE, aluminium and black tape layers and each plate was read out by two photosensors. This wrapping improved the light collection by a factor of 2 and produced a better response uniformity on the plate surface. In addition, the electronics settings that optimize the detection of hard cosmic events, such as discrimination thresholds and photosensor high voltage bias, were determined. A hard cosmic rate of 2.5 events/s was measured, from which an efficiency of the cosmic veto of 85% is drawn by comparison to the cosmic ray rate at sea level. Finally, the dependence of the hard cosmic rate on the distance between the plastic scintillator plates was fitted to a second order polynomial, which enables to change this distance without needing to perform a new calibration of the veto. A 60% reduction of the hard cosmic ray events due to the active veto was obtained through simulations. Therefore, a 92.7% suppression of the cosmic ray rate by the whole background rejection system was obtained from simulations. The simulated background rejection of hard cosmic events is smaller than that found experimentally

so the total cosmic ray suppression is expected to be larger than the simulated one. The actual cosmic ray suppression will be measured at the Arrocampo site.

3. A detailed analysis of the Arrocampo water revealed the presence of high concentrations of organic components at the site. The TRITIUM LARUEX team designed and installed a water purification system, consisting of several filtering stages that eliminate all organic matter and mineral particles of more than 1 μm in size. A conductivity close to 10 μS/cm (two orders of magnitude less than the raw water) was achieved. Furthermore, the water tritium activity did not change after the purification process.

4. Four different detector prototypes, called TRITIUM-IFIC-0, TRITIUM-IFIC-1, TRITIUM-Aveiro and TRITIUM-IFIC-2, listed in chronological order, were developed by the TRITIUM collaboration. The first two prototypes, TRITIUM-IFIC-0 and TRITIUM-IFIC-1 (developed in this PhD thesis), were used as a proof of concept for the detection of tritium in water with scintillating fibres and to identify the different issues that affect the detection efficiency.

The results obtained from the first prototype demonstrated that a straight arrangement of the scintillating fibres was crucial for tritium detection. A surface-conditioning method of scintillating fibres was implemented in the TRITIUM-IFIC-1 prototype which improved the tritium detection efficiency. The use of a PTFE vessel was also found to improve the light collection due to its optical properties (reflectivity close to 93% for visible light). These modifications resulted in a factor of 10 increase in the measured count rate of tritium over the first prototype.

In the latest prototypes, two photosensors in coincidence were employed to reduce the photosensor noise. These two prototypes have a similar design but with subtle differences. One of the most important differences is the scintillating fibre diameter (2 mm for the

TRITIUM-Aveiro prototype and 1 mm for the TRITIUM-IFIC-2 prototype). Fibres of 1 mm enable to fit more of them in the same volume. This increases the total active area of the prototype (and therefore, its tritium detection efficiency) and the signal-to-background ratio (improving the MDA). Fibres of 2 mm are stiffer which may facilitate the water flow through the fibre bundle and increase the effective detection area. It was obtained from simulations that the cosmic ray rate in the energy range of interest is a factor 2 higher for scintillating fibres of 2 mm. Additional measurements need to be done to decide the fibre diameter of the final detector. The second important difference between the TRITIUM-Aveiro and TRITIUM-IFIC-2 prototypes is the type of photosensor proposed. TRITIUM-Aveiro uses PMTs and for TRITIUM-IFIC-2 SiPM arrays are proposed. SiPM arrays have some advantages over PMTs such as a higher photodetection efficiency which would increase the detection efficiency of the TRITIUM detector. Furthermore, the SiPMs do not need high voltage which implies a reduction of the TRITIUM monitor cost. However, SiPM arrays have some disadvantages as the need to read more channels out and to implement a gain stabilization method due to the strong dependence of SiPM gain on temperature.

The specific efficiency obtained with the TRITIUM-IFIC-2 prototype, $(141 \pm 6) \times 10^{-6}$ s^{-1}L kBq^{-1}cm^{-2}, is an order of magnitude better than that obtained with the TRITIUM-Aveiro prototype, $(16 \pm 5) \times 10^{-6}$ s^{-1}L kBq^{-1}cm^{-2}, most probably due to the surface-conditioning of the fibres of the IFIC prototype. In addition, 677 Bq/L and 218 Bq/L MDAs were obtained for the TRITIUM-IFIC-2 prototype for integration times of 10 min and 1 h, respectively. This is to be compared to 29.8 kBq/L and 3.6 kBq/L MDAs for the TRITIUM-Aveiro prototype for integration times of 1 min and 1 h, respectively. An integration time of 1 h can still be considered quasi-real-time. The lower the MDA the smaller the tritium activity that can be discriminated from the background.

A summary of the state-of-the-art of tritium detection in water is shown in Table 7.1 which includes the results obtained with the four different prototypes developed by the TRITIUM collaboration. As it can be seen in this table, TRITIUM-IFIC-2 ameliorates significantly the current state-of-the-art. The specific efficiency and the MDA are almost an order of magnitude better than the results reported in the literature.

Reference	$\eta_{det} \times 10^{-3}$ L kBq^{-1}s^{-1}	F_{sci} cm^2	$S_{det} \times 10^{-6}$ L kBq^{-1}s^{-1} cm^{-2}	MDA kBq L^{-1}
[Mur67]	0.39	123	3.13	370
[Mog69]	4.50	> 424	< 10.6	37
[Osb70]	12	3000	4	37
[Sin85]	41	3000	13.7	< 37
[Hof92a]	2.22	~ 100	< 22.2	25
T-IFIC-0†	2.1 ± 0.8	219	10 ± 4	100*
T-IFIC-1†	38.4 ± 1.6	402	96 ± 4	100*
T-Aveiro†	64 ± 19	4072	16 ± 5	3.6**
T-IFIC-2†	711 ± 27	5027	141 ± 6	0.22**

Table 7.1: Results of scintillator detectors developed by different experiments (including the TRITIUM project) for tritiated water detection. This table shows the detector efficiency (η_{det}), its active surface (F_{sci}), its specific efficiency ($S_{det} = \eta_{det}/F_{sci}$, defined as efficiency normalized to the active surface) and its MDA.
* Specific activity measured, not MDA.
** MDA measured for 1 h integration time.
† This Thesis.

The modular structure of the TRITIUM monitor allows for scalability, which means that a lower MDA can be achieved by using a larger number of modules. The MDA of the TRITIUM monitor is expected to decrease with the square root of the number of modules. Therefore, as shown in Figure 5.21, an MDA of 100 Bq/L (goal of the TRITIUM project) could be achieved by using 5 TRITIUM-IFIC-2 modules and

an integration time of 1 h. It has to be taken into account that the MDA reported in this PhD work was measured without the background rejection system. The tritium MDA is expected to improve when this system is included.

5. The stability of the tritium detection efficiency of TRITIUM-IFIC-2 was monitored for six months, obtaining a stable detector response during this time with a relative standard deviation of 2.5% for the measured tritium rate.

6. Finally, simulations of a TRITIUM monitor based on the TRITIUM-IFIC-2 design were carried out to determine the dependence of the tritium detection efficiency and activity resolution on integration time and the number of modules. These simulations allow us to determine the number of modules needed in the TRITIUM monitor and the integration time to be used. With 5 modules and an integration time of 1 h, a tritium activity resolution of 100 Bq/L is expected. This configuration is also one that has an MDA of 100 Bq/L as proven by the measurements (point 4).

At present, the lead shielding, the water purification system and a TRITIUM-Aveiro module are installed at the Arrocampo site. Two additional TRITIUM-Aveiro modules and an active veto are planned to be installed as soon as possible. Moreover, three TRITIUM-IFIC-2 modules and an active veto are ready to be installed too. Their installation was delayed due to the coronavirus pandemic.

Chapter 8

Conclusions of this thesis

In this chapter, the main results and conclusions obtained in this PhD thesis are the following:

1. A scalable modular monitor for measuring low activities of tritium in water is proposed. The goal of this monitor is to reach a sensitivity of 100 Bq/L of tritium activity, which is the maximum level allowed for drinking water by the EU directive. The modularity allows reaching the required sensitivity by selecting a given integration time and including the corresponding number of modules.

2. The IFIC modules of the proposed TRITIUM monitor consist of 1 mm diameter scintillating fibres read out by photosensors.

3. Three different prototypes of the TRITIUM-IFIC module in which different improvements were successively incorporated were developed.

4. A surface-conditioning method for the scintillating fibres, consisting of specific rules for cleaving, polishing and cleaning the fibres was developed. This conditioning method was applied to the selected 1 mm

     diameter uncladded scintillating fibres from Saint-Gobain. An improvement of the fibre photon collection efficiency of a factor of 2 due to polishing and an additional 25% due to cleaning was obtained.

5. Although most of the laboratory tests were carried out with PMTs to read out the scintillating fibres, SiPM arrays are proposed by the TRITIUM Valencia team for the final monitor.

6. An S13360-1375 SiPM from Hamamatsu, selected for the monitor, was characterized. The most relevant parameters for tritium detection of this photosensor such as breakdown voltage and gain were measured.

7. As SiPM gain varies strongly with temperature, a stabilization method to maintain the gain constant with temperature was implemented. This method, which consists in compensating the gain variations with the bias voltage, was tested in the $[20-30]°$C temperature range of interest. Relative variations of the gain of the order of 0.1% were found which guarantees a stable operation of the photosensors.

8. In order to obtain the required tritium activity sensitivity, a background rejection system consisting of a lead shield castle and an active plastic scintillator veto was proposed and implemented.

9. The passive background rejection system was simulated. A reduction factor of the cosmic ray events detected by TRITIUM-IFIC-2 of 5.5 was obtained.

10. An active veto based on plastic scintillators read out by photosensors was designed and built.

11. The characterization of the active veto was done and the optimal parameters for the detection of hard cosmic rays were determined. A count rate of 2.5 events/s was measured, which gives an efficiency for cosmic ray detection of 85% by comparing this counting rate to the cosmic ray rate at sea level quoted in the literature.

12. The active veto was simulated, obtaining a suppression of 60% of the cosmic rays that cross the lead shield and are detected by TRITIUM-IFIC-2.

13. The total background suppression by the rejection system obtained from simulations for TRITIUM-IFIC-2 is 92.5%.

14. A specific efficiency $\eta = (141 \pm 6) \times 10^{-6}$ $s^{-1}L$ $kBq^{-1}cm^{-2}$ for the TRITIUM-IFIC-2 prototype was measured, which is about an order of magnitude higher than the specific efficiencies reported in the literature. The state-of-the-art of tritium detection with plastic scintillators is substantially improved.

15. The MDA obtained with TRITIUM-IFIC-2 is 677 Bq/L for 10 min integration time and 218 Bq/L for 1 h integration time.

16. The goal of the TRITIUM project of measuring an MDA of 100 Bq/L in quasi-real-time is expected to be reached with 5 TRITIUM-IFIC-2 prototypes read out in parallel and 1 h integration time.

17. Simulations of the detection resolution of a TRITIUM monitor based on TRITIUM-IFIC-2 were done. A resolution of 100 Bq/L for an integration time of 1 h and five modules was obtained.

18. Three TRITIUM-IFIC-2 prototypes with the corresponding active veto are ready to be installed at the Arrocampo site as soon as possible.

Capítol 9

Resum en Valencià

9.1 El triti i l'energia nuclear

La humanitat ha estat exposada a la radioactivitat des de l'inici dels temps, ja siga procedent de fonts extraterrestres o de la pròpia escorça terrestre. Des que Henri Becquerel va descobrir la radioactivitat en 1896, s'ha desenvolupat molta tecnologia nuclear en diferents camps com ara la medicina, la investigació, la producció d'energia, etc. Aquesta creació de fonts nuclears antropogèniques ha conduït a un excés d'elements radioactius alliberats al medi ambient i, consegüentment, a un augment de la dosi radioactiva a què els éssers humans ens veiem afectats. Aquest augment es pot observar a la Figura 9.1, que mostra la distribució de la mitjana anual de la dosi radioactiva rebuda per la població mundial.

A causa d'aquest augment dels nivells de radioactivitat en el medi ambient és important fer un control per assegurar que aquests es troben per davall dels límits considerats segurs per a la població. A Espanya, aquest control el realitza el Consell de Seguretat Nuclear (CSN) [Con], l'única autoritat a Espanya en matèria de seguretat nuclear i radioprotecció. Per
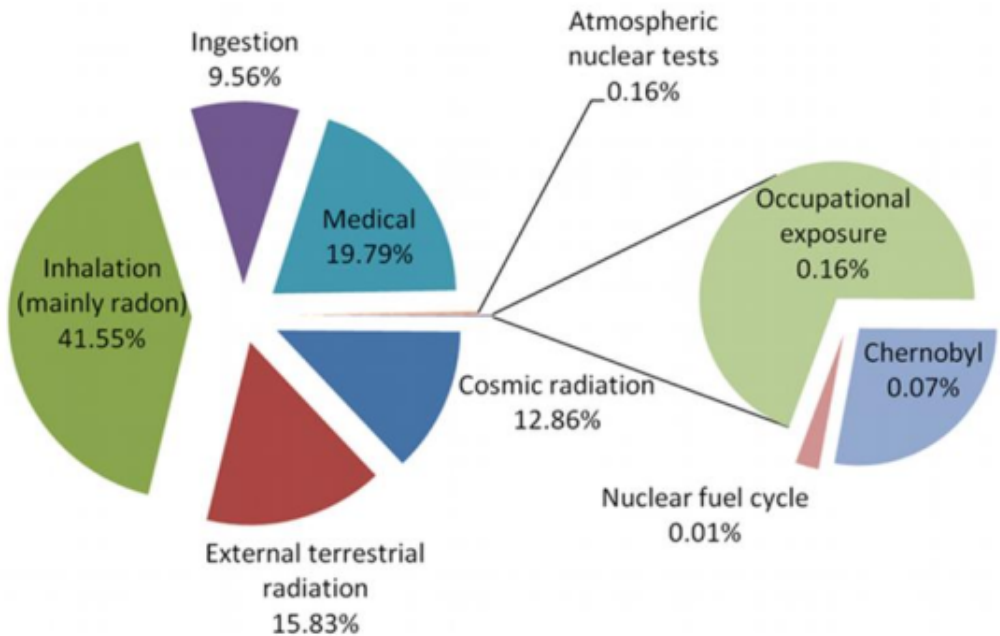
Figure 9.1 – Distribució de l'origen de la dosi radioactiva rebuda per la població mundial [Thea].

realitzar aquesta tasca de control, el CSN disposa de diverses xarxes entre les quals es troba la xarxa d'estacions de monitoratge (REM per les sigles en castellà). En aquesta, al voltant de 20 laboratoris espanyols prenen mostres en diferents punts del país per caracteritzar, quantificar i controlar les concentracions de radioisòtops presents en el medi ambient.

Un dels radioisòtops habitualment mesurat en aquests tests és el triti, el tercer isòtop de l'hidrogen. Es tracta d'un element amb una vida mitjana de $T_{1/2} = 12,32$ anys que únicament es desintegra via β^- emetent un electró i un neutrí a través del procés:

$$\mathrm{^3_1H} \longrightarrow \mathrm{^3_2He} + \mathrm{e}^- + \overline{\nu}_\mathrm{e} \tag{9.1}$$

El nivell de triti en el medi ambient, excloent les fonts antropogèni-

ques radioactives actuals, es troba entre 1 i 4 Bq/L, més gran que l'esperat $(0, 6 - 1, 2$ Bq/L$)$ a causa de les proves nuclears realitzades en el passat [Cal10]. Aquest nivell augmenta fins a 10 Bq/L en els llocs al voltant de les centrals nuclears i fins a entre 20 i 50 Bq/L al lloc on la central nuclear descarrega l'aigua emprada en la refrigeració del nucli [Cal10]. Un exemple d'aquest augment el trobem als tests realitzats pel REM al voltant de la central nuclear de Cofrents, València. En aquests tests el triti és mesurat en tres punts del riu Júcar assenyalats en la Figura 9.2, els quals es troben a 6 km abans de la central nuclear, 1 km després i 5 km després, respectivament representats pels punts P1, P2 i P3. Les mesures de triti en aquestes zones són respectivament representades en les gràfiques de la Figura 9.3. En aquestes gràfiques el límit de detecció i l'activitat mesurada per al triti es representen en punts blancs i verds respectivament. Com es pot comprovar, el nivell de triti augmenta just després de la central nuclear i, gradualment es va reduint a causa de la dissolució del triti en l'aigua. És important remarcar que, encara que aquests nivells de triti si han augmentat a causa de la central nuclear, aquests mai han sobrepassat el límit permés. A Espanya, aquest límit és fixat per la directiva del consell EURATOM a 100 Bq/L per a l'aigua potable [Eur14] mentre que el màxim nivell de triti mesurat des de l'any 2006 únicament és de 32 Bq/L. Aquests nivells de triti també han sigut mesurats en altres dos punts d'aigües subterrànies, l'u situat 1 km abans de la central nuclear i l'altre situat 1 km després, representats pels punts S1 i S2 de la Figura 9.2. En aquest cas, com es pot veure en les gràfiques de la Figura 9.4, el nivell de triti no es veu afectat, ja que la central nuclear únicament utilitza l'aigua del riu per a la refrigeració.

El triti és el radioisòtop amb una energia de desintegració més baixa (una energia màxima de $Q_\beta = 18.6$ keV), raó per la qual presenta una baixa penetració en la pell. No obstant això, el triti pot arribar a ser altament perjudicial si s'introdueix en el cos, ja siga ingerit o inhalat, ja que pot participar en reaccions químiques substituint a l'hidrogen i romandre en el cos fins a 50 dies [Mar72, Lee18], temps durant el qual s'està rebent radia-
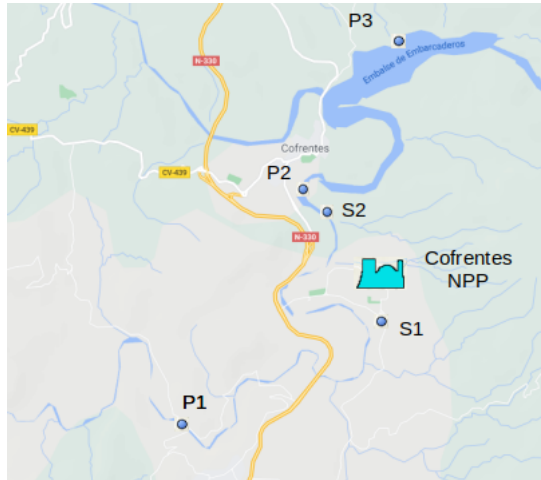
Figure 9.2 – Punts de mesura de triti al voltant de la central nuclear de Cofrents.

ció. Es tracta d'un element radioactiu que afecta la salut dels organismes vius si estan exposats a quantitats altes o de forma crònica, i poden arribar a causar mutacions de l'ADN, mort cel·lular, pèrdua de la funcionalitat d'òrgans o desenvolupar tumors [Str93]. A causa del perill que representa el triti per a la salut dels éssers vius, molts països han creat lleis per regular l'alliberament de triti al medi ambient. Com ja s'ha comentat anteriorment, a Espanya, igual que a França i Alemanya, aquest límit és fixat per la directiva de EURATOM a 100 Bq/L per a l'aigua potable. Aquest és un dels límits més restrictius entre els implantats als diferents països.

Les tècniques utilitzades hui en dia per a la mesura del triti, com pot ser el recompte en centellejadors líquids (LSC per les seues sigles en anglés) o la mesura amb plàstics centellejadors llegits per fotosensors, presenten l'inconvenient que o bé necessiten molt de temps per a realitzar la mesura (més de dos dies) o bé no són capaços de mesurar activitats tan baixes (mínima activitat detectable (MDA per les sigles en anglés) de milers de Bq/L en el millor dels casos), impossibilitant-los per a ser emprats per a un monitoratge del triti ambiental en temps quasireal (menys d'una hora).
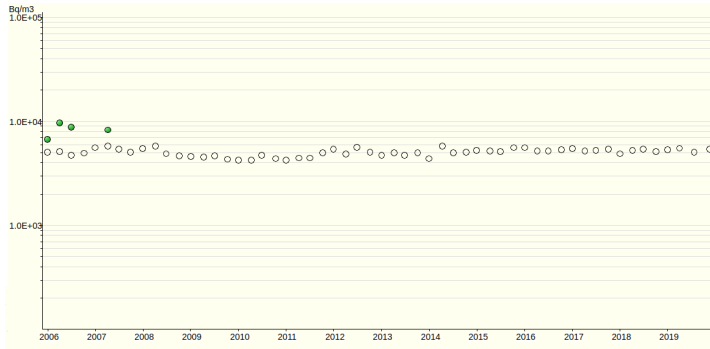
(a)
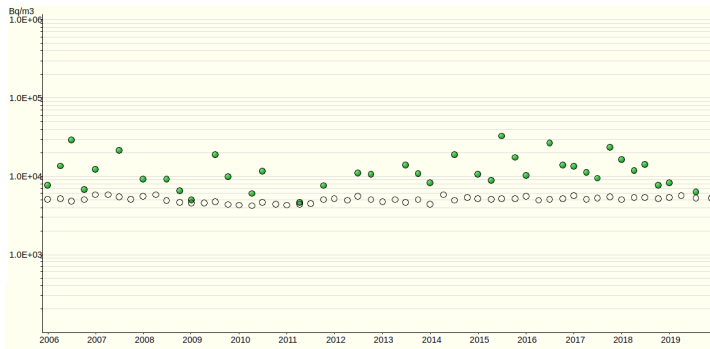
(b)
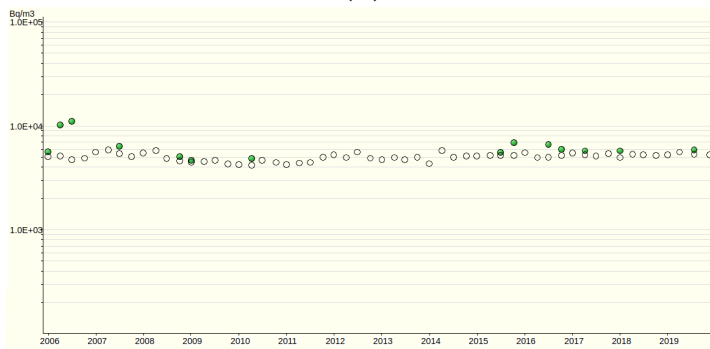
(c)

Figure 9.3 – Nivells d'activitat de triti en aigües superficials del riu Júcar des del gener de 2006 fins al novembre de 2019. (a) Punt de mostra situat a 6 km de la central nuclear riu amunt. (b) 1 km riu avall. (c) 5 km riu avall. Els punts blancs i verds representen el límit de detecció i l'activitat mesurada respectivament. El màxim nivell de triti mesurat és al voltant de 32 Bq/L. [CSNb]
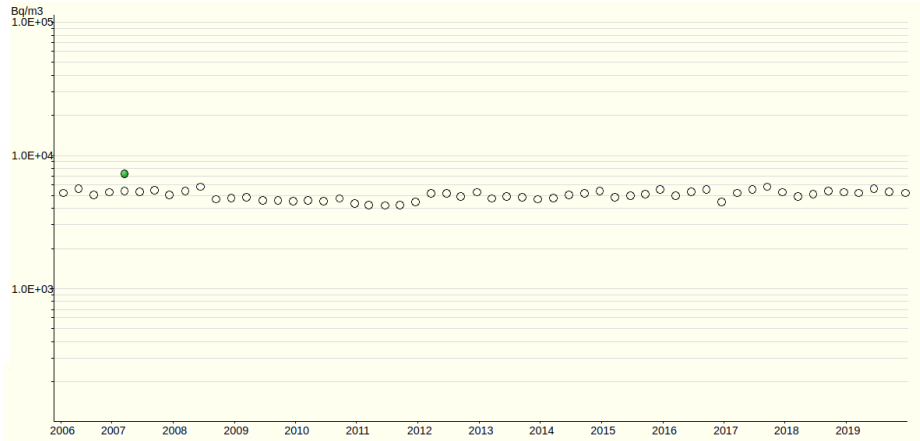
(a)
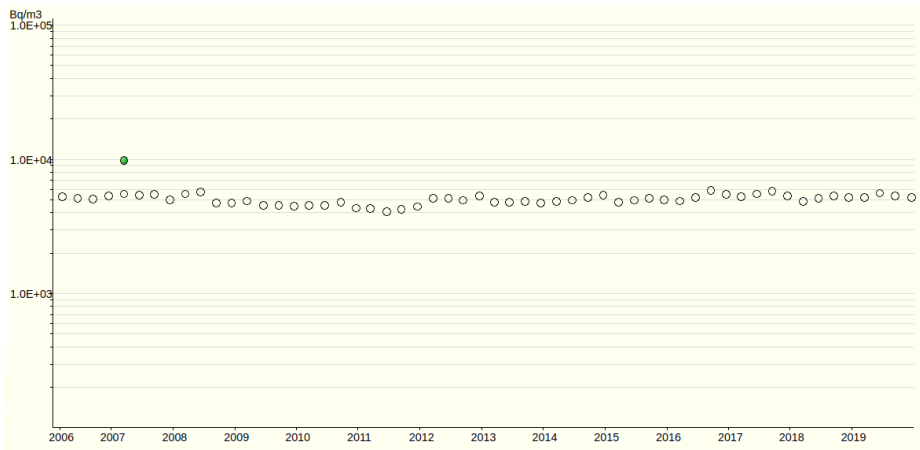
(b)

Figure 9.4 – Nivells de l'activitat del triti en aigües subterrànies al voltant de la central nuclear de Cofrents mesurats des del gener de 2006 fins al novembre de 2019 [CSNb]. (a) 1 km de la central nuclear riu amunt. (b) 1 km de la central nuclear riu avall [CSNb].

Per a superar aquests inconvenients es va proposar l'any 2016 el projecte anomenat TRITIUM (triti amb anglés), amb títol "Disseny, construcció i manteniment d'una estació automàtica per al monitoratge de baixos nivells d'activitat del triti en aigua". TRITIUM és una col·laboració internacional formada per 6 institucions procedents de 3 països europeus, França, Portugal i Espanya. L'objectiu d'aquest projecte és desenvolupar un monitor de nivells de triti que permeta obtenir mesures en temps quasireal. Per a complir aquesta necessitat de temps quasireal és imprescindible que el detector siga capaç de realitzar mesures "in situ", és a dir, al mateix lloc on es pren la mostra.

Com es veurà en la secció 9.2, la col·laboració TRITIUM aposta per un disseny del detector basat en milers de fibres centellejadores llegides per fotosensors. Aquestes fibres es posen directament en contacte amb la mostra a analitzar (aigua), les quals són capaces de detectar part dels decaïments radioactius del triti. A més, com es discutirà en la secció següent, s'han afegit alguns elements addicionals a aquest detector per tal de millorar la seua sensibilitat a la detecció del triti, com ara un sistema de rebuig del fons radioactiu i un sistema de purificació de l'aigua. L'objectiu final del projecte TRITIUM serà instal·lar el monitor construït a la presa d'Arrocampo, a Extremadura (Espanya) al punt on l'aigua utilitzada per refrigerar el nucli de la central nuclear d'Almaraz és alliberada al riu Tajo. L'aigua d'aquest riu és utilitzada per espanyols i portuguesos, tant pel consum com pel regadiu, de manera que preservar-ne el correcte estat d'aquesta és una necessitat prioritària de la qual depén directament la salut de les persones.

9.2 Principis del disseny i components del monitor TRITIUM

9.2.1 Vista general del monitor TRITIUM

El monitor desenvolupat per la col·laboració s'anomena TRITIUM i consisteix de tres parts principals:

1. El detector de triti, on es realitza la mesura de la mostra d'aigua. Aquest està format per diversos mòduls llegits en paral·lel. El disseny modular li confereix la propietat d'escalabilitat, permetent-li millorar certes característiques com l'eficiència o l'activitat mínima detectable de triti simplement amb la utilització de més mòduls.

   Cadascun d'aquests mòduls està format per centenars de fibres centellejadores que entren en contacte directe amb la mostra d'aigua a mesurar. Aquestes fibres són capaces de detectar part de les desintegracions de triti que tenen lloc i són llegides per diversos fotosensors, el senyal dels quals és analitzat per l'electrònica corresponent.

2. El sistema de purificació d'aigua, el qual prepara la mostra abans d'introduir-la al detector. Aquest sistema és utilitzat per dos motius principals. En primer lloc, per a eliminar qualsevol partícula amb un diàmetre superior a 1 μm que es trobe dissolta a l'aigua, la qual podria ser depositada sobre les fibres centellejadores. Pel fet que el recorregut lliure mitjà del triti és de només $5-6$ μm en la matèria, aquesta deposició provocaria una disminució de l'eficiència de detecció del triti. En segon lloc, per a eliminar qualsevol element radioactiu (diferent del triti) dissolt a l'aigua, com per exemple el ^{40}K que es troba de manera natural al medi ambient, ja que aquest seria comtabilitzat pel detector com un esdeveniment de triti, falsejant les mesures.

3. El sistema de rebuig del fons radioactiu, utilitzat per suprimir en la mesura del que siga possible el fons radioactiu en el lloc de treball. Aquest sistema es divideix en dues parts. Un castell de plom que envolta el detector, el qual para gran part de les partícules amb energies inferiors a 200 MeV, procedents principalment del fons radioactiu natural del lloc de treball i dels rajos còsmics. Un veto actiu emprat per a reduir els esdeveniments detectats procedents de rajos còsmics amb energies superiors a 200 MeV.

Tant el sistema de purificació de l'aigua com el sistema de rebuig del fons radioactiu són fonamentals, ja que permeten reduir gran part del fons radioactiu mesurat pel detector, una tasca essencial per a aconseguir l'objectiu del projecte (mesurar activitats de triti tan baixes com 100 Bq/L). Finalment aquestes tres parts són controlades per diversos aparells electrònics que, en últim lloc, emetran un senyal d'alarma en cas que el límit legal fixat a Espanya per al triti en aigües potables (100 Bq/L) siga superat. La idea final seria poder incloure aquest monitor a la xarxa d'estacions automàtiques del CSN (REA per les sigles en castellà) [CSNa]. Aquesta és una xarxa formada per detectors de diferents tipus que mesuren en temps quasireal les concentracions d'alguns dels diferents isòtops radioactius que es troben al medi ambient.

9.2.2   Components del detector TRITIUM

El detector TRITIUM, de la mateixa manera que el veto actiu del sistema de rebuig del fons radioactiu, consisteix en tres elements. El plàstic centellejador, que genera fotons en l'espectre visible com a resposta a la detecció d'una partícula, ja siga un decaïment del triti a la mostra o un esdeveniment del fons radioactiu. Els fotosensors, que detecten aquests fotons visibles i, com a conseqüència, generen un pols elèctric. L'electrònica, encarregada de processar i analitzar aquests polsos elèctrics. A la Figura 9.5 es pot veure

un esquema del detector descrit.
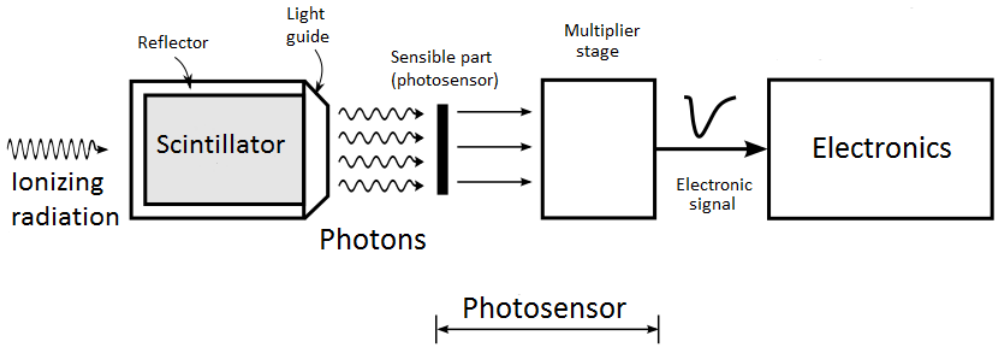
Figure 9.5 – Esquema d'un detector de centelleig.

9.2.2.1 Fibres Centellejadores

Els plàstics centellejadors són plàstics dopats amb molècules fluorescents, els quals són utilitzats per detectar les partícules d'interés. Aquests es poden mecanitzar de moltes formes diferents, d'entre les quals, l'emprada pel projecte TRITIUM és la fibra (1 mm o 2 mm de diàmetre i 20 cm de longitud utilitzada en el detector de triti) i el bloc ($17 \times 45 \times 1$ cm^3 utilitzada en el veto actiu).

En els plàstics centellejadors, les partícules que els travessen depositen part de la seua energia cinètica, la qual excita els electrons de les molècules fluorescents. Finalment aquests electrons es desexciten en nanosegons mitjançant un procés anomenat fluorescència, a través del qual emeten fotons a una longitud d'ona que pertany a l'espectre visible. Aquest espectre d'emissió presenta un pic centrat a una longitud d'ona que depén de la molècula fluorescent. En el cas dels plàstics centellejadors utilitzats en el projecte TRITIUM, la molècula fluorescent conté fluor, el qual presenta un pic d'emissió al voltant de 435 nm, com es pot comprovar en la Figura 9.6. El nombre de fotons generats per a una mateixa energia depositada
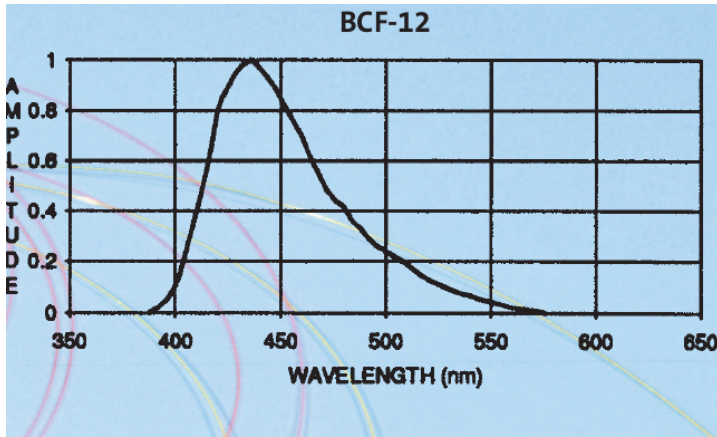
(a)
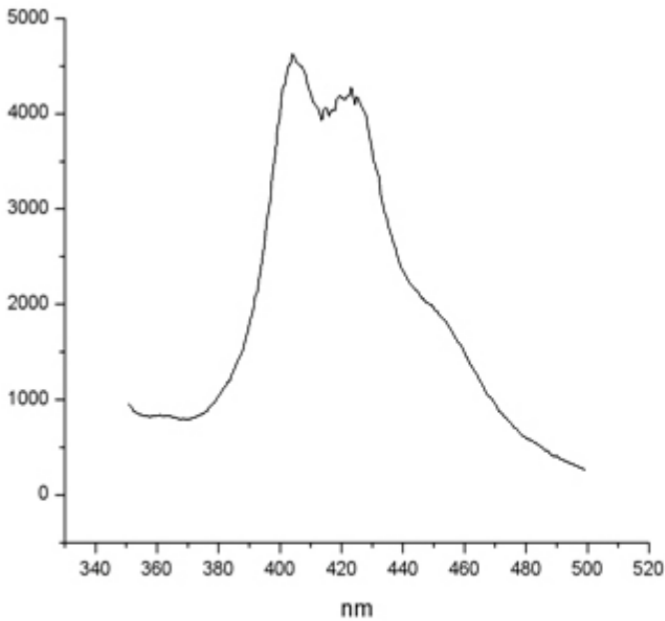
(b)

Figure 9.6 – Espectre d'emissió de a) les fibres centellejadores de Saint Gobain, model BCF-12, utilitzades en el detector de triti [Sai21b] b) bloc de plàstic centellejador d'Epic Crystals utilitzat en el sistema de rebuig del fons radioactiu[Epi20].

(a)   **(b)**
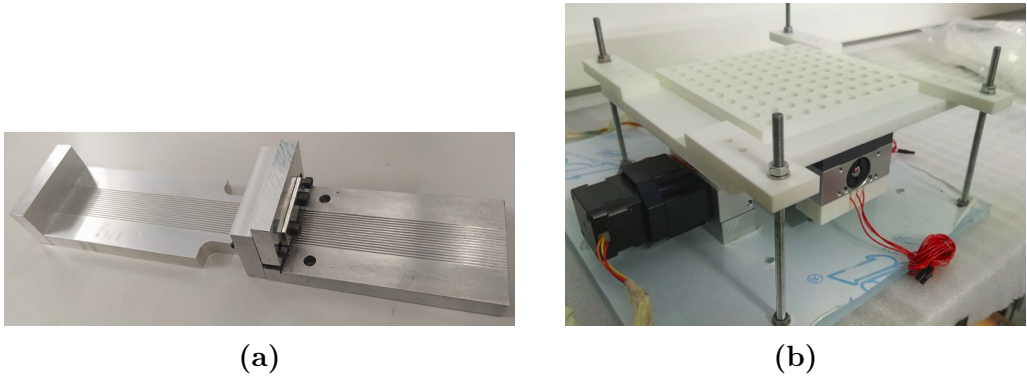
Figure 9.7 – Màquines desenvolupades al projecte TRITIUM per a a) tallar fibres centellejadores i b) polir fibres centellejadores en massa.

està descrit per una estadística poissoniana. A més, el nombre de fotons que es produeixen depén linealment de l'energia depositada dins d'un rang d'energies de la partícula.

La col·laboració TRITIUM ha realitzat estudis per quantificar algunes de les propietats més rellevants d'aquestes fibres per a la detecció del triti en aigua, com ara la dispersió del nombre de fotons per a un mateix esdeveniment o l'eficiència de col·lecció de fotons, obtenint $2,86\%$ i $(76 \pm 8)\%$ respectivament. També s'ha desenvolupat un mètode per a incrementar la quantitat de senyal llegida pels fotosensors que consisteix a tallar, polir i netejar les fibres seguint uns protocols adequats. Per això, va caldre desenvolupar diferents màquines, les quals es mostren a la Figura 9.7, basades en la tecnologia Arduino. També va caldre accedir a l'interior d'una sala blanca per garantir un alt grau de neteja. La millora obtinguda amb aquest mètode es va quantificar en més d'un factor dos.

9.2.2.2 Fotosensors

Els fotons creats en el plàstic centellejador són detectats pels fotosensors. La col·laboració TRITIUM està investigant dos tipus de fotosensors amb di-

ferents propietats físiques, els tubs fotomultiplicadors (PMTs) i les matrius de fotomultiplicadors de silici (SiPMs), mostrats a la Figura 9.8. Tots dos utilitzen l'efecte fotoelèctric per transformar els fotons detectats en electrons. El PMT col·lecta i multiplica aquests fotons a través d'una cadena de dínodes mentre que la matriu de SiPMs ho fa en l'interior de fotodíodes d'allau operant en mode Geiger i en paral·lel.
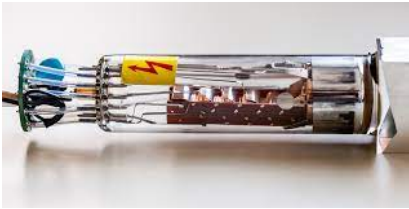
(a)
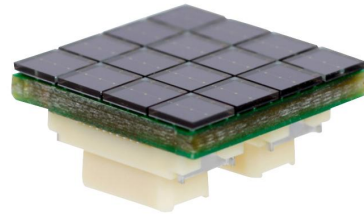
(b)

Figure 9.8 – a) Tub fotomultiplicador. b) Matriu de fotomultiplicadors de silici.

Els dos fotosensors posseeixen una àrea activa optimitzada per a la detecció de fotons, normalment en l'espectre visible. La probabilitat que el PMT i el SiPM produeixen un senyal com a resposta a la detecció de fotons ve determinada per l'eficiència quàntica i l'eficiència de fotodetecció, respectivament, els espectres dels quals es mostren a la Figura 9.9 en funció de la longitud d'ona. És important escollir el fotosensor adequat per tal que l'espectre d'emissió del centellejador, Figura 9.6, se superpose tant com siga possible amb l'eficiència de detecció del fotosensor, Figura 9.9, ja que l'eficiència del detector resultant dependrà del producte de tots dos. Finalment els fotosensors emeten un senyal elèctric que porta informació de l'esdeveniment, el qual és amplificat per a poder ser mesurat i analitzat. Aquest senyal és proporcional al nombre de fotons detectats i, per tant, a l'energia depositada al centellejador per la partícula ionitzant. A partir de cert valor d'energia es perd la linealitat i es produeix allò que s'anomena saturació. Entre les principals diferències entre aquests dos fotosensors trobem que el SiPM no necessita alt voltatge per funcionar (típicament inferior a 70 V),
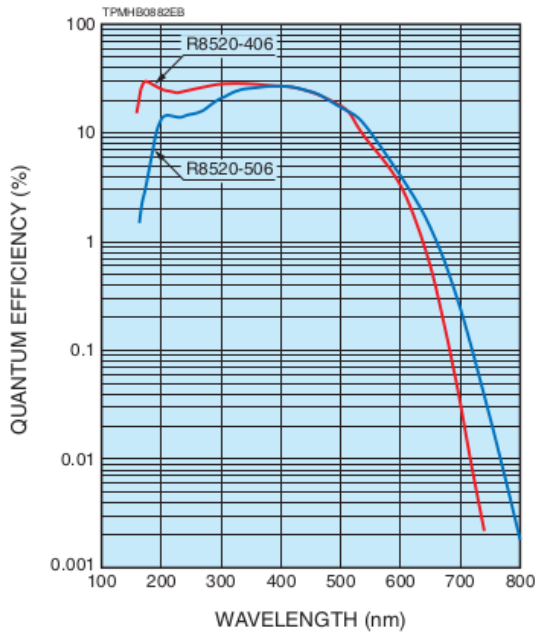
(a)
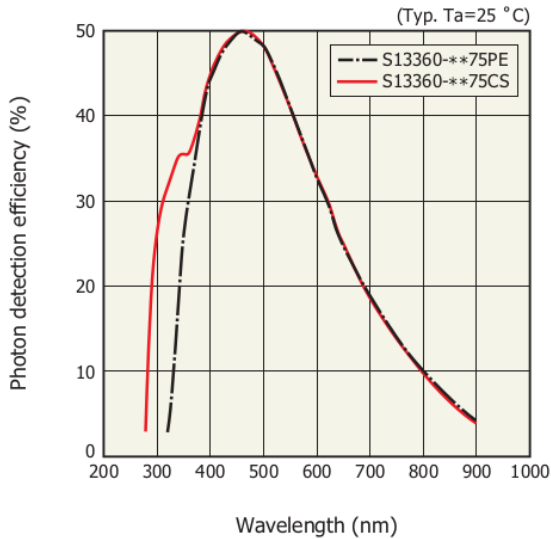
(b)

Figure 9.9 – a) Eficiència quàntica del PMT model R8520-406 de Hamamatsu Photonics [Ham19]. b) Eficiència de fotodetecció del fotomultiplicador de silici model S13360-6075 de Hamamatsu Photonics [Ham16b].

té una major eficiència de detecció i és més robust mentre que el PMT presenta un soroll electrònic més baix. A més, les propietats dels SiPMs varien fortament en funció de la temperatura.

La col·laboració TRITIUM ha realitzat una caracterització detallada dels SiPMs obtenint, amb gran precisió, resultats que estan d'acord amb els esperats segons el fabricant. A més, s'ha posat a prova amb èxit un protocol per mantenir estable el guany dels SiPMs quan es produeixen variacions de la temperatura. Finalment, entre aquests dos fotosensors emprats, s'escollirà aquell per a qui s'obtinguen millors resultats per a la detecció del triti.

9.2.2.3 Electrònica

L'electrònica rep i processa el senyal elèctric emés pel fotosensor i emmagatzema la informació pertinent. Les diferents tasques executades per l'electrònica són aplicar llindars d'energia sobre el senyal (utilitzats per descartar senyals no pertanyents a esdeveniments de triti), amplificar el senyal (per tindre millor precisió en les operacions realitzades sobre aquest) i aplicar coincidències (per reduir el nombre d'esdeveniments no pertanyents al triti). Finalment es realitza un histograma dels senyals que han superat totes les etapes anteriors, obtenint un espectre d'energia. L'electrònica depén del tipus de senyal que reba i, per tant, del tipus de fotosensor emprat. A causa d'això, en la col·laboració TRITIUM s'utilitzen electròniques diferents, una per a les matrius de SiPMs i altra per als PMTs:

1. L'electrònica emprada per a quan s'utilitzen matrius de SiPMs s'anomena PETsys [PET], mostrada a la Figura 9.10, un sistema comercial desenvolupat específicament per a treballar amb matrius de SiPMs.

2. L'electrònica emprada quan s'utilitzen PMTs en assajos a l'interior de laboratoris es basa en tecnologia NIM, la qual és un tipus de tecnologia

Figure 9.10 – Sistema comercial PETsys.

modular. L'equip portugués de la col·laboració TRITIUM va disse-
nyar i construir una electrònica específica que està basada en diverses
targetes de circuit imprés (PCB per les sigles en anglés) les quals són
utilitzades en Arrocampo, l'emplaçament final del detector.

9.2.3 Sistema de purificació de l'aigua

La composició química de l'aigua del riu Tajo va ser mesurada a través d'una
anàlisi fisicoquímica realitzada sobre una mostra. En aquesta anàlisi es va
trobar una alta quantitat de partícules i ions dissolts, donant lloc a una alta
conductivitat ($\sim 1000~\mu$S/cm). També es va utilitzar un detector de germa-
ni d'alta puresa (HPGe per les sigles en anglés) per realitzar una identificació
dels elements radioactius gamma presents en la mostra. Es va detectar la
presència de quantitats mesurables de ^{40}K i ^{226}Ra. Aquestes partícules han
de ser eliminades per dos motius. En primer lloc, perquè podrien depositar-
se sobre les fibres centellejadores, provocant una disminució de l'eficiència
del detector en la detecció del triti. En segon lloc, perquè aquests elements
radioactius podrien ser detectats i comptabilitzats com a desintegracions de
triti, sobreestimant l'activitat de la mostra. Per a complir aquesta tasca, la

col·laboració TRITIUM va dissenyar un sistema de purificació de l'aigua, l'esquema del qual es mostra en la Figura 9.11. Aquest sistema es basa en quatre estacions successives, compostes per diversos tipus de filtres a més d'un llum ultraviolat, amb els quals es realitza un filtratge cada volta més fi. El filtratge final aconseguit amb aquest sistema és fins partícules de la grandària d'1 μm, amb el qual s'aconsegueixen conductivitats de la mostra de l'ordre de 10 μS/cm, dos ordres de magnitud inferior a la mostra inicial. Amb aquest sistema s'aconsegueix generar un total de $1,480$ m^3/h d'aigua
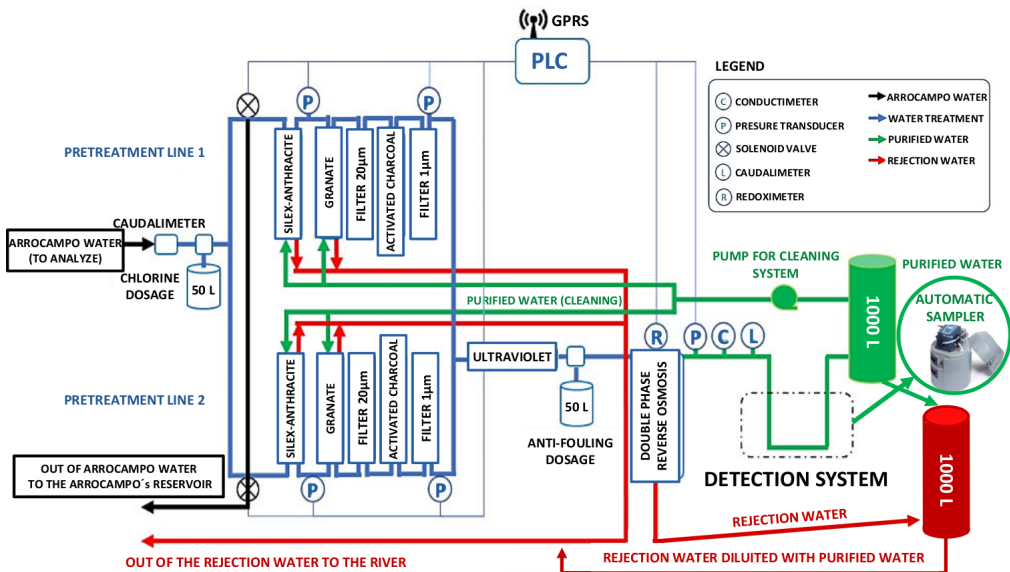
Figure 9.11 – Esquema del sistema de purificació de l'aigua.

purificada, que supera altament els requeriments del detector de triti. A més, també es va comprovar que el procés de purificació no afecta la concentració de triti de la mostra, requeriment important per a l'objectiu del projecte. Per a aquesta tasca es va utilitzar un comptador de líquid centellejador (LSC per les sigles en anglés) per a mesurar l'activitat de triti en mostres d'aigua abans i després de ser sotmeses al procés de purificació. Com es pot comprovar a la Taula 9.1, l'activitat de triti de les mostres va romandre invariant al procés de purificació.

Data	Abans (Bq/L)	Després (Bq/L)
7/8/18	24 ± 3	26 ± 4
11/12/19	$13,2 \pm 2,1$	$13,9 \pm 2,2$
15/01/20	31 ± 4	30 ± 4

Taula 9.1: Mesures de l'activitat del triti de diverses mostres d'aigua abans i després del procés de purificació.

9.2.4 Sistema de rebuig del fons radioactiu

La mínima activitat de triti que el detector TRITIUM pot mesurar està limitada per la incertesa del fons radioactiu la qual, com que segueix una estadística de Poisson, depén del nombre d'esdeveniments que es detecten procedents del fons radioactiu. Per tant, per reduir en la mesura del possible la mínima activitat de triti mesurable, s'ha de minimitzar tant com siga possible els esdeveniments detectats procedents del fons radioactiu. El fons radioactiu que és mesurat pel detector TRITIUM procedeix de dues fonts principals, els elements radioactius presents al medi ambient (principalment ^{40}K i ^{226}Ra) i la radiació còsmica.

Per a reduir el nombre d'esdeveniments del fons radioactiu detectats pel detector TRITIUM s'ha dissenyat i construït un sistema de rebuig del fons radioactiu que consisteix en dues parts:

1. Un castell de plom amb parets de 5 cm de gruix, mostrat a la Figura 9.12a, a l'interior del qual se situa el detector. Aquest frena les partícules de menor energia (fins a 200 MeV), les quals procedeixen principalment de les partícules radioactives del medi ambient i part dels rajos còsmics.

2. Un veto actiu, que consisteix en dos blocs de plàstic centellejador, amb un espectre d'emissió mostrat a la Figura 9.6b, els quals són llegits per PMTs model R8520 − 406 de Hamamatsu Photonics. Aquests

plàstics estan envoltats amb capes de PTFE, alumini i cinta negra per a millorar la col·lecció dels fotons generats i la uniformitat del senyal. La millora en col·lecció de fotons generats va ser experimentalment un factor dos. Aquests estan situats a l'interior del castell de plom, un dalt i l'altre baix del detector de triti, com es pot veure a la imatge 9.12b. Els plàstics centellejadors són llegits en anticoincidència amb el detector de triti per a eliminar els esdeveniments del fons que aconsegueixen travessar el castell de plom, principalment rajos còsmics amb energies superiors al 200 MeV.

Es va mesurar l'espectre d'energia de rajos còsmics durs (energies superiors a 200 MeV), el qual es mostra a la Figura 9.13. Aquest espectre es va utilitzar per a determinar la freqüència de rajos còsmics mesurats, $2, 5$ esdeveniments/ sec, la qual, comparant amb l'esperat per a un veto actiu d'aquestes dimensions al nivell del mar, va permetre obtenir una eficiència de detecció dels rajos còsmics d'alta energia al voltant d'un 85%.

9.3 Prototips del detector TRITIUM

En la col·laboració TRITIUM, un total de quatre prototips del detector de triti van ser desenvolupats. Els dos primers, anomenats TRITIUM-IFIC-0 i TRITIUM-IFIC-1, són prototips a una escala menor. Aquests van ser utilitzats com a prova de concepte per aprendre sobre la detecció de triti en aigua i estudiar la viabilitat de possibles millores per a optimitzar-la. Els dos darrers prototips, anomenats TRITIUM-Aveiro i TRITIUM-IFIC-2, són prototips funcionals amb un disseny similar, emprats per a avaluar la importància de certes diferències subtils en el disseny i elaborar un prototip final que incloga aquelles opcions que optimitzen l'eficiència de la detecció del triti. Durant l'emplenat d'aquests prototips amb aigua tritiada es van realitzar diverses proves d'estanquitat per garantir la radioseguretat
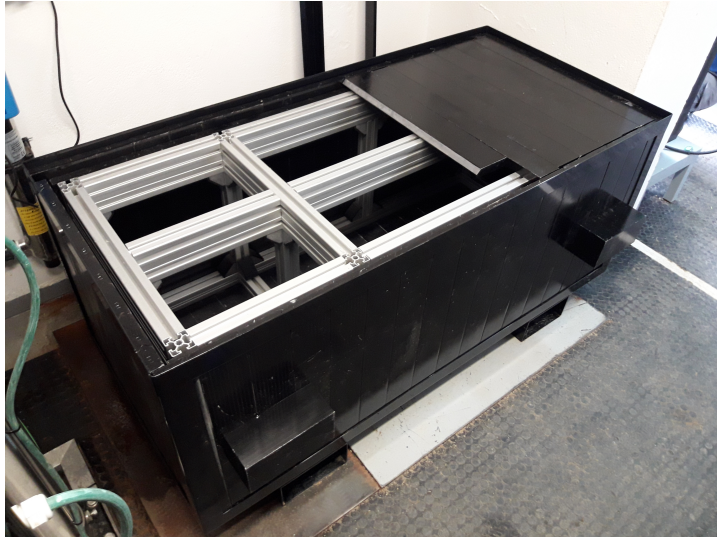
(a)
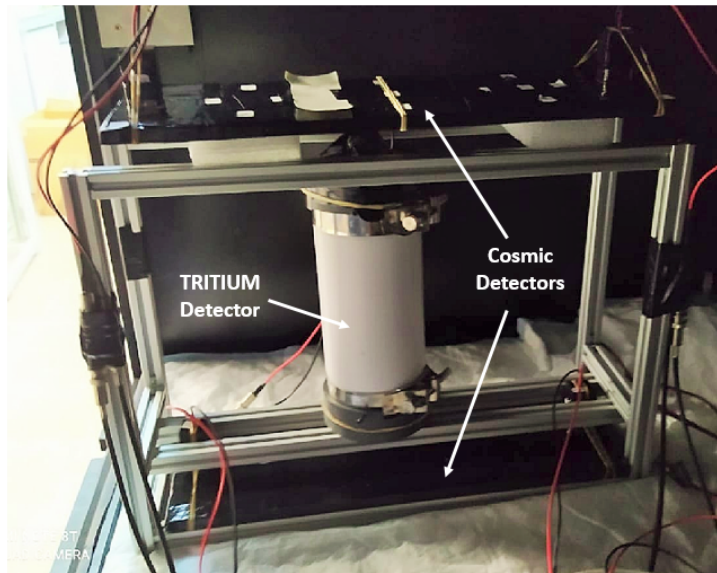
(b)

Figure 9.12 – Parts del sistema de rebuig del fons radioactiu dissenyat per la col·laboració TRITIUM: a) Castell de plom. b) Veto actiu.
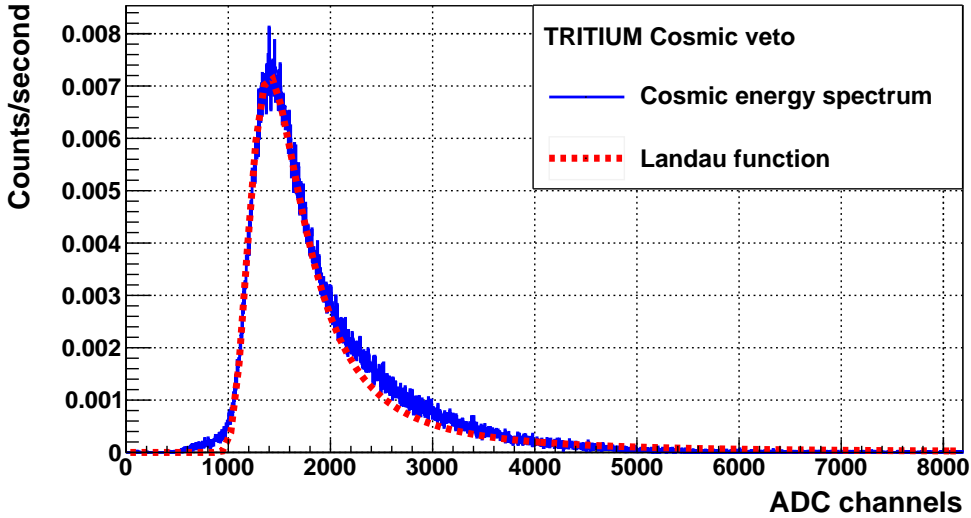
Figure 9.13 – Espectre d'energia dels rajos còsmics d'alta energia (energies superiors a 200 MeV) mesurat amb el veto actiu desenvolupat a la col·laboració TRITIUM.

de l'entorn. De forma complementària, es van realitzar diverses simulacions amb la llibreria Geant 4 [GEA], utilitzades per obtenir més informació sobre quines possibles millores en els dissenys dels prototips incrementarien les característiques rellevants del monitor.

9.3.1 Prototips inicials

El primer prototip del detector de triti desenvolupat en la col·laboració TRI-TIUM s'anomena TRITIUM-IFIC-0, el qual va ser dissenyat i construït als tallers de l'IFIC. Amb aquest prototip es pretenia provar la viabilitat de la tecnologia proposada per la col·laboració TRITIUM (fibres centellejadores llegides per fotosensors) per a la detecció de baixes activitats de triti a l'aigua. Aquest prototip consisteix en un conjunt de 35 fibres centellejadores, mostrades a la Figura 9.14b, d'1 mm de diàmetre i 20 cm de longitud.

Aquestes van ser polides manualment i es van unir amb una peça metàl·lica als extrems, la qual és utilitzada per fixar-les a l'atuell del prototip. Aquest atuell, mostrat a la Figura 9.14c, consisteix en una estructura de PVC. La forma corbada d'aquest li confereix una major radioseguretat al preu d'una menor eficiència de detecció del triti, un preu a pagar en els primers prototips, on simplement es pretenia realitzar una prova de concepte i no un disseny final optimitzat. Dos PMTs calibrats, model $R8520 - 06ESL$ de Hamamatsu Photonics [Ham19], van ser assemblats a aquestes fibres amb greix òptic [Saib] i llegits en coincidència.

Com ja hem comentat a la secció 9.2.4, el detector presenta una taxa de recompte no nul·la en absència de font radioactiva a causa de l'existència del fons radioactiu. Aquesta radioactivitat mesurada pel detector ha de ser quantificada i sostreta de la mesura amb font radioactiva per determinar l'activitat d'aquesta (aigua tritiada en el nostre cas). Per a complir aquesta tasca es van construir dos prototips idèntics, un omplit únicament amb aigua hiperpura, al que ens referirem com el prototip del fons i servirà per a determinar aquest fons radioactiu, i un altre omplit amb una dissolució d'aigua tritiada d'activitat específica coneguda (A = 99,696 kBq/L), al que ens referirem com el prototip del senyal. L'activitat del triti mesurada pel prototip és obtinguda com la diferència de la mesura dels dos prototips. A penes es van mesurar esdeveniments utilitzant la coincidència dels dos PMTs, probablement a causa, entre altres coses, del disseny corbat de l'atuell, per tant es va fer la mesura individual dels PMTs. L'espectre d'energia mesurat al prototip del senyal, el prototip del fons i la diferència (espectre d'energia del triti) es mostren a la Figura 9.15. Les taxes de comptatge mesurades per a les tres situacions, obtingudes com la integral dels respectius espectres d'energia, són mostrades a la Tabla 9.2.

Tenint en compte l'activitat inicial coneguda i l'àrea activa del detector, s'obté una eficiència específica de detecció del triti de

$$S = (9,6 \pm 3,9) \cdot 10^{-6} \text{ L kBq}^{-1}\text{s}^{-1}\text{cm}^{-2}$$

(a)
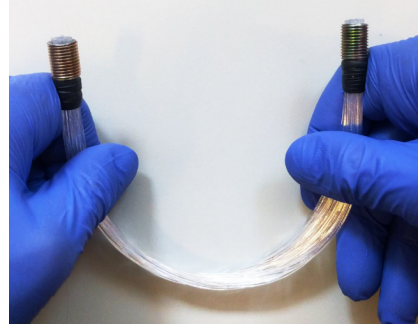
(b)
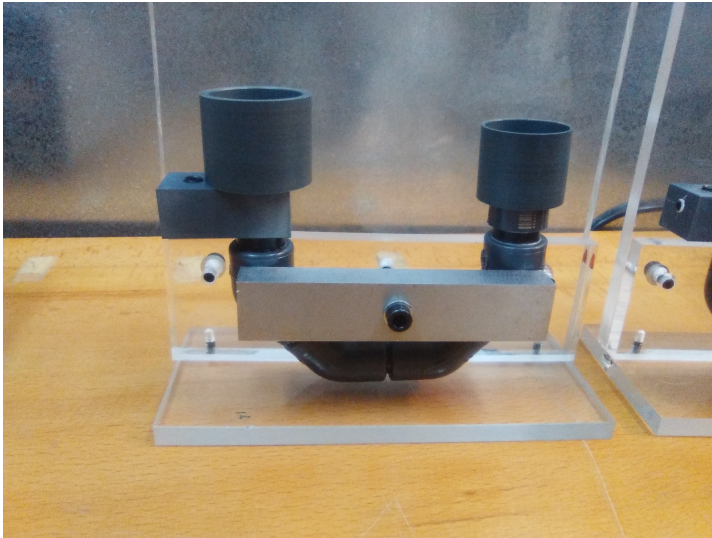
(c)

Figure 9.14 – a) Peça metàl·lica utilitzada per a unir les fibres centelle-jadores a l'atuell del prototip TRITIUM-IFIC-0. b) Feix de fibres centelle-jadores utilitzades en el prototip TRITIUM-IFIC-0. c) Atuell del prototip TRITIUM-IFIC-0.
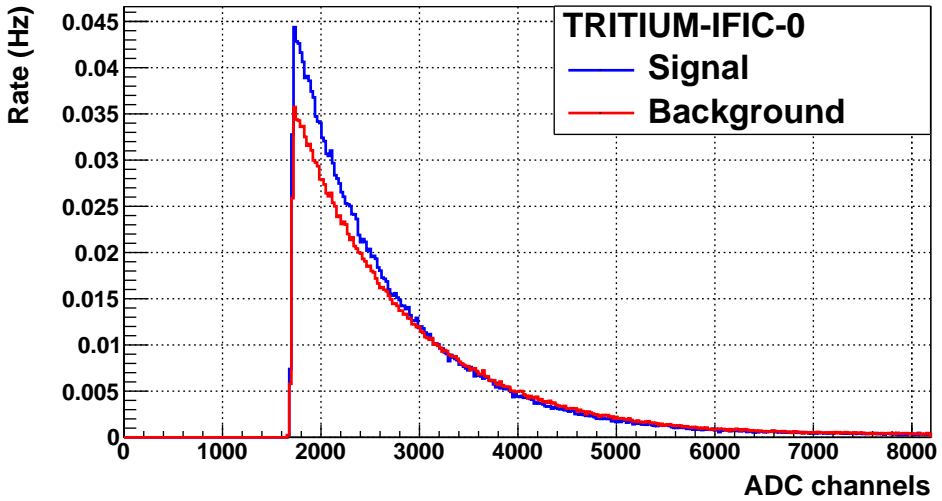
(a) .
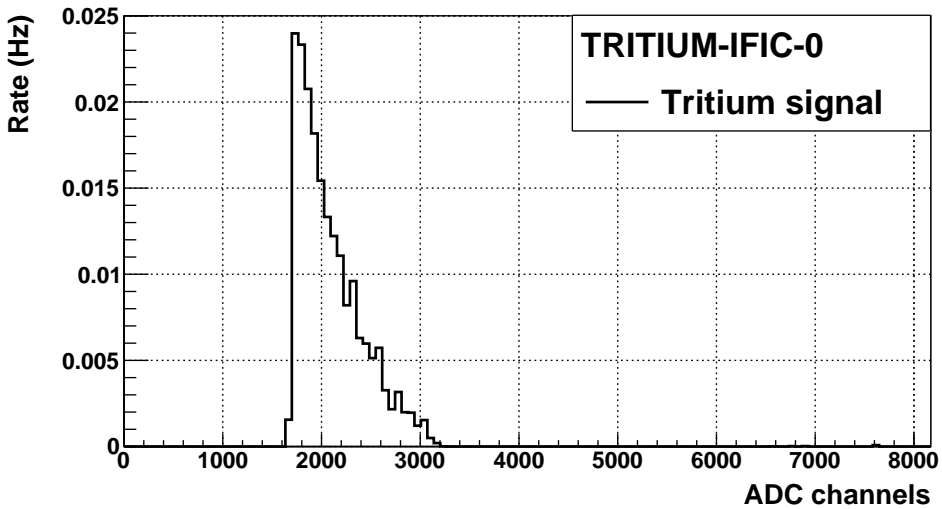
(b)

Figure 9.15 – Espectres d'energia mesurats amb el prototip TRITIUM-IFIC-0. a) Espectres mesurats amb els prototips de senyal i fons. b) Espectre del triti.

Espectres	Taxa
Prototip del senyal	$2,27 \pm 0,06$
Prototip del fons	$2,06 \pm 0,06$
Espectre de triti	$0,21 \pm 0,09$

Taula 9.2: Taxes de comptatge mesurades amb el prototip TRITIUM-IFIC-0.

eficiència similar a algunes de les obtingudes en detectors de triti desenvolupats en altres col·laboracions [Mur67, Mog69]. Es van trobar els següents problemes en aquest prototip:

1. Es va comprovar amb un test de laboratori que la curvatura de les fibres produïa una pèrdua excessiva de fotons, ja que aquests necessitaven fer més reflexions fins a arribar als fotosensors. Aquest problema es va resoldre simplement dissenyant un atuell per al prototip TRITIUM-IFIC-1 on les fibres estigueren rectes.

2. A més es va aplicar un protocol de neteja de les superfícies de les fibres utilitzades al prototip TRITIUM-IFIC-1. Amb aquest s'aconsegueix incrementar l'eficiència de col·lecció dels fotons al voltant d'un 30%.

3. També es va observar que els fotons que havien escapat de les fibres eren ràpidament absorbits per l'atuell de PVC i, per tant, perduts. Un material més adequat per l'atuell seria, per exemple, el politetrafluoroetilè (PTFE), que presenta un factor de reflexió dels fotons visibles d'aproximadament el 95%, augmentant la probabilitat de qué el fotó puga ser detectat pels fotosensors.

4. Finalment, s'utilitza una estructura per a mantenir una distància d'1 cm entre fibres. Aquesta modificació va ser utilitzada per a assegurar que l'aigua tritiada cobrisca tota la superfície activa del detector.

Tenint en compte tots aquests problemes identificats en el disseny del primer prototip, es va dissenyar i construir als tallers de l'IFIC un segon prototip, anomenat TRITIUM-IFIC-1, mostrat a la Figura 9.16, on totes les modificacions proposades foren implementades. El prototip TRITIUM-

Figure 9.16 – Vista general del prototip TRITIUM-IFIC-1.

IFIC-1 consisteix en 64 fibres d'1 mm de diàmetre i 20 cm de longitud polides manualment i organitzades en una matriu de PTFE de 8×8, mostrada a la Figura 9.17. Aquesta matriu de fibres està situada a l'interior d'un atuell de PTFE i és llegida per un PMT calibrat model $R8520 - 460$ de Hamamatsu Photonics [Ham19] acoblat amb greix òptic [Saib]. Es van mesurar espectres d'energia similars al cas del prototip anterior, els quals es mostren a la Figura 9.18. L'activitat de la dissolució de triti utilitzada va ser la mateixa que la utilitzada en l'experiència anterior. Les taxes de recomptes mesurades pel prototip TRITIUM-IFIC-1 són mostrades a la Taula 9.3

L'eficiència específica de detecció del triti obtinguda per a aquest
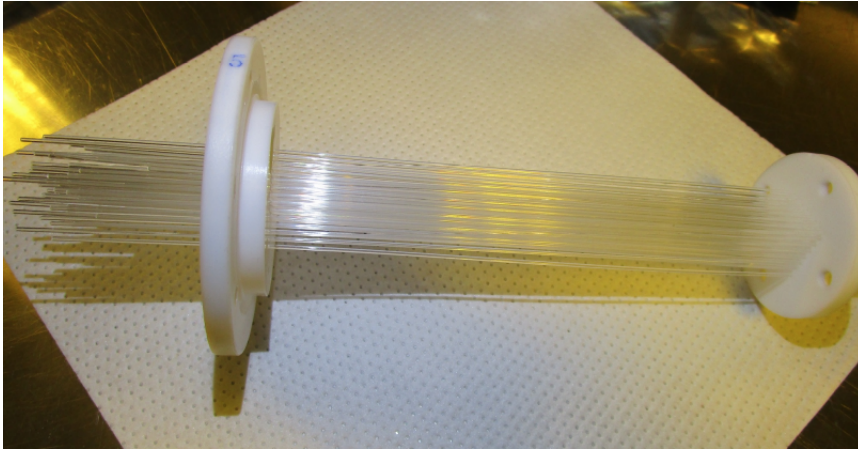
Figure 9.17 – Estructura de PTFE utilitzada al prototip TRITIUM-IFIC-1.

Espectres	Taxa
Prototip del senyal	$7,82 \pm 0,11$
Prototip del fons	$3,99 \pm 0,08$
Espectre de triti	$3,83 \pm 0,13$

Taula 9.3: Taxes de comptatge mesurades amb el prototip TRITIUM-IFIC-1.

detector és

$$S = (9,6 \pm 0,4) \cdot 10^{-5} \text{ L kBq}^{-1}\text{s}^{-1}\text{cm}^{-2}$$

un ordre de magnitud millor que l'obtinguda amb el prototip anterior. Aquest ordre de magnitud es deu al conjunt de totes les modificacions realitzades en aquest disseny. Aquesta eficiència específica obtinguda és similar a la millor eficiència específica obtinguda fins ara amb detectors de triti similars desenvolupats en altres col·laboracions [Hof92a, Hof92b]. Veiem per tant que el detector de triti desenvolupat en la col·laboració TRITIUM és competitiu amb els detectors similars desenvolupats fins ara.
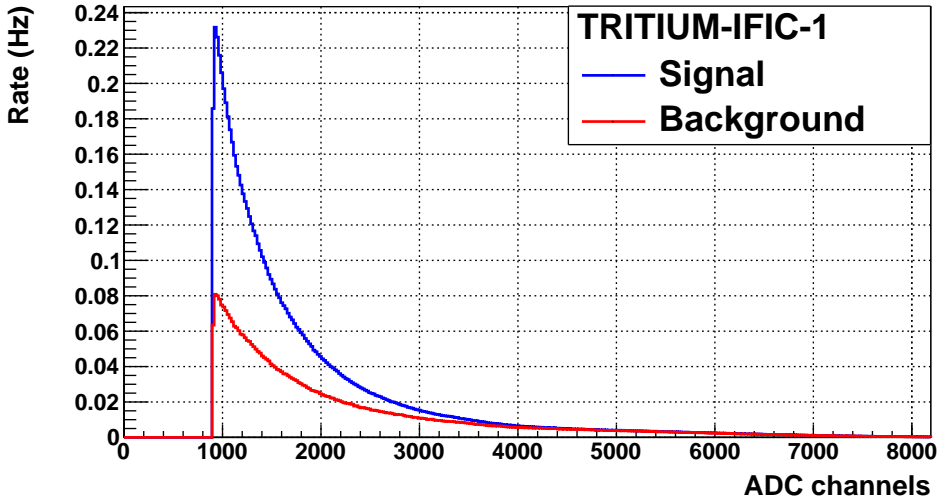
(a)
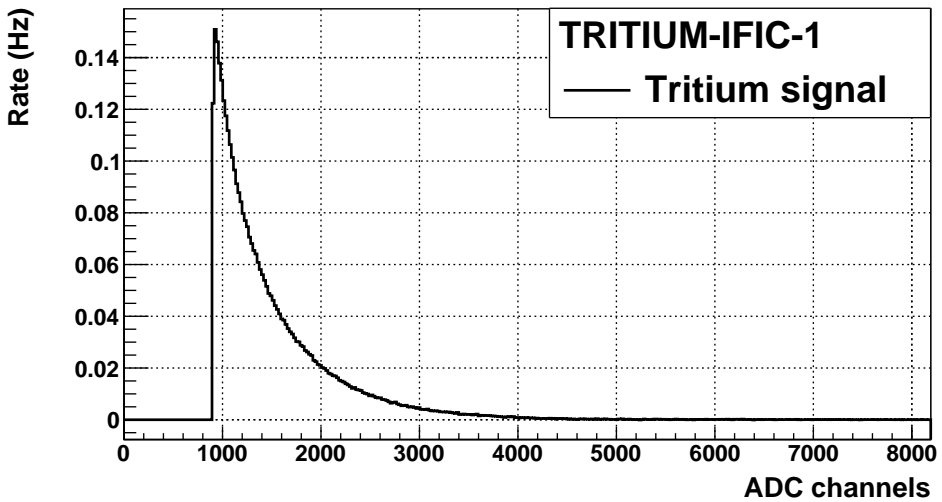
(b)

Figure 9.18 – Espectres d'energia mesurats amb el prototip TRITIUM-IFIC-1. a) Espectre d'energia de senyal i fons. b) Espectre d'energia del triti.

9.3.2 Últims prototips

S'ha dissenyat i construït dos prototips, anomenats TRITIUM-Aveiro i TRITIUM-IFIC-2, amb un disseny funcional i optimitzat per a la detecció del triti en els que tots els problemes identificats en els dos primers prototips han sigut resolts. Aquests dos prototips, mostrats a la figura 9.19, presenten un disseny similar que consisteix en un atuell de PTFE a l'interior del qual se situen les fibres centellejadores. Per permetre la utilització d'un gran nombre de fibres (cents) aquestes es van situar lliurement dins l'atuell, prescindint de la matriu de PTFE i amb una densitat de fibres que permeta fluir l'aigua a través d'elles. A més, es van realitzar coincidències entre dos PMTs acoblats amb greix òptic a cada extrem de les fibres, necessari per a reduir el fons radioactiu tant com siga possible. Per poder realitzar de forma segura aquesta coincidència va ser necessari implementar en l'atuell dues finestres de polimetilmetacrilat (PMMA) que permeten als fotons generats a les fibres (dins de l'atuell) arribar fins als PMTs (fora de l'atuell). Els PMTs utilitzats en cada prototip són del model $R2154 - 02$ de Hamamatsu [Ham10] per a TRITIUM-Aveiro (el qual conté 360 fibres) i el model $R8520 - 406$ de Hamamatsu [Ham19] per a TRITIUM-IFIC-2 (el qual conté 800 fibres). Aquests dos prototips presenten diferències subtils en el disseny. Entre les més importants es troben:

1. El diàmetre de les fibres, 2 mm per a les utilitzades en TRITIUM-Aveiro i 1 mm per a les utilitzades en TRITIUM-IFIC-2. Un diàmetre més gran li confereix una major rigidesa al prototip i millora el flux de l'aigua a través de les fibres. No obstant això, també implica una relació senyal/fons menor, donant lloc a una eficiència més baixa i, per tant, a una MDA per al triti més alta.

2. A més, el protocol de tractament de la superfície de les fibres centellejadores no va ser aplicat a les fibres utilitzades en TRITIUM-Aveiro, ja que aquest encara no estava desenvolupat. Com s'ha provat amb tests experimentals, aquest tractament millora la intensitat del senyal

en més d'un factor dos, que a causa dels xicotets senyals generats pels esdeveniments del triti implica una millora substancial en l'eficiència de detecció.

3. L'ús de fotosensors diferents. TRITIUM-Aveiro utilitza dos PMTs en coincidència mentre que la proposta per a TRITIUM-IFIC-2 és utilitzar matrius de SiPMs. Els SiPMs tenen una major eficiència de fotodetecció, que dona com a resultat una major eficiència de la detecció del triti. No obstant això, aquests presenten un soroll electrònic més alt, incrementant el fons mesurat pel detector.

Totes aquestes opcions seran provades i aquelles amb millors resultats seran implementades al prototip final. L'objectiu d'aquests prototips és mesurar l'eficiència de la detecció del triti i la MDA. Per tant, l'activitat de la dissolució d'aigua tritiada emprada va ser 30 i 10 kBq/L per a TRITIUM-Aveiro i TRITIUM-IFIC-2, respectivament. Aquesta activitat és inferior a la utilitzada en els prototips inicials.

Els espectres d'energia mesurats amb TRITIUM-IFIC-2 i les respectives taxes de comptatge mesurades són mostrades a la Figura 9.20 i a la Taula 9.4, respectivament. TRITIUM-Aveiro utilitza una electrònica diferent que mesura directament taxes de comptatge sense la necessitat d'obtenir els espectres d'energia. Aquestes taxes obtingudes són també mostrades a la Taula 9.4.

Espectres	TRITIUM-Aveiro	TRITIUM-IFIC-2
Prototip del senyal	$10,9 \pm 0,4$	$19,05 \pm 0,18$
Prototip del fons	$9,0 \pm 0,4$	$11,54 \pm 0,14$
Espectre de triti	$1,9 \pm 0,6$	$7,11 \pm 0,23$

Taula 9.4: Taxes de comptatge mesurades amb el prototip TRITIUM-IFIC-2.

(a)

(b)

Figure 9.19 – a) Atuell de TRITIUM-Aveiro. b) Atuell de TRITIUM-IFIC-2.
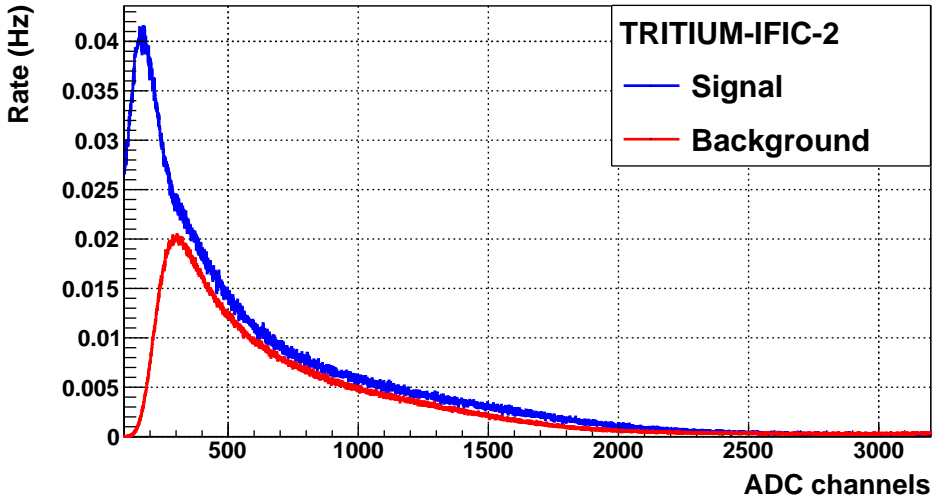
(a)
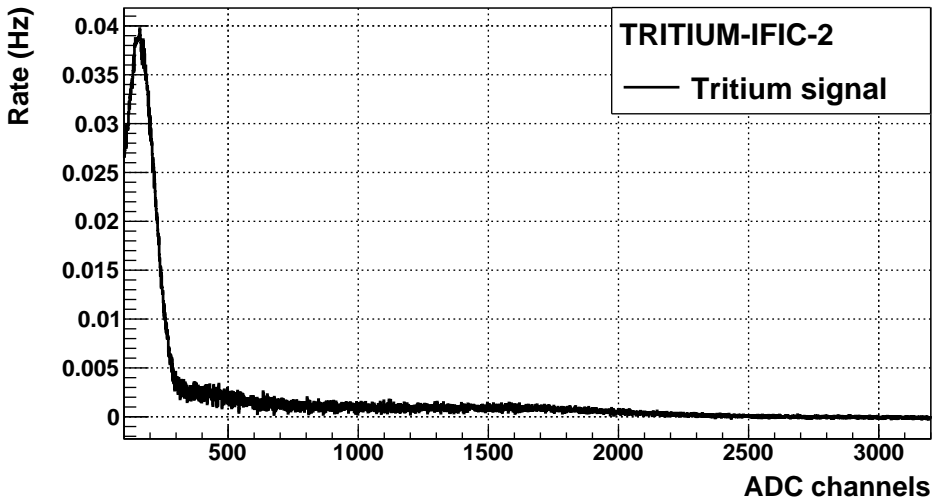
(b)

**Figure 9.20** – Espectres d'energia mesurats amb TRITIUM-IFIC-2. a) Espectre d'energia de senyal i fons. b) Espectre d'energia del triti.

L'eficiència específica de la detecció del triti en aigua és

$$S = (1,6 \pm 0,5) \cdot 10^{-5} \text{ L kBq}^{-1}\text{s}^{-1}\text{cm}^{-2}$$

$$S = (14,1 \pm 0,6) \cdot 10^{-5} \text{ L kBq}^{-1}\text{s}^{-1}\text{cm}^{-2}$$

per a TRITIUM-Aveiro i TRITIUM-IFIC-2, respectivament. Com es pot observar, l'eficiència de TRITIUM-IFIC-2 millora l'obtinguda amb els prototips anteriors i els detectors de triti similars desenvolupats fins ara [Hof92a, Hof92b]. Veiem per tant que s'ha superat l'estat actual de l'art de la detecció de triti en l'aigua utilitzant plàstics centellejadors. No obstant això, trobem una eficiència específica inferior a l'esperada per al prototip TRITIUM-Aveiro. Tot indica que aquest dèficit d'eficiència és causat principalment per l'absència del tractament de la superfície a les fibres centellejadores, una cosa que ha de ser estudiat amb més deteniment.

La mínima activitat de triti mesurable pels prototips s'obté aplicant el criteri de Currie [Kno10]. Els valors obtinguts són $3,6$ i $0,2$ kBq/L per a mesures d'una hora per a TRITIUM-Aveiro i TRITIUM-IFIC-2, respectivament.

L'estabilitat de l'eficiència del prototip TRITIUM-IFIC-2 es va comprovar fent mesures al llarg de mesos, les quals es mostren a la Figura 9.21. Com es pot observar, no s'aprecia cap decreixement durant els sis mesos de mesura, obtenint-se un comportament estable del detector amb una desviació estàndard relativa de la taxa de comptatge del $2,5\%$.

El prototip TRITIUM-Aveiro va ser instal·lat en Arrocampo el 27 de març de 2019 i va estar prenent mesures del fons radioactiu durant més de quatre mesos, fins al 18 d'agost de 2019. En aquestes mesures, mostrades a la Figura 9.22, es pot observar una gran estabilitat al voltant d'una taxa de comptatge de $9,31$ Hz. També s'observa un pic el dia 2 de maig causat per l'obertura del castell de plom.
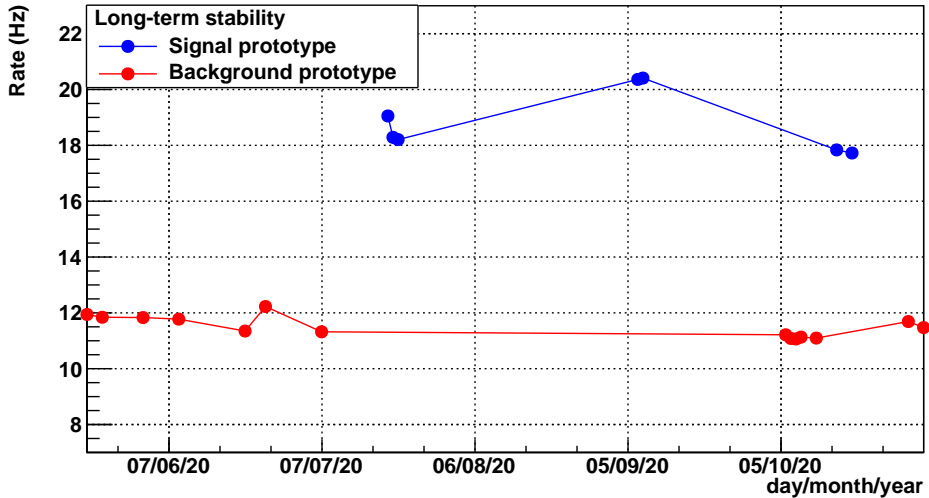
Figure 9.21 – Taxes de comptatge de fons i senyal mesurades amb el prototip TRITIUM-IFIC-2 al llarg de diversos mesos.

9.3.3 Disseny modular del detector TRITIUM

El monitor TRITIUM presenta un disseny modular, és a dir, consta de diversos prototips, anomenats mòduls quan formen part del monitor, que són llegits en paral·lel. Un disseny esquemàtic del monitor format per 10 mòduls TRITIUM-IFIC-2 es mostra a la Figura 9.23. Aquesta modularitat és una de les propietats més rellevants del monitor, ja que li confereix la possibilitat de millorar algunes de les seues característiques de forma proporcional al nombre de mòduls. Una de les propietats més importants per al projecte TRITIUM és la MDA, la millora del qual depén proporcionalment a l'arrel quadrada del nombre de mòduls. La Figura 9.24 mostra el comportament esperat del MDA per al monitor TRITIUM basat en els resultats experimentals obtinguts amb TRITIUM-IFIC-2 en funció del nombre de mòduls. La línia de color roig mostra l'objectiu del projecte TRITIUM de 100 Bq/L. Com es pot veure, s'espera aconseguir aquest objectiu amb 5 mòduls TRITIUM-IFIC-2 llegits en paral·lel.
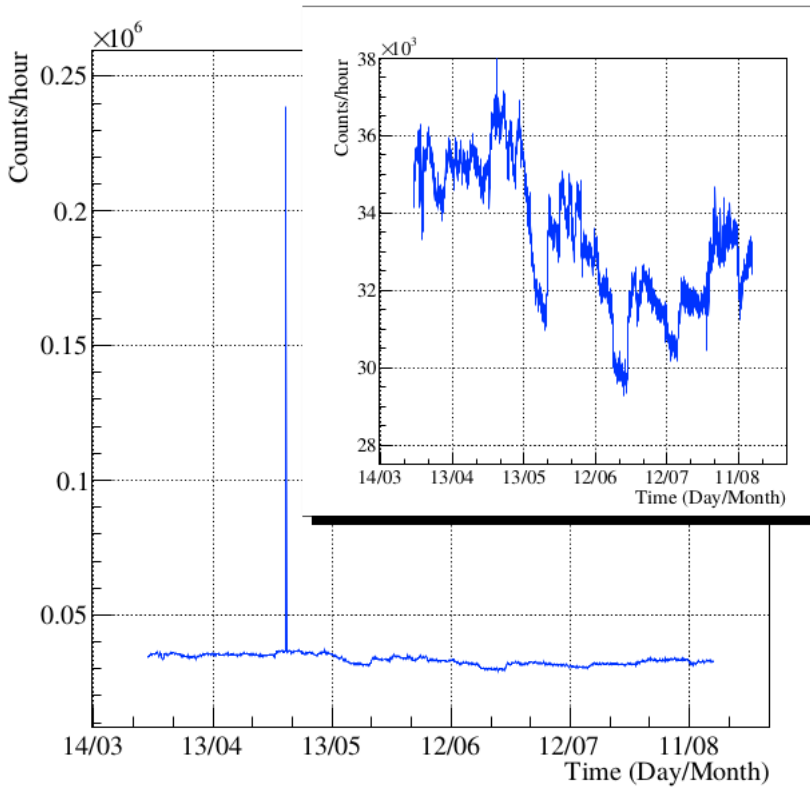
Figure 9.22 – Mesures del fons radioactiu d'Arrocampo obtingudes amb el prototip TRITIUM-Aveiro.[Aze22].

Amb l'ajuda de simulacions es va estudiar com varia la resolució del monitor en funció del nombre de mòduls, paràmetre que indica la mínima variació de l'activitat de triti que és possible identificar. Com es pot observar a la Figura 9.25, resolucions més baixes són obtingudes amb més mòduls, permetent diferenciar variacions més xicotetes de l'activitat de la mostra. Amb 5 mòduls TRITIUM-IFIC-2 llegits en paral·lel s'aconsegueix identificar correctament variacions de l'activitat del triti de 100 Bq/L en mesures d'1 h.
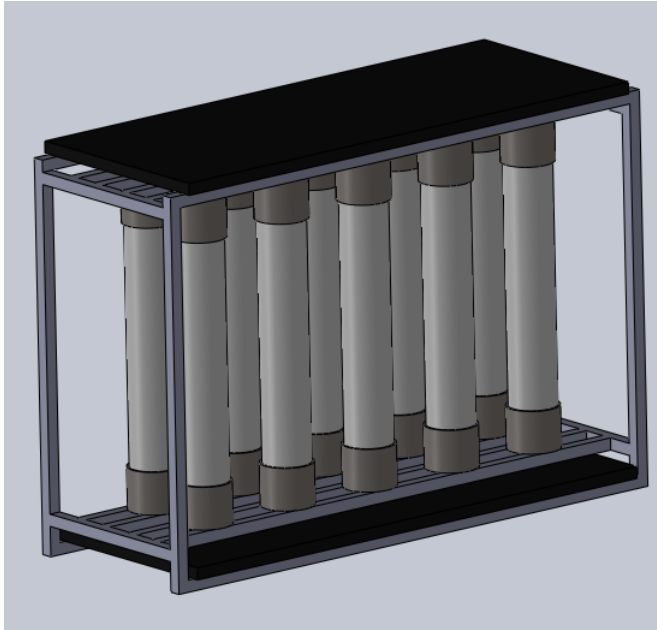
Figure 9.23 – Disseny esquemàtic del monitor TRITIUM basat en el prototip TRITIUM-IFIC-2.

9.4 Estat actual i resum dels resultats obtinguts en el projecte TRITIUM

El triti és un dels elements radioactius produïts més abundantment en instal·lacions nuclears. A causa de la seua radiotoxicitat, l'exposició a un excés de triti podria afectar la salut humana i el medi ambient, motiu pel qual molts països han implementat un límit legal per al triti en aigües potables. Aquest límit és establert a Espanya a 100 Bq/L pel CSN seguint la directiva del consell EURATOM [Eur14].

El projecte TRITIUM es va fundar amb l'objectiu de dissenyar i construir un monitor capaç de mesurar en temps quasireal (1 h o menys) activitats de triti en l'aigua inferior al límit legal. El monitor construit fins ara, anomenat TRITIUM consta de tres parts, el detector de triti, on es
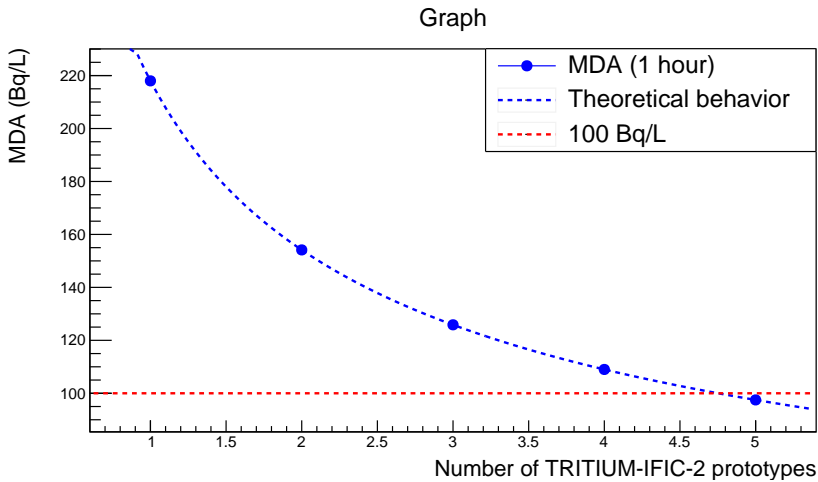
Figure 9.24 – Mínima activitat de triti detectable pel monitor TRITIUM en funció del nombre de mòduls TRITIUM-IFIC-2 emprats.

fa la mesura de l'activitat del triti en aigua, el sistema de rebuig del fons radioactiu, destinat a minimitzar el fons radioactiu mesurat pel detector de triti, i el sistema de purificació de l'aigua, utilitzat per a eliminar partícules i minerals a la mostra d'aigua que pugen reduir l'eficiència del detector. Els avanços realitzats fins ara per la col·laboració TRITIUM es llisten a continuació:

1. Es va construir un monitor per a mesurar baixes activitats de triti en aigua. Aquest presenta un disseny modular el qual li confereix la propietat d'escalabilitat, és a dir, algunes de les característiques relle- vants del detector, com ara l'MDA o la resolució, poden ser millorades mitjançant la utilització de més mòduls llegits en paral·lel.

2. Es van dissenyar, construir i caracteritzar un total de quatre proto- tips del detector de triti basats en fibres centellejadores llegides per fotosensors. Amb aquests prototips fou possible identificar i soluci- onar problemes greus en el disseny, a més d'implementar possibles modificacions que optimitzen la detecció del triti.
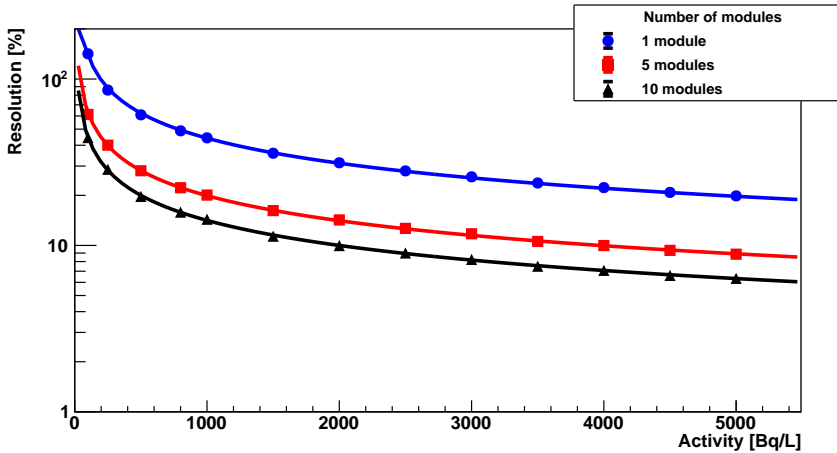
Figure 9.25 – Resolució del monitor TRITIUM basat en mòduls TRITIUM-IFIC-2 en funció del nombre de mòduls.

3. Es van realitzar diverses simulacions amb la llibreria Geant4 per comparar diversos dissenys del detector. L'objectiu d'aquestes simulacions era decidir la configuració que optimitza l'eficiència de detecció del triti en aigua.

4. Es va desenvolupar un protocol de tractament de la superfície de les fibres centellejadores que va ser avaluat, obtenint una millora de la col·lecció de fotons de més d'un factor 2. També es va realitzar una caracterització de les fibres centellejadores, obtenint una eficiència de col·lecció de $(76 \pm 8)\%$ i una incertesa en el nombre de fotons llegits pel fotosensor d'al voltant d'un 3%.

5. Així mateix, es va caracteritzar un SiPM, model S13360-1375 de Hamamatsu on molts dels paràmetres rellevants per al projecte TRTI-UM, com per exemple el guany, van ser mesurats amb una excel·lent precisió (resolució de l'espectre del fotoelectró al voltant de l'1%). A més, a causa de la forta dependència del resposta del SiPM amb la temperatura, es va aplicar amb èxit un mètode d'estabilització del guany, obtenint una variació d'al voltant del $0,1\%$ en el rang de tem-

peratures de treball ($[20 - 30]°$C).

6. Es va dissenyar, construir i caracteritzar un sistema de rebuig del fons radioactiu basat en dues parts, un castell de plom amb parets de 5 cm de gruix i un veto actiu basat en plàstics centellejadors. A partir de simulacions es va obtenir una reducció del nombre de rajos còsmics detectats pel monitor TRITIUM d'un factor $5, 5$ a causa del castell de plom i del 60% a causa del veto actiu, donant una reducció total del $92, 7\%$. Aquesta reducció causada pel veto actiu s'inferior a l'obtinguda experimentalment, probablement causat pel fet de no incloure el recobriment del veto en les simulacions. Per tant, s'espera un factor de reducció total major a l'obtingut per simulacions.

7. També es va dissenyar, construir i caracteritzar un sistema de purificació de l'aigua, necessari per a eliminar les partícules i els minerals dissolts. Amb aquest sistema va ser possible assolir nivells de conductivitat de l'aigua d'al voltant de 10 μS/cm sense afectar l'activitat del triti.

8. Amb el prototip TRITIUM-IFIC-2, l'últim prototip desenvolupat en la col·laboració TRITIUM, es va obtenir una eficiència específica en la detecció del triti de

$$S = (14, 1 \pm 0, 6) \cdot 10^{-5} \text{ L kBq}^{-1}\text{s}^{-1}\text{cm}^{-2}$$

i un MDA de 220 Bq/L per a mesures d'1 hora, millorant l'actual estat de l'art de la detecció del triti.

9. A partir dels resultats experimentals obtinguts amb TRITIUM-IFIC-2 i tenint en compte la propietat d'escalabilitat del monitor, s'espera aconseguir l'activitat de 100 Bq/L, objectiu del projecte TRITIUM, amb 5 mòduls llegits en paral·lel.

10. L'estabilitat del prototip TRITIUM-IFIC-2 va ser provada al llarg de diversos mesos, tant pel senyal com pel fons, obtenint una desviació

estàndard relativa d'al voltant de $2,5\%$.

Actualment el prototip TRITIUM-Aveiro està instal·lat a Arrocampo juntament amb el sistema de purificació de l'aigua i el castell de plom. Aquest prototip ha estat realitzant mesures del fons radioactiu d'Arrocampo durant més de quatre mesos, mostrant una gran estabilitat. En un futur pròxim s'espera poder instal·lar dos prototips TRITIUM-Aveiro addicionals i un veto actiu. A més, tres mòduls TRITIUM-IFIC-2 i un veto actiu estan llests per ser instal·lats tan prompte com siga possible.

Appendices

Appendix A

Electronics for the SiPM Characterization

The electronics employed to characterize the S13360-6075 SiPM from Hamamatsu is described in this appendix. This electronics consists of three different PCBs connected through HDMI connectors:

1. In the first PCB, shown in Figure A.1, up to 8 SiPMs and one temperature sensor are connected. This PCB is placed inside a light-tight box from Thorlabs [Thoa]. This black box has a small hole of 1 mm diameter prepared to introduce an optical fibre[1] to illuminate SiPMs with a 430L LED from Thorlabs [Tho18]. The spectrum of this LED, shown in Figure A.4, was measured with a spectrometer. The emission peak is located at 436 nm with an FWHM of 19 nm. With the help of this LED, the light emission of the TRITIUM scintillating fibres was simulated to calibrate the SiPMs at the working wavelength.

2. In the second PCB, shown in Figure A.2, the signals of the SiPMs are summed and amplified by a factor of either $G = 4187$ or $G = 10761$,

---

[1]The optical fibre used is BCF-98 from Saint-Gobain [Sai21a]

depending on the input resistance of the oscilloscope, 50 Ω or 1 MΩ respectively. This PCB includes a differential amplifier to reduce the electronic noise of the system.

3. In the third PCB, shown in Figure A.3, the different input and output signals are rearranged to avoid crosstalk. The input signals are the supply voltage of the SiPMs and the PCBs (± 6 V) and the output signals are the temperature sensor signal and the sum of the SiPM signals. The output signal of the third PCB is recorded by an MSO44X oscilloscope from Tektronix [Tek21].
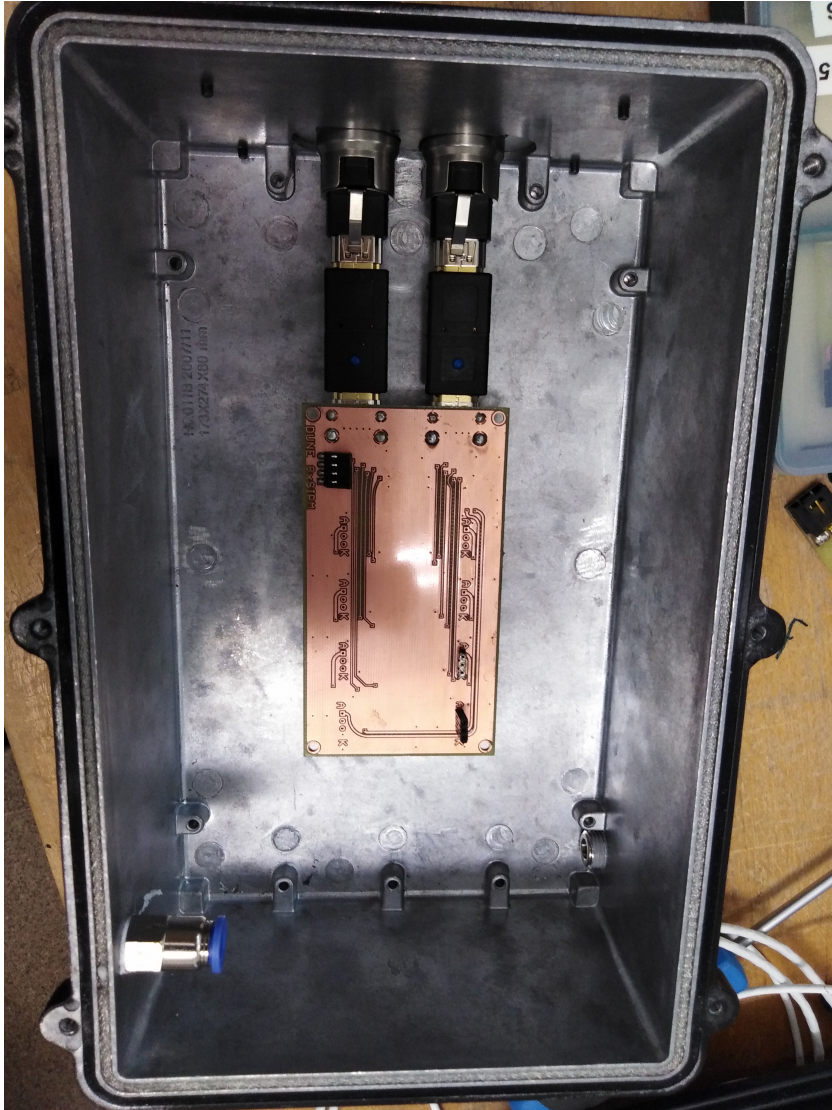
Figure A.1 – The PCB 1 in which up to 8 SiPMs are connected inside the black box.
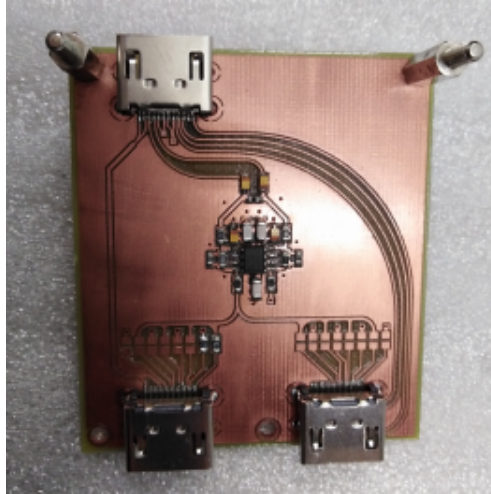
Figure A.2 – The PCB 2 in which the SiPMs output signals are summed and amplified.
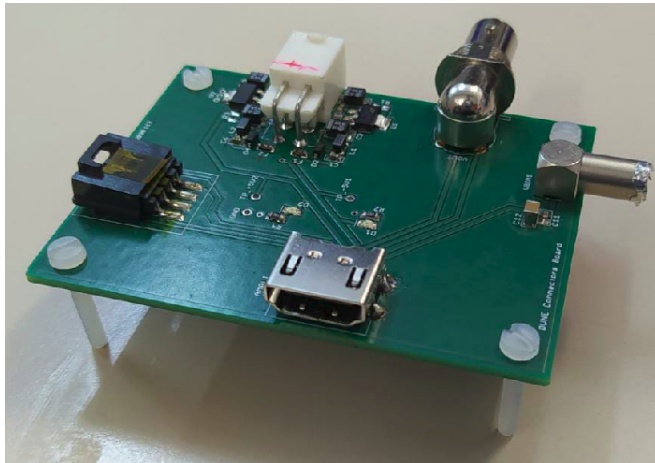
Figure A.3 – The PCB 3, in which the input and output signals of the system are rearranged.
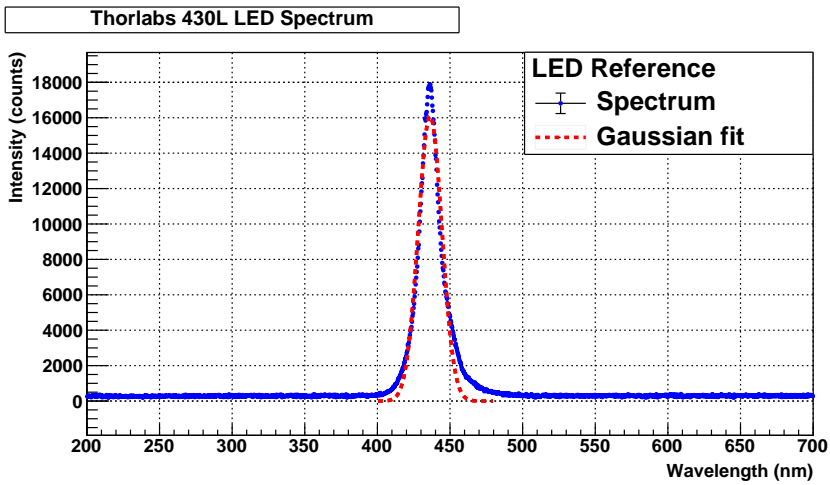
Figure A.4 – The LED emission spectrum.

Appendix B

The Water Purification System

In this appendix, several pictures of the water purification system are shown. The scheme of the whole water purification system is shown in Figure B.1. The gross filtering stage made of silex-anthracite and garnet filters, the fine filtering stage consisting of a 20 μm filter and the super-fine filtering stage composed of a 1 μm filter of active carbon and UV lamps, are shown in Figure B.2. The double phase reverse osmosis and the containers in which pure and reject water are gathered after treatment are displayed in Figure B.3. Two displays of the Siemens Programmable Logic Controller (PLC) that controls the water purification system are shown in Figure B.4. Finally, a picture of the whole water purification system is displayed in Figure B.5. Samples of raw, rejected and pure water are shown in Figure B.6, where their difference in turbidity are seen.

Figure B.1 – Scheme of the water purification system.
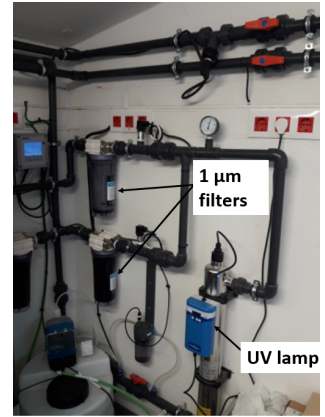
Figure B.2 – Different stages of filtration of the water purification system. a) The gross filtering stage. b) The fine filtering stage. c) The super-fine filtering stage.

(a)

(b)

Figure B.3 – a) Doble phase reverse osmosis stage. b) Containers used to gather the output water of the water purification system.

(a)
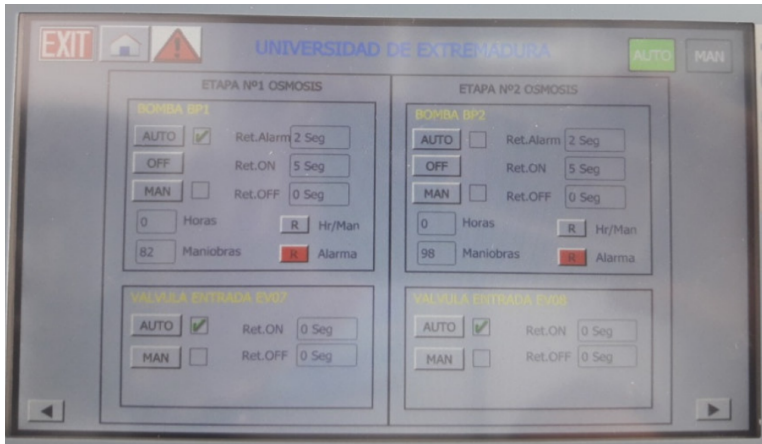
(b)

Figure B.4 – Siemens PLC displays of the remote control of the water purification system.

Figure B.5 – Picture of the water purification system.
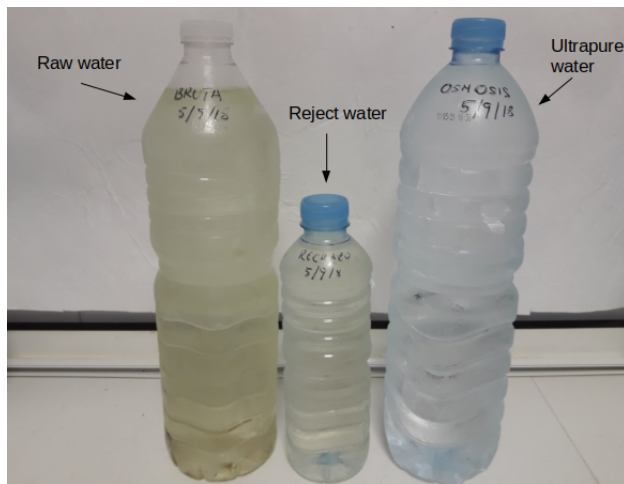
Figure B.6 – Raw, reject and pure water obtained with the water purification system.

Appendix C

Preparation of Tritiated Water Sources

Radioactive liquid sources were prepared from 1.86 g (uncertainty of 0.05%) of tritiated water, purchased from PTB [Phy]. The activity of this tritium source was 26.8 MBq/g (uncertainty of 2.24%, reference date of 1/1/2017). This source was dissolved in 500 mL (uncertainty of 0.05%) of hyper-pure water (conductivity of 0.72 μS/cm), resulting in a solution of 500 mL of tritiated water with an activity of 100 kBq/g (uncertainty of 2.24%), that is 99.7 kBq/L (uncertainty of 2.24%) at STP. The radioactive sources with smaller activity are prepared by dilution of this initial radioactive source with hyper-pure water.

Appendix D

Electronic System of TRITIUM-Aveiro

The electronics of the TRITIUM-Aveiro prototype consist of:

1. A PCB designed to power the PMTs with a negative high voltage which consists of several C11152-01 HV power supplies from Hamamatsu Photonics [Ham15]. This PCB is controlled by a MAX5500 DAC[1] from Maxim Integrated [Max09]. Its electronic scheme is shown in Figure D.1. An Arduino Mega controls the DAC communication and is connected to a Raspberry Pi that runs the whole system. A graphical interface, shown in Figure D.2, was developed to set up the different options in an easy way.

2. An electronic chain which consists of several PCBs that process and analyzes the system signals. Its scheme, shown in Figure D.3, consists of two lines for the PMT signals of the prototype and another one for the active veto PMT.

---

[1]Digital-to-Analogue Converter
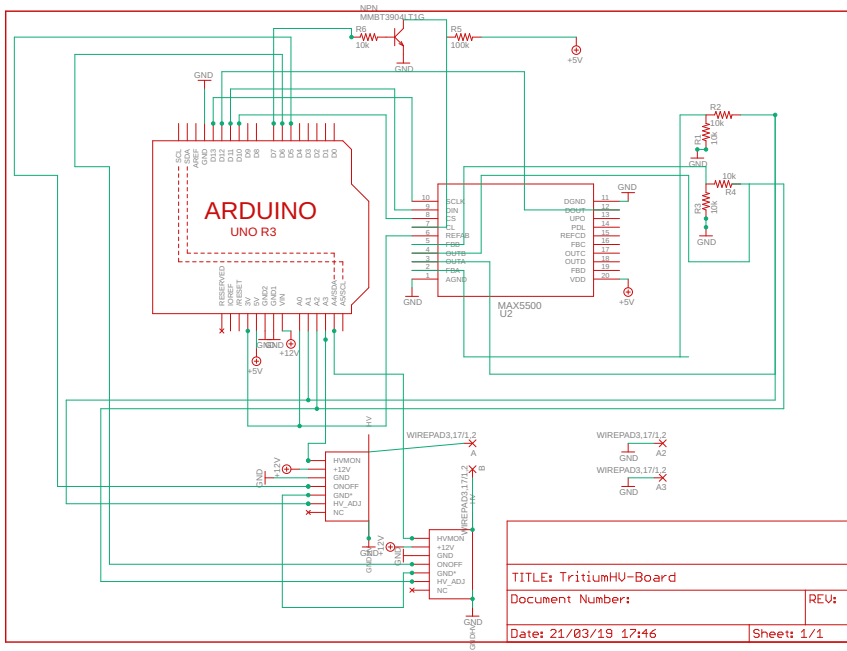
Figure D.1 – Electronic scheme of the PCB designed to power the PMTs of the Aveiro prototype.

To test this electronic chain, a plastic scintillator of $10 \times 10 \times 1$ cm^3 was used as a veto signal. Four different $50 \times 30 \times 2$ cm^3 rectangular vetoes made of plastic scintillator from Saint-Gobain [Sai21c] are being built. The vetoes are read out by 2" R2154-02 PMTs from Hamamatsu Photonics [Ham10]. The PMT signals of the prototype are preamplified and shaped by a CR111 preamplifier from CREMAT Inc. [CRE20]. To reduce electronic noise and signal loss, both preamplifiers are connected as close as possible to the PMTs and they are placed inside aluminium boxes which act as Faraday cages. Each preamplifier is followed by a differentiator stage which reduces the width of the signal and an OPA656 operational amplifier from Texas Instruments [Tex15]. An LT111 fast comparator from Linear Technology [Lin] is used to set a threshold that removes PMT signals with low amplitude
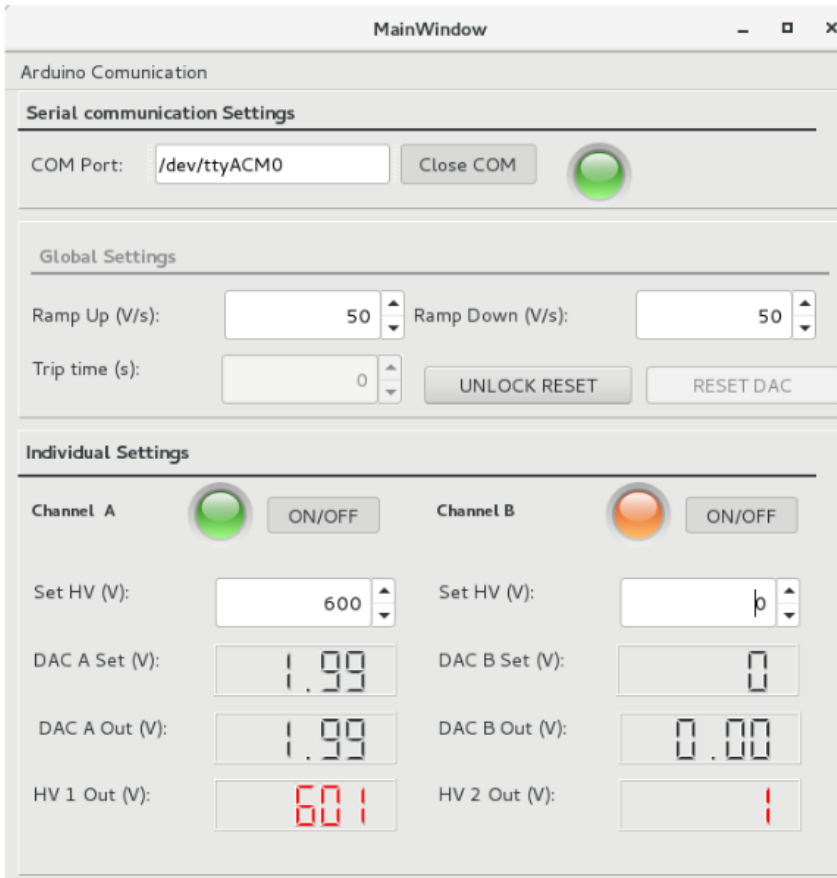
Figure D.2 – Graphical user interface developed to control the prototype.

(dark counts of the PMTs). A MAX5500 DAC is used to configure the thresholds. As the time width of the amplifier output signal is 200 μs, a second differentiator was included to reduce random coincidences. To restore a 5V square signal a second comparator was added. Finally, a tunable pulse stretcher based on a SN74AHC1 OR gate from Texas Instruments [Tex17] sets the signal time width to 100 ns, obtaining a system coincidence window of 200 ns.

The veto line consists of an inverter, which gives 0 V when there is a veto signal and 5 V otherwise. A stretcher sets the signal time width
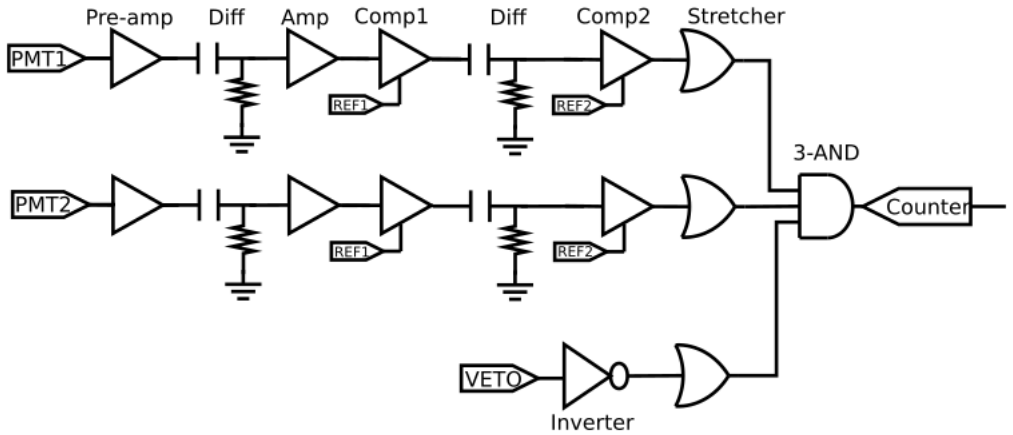
Figure D.3 – Electronic scheme of the DAQ that process and analyze the signal of the TRITIUM-Aveiro prototype.

to 100 ns.

The signals from the three lines are introduced into a 3-input SN74LVC1G11 AND gate from Texas Instruments [Tex16] which generates an output signal when both PMT signals are in coincidence and the veto signal is in anti-coincidence. The output signal of this stage is connected to a pulse counter.

The GPIO pins of a Raspberry Pi are used to communicate with the system and configure the threshold levels. A graphical user interface, shown in Figure D.4, was developed to set the counter system in an easy way. In Figure D.5, screenshots for accepted and rejected events are displayed.
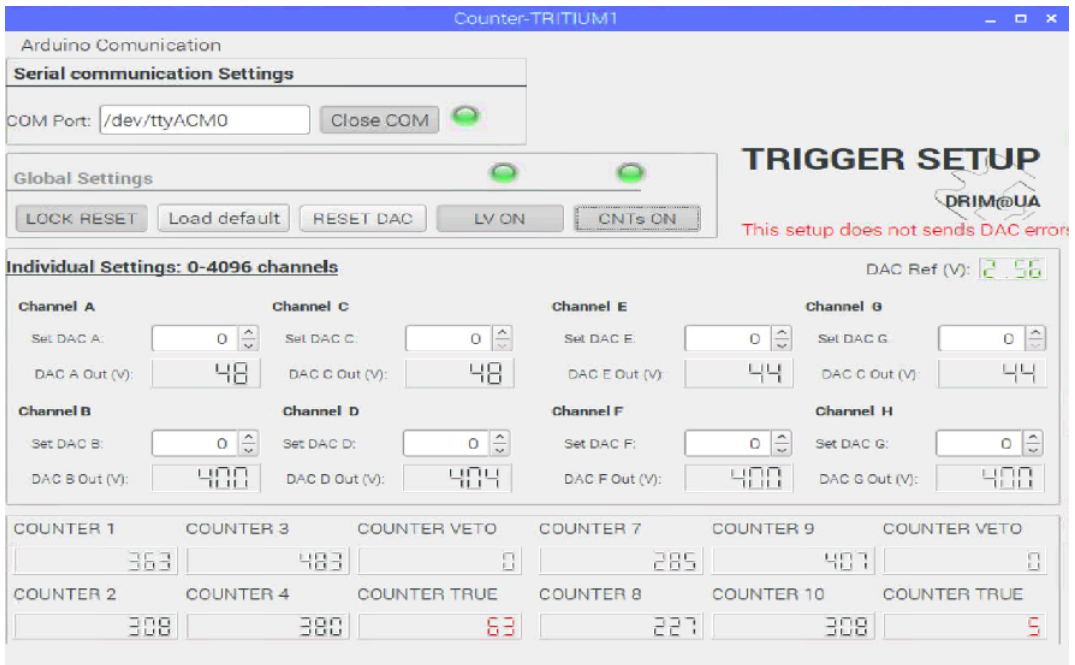
Figure D.4 – Graphical user interface used to manage the counter system.
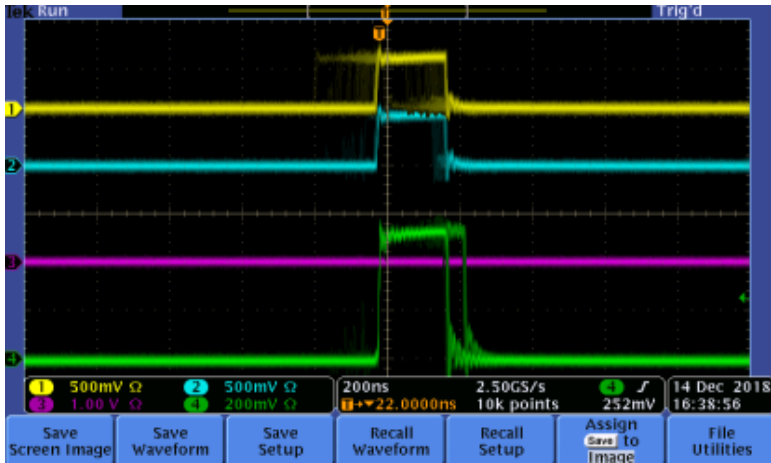
(a)
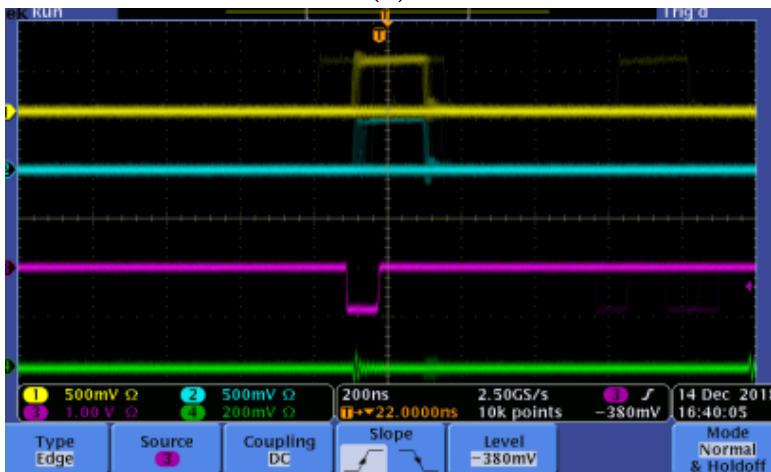
(b)

Figure D.5 – The yellow and blue lines are the prototype PMT signals, the pink line is the veto PMT signal and the green line is the AND logic output. a) Tritium event accepted since the veto is not fired. b) Background event rejected as the veto is fired.

Bibliography

[Ago03]   Agostinelli, S. et al., *Geant4— A Simulation Toolkit*, Nuclear Instruments and Methods in Physics Research Section A: Accelerators, Spectrometers, Detectors and Associated Equipment **506** (2003) 250–303, URL `http://dx.doi.org/10.1016/S0168-9002(03)01368-8`.

[AH99]   Al-Haddad, M., Fayoumi, A. and Abu-Jarad, F., *Calibration of a Liquid Scintillation Counter to Assess Tritium Levels in Various Samples*, Nuclear Instruments and Methods in Physics Research Section A: Accelerators, Spectrometers, Detectors and Associated Equipment **438** (1999) 356–361, URL `http://dx.doi.org/10.1016/S0168-9002(99)00272-7`.

[Ale11]   Alecu, C. G. et al., *Reachable Accuracy and Precision for Tritium Measurements by Calorimetry at TLK*, Fusion Science and Technology **60** (2011) 937–940, URL `http://dx.doi.org/10.13182/FST11-A12569`.

[All11]   Allegro MicroSystems, *Driver Pololu A4988, DMOS Microstepping Driver with Translator And Overcurrent Protection*, Allegro MicroSystems (2011).

[Alv39]   Alvarez, W., L. and Cornog, R., *Helium and Hydrogen of Mass 3*, Phys. Rev. **56** (1939) 613–613, URL `http://dx.doi.org/10.1103/PhysRev.56.613`.

[Amp]   AmpTek, Materials Analysis Division, *MCA8000D, Pocket MCA, Digital Multichannel Analyzer*, AmpTek, Materials Analysis Division, Bedford Massachusetts, USA.

[ARD]   ARDUINO, *Arduino UNO REV3*, `https://www.arduino.cc/`.

[Arg11]   Argyriades, J. et al., *Spectral Modeling of Scintillator for the NEMO-3 and SuperNEMO Detectors*, Nuclear Instruments and Methods in Physics Research Section A: Accelerators, Spectrometers, Detectors and Associated Equipment **625** (2011) 20–28, URL `http://dx.doi.org/10.1016/j.nima.2010.09.027`.

[Aze18]   Azevedo, C. D. R. et al., *TRITIUM - A Real-Time Tritium Monitor System for Water Quality Surveillance*, in *2018 IEEE Nuclear Science Symposium and Medical Imaging Conference Proceedings (NSS/MIC)*, IEEE, Sidney, NSW, Australia, 1–6, URL `http://dx.doi.org/10.1109/NSSMIC.2018.8824700`.

[Aze20a]   Azevedo, C. et al., *Simulation Results of a Real-Time in Water Tritium Monitor*, Nuclear Instruments and Methods in Physics Research Section A: Accelerators, Spectrometers, Detectors and Associated Equipment **982** (2020) 164555, URL `http://dx.doi.org/10.1088/0370-1298/64/10/303`.

[Aze20b]   Azevedo, C. et al., *TRITIUM - A Quasi Real-Time Low Activity Tritium Monitor for Water*, in *European Physical Journal Web of Conferences*, volume 225, EPJ Web of Conferences, Portoroz, Slovenia, 03008, URL `http://dx.doi.org/10.1051/epjconf/202022503008`.

[Aze22]   Azevedo, C. et al., *Development of a Real-Time Tritium-in-Water Monitor* (2022), arXiv:2202.11068v1.

[BD13]   Bükki-Deme, A., Alecu, C., Kloppe, B. and Bornschein, B., *First Results With the Upgraded TLK Tritium Calorimeter IGC-V0.5*, Fusion Engineering and Design **88** (2013) 2865–2869, URL `http://dx.doi.org/10.1016/j.fusengdes.2013.05.066`.

[Ber98a]   Berthold, J. W. and Jeffers, L. A., *In-situ Tritium Beta Detector*, Technical Report AC21-96MC33128, Office of Scientific and Technical Information (OSTI.GOV), U.S. Department of Energy (1998), URL `http://dx.doi.org/10.2172/836625`.

[Ber98b]   Berthold, J. W. and Jeffers, L. A., *Phase 1 Final Report for In-Situ Tritium Beta Detector*, Technical Report AC21-96MC33128, Office of Scientific and Technical Information (OSTI.GOV), U.S. Department of Energy (1998), URL `http://dx.doi.org/10.2172/2225`.

[Bir51]   Birks, J. B., *Scintillations from Organic Crystals: Specific Fluorescence and Relative Response to Different Radiations*, Proceedings of the Physical Society. Section A **64** (1951) 874–877, URL `http://dx.doi.org/10.1088/0370-1298/64/10/303`.

[Bla91]   Blauvelt, R. K., Deaton, M. R. and Gill, J. T., *Health Physics Manual of Good Practices for Tritium Facilities*, Technical Report MLM-3719, Office of Scientific and Technical Information (OSTI.GOV), U.S. Department of Energy (1991), URL `http://dx.doi.org/10.2172/266889`.

[Bor19]   Born, Max and Wolf, Emil, *Principles of Optics: 60th Anniversary Edition*, Cambridge University Press, Cambridge, 7 edition (2019), URL `http://dx.doi.org/10.1017/9781108769914`.

[Bra15]   Bray, C., Pailloux, A. and Plumeri, S., *Tritiated Water Detection in the* 2.17 *μm Spectral Region by Cavity Ring Down Spectroscopy*, Nuclear Instruments and Methods in Physics Research

Section A: Accelerators, Spectrometers, Detectors and Associated Equipment **789** (2015) 43–49, URL `http://dx.doi.org/10.1016/j.nima.2015.03.064`.

[Bru19a] Brun, R. and Fons Rademakers, R., *ROOT - An Object Oriented Data Analysis Framework*, Nuclear Instrumentation and Method in Physics **389** (2019), URL `https://root.cern.ch/`.

[Bru19b] Brun, R. and Fons Rademakers, R., *ROOT - An Object Oriented Data Analysis Framework*, in *AIHENP'96 Workshop*, AIHENP, Lausanne, Switzerland, URL `https://root.cern.ch/`.

[Bui94] Buiteveld, H., Hakvoort, J. H. M. and Donze, M., *Optical Properties of Pure Water*, in J. S. Jaffe (Ed.), *Ocean Optics XII, Bergen, Norway, 26 October 1994*, volume 2258, International Society for Optics and Photonics, SPIE, Honolulu, Hi, USA, 174–183, URL `http://dx.doi.org/10.1117/12.190060`.

[Bun06] Bundesamt für Strahlenschutz, *Umweltradioaktivität und Strahlenbelastung : Jahresbericht 2005*, Technical report, Bundesamt für Strahlenschutz (2006), uRI: urn:nbn:de:0221-20100331990.

[CAE] CAEN SpA, *Quad Scaler And Preset Counter-Timer, N1145*, CAEN SpA.

[CAE91] CAEN SpA, *Model 84, 4 Channels Discriminator*, CAEN SpA (1991).

[Cal06] California EPA, *Responses to Major Comments on Technical Support Document Public Health Goal For Tritium In Drinking Water*, Office of Environmental Health Hazard Assessment, OEHHA, California, USA (2006).

[Cal10] Calmon, P. and Garnier-Laplace, J., *Tritium and the Environment. Radionuclide Sheet*, `https://www.irsn.fr/EN/Research/publications-documentation/radionuclides-`

sheets/environment/Pages/Tritium-environment.aspx
(2010), Institut de Radioprotection et de Sureté Nucléaire
(IRSN).

[CER]   CERN, *Module Coincidence 5 IN - 7 OUT FE260, N6234*,
            CERN.

[Che13]   Chen, Z., Peng, S., Meng, D., He, Y. and Wang, H., *Theoretical
            Study of Energy Deposition in Ionization Chambers for Tritium
            Measurements*, Review of Scientific Instruments **84** (2013) 650–
            659, URL http://dx.doi.org/10.1063/1.4825032.

[Com]   Computational Nuclear Physics Group (CNP), *Physics Simu-
            lation Packages, CRY (Cosmic-Ray Particle Showers)*, https:
            //nuclear.llnl.gov/simulation/.

[Con]   Consejo de Seguridad Nuclear (CSN), https://www.csn.es/
            home.

[CRE20]   CREMAT Inc., *CR 111-R2.1 Charge Sensitive Preamplifier*,
            CREMAT Inc., 07 (2020).

[CSNa]   CSN, *Red de Estaciones Automáticas (REA)*, https://www.
            csn.es/mapa-de-valores-ambientales.

[CSNb]   CSN, *Red de Estaciones de Muestreo (REM)*, https://www.csn.
            es/kprgisweb2/index.html?lang=es.

[Dep16]   Department of Energy (DOE), *DOE Handbook Primer on Tri-
            tium Safe Handling Practices*, U. S. Department of Energy Wash-
            ington, D.C. 20585 (2016).

[DYC]   DYCOMETAL, *Climatic Chamber Model CCK 85*, DY-
            COMETAL.

[Dé17]   Département Fédéral de l'Interieur (DFI), *Ordonnance du DFI
            sur les Substances Etrangeres et les Composants dans les Denreés*

Alimentaires (817.021.23), The Federal Council (Swiss Government), Switzerland (2017).

[EIA20]   EIA, *International Energy Outlook 2021 with projections to 2050*, U. S. Energy Information Administration, Office of Energy Analysis, U.S. Department of Energy, Washington, DC 20585, Washington, DC 20585, United States (2020).

[Env]   Environmental Protection Division, BNL, *Why is the High Flux Beam Reactor Being Decommissioned?*, `https://www.bnl.gov/hfbr/decommission.php`.

[EPA01]   EPA, *Radionuclides Rule: A Quick Reference Guide*, Technical Report EPA 816-F-01-003, (2001).

[Epi20]   Epic-Crystal, *Plastic Scintillator of Epic Crystal*, Epic-Crystal (2020).

[Eur13]   European Atomic Energy Community, *Laying Down Requirements for the Protection of the Health of the General Public with Regard to Radioactive Substances in Water Intended for Human Consumption*, Council directive 2013/15/euratom (2013).

[Eur14]   European Atomic Energy Community (EUROATOM), *Council Directive 2013/59/Euratom of 5 December 2013*, `https://eur-lex.europa.eu/eli/dir/2013/59/oj` (2014).

[Eur16]   Europa Press, *China Construirá al Menos 60 Centrales Nucleares en la Próxima Década*, `https://www.europapress.es/internacional/noticia-china-construira-menos-60-centrales-nucleares-proxima-decada-20160916210159.html` (2016).

[Eva95]   Evans, R. D., *The Atomic Nucleus*, McGraw-Hill, Inc., Bombay (1995), URL `https://www.academia.edu/28858622/Evans_The_atomic_nucleus`.

[Fer19]   Fermilab, *Tritium at Fermilab*, `https://www.fnal.gov/pub/tritium/` (2019).

[Fin93]   Finnish Centre for Radiation and Nuclear Safety, *Radiation and Nuclear Safety Authority. Radioactivity of Household Water*, Helsinki, Finland (1993).

[GEA]   GEANT4 Collaboration, *Geant4: A Toolkit for the Simulation of the Passage of Particles Through Matter*, `https://geant4.web.cern.ch/node/1`.

[Gob16]   Gobierno de España, *Real Decreto 314/2016, de 29 de julio, por el que se modifican el Real Decreto 140/2003, de 7 de febrero, por el que se establecen los criterios sanitarios de la calidad del agua de consumo humano, el Real Decreto 1798/2010, de 30 de diciembre, por el que se regula la explotación y comercialización de aguas minerales naturales y aguas de manantial envasadas para consumo humano, y el Real Decreto 1799/2010, de 30 de diciembre, por el que se regula el proceso de elaboración y comercialización de aguas preparadas envasadas para el consumo humano.* (2016) 53106–53126.

[GRB]   GRBL, *GRBL Package of Arduino*, `https://github.com/grbl/grbl/wiki`.

[Gui11]   Guillén, M., Pérez-Cabello, F. and Casterad, M., *Aplicabilidad del uso de un panel de PTFE (politetrafluroetileno) como blanco de referencia*, in *XIV Congreso de la Asociación Española de Teledetección*, Asociación Española de Teledetección, Mieres, Spain, 4, URL `http://dx.doi.org/10.1109/NSSMIC.2007.4437209`.

[Hag07]   Hagmann, C., Lange, D. and Wright, D., *Cosmic-ray Shower Generator (CRY) for Monte Carlo Transport Codes*, in *2007 IEEE Nuclear Science Symposium Conference Record*, IEEE,

Honolulu, Hi, USA, 1143–1146, URL `http://dx.doi.org/10.1109/NSSMIC.2007.4437209`.

[Hai14]   Haight, R., Wermer, J. and Fikani, M., *Tritium Production by Fast Neutrons on Oxygen: An Integral Experiment*, Journal of Nuclear Science and Technology **39** (2014) 1232–1235, URL `http://dx.doi.org/10.1080/00223131.2002.10875326`.

[Ham10]   Hamamatsu Photonics K.K., *Photomultiplier tube R2154-02 2*, `https://www.hamamatsu.com/eu/en/product/type/R2154-02/index.html` (2010).

[Ham15]   Hamamatsu Photonics K.K., *High Voltage Power Supply C11152-01*, `https://www.hamamatsu.com/jp/en/product/type/C11152-01/index.html` (2015).

[Ham16a]   Hamamatsu Photonics K.K., *MPPC Multi-Pixel Photon Counter S13360-1325*, `https://www.hamamatsu.com/eu/en/product/type/S13360-1325PE/index.html` (2016).

[Ham16b]   Hamamatsu Photonics K.K., *MPPC Multi-Pixel Photon Counter) S13360-1375*, `https://www.hamamatsu.com/jp/en/product/type/S13360-1375CS/index.html` (2016).

[Ham16c]   Hamamatsu Photonics K.K., *MPPC Multi-Pixel Photon Counter S13360-6050*, `https://www.hamamatsu.com/eu/en/product/type/S13360-6050CS/index.html` (2016).

[Ham16d]   Hamamatsu Photonics K.K., *MPPC Multi-Pixel Photon Counter S13360-6075*, `https://www.hamamatsu.com/eu/en/product/type/S13360-6075CS/index.html` (2016).

[Ham16e]   Hamamatsu Photonics K.K., *MPPC Multi-Pixel Photon Counter S13361-6050-04*, `https://www.hamamatsu.com/eu/en/product/optical-sensors/mppc/mppc_mppc-array/S13361-6050NE-04.html` (2016).

[Ham19]   Hamamatsu Photonics K.K., *Photomultiplier Tube R8520-406/R8520-506*, `https://www.hamamatsu.com/eu/en/product/type/R8520-406/index.html` (2019).

[Han]   Hanna Instruments, *Multiparamétrico con Opciones GPS, Sonda Autoregistradora, Turbidez e ISE*, Hanna Instruments.

[Hof92a]   Hofstetter, K. J. and Wilson, H. T., *Aqueous Effluent Tritium Monitor Development*, Fusion Technology **21** (1992) 446–451, URL `http://dx.doi.org/10.13182/FST92-A29786`.

[Hof92b]   Hofstetter, K. J. and Wilson, H. T., *Continuous Tritium Effluent Water Monitor at the Savannah River Site*, Technical Report DE93002157, Office of Scientific and Technical Information (OSTI.GOV), U.S. Department of Energy (1992).

[Hou18]   Hou, X., *Tritium and ^{14}C in the Environment and Nuclear Facilities: Sources and Analytical Methods*, Journal of Nuclear Fuel Cycle and Waste Technology **16** (2018) 11–39, URL `http://dx.doi.org/10.7733/jnfcwt`.

[Hyd16]   Hydro Quebec, *Résultats du Programme de Surveillance de l'Environnement du Site de Gentilly-2*, National Library, Québec, Canada (2016).

[IAE]   IAEA, *Nuclear Data Services*, `https://www-nds.iaea.org`.

[ICR91]   ICRP, *1990 Recommendations of the International Commission on Radiological Protection, Publication 60*, Ann. ICRP **21** (1991) 1–193, URL `https://www.icrp.org/publication.asp?id=icrp%20publication%2060`.

[ICR96]   ICRP, *Age-Dependent Doses to Members of the Public From Intake of Radionuclides: Part 5. Compilation of Ingestion and Inhalation Dose Coefficients, Publication 72*, Ann. ICRP **26**

(1996) 1–91, URL `https://www.icrp.org/publication.asp?id=ICRP%20Publication%2072`.

[IGU]   IGUS S.L., *Carro transversal Drylin-SLW*, `https://www.igus.es/info/linear-guides-drylin-cross-slide`.

[Ind]   Industrial Fiber Optics, *POF Cutter Block*, `https://i-fiberoptics.com/tool-detail.php?id=105&cat=cutters`.

[Inta]   International Commission on Radiological Protection (ICRP), `https://www.icrp.org/`.

[Intb]   International Commission on Radiological Units and Measurements (ICRU), `https://www.icru.org/`.

[Intc]   International Society of Radiology (ISR), `https://www.isradiology.org/`.

[Int07]   International Council for Science (UCSU), World Data System, *NRB-99 Radiation Safety Norms*, World Data Centers, Russia and Ukraine (2007).

[Int14]   International Energy Agency, *Key World Energy Statistics*, `https://www.iea.org/publications/freepublications/publication/KeyWorld2014.pdf` (2014).

[Int16]   Interreg Sudoe Program, *TRITIUM Project*, `https://www.interreg-sudoe.eu/gbr/projects/the-approved-projects/158-design-construction-and-commissioning-of-a-low-level-tritium-monitor-for-water` (2016).

[Int19]   Integrated Circuits, *Driver TMC2208, Step/Dir Drivers for Two-Phase Bipolar Stepper Motors up to 2A peak- StealthChop for Quiet Movement- UART Interface Option*, Integrated Circuits (2019).

[ISO]   ISOTECH, *GPS-4303 Digital Bench Power Supply With UKAS Calibration, 4 Output*, ISOTECH.

[JB10]   Jean-Baptiste, P. et al., *^{3}He Mass Spectrometry for Very Low-Level Measurement of Organic Tritium in Environmental Samples*, Journal of Environmental Radioactivity **101** (2010) 185–190, URL `http://dx.doi.org/10.1016/j.jenvrad.2009.10.005`.

[Keia]   Keithley Instruments, *Model 6487 Picoammeter/Voltage Source*, Keithley Instruments.

[Keib]   Keithley Instruments, *Model 6517B Electrometer User's Manual*, Keithley Instruments.

[Khe02]   Kherani, N., *An Alternative Approach to Tritium-in-Water Monitoring*, Nuclear Instruments and Methods in Physics Research Section A: Accelerators, Spectrometers, Detectors and Associated Equipment **484** (2002) 650–659, URL `http://dx.doi.org/10.1016/S0168-9002(01)02008-3`.

[Kno10]   Knoll, G. F., *Radiation Detection and Measurement*, John Wiley & Sons, Inc., 4 edition (2010), URL `https://www.wiley.com/en-sg/Radiation+Detection+and+Measurement,+4th+Edition-p-9780470131480`.

[Law06]   Law, S. et al., *Cleaving of Microstructured Polymer Optical Fibres*, Optics Communications **258** (2006) 193–202, URL `http://dx.doi.org/10.1016/j.optcom.2005.08.011`.

[LeC]   LeCroy, *Model 465 Coincidence Unit*, LeCroy.

[Lee18]   Lee, J. et al., *Tissue Distribution, Excretion and Effects on Genotoxicity of Tritium Following Oral Administration to Rats*, Nuclear Engineering and Technology **51** (2018), URL `http://dx.doi.org/10.1016/j.net.2018.09.013`.

[Leo94]   Leo, W. R., *Techniques for Nuclear and Particle Physics Experiments: a How-to Approach*, Springer-Verlag Berlin Heidelberg GmbH, New York, 2 edition (1994), URL `http://dx.doi.org/10.13182/FST92-A29786`.

[Lev11]   Leverington, B. D., Anelli, M., Campana, P. and Rosellini, R., *A 1 mm Scintillating Fibre Tracker Readout by a Multi-anode Photomultiplier* (2011), URL `http://dx.doi.org/10.48550/arXiv.1106.5649`, arXiv:1106.5649v2.

[Lin]   Linear Technologies, Inc., *LT111A Voltage Comparator*, Linear Technologies, Inc.

[Lin20]   Lin, Z., *Simulation and Optimization Design of SiC-Based PN Betavoltaic Microbattery Using Tritium Source*, Crystals **10** (2020) 1–11, URL `http://dx.doi.org/10.3390/cryst10020105`.

[Mar72]   Martin, J. R. and Koranda, J. J., *Biological Half-Life Studies of Tritium in Chronically Exposed Kangaroo Rats*, Radiation Research **50** (1972) 426–440, URL `http://dx.doi.org/10.2307/3573500`.

[Mas21]   Masuda, T. and Yoshioka, T., *Estimation of Radiation Dose from Ingested Tritium in Humans by Administration of Deuterium-Labelled Compounds and Food*, Scientific Reports **11** (2021) 1232–1235, URL `http://dx.doi.org/10.1038/s41598-021-82460-5`.

[Mat07]   Matsuyama, M., Torikai, Y., Hara, M. and Watanabe, K., *New Technique for Non-Destructive Measurements of Tritium in Future Fusion Reactors*, International Atomic Energy Agency (IAEA) **47** (2007) S464–S468, URL `http://dx.doi.org/10.1088/0029-5515/47/7/s09`.

[Mat08]   Matsuyama, M., *Development of a New Detection System for Monitoring High-Level Tritiated Water*, Fusion Engineering and Design **83** (2008) 1438–1441, URL `http://dx.doi.org/10.1016/j.fusengdes.2008.05.023`, proceedings of the Eight International Symposium of Fusion Nuclear Technology.

[Max09]   Maxim Integrated, *Low-Power, Quad, 12-Bit, Votlage-Output DACs with Serial Interface*, Maxim Integrated (2009).

[Mer15]   Mertens, S. et al., *Sensitivity of Next-Generation Tritium Beta-Decay Experiments for keV-Scale Sterile Neutrinos*, Journal of Cosmology and Astroparticle Physics **2015** (2015) 1–24, URL `http://dx.doi.org/10.1088/1475-7516/2015/02/020`.

[Mir]   Mirion Technologies (Camberra) SAS, *Tennelec Model TC 952 High Voltage Supply*, Mirion Technologies (Camberra) SAS.

[Mog69]   Moghissi, A., Kelley, H., Phillips, C. and Regnier, J., *A Tritium Monitor Based on Scintillation*, Nuclear Instruments and Methods **68** (1969) 159, URL `http://dx.doi.org/10.1016/0029-554X(69)90705-8`.

[Mur67]   Muramatsu, M., Koyano, A. and Tokunaga, N., *A Scintillation Probe for Continuous Monitoring of Tritiated Water*, Nuclear Instruments and Methods **54** (1967) 325–326, URL `http://dx.doi.org/10.1016/0029-554X(67)90645-3`.

[Nan06]   Nanotec, *ST4209S1404-A - Stepper Motor NEMA 17*, Nanotec (2006).

[NHM21]   NHMRC, NRMMC, *Australian Drinking Water Guidelines Paper 6. National Water Quality Management Strategy*, National Health and Medical Research Council, National Resource Management Ministerial Council, Commonwealth of Australia, Camberra (2021).

[Nie15]   Niemes, S., Sturm, M., Michling, R. and Bornschein, B., *High Level Tritiated Water Monitoring by Bremsstrahlung Counting Using a Silicon Drift Detector*, Fusion Science and Technology **67** (2015) 507–510, URL `http://dx.doi.org/10.13182/FST14-T66`.

[Noe19]   Noelia Lopez Redondo, *Estados Unidos Anuncia una Inversión de 35 Millones para las Centrales Nucleares*, *Energy News*, `https://www.energynews.es/estados-unidos-centrales-nucleares/` (2019).

[Oli34]   Oliphant, M. L., Harteck, P. and Rutherford, E., *Transmutation Effects observed with Heavy Hydrogen*, The Royal Society Publishing **133** (1934) 23–28, URL `http://dx.doi.org/10.1098/rspa.1934.0077`.

[OME94]   OME, *Ontario Drinking Water Objectives*, Ontario Ministry of Environment, Toronto, Ontario (1994).

[ORTa]   ORTEC, AMETEK, *Model 416A Gate and Delay Generator*, ORTEC, AMETEK, South Illinois Ave., Oak Ridge, USA.

[ORTb]   ORTEC, AMETEK, *Model 575A Amplifier*, ORTEC, AMETEK, South Illinois Ave., Oak Ridge, USA.

[ORTc]   ORTEC, AMETEK, *Model 671 Spectroscopy Amplifier*, ORTEC, AMETEK, South Illinois Ave., Oak Ridge, USA.

[ORTd]   ORTEC, AMETEK, *Model 9326 FastPreamplifier*, ORTEC, AMETEK, South Illinois Ave., Oak Ridge, USA.

[ORTe]   ORTEC, AMETEK, *Model CF8000 Octal Constant-Fraction Discriminator*, ORTEC, AMETEK, South Illinois Ave., Oak Ridge, USA.

[Osb70]   Osborne, R., *Detector for Tritium in Water*, Nuclear Instruments and Methods **77** (1970) 170–172, URL `http://dx.doi.org/10.1016/0029-554X(70)90596-3`.

[OSI]   OSI Optoelectronics, *Characteristics and Applications*, `https://osioptoelectronics.com/standard-products/silicon-photodiodes.aspx`.

[OSO17]   OSOYOO, *CNC Shield V3.0*, OSOYOO (2017).

[Pal07]   Palomo, M., Peñalver, A., Aguilar, C. and Borrull, F., *Tritium Activity Levels in Environmental Water Samples from Different Origins*, Applied Radiation and Isotopes **65** (2007) 1048–1056, URL `http://dx.doi.org/10.1016/j.apradiso.2007.03.013`.

[PET]   PETsys, *PETsys Electronics*   ,
`https://www.petsyselectronics.com/web/`.

[PF81]   Pietrzak-Flis, Z., Radwan, I., Major, Z. and Kowalska, M., *Tritium Incorporation in Rats Chronically Exposed to Tritiated Food or Tritiated Water for Three Successive Generations*, Journal of Radiation Research **22** (1981) 434–442, URL `http://dx.doi.org/10.1269/jrr.22.434`.

[Phi]   Phillips Scientific, *Model 740 Quad Linear Fan-In/Out*, Phillips Scientific.

[Phy]   Physikalish-Technische Bundesanstalt (PTB), `https://www.ptb.de/cms/`.

[Ras]   Raspberry Pi Foundation, `https://www.raspberrypi.org/`.

[Rat00]   Rathnakaran, M., Revetkar, R. M., Samant, R. K. and Abani, M. C., *A Real-time Tritium-In-Water Monitor for Measurement Of Heavy Water Leak To The Secondary Coolant*, in *IRPA-10:*

10. International Congress of the International Radiation Protection Association, Japan Health Physics Society, Hiroshima, Japan, URL `https://inis.iaea.org/search/search.aspx?orig_q=RN:32015986`.

[Red19]   Red Eléctrica de España, *Informe del Sistema Eléctrico Español*, `https://www.ree.es/es/datos/publicaciones/informe-anual-sistema/informe-del-sistema-electrico-espanol-2019` (2019).

[Roi10]   Roithner LaserTechnik Gmbh, *LED435-03, 20 mW, 20 mA*, Roithner LaserTechnik Gmbh (2010).

[Ré18]   Réseau National de mesures de la radioactivité de l'environmennement, *Bilan de l'État Radiologique de l'Environnement Français de 2015 à 2017*, Institut de Radioprotection et de Sûreté Nucléaire (IRSN), France (2018).

[Sag12]   Sagawa, H. and Urabe, I., *Estimation of Absorbed Dose Rates in Air Based on Flux Densities of Cosmic Ray Muons and Electrons on the Ground Level in Japan*, Journal of Nuclear Science and Technology **38** (2012) 1103–1108, URL `http://dx.doi.org/10.1080/18811248.2001.9715142`.

[Saia]   Saint-Gobain Crystals, `https://www.crystals.saint-gobain.com/#`.

[Saib]   Saint-Gobain Crystals, *BC-630, Silicone Optical Grease*, `https://www.crystals.saint-gobain.com/`.

[Sai21a]   Saint-Gobain Crystals, *Optical fiber BCF-98*, Saint-Gobain Crystals, United States (2021).

[Sai21b]   Saint-Gobain Crystals, *Scintillating Optical Fibers, It's What's Inside that Counts*, Saint-Gobain Crystals, United States (2021).

[Sai21c]   Saint-Gobain Crystals, *Scintillating Plastic Grown with Polymeric Method*, Saint-Gobain Crystals, United States (2021).

[San]   San Nopco Limited, Japan, *Wetting Agents*, `https://www.sannopco.co.jp/eng/products/function/function4.php`.

[Saw00]   Sawodni, A., Pazdur, A. and Pawlyta, J., *Measurements of Tritium Radioactivity in Surface Water on the Upper Silesia Region*, Geochronometría **18** (2000) 23–28, URL `http://yadda.icm.edu.pl/baztech/element/bwmeta1.element.baztech-article-BAT3-0035-0005`.

[Sen17]   SensL Sense Light, *Introduction to the SPM Technical Note*, SensL Sense Light (2017).

[Sha97]   Shah, K. S., Gothoskar, P., Farrell, R. and Gordon, J., *High Efficiency Detection of Tritium Using Silicon Avalanche Photodiodes*, IEEE Transactions on Nuclear Science **44** (1997) 774–776, URL `http://dx.doi.org/10.1109/23.603750`.

[Sig94]   Sigg, R., McCarty, J., Livingston, R. and Sanders, M., *Real-time Aqueous Tritium Monitor Using Liquid Scintillation Counting*, Nuclear Instruments and Methods in Physics Research Section A: Accelerators, Spectrometers, Detectors and Associated Equipment **353** (1994) 494–498, URL `http://dx.doi.org/10.1016/0168-9002(94)91707-8`.

[Sin85]   Singh, A., Ratnakaran, M. and Vohra, K., *An On-Line Tritium-in-Water Monitor*, Nuclear Instruments and Methods in Physics Research Section A: Accelerators, Spectrometers, Detectors and Associated Equipment **236** (1985) 159–164, URL `http://dx.doi.org/10.1016/0168-9002(85)90141-X`.

[Sol17]   Soler Cambra, A., *Contribución al Desarrollo de un Prototipo de Detector de Fibras Centelleadoras para la Medición de Tritio en*

Agua (2017), Trabajo final de grado (TFG) de la Universidad de Valencia.

[Spi97]   Spinelli, A. and Lacaita, A., *Physics and Numerical Simulation of Single Photon Avalanche Diodes*, IEEE Transactions on Electron Devices **44** (1997) 1931–1943, URL http://dx.doi.org/10.1109/16.641363.

[SR15]   Sáez-Rodríguez, D., Nielsen, K., Bang, O. and Webb, D. J., *Simple Room Temperature Method for Polymer Optical Fibre Cleaving*, Journal of Lightwave Technology **33** (2015) 4712–4716, URL http://dx.doi.org/10.1109/JLT.2015.2479365.

[Str93]   Straume, T. and Carsten, A. L., *Tritium Radiobiology and Relative Biological Effectiveness*, Health Physics **65** (1993) 657–72, URL http://dx.doi.org/10.1097/00004032-199312000-00005.

[Szu15]   Szucs, T. et al., *Cosmic-Ray-Induced Background Intercomparison with Actively Shielded HPGe Detectors at Underground Locations*, The European Physical Journal A **51** (2015) 1–9, URL http://dx.doi.org/101140/epja/i2015-15033-0.

[Tek21]   Tektronix, Inc., *Mixed Signal Oscilloscope, Model MSO44*, Tektronix, Inc. (2021).

[Tel17]   Teledyne LeCroy, *WaveRunner 6 Zi Oscilloscopes400 MHz –4 GHz*, Teledyne LeCroy (2017).

[Tex14]   Texas Instruments, *DRV8825 Stepper Motor Controller IC*, Texas Instruments (2014).

[Tex15]   Texas Instruments, *OPA656 Wideband, Unity-Gain Stable, FET-Input Operational Amplifier*, Texas Instruments (2015).

[Tex16]   Texas Instruments, *SN74LVC1G11DBVR Single 3-Input Positive-AND Gate*, Texas Instruments (2016).

[Tex17]   Texas Instruments, *SN74AHC1G32 Single 2-Input Positive-OR Gate*, Texas Instruments (2017).

[Thea]   The International Atomic Energy Agency (IAEA), `https://www.iaea.org/`.

[Theb]   The United Nations Scientific Committee on the Effects of Atomic Radiation (UNSCEAR), `https://www.unscear.org/`.

[The96]   Theodórsson, P., *Measurement of Weak Radioactivity*, World Scientific (1996), URL `http://dx.doi.org/10.1142/2800`.

[Thoa]   Thorlabs, Inc., `https://www.thorlabs.com/`.

[Thob]   Thorlabs Inc., *BK5 - Black Nylon, Polyurethane-Coated Fabric, 5' × 9' (1.5m × 2.7m) × 0.005" (0.12 mm) Thick*, Thorlabs Inc.

[Thoc]   Thorlabs Inc., *Fiber Polishing Supplies*, Thorlabs Inc.

[Tho06]   Thorlabs Inc., *Guide to Connectorization and Polishing Optical Fibers*, Thorlabs Inc. (2006).

[Tho18]   Thorlabs, Inc., *LED430L - 430 nm LED with a Glass Lens, 8 mW, TO-18*, Thorlabs, Inc. (2018).

[Val07]   Valverde Hermosilla, M., *Interacción Neutrino-núcleo a Energías Intermedias*, Ph.D. thesis, University of Granada, Granada, Spain (2007).

[Wen]   Wenzel Electronik GmbH, *Model N 1330-4 High Voltage Power Supply*, Wenzel Electronik GmbH.

[WHO17]   WHO, *Guidelines for Drinking-Water Quality*, volume 1, World Health Organization, Geneva, 3 edition (2017).

[Wor20]   World Nuclear Association, *Three mile island accident*, `https://www.world-nuclear.org/information-`

`library/safety-and-security/safety-of-plants/three-mile-island-accident.aspx` (2020).

[Zyl20]   Zyla, P.A. et al., *Review of Particle Physics*, Prog. Theor. Exp. Phys. **2020** (2020) 083C01, URL `http://dx.doi.org/10.1093/ptep/ptaa104`.